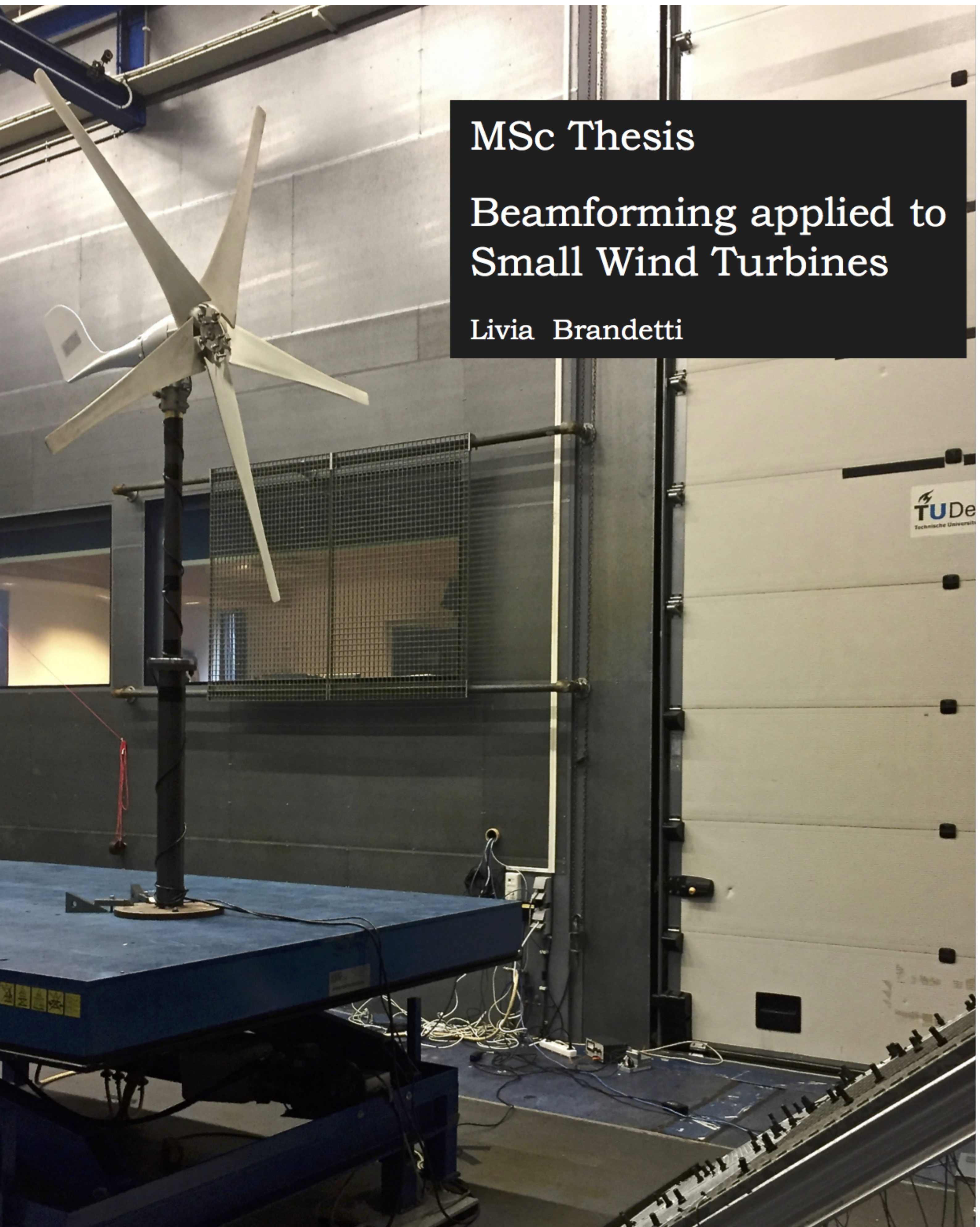

MSc Thesis

Beamforming applied to Small Wind Turbines

Livia Brandetti

TU Delft Delft University of Technology

Challenge the future

MSc Thesis

Beamforming applied to Small Wind Turbines

by

Livia Brandetti

to obtain the degree of Master of Science
at the Delft University of Technology,
to be defended publicly on Thursday September 27, 2018 at 14:00.

Student number:	4623789	
Project duration:	January 10, 2018 – September 27, 2018	
Thesis committee:	Prof. dr. D. G. Simons	TU Delft, C & O, ANCE, Chairman
	Dr. ir. M. Snellen	TU Delft, C & O, ANCE, Supervisor
	Dr. ir. F. Avallone	TU Delft, WE, Supervisor
	Dr. ir. M. Zaayer	TU Delft, WE

An electronic version of this thesis is available at `http://repository.tudelft.nl/`.

Summary

The increase of energy consumption as well as the need to reduce green house emissions trigger the shift from a fossil-fuel based society towards a sustainable society. With a constant increase in the installed power capacity, wind plays a key role in the global energy framework. The improvement of the technology opens up new targets for the wind development [28]. In particular, the installation of small wind turbines in the urban environment represents a promising solution to supply residential power. Whilst, some of the problems faced by large-scale wind farms, like losses in the electrical distribution and transportation system, can be reduced. However, the immaturity of the technology leads to elevated capital costs and technical challenges [41]. Among these disadvantages, the siting near human activities is limited by the sound emitted by small wind turbines [65].

The current work focuses on the aerodynamic noise produced by horizontal-axis small wind turbines. For this purpose, the rotational beamforming algorithm, ROSI (i.e. ROtating Source Identifier), together with microphone array measurements, have been used. The ability of the method to follow the movement of the sound source is essential to correctly localize and quantify the rotating sound source. ROSI is applied in the time domain: first, for every source position a time history reconstruction of the signal recorded at each microphone is performed. Then, the microphone signals are sampled for every emission time, leading to the de-Dopplerisation of the signals. Last step is to sum all de-Dopplerised signals and to repeat this procedure for each scan point [33].

In order to validate the technique, the ROSI performance has been investigated with an increasing degree of uncertainty: initially, under ideal and know conditions with simulated datasets and, then, applying ROSI to experimental data. The results of the simulations show that ROSI is not influenced neither by the rotational speed of the source or by the selected time snapshot. Furthermore, the differences in the beamformed results always agree with the differences in the source level, proving that ROSI can be used to compare different blade or turbine geometries. Additionally, the ROSI performance is in agreement with the Rayleigh limit. In fact, if the spacing between the sound source is below the Rayleigh limit, the sources are not distinguished as separated and their SPLs are not correctly estimated. As regards the experimental approach, a small-scale prototype simulating the acoustic of a small wind turbine was tested in the Anechoic Tunnel facility while an upwind turbine was measured in the Open Jet Facility, varying both the wind speeds of the tunnel and the rotational speed of the blades. The two facilities are located at the TU Delft University. During the first experiment, the measurement geometry is verified and the resulting outcomes are compared with the simulations. It is confirmed both that the rotational speed does not limit the ROSI performance and that the source localization and quantification are affected by the Rayleigh limit. As regards the last experiment, the ROSI uncertainty is investigated in a non-anechoic environment. In the range of frequencies where the wind turbine noise is expected (i.e. 500 Hz - 2000 Hz [60]), the high levels of background noise do not allow to localize and to quantify the main noise sources in the small wind turbine. Thus, the wind turbine noise is not assessed and the experimental data are not compared with the analytical noise models, provided in literature.

Acknowledgements

Delft, 27^{th} September 2018

It was the 22nd of August 2016 when I arrived in Delft to start my Master in Sustainable Energy Technology. Today, this incredible journey will come to an end and I am so grateful to every single moment and to every single thing that I have learnt. I am very proud of this nine-months research and I would like to thank all the people who have participated.
First of all, I would like to thank Prof dr. Dick Simons for being my graduation professor and for giving me an insight of all the acoustic phenomena occurring in my project.
Thanks to Dr. Mirjam Snellen, one of my supervisor, for introducing me in the world of acoustic imaging and for teaching me how to be a meticulous researcher. Every meeting was for me an opportunity to learn and to understand the true essence of this research.
Many thanks to my daily supervisor, Dr. Francesco Avallone. Thanks for your feedbacks, your great enthusiasm and your patience. Thanks for sharing with me your motivation and your attention to details (because the Devil is in the details!). Every day I was able to appreciate how much love you put in your job. I will always be grateful to you!
A big applause to Dr. Daniele Ragni! Even if you are not my supervisor, you have been always available to solve any kind of issues and to give me advices and support. Thanks for helping me in the preparation of all the experimental set-up, for carrying microphone arrays from one lab to another and for always sharing your energy with me. Together with Francesco, you helped me to grow both personally and professionally, by stimulating my interest in the research.
Then, I would like to thank Dr. Michiel Zaayer for his interest in my project by being part of my Thesis Committee today.
This biggest achievement would have never been possible without my friends and my family.
Thanks to Marco, Andrea, Raffaello, Nicola, Filippo and Giacomo for being my family in these two years. A special thanks to Francesca, for always being there since the beginning. We literally lived in the library these past months but in the end we made it!
Thanks to all the guys from the WE Master Thesis room for laughing, stressing, eating (cake is always a good idea!) and having fun together.
Thanks to my best friend Maria Luisa. We discovered Delft together for the first time and we immediately fall in love. A distance of 1,634 km is nothing for us!
Thanks to Carolina, the shape of my heart, for encouraging me to start this adventure and for always giving me the best advice.
Thanks to all the rest of my friends in Rome and around the World. You are simply amazing!
Thanks to Francesca, Fabiana, Tullia and Roberto because you have always made me feel the little genius of this family.
Thanks to my dad and my sister, Giulia, who are the sunshine of my life. Thanks for supporting me in every decision, for always believing in me and for always being so proud of me. You will do whatever you can for making me happy. I am so lucky and I love you so much!
Thanks to my mum, my inspiration and my strength. You are next to me every single day of my life. I hope you will be proud of me because everything is for you!
Last but not least, thanks to Alessandro, the love of my life. You have been involved in this project more than anyone else. Thanks for listening to my presentations, for giving me feedbacks, for understanding me and my craziness and for living the Dutch's life with me. We are stargazers and everything amazes us. I love you!

Enjoy the reading!

Livia Brandetti

Contents

Symbols

Abbreviations

A-Tunnel	Anechoic-Tunnel
BPM	Brooks, Pope and Marcolini
CB	Conventional Beamforming
CCP	Constant Current Power
CFD	Computational Fluid Dynamics
DAS	Data Acquisition System
DC	Direct Current
DFT	Discrete Fourier Transform
DNS	Direct Numerical Simulation
EU	European Union
FFT	Fast Fourier Transform
FH-W	Ffwocs Hall - Williams
HAWT	Horizontal Axis Wind Turbine
IEC	International Electrotechnical Commission
IIR	Infinite Impulse Response
LBL-VS	Laminar Boundary Layer - Vortex Shedding Noise
LES	Large Eddy Simulation
NI	National Instruments
OJF	Open Jet Facility
ROSI	ROtating Source Identifier
SPI	Source Power Integration
SS	Separation-Stall noise
TBL-TE	Turbulent Boundary Layer - Trailing Edge Noise
TEB-VS	Trailing Edge Blunt - Vortex Shedding Noise

TP	Tip Noise	
TU	Technische Universiteit	
VAWT	Vertical Axis Wind Turbine	

Greek symbols

α	angle of attack	[degree]
α_{tip}	angle of attack of the tip blade	[degree]
δ_c	characteristic length of the turbulence	[m]
δ_l	boundary layer thickness	[m]
$\delta_{l,p}$	boundary layer thickness at the pressure side	[m]
δ_l^*	boundary layer displacement thickness	[m]
$\delta^*_{\mathrm{l,avg}}$	average between the boundary layer displacement thickness at the pressure side and at the suction side	[m]
$\delta^*_{l,p}$	boundary layer displacement thickness at the pressure side	[m]
$\delta^*_{l,s}$	boundary layer displacement thickness at the suction side	[m]
δt	time delay	[s]
$\delta t_{m,0}$	time delay between microphone m and scan point 0	[s]
$\delta t_{m,j}$	time delay between microphone m and scan point j	[s]
θ	angle between velocity vector and source-observer line	[degree]
κ	directivity angle	[degree]
λ	source wavelength	[m]
λ'	observed wavelength	[m]
ν	kinematic viscosity of the fluid	[m^2/2]
ξ_j	coordinates of the scan point j	[-]
ρ	density of the fluid	[kg/m^3]
ρ_∞	air density	[kg/m^3]
Ψ	trailing edge solid angle	[degree]
$\vec{\Omega}$	rotational speed of the sound source	[rps]

Roman symbols

A	area	[m^2]
b	frequency component	[-]
$\vec{B}$	source auto-power	[-]
B_j	source auto-power for scan point j	[-]
c	sound speed	[m/s]
$\vec{C}$	Cross Spectral Matrix	[-]
D	array aperture	[m]
$\bar{D}_l$	directivity function	[-]
$\bar{D}_{\mathrm{H}}$	directivity function	[-]
DI	directivity index	[dB]
f	frequency	[Hz]
$f^{'}$	observed frequency	[Hz]
f_b	frequency component of the acoustic signal	[Hz]
f_L	lower frequency	[Hz]
$f_{L/2}$	upper limit for the frequency	[Hz]
f_n	nominal frequency	[Hz]
$f_{n,max}$	frequency of the primary tone	[Hz]
$f_{n,tone}$	frequency of the n tone	[Hz]
f_{peak}	peak frequency	[Hz]
f_s	sampling frequency	[Hz]
$f_{s,center}$	center frequency of the broadband sound	[Hz]
f_U	upper frequency	[Hz]
F(St)	universal sepctral shape function	[-]
F_1	spectral shape function defined for TBL-TE noise and separation noise	[-]
$\mathrm{F}_1^{'}$	spectral shape function defined for TBL-TE noise and separation noise	[-]
F_2	spectral shape function defined for TBL-TE noise and separation noise	[-]

F_3	spectral shape function defined for for LBL-VS noise	[-]
F_4	spectral shape function defined for LBL-VS noise	[-]
F_5	spectral shape function defined for LBL-VS noise	[-]
$\vec{g}$	steering vector	[-]
g_m	component of steering vector	[-]
h	altitude	[m]
h_t	trailing edge thickness	[m]
He	Helmholtz number	[-]
I	sound intensity	[W/m^2]
I_0	reference sound intensity	[W/m^2]
j	scan point	[-]
J	total number of scan points	[-]
k	wave number	[m^{-1}]
K	empirical constant	[-]
K_1	constant	[-]
K_2	constant	[-]
l	sample	[-]
l_s	length of the surface	[m]
L	lift	[N]
$\mathscr{L}$	characteristic turbulence correction scale	[m]
L_a	A-weighted sound pressure level	[dB]
L_b	span length of the blade	[m]
L_c	airfoil chord	[m]
L_s	total number of samples	[-]
L_{TP}	span wise extent of the vortex at the trailing edge	[m]
m	number of microphone	[-]
M	Mach number	[-]
$M^{'}$	total number of microphones	[-]

MLW	Main Lobe Width	[dB]
MSL	Maximum Side lobe Level	[dB]
$\mathcal{N}$	non-linear operator	[-]
N_{blades}	number of blades of a wind turbine	[-]
OASPL	Overall A-weighted Sound Pressure Level	[dBA]
OSPL	Overall Sound Pressure Level	[dB]
p	sound pressure signal	[Pa]
p'	instantaneous sound pressure signal	[Pa]
p_e	effective pressure	[Pa]
$p_{e,noise}$	effective noise pressure	[Pa]
$p_{\vec{\xi}_0}$	pressure at scan point $\vec{\xi}_0$	[Pa]
p_j	reconstructed sound pressure fo scan point j	[Pa]
p_m	pressure measured by microphone m	[Pa]
p_{max}	maximum pressure	[Pa]
p_{ref}	reference pressure	[Pa]
$\tilde{p}_{m,l}$	discretisation of sound pressure measured by microphone m	[Pa]
P	Fourier transform of sound pressure	[Pa]
$\vec{P}$	pressure vector	[Pa]
P_{ξ_j}	Fourier transform of sound pressure at scan point ξ_j	[Pa]
P_{ξ_0}	Fourier transform of sound pressure at scan point ξ_0	[Pa]
P_m	Fourier transform of sound pressure at microphone m	[Pa]
PBL	Pressure Band Level	[dB]
PSD	Power Spectral Density	[dB/Hz]
PSL	Pressure Spectrum Level	[dB]
PWL	Power Watt Level	[dB]
q	incoherent sound source	[-]
Q	total number of incoherent sound source	[-]
r	distance between the microphone and the sound source	[m]

r_0	reference distance from the sound source	[m]
$r_{m,0}$	distance between microphone m and scan point 0	[m]
$\vec{r}_{m,j}$	distance between microphone m and scan point j	[-]
R	distance between the receiver and the edge of the airfoil	[m]
R_a	Rayleigh limit	[-]
R_e	Reynolds number	[-]
$R_{e,0}$	reference Reynolds number	[-]
$\mathrm{R}_{\mathrm{rotor}}$	rotor radius	[m]
RPM	rotational speed	[rpm]
RPS	Round Per Second	[Hz]
S	power spectral density	[Pa^2]
$\mathscr{S}$	non-linear operator	[-]
$\hat{S}_{yx}$	cross-spectral density function	[$\mathrm{Pa}^2/\mathrm{Hz}$]
Scaled $\mathrm{SPL}_{1/3}$	normalization form of one-third octave Sound Pressure Level	[dB]
SIL	Sound Intensity Level	[dB]
SNR	Signal-to-Noise ratio	[dB]
SPL	Sound Pressure Level	[dB]
$\mathrm{SPL}_{1/3}$	one-third octave Sound Pressure Level	[dB]
SPL_{α}	angle of attack contribution to the Sound Pressure Level	[dB]
$\mathrm{SPL}_{\mathrm{av}}$	average Sound Pressure Level measured at the same distance	[dB]
$\mathrm{SPL}_{\mathrm{LBL\text{-}VS}}$	Sound Pressure Level of LBL-VS noise	[dB]
$\mathrm{SPL}_{\mathrm{p}}$	pressure side contribution to the Sound Pressure Level	[dB]
$\mathrm{SPL}_{\mathrm{s}}$	suction side contribution to the Sound Pressure Level	[dB]
$\mathrm{SPL}_{\mathrm{TBL\text{-}TE}}$	Sound Pressure Level of the TBL-TE noise	[dB]
$\mathrm{SPL}_{\mathrm{TEB\text{-}VS}}$	Sound Pressure Level of the TEB-VS noise	[dB]
$\mathrm{SPL}_{\mathrm{tot}}$	Total Sound Pressure Level	[dB]
$\mathrm{SPL}_{\mathrm{total}}$	Total Sound Pressure Level for TBL-TE noise and separation noise	[dB]
$\mathrm{SPL}_{\mathrm{TP}}$	Sound Pressure Level of the Tip noise	[dB]

St	Strouhal number	[-]
St'	Strouhal number defined for LBL-VS noise	[-]
St''	Strouhal number defined for TP noise	[-]
St'''	Strouhal number defined for TEB-VS noise	[-]
St_1	Strouhal number defined for TBL-TE and separation noise	[-]
$\mathrm{St}_1^{'}$	Strouhal number defined for LBL-VS noise	[-]
St_2	Strouhal number defined for TBL-TE and separation noise	[-]
St_p	Strouhal number defined for the SPL at the pressure side	[-]
St_s	Strouhal number defined for the SPL at the suction side	[-]
$\mathrm{St}_{\mathrm{peak}}$	maximum value of the Strouhal number	[-]
$\mathrm{St}_{\mathrm{peak}}^{'}$	maximum value of the Strouhal number defined for LBL-VS noise	[-]
$\mathrm{St}_{\mathrm{peak}}^{'''}$	maximum value of the Strouhal number defined for TEB-VS noise	[-]
t	time	[s]
T	period	[s]
T_s	time snapshot	[s]
u_e	boundary layer edge velocity	[m/s]
U	freestream velocity	[m/s]
U_∞	flow speed	[m/s]
U_{yz}	cross-correlation function	[Pa^2]
U_{yy}	auto-correlation function	[Pa^2]
v	source velocity vector	[m/s]
v_r	particle velocity in the direction r	[m/s]
V	flight speed	[m/s]
$w_{m,j}$	weight factor between microphone m and scan point j	[-]
W	acoustic power emitted by the sound source	[W]
W_0	reference acoustic power	[W]
$\vec{x}_m$	coordinates of microphone m	[-]

y	sound pressure signal	[Pa]
Y	distance between the microphone phased array and the scan plane	[m]
z	distance from the microphone array	[m]

List of Figures

List of Tables

1
Introduction

1.1. Overview

In 2015, more than 190 states participated at the Paris Climate Change Conference. For the first time, all the nations fought for a common cause: the climate change and its effects. The overall response was to keep the rise of the global temperature well below 2°C above the pre-industrial levels and to put efforts to limit the increase to 1.5°C above pre-industrial levels [89]. To achieve these ambitious goals and to overcome the increase in the energy consumption, a shift from a fossil-fuel based society towards a sustainable society is required. In this scenario, wind represents one of the most promising energy carrier.

By comparing the European total installed power capacity in 2007 and in 2017 (Figure 1.1), the increasing share of renewable energy is clearly noticeable [97]. In particular, wind accounts for the largest percentage among renewables and its power capacity is expected even to double in 2030 [96]. The growing role of wind in the global energy framework boosts the development of the technology [20]. New targets are opening up: offshore and urban. Offshore wind energy has gained more interest in the recent years. The high wind source potential can be exploited by large wind farms, with an average size of 493 MW [98]. However, its market competitiveness is limited by elevated costs as well as by technology risks. Along with the offshore locations, urban areas have become attractive sites for the future of wind energy. The installation of small wind turbines represent a cost-effective solution to meet the electricity demand of householders [84]. Furthermore, with these off-grid devices, some of the barriers faced by wind farms, like losses in the electrical distribution and transportation systems, can be reduced [56].

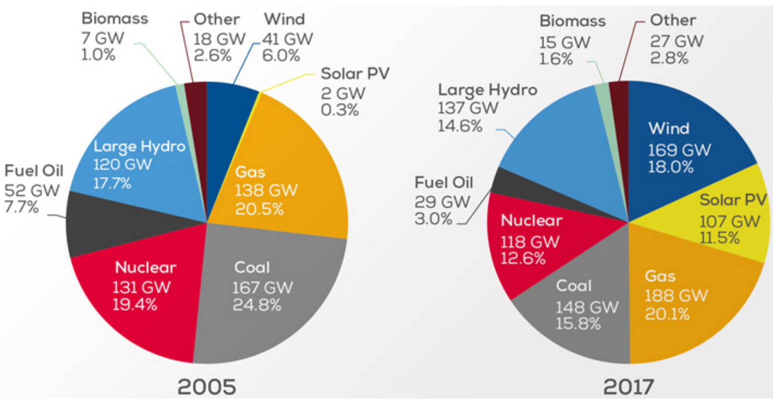

Figure 1.1: Share in the EU's total installed power capacity in 2005 and in 2017 [97].

1.2. Small wind turbines

According to the IEC safety standard 61400-2, a wind turbine with a rotor swept area[1] smaller than 200 m^2 and with a power generation of less than 50 kW is defined as a small wind turbine [39].

Small wind turbines can be either horizontal-axis wind turbine (HAWT) or vertical-axis wind turbine (VAWT). Since VAWTs are characterized by lower productivity and by higher variable loads, they have not been adopted as widely as HAWTs [52]. Thus, the main focus of the current work is on HAWTs. In Figure 1.2, several examples of this turbine's category are shown with a variable number of twisted blades, from two to seven. In the absence of a yaw system, some turbines are equipped with a tail fin to adjust the rotor with the wind and to minimize the yaw angle[2] [101]. In addition, according to the rotor orientation, they can be classified in upwind turbines, if the rotor is facing the wind, and in downwind turbines, if the rotor is located on the lee side of the tower [73]. These two rotor configurations are depicted in Figure 1.3 [52].

Figure 1.2: Examples of small wind turbine. Starting from the left side: 10 kW Bergey Excel turbine [9], 0.7 kW WindChallenge downwind turbine [95] and 0.4 kW five-bladed wind turbine [17].

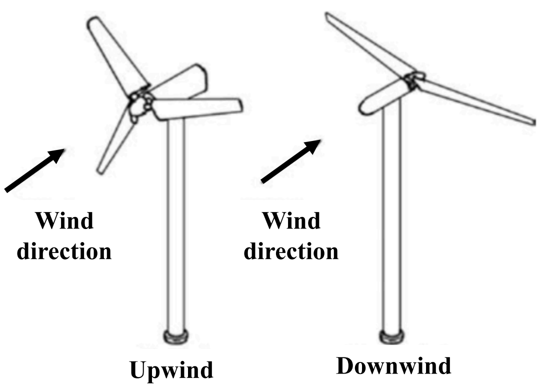

Figure 1.3: Rotor configurations for HAWT [52]. Left: upwind configuration. Right: downwind configuration.

[1]The rotor swept area is equal to πR_{rotor}^2 with R_{rotor}, the rotor radius of the wind turbine. A rotor swept area small than 200 m^2 corresponds to $R_{\text{rotor}} < 8$ m [102].
[2]The yaw angle is defined as the angle between the turbine's axis and the wind direction [101].

1.3. Problem statement

In the urban environment, the wind regime is characterized by low wind speeds and high levels of turbulence, due to the presence of obstacles. Furthermore, as every new technology, small wind turbines are facing elevated capital costs and technical challenges for their extensive development [41]. Among these issues, the sound emitted represents a constraint for their siting near human activities. In contrast with aircraft and road traffic, a unique characteristic of wind turbine is that the sound is continuously generated during day and night [38].

For the assessment of the noise, three primary factors have to be analyzed: noise sources, propagation path and receivers, which are illustrated in Figure 1.4 [38].

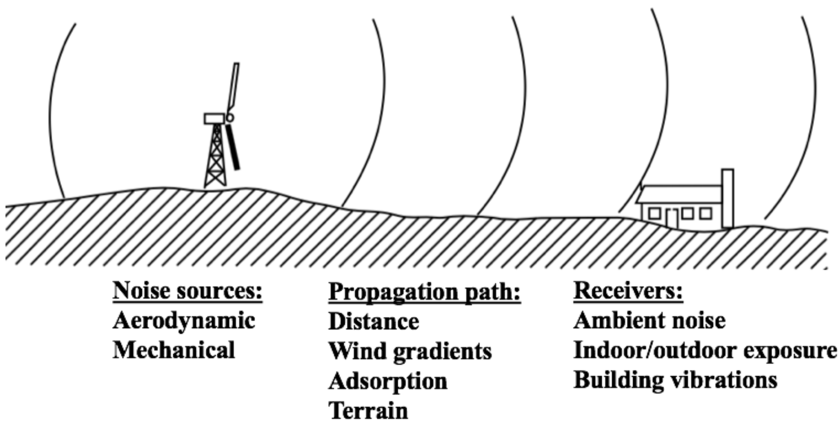

Figure 1.4: Primary factors for the assessment of wind turbine noise [38].

Two main categories of noise can be produced by these operating systems: **aerodynamic** and **mechanical**. The first one is emitted by the interaction of the airflow with the blades while the latter is caused by the dynamic response of the moving mechanical components [52]. Nowadays, the major focus is on aerodynamic noise, proving that mechanical noise has been already optimized [93].

Considering the propagation path, the wind gradient represents the most important element. In fact, the noise propagation can be amplified by the wind in a specific direction as well as obstruct in others [38]. However, since small wind turbines are placed very close to the receivers [74], the propagation path will not be discussed in this research.

As regards the third factor in Figure 1.4, the acoustic impact of a wind turbine is often a subjective perception and is linked with the nature of the receiver [52]. In the case of human ear, the small pressure fluctuations associated with the generation of the sound can be recognized for different range of frequencies[3]. However, humans result more susceptible to certain frequency (i.e. 2 kHz - 6 kHz) and their sensitivity is not linear with the amplitude of the sound wave [69]. In order to adapt the recorded sound perception to the human sound sensibility[4], filters are used. Figure 1.5 depicts several types of filter: **A-Weighting**, **B-Weighting** and **C-Weighting**. The first one is the most adopted with sound of medium intensity, while the last one is used for loud sound. The B-Weighting is not commonly applied and it assesses medium-loud sounds [65]. The weighting can be recognized in the unit, e.g. dB(A) when the A-scale is employed. In the report, the A-weighting filter will be applied.

Effects of the noise on people can be distinguished in [52]:

1. **subjective**, i.e. annoyance and dissatisfaction;

[3] The audible frequencies for a human range between 20 Hz and 20 kHz [69].
[4] Note that the limits for human hearing and for human pain correspond to an SPL of 0 dB and of 140 dB, respectively [64].

2. **interference with activities**, e.g. sleeping;
3. **physiological**, e.g. hearing loss.

In general, workers in the aircraft sector can be subjected to all the above-mentioned disturbances while the noise impact of a wind turbine leads only to the first two effects [31].

The perception of wind turbine noise is also linked to the ambient sound. In fact, if the background noise and the wind turbine noise have the same magnitude, the latter will be confused with the background [65].

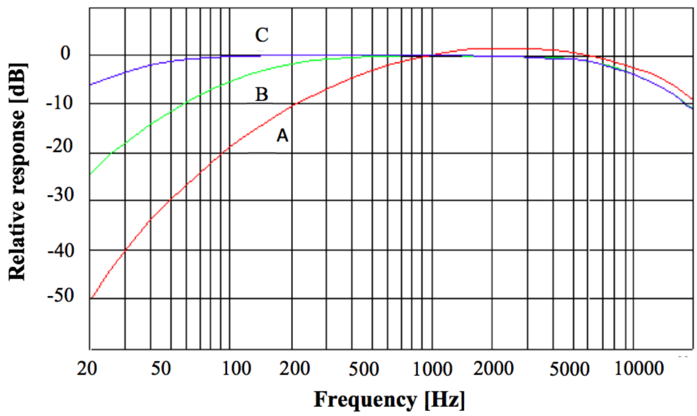

Figure 1.5: A, B and C-Weighting Frequency Scales [91].

1.4. Objective and research approach

The main objective of this research is:

to assess the noise emitted by a small wind turbine, focusing on the aerodynamic noise sources.

For this goal, the source mechanisms need to be known. Beamforming algorithms with microphone phased array have become a standard method for the localization and quantification of sound sources [77]. The acoustic array records the signals coming from the sound source. Then, through the adoption of the beamforming, the recorded signals are translated into a source map, which shows the magnitude and the location of the sound source [59].

The most adopted technique is the conventional beamforming (CB), which has been widely used to investigate stationary sound sources. The basic principle is to assume the acoustic array and the measurement object spatially fixed to each other and to consider a stationary scan plane, with a certain number of scan points, where sound sources are expected to be located [43]. This technique can be carried out:

- in the time domain, where the time delays between the emission of the sound signal and the received signal at the microphones are evaluated [103];
- in the frequency domain, where microphone signals are delayed in phase.

Even if conventional beamforming shows several advantages, like simplicity and robustness, it is not able to correctly reconstruct the sound field of a rotating source. In fact, in this case, the distance between the source and the receiver is time-dependent [83].

In presence of rotating objects, like wind turbine rotors, the abilities to follow the motion of the source and to take into account the frequency shift are important. In particular, if multiple noise sources are assessed, their correct detection is essential to define noise abatement strategies [101].

This is the reason why during this project a rotational beamforming algorithm (i.e. ROSI, ROtating Source

Identifier) will be used. The main difference with the conventional beamforming is that the scan plane rotates following the movement of the noise sources [33]. To accurately evaluate the wind turbine noise with ROSI, the following research question will be addressed:

> *What is the ROSI performance for localizing and quantifying rotating sound sources, like small wind turbines?*

First, the source localization and the source quantification will be investigated under ideal and known conditions. Three simulated datasets will be analyzed: a single rotating point source, multiple spatially separated sound sources and distributed sources. The ROSI uncertainty will be determined through the difference between the input and the ROSI output. In addition, multiple simulations will be performed varying the source levels. If the differences in the beamformed results agree with differences in the source levels, ROSI can be used to compare different blades or turbine geometries.

Then, the degree of uncertainty will be increased applying ROSI to experimental data. Two experiments will be conducted to answer the main research question:

1. An experimental verification of the measurement geometry will be carried out in the Anechoic Tunnel facility of TU Delft University. The use of a small-scale academic prototype will simulate the acoustic of a urban wind turbine. In this way, it is possible to assess if all the input parameters for the detection of the noise level are correctly retrieved. This aim can be translated in the following sub-question:

   > *Knowing the location of a rotating source in an anechoic environment, is ROSI able to correctly localize and quantify the sound level?*

2. A small HAWT with an upwind configuration will be tested in the Open Jet Facility of TU Delft University. An analysis of the main noise sources will be carried out, varying both the wind speed of the tunnel and the rotational speed of the blades. Different blades and turbine geometries will be adopted. Follows that:

   > *In presence of a non-anechoic environment, is ROSI able to correctly localize and quantify the sound emitted by a small wind turbine?*

By answering these two sub-questions, the assessment of the noise emitted by a small wind turbine will be achieved. For a more detailed analysis, all the measurements will be compared with analytical models, developed along the years to characterize the different types of wind turbine noise.

On the base of these evidences, strategies for the noise abatement will be provided together with recommendations for future researches.

1.5. Structure of the report

After the introduction, the current research is structured as follows:

- Chapter 2 presents an overview of the fundamental concepts for acoustic;
- Chapter 3 evaluates the different noise sources for a wind turbine, with a particular attention to the noise prediction models present in literature;
- Chapter 4 describes the beamforming techniques applied in aeroacoustics measurements. First, the conventional beamforming is analyzed, followed by the description of the ROtating Source Identifier;
- Chapter 5 provides information about the set-up of the two experiments;
- In Chapter 6, the ROSI uncertainty is investigated with different simulated datasets;
- The ROSI application to the experimental data is discussed in Chapter 7;
- Chapter 8 is the last section, where conclusions and recommendations are drawn.

2

Fundamental concepts of acoustic

This Chapter describes the basic concepts of acoustic, which are essential to understand the entire research. The first section introduces the definition of the sound and the main characteristics of sound waves. Then, the physical variables to quantify the sound are presented. Fundamental for the present study are the effects of a moving sound source, which are illustrated in the third section. The last section defines how a Fourier transform is performed and how the sound spectrum is evaluated.

2.1. Sound

Sound is a pressure fluctuation, which propagates through a medium in the form of a longitudinal wave and with a constant speed [64]. The sound unwanted by the receiver is called noise.

These disturbances are characterized with the following quantities [34]:

- c, **sound speed** [m/s] depends on the fluid through which the sound pressure travels. In atmospheric air, it is equal to 340 m/s [52];
- f, **frequency** [Hz] is the number of pressure wave cycles per second;
- T, **period** [s] is the time to complete one pressure wave cycle;
- λ, **wavelength** [m] is the distance travelled by the pressure wave during one cycle.

Equation 2.1 provides a relation between these parameters while Figure 2.1 visualizes them.

$$\lambda = \frac{c}{f} \quad \text{with} \quad f = \frac{1}{T} \tag{2.1}$$

The longitudinal characteristic of the wave implies that particle displacement is in direction of the wave propagation. At a constant time, the two-dimensional plane, where the particle displacement is the same, is called wave front [79].

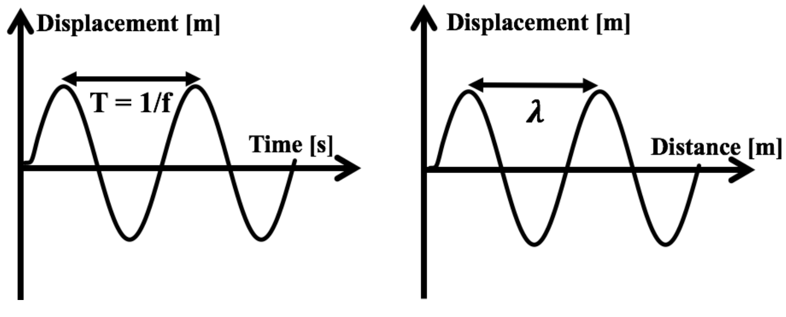

Figure 2.1: Characteristic variables for a sound pressure wave: period, frequency and wavelength. Time domain on the left side and space domain on the right side.

2.1.1. Sound fields

The region where the pressure wave travels is called the sound field. The sound fields are classified as [40]:

- **Free field**, when in the space of interest no obstacles affect the travel of the sound wave. The absence of reflections from objects, wall or ground surface is often required during acoustic measurements [69]. This is the reason why, anechoic chambers have been designed. Any reflections of the sound are avoided because the interior surfaces are constructed to have a high wall absorption. In this ideal environment, one of the experiment of the current research will be performed.

- **Near field**, is a region close to the sound source. Here, the propagation of the sound is influenced by the emission characteristics of the source. Since the relationship between sound pressure and distance is not fixed and the curvature of the wave front plays a role, this field is not taken into account in noise measurements [69].

- **Far field**, where sound pressure results to be inversely proportional to the distance [91]. In this case, the receiver is at great distance from the sound source. Thus, the propagation of the sound can be characterized by plane waves[1] [77].

2.2. Quantification of sound

In order to measure the sound, several physical quantities can be used. The most common are the Sound Power Level, the Sound Intensity Level, the Sound Pressure Level, the Signal-to-Noise ratio and the Directivity Index.

2.2.1. Sound Power Level

Sound Power Level or Power Watt Level (PWL) can be defined through [79]:

$$\mathrm{PWL} = 10\log\left(\frac{W}{W_0}\right) \tag{2.2}$$

where W is the acoustic power of the sound source (i.e. the energy emitted by the source per unit of time), and W_0 is the reference acoustic power, equals to 10^{-12} W [29]. PWL is measured in decibel.

2.2.2. Sound Intensity Level

The energy transmitted by a sound pressure per unit time per unit area is called **sound intensity** I [79]. If a point source in a free field is analyzed, the energy is uniformly emitted in all the directions. Thus, the sound intensity is constant in every spherical surface that surrounds the sound source and it is defined as the sound power per unit area [91]:

$$I(r) = \frac{W}{4\pi r^2} \tag{2.3}$$

in which r is the radius of the sphere.

In general, sound intensity at certain distance r from the sound source is equal to

$$I = \frac{1}{T}\int_0^T \frac{p'\,dA\,dr}{dt\,dA}\,dt = \frac{1}{T}\int_0^T p'\,v_r\,dt \tag{2.4}$$

with p' the instantaneous sound pressure, dA is the area normal to the direction of travel and v_r the particle velocity in the direction r.

It is important to highlight that in a free field the relationship between the effective pressure and the sound

[1] For plane waves, the wave fronts are always parallel between each other [77].

intensity in the direction of the sound propagation follows to the so-called acoustic analogy of Ohm's law [69]:

$$I = \frac{p_e^2}{\rho_\infty c} \tag{2.5}$$

The denominator of the right-hand side is defined as the **characteristic acoustic resistance** of the medium.

Knowing the intensity of the sound, it is possible to characterize the Sound Intensity Level (SIL). Also in this case a logarithmic scale is used [64]

$$\mathrm{SIL} = 10\log\frac{I}{I_0} \tag{2.6}$$

where I_0 represents the reference sound intensity with a value of 10^{-12} W/m^2 [69].

2.2.3. Sound Pressure Level

Sound Pressure Level (SPL) uses a logarithmic decibel scale to represent the ratio between the effective pressure, p_e, and a reference pressure, p_{ref} [23]:

$$\mathrm{SPL} = 20\log\left(\frac{p_e}{p_{ref}}\right) \tag{2.7}$$

Here, the reference pressure represents the hearing threshold at 1 kHz and it is equals to $2\cdot10^{-5}$Pa, in air. The effective pressure is calculated as the Root-Mean-Square of the acoustic pressure [79].

Considering Equations 2.5, 2.6, 2.7, it is possible to define the relationship between the SIL and the SPL as

$$\mathrm{SPL} = \mathrm{SIL} + 10\log\left(\frac{I_0\rho_\infty c}{p_{ref}^2}\right) = \mathrm{SIL} + 0.18 \tag{2.8}$$

In the right-hand side of Equation 2.8, the reference values of I_0 and p_{ref} and the standard value of air density at sea level (i.e. 1.225 kg/ m^3) are substituted. However, if the air density is not equal to the standard value at sea level, Equation 2.8 can be correct as:

$$\mathrm{SPL} = \mathrm{SIL} + 0.18 + 10\log\left(\frac{\rho_\infty c}{(\rho_\infty c)_0}\right) \tag{2.9}$$

In practice, the difference between SPL and SIL is so small (i.e. less than 1 dB) under all atmospheric conditions that these parameters are numerically identical [69].

When Q incoherent sound sources (i.e. sound sources with different waveforms and variable phase differences) are present, the total SPL is expressed as [58]:

$$\mathrm{SPL_{tot}} = 10\log\sum_{q=1}^{Q} 10^{\frac{\mathrm{SPL}q}{10}} \tag{2.10}$$

with SPLq the sound pressure level for sound source q.

2.2.4. Signal-to-Noise ratio

The Signal-to-Noise ratio (SNR) is calculated as [88]:

$$\mathrm{SNR} = 20\log\left(\frac{p_e}{p_{e,noise}}\right) \tag{2.11}$$

in which $p_{e,noise}$ is the effective pressure of the noise.

2.2.5. Directivity Index

Generally, when the size of the sound source prevails to the wavelength of the sound, the source tends to be directional. The sound emitted by a rotating source, like a wind turbine, presents a strong directionality. As a result, the noise field is linked not only to the distance from the source but also to its angular position [69].

In order to quantify this directional pattern, the directivity index (DI) is adopted, which is described as [79]

$$\mathrm{DI}(\kappa) = \mathrm{SPL}(\kappa) - \mathrm{SPL}_{\mathrm{av}} = \mathrm{SPL}(\kappa) - 10\log\frac{W}{4\pi r^2} \tag{2.12}$$

Here, $\mathrm{SPL}(\kappa)$ is calculated in a specific direction κ and $\mathrm{SPL}_{\mathrm{av}}$ is the average Sound Pressure Level measured at the same distance, r [69]. The second variable on the right side of Equation 2.12 is computed from the ratio between the acoustic power and the surface of the sphere with radius r.

2.3. Effects of a moving sound source

When a moving sound source is analyzed, the effect of Doppler frequency shift as well as the convective amplification have to be taken into account [103]. The acoustic field is affected in two ways: the Doppler effect alters the frequency of sound while the convective amplification influences the sound level.

2.3.1. The Doppler frequency shift

If the source moves and the sound receiver is at rest, Equation 2.1 is not valid. The center of the radiated wave fronts is slightly displaced, according to the movement of the source, and the position vector changes with a speed of dr/dt. Thus, the observed wavelength, λ' can be expressed as [69]:

$$\lambda' = \frac{c + dr/dt}{f} \quad \text{with} \quad \frac{dr}{dt} = \frac{\vec{v}\cdot\vec{r}}{\|\vec{r}\|} \tag{2.13}$$

where $\vec{v}$ is the source velocity vector and $\vec{r}$ is the distance vector between the receiver and the source. In the case of a sound source moving away from the receiver, dr/dt is bigger than zero. This results in an increase of the wavelength of

$$\frac{\lambda'}{\lambda} = \frac{c + dr/dt}{c} \tag{2.14}$$

Follows that, the ratio between the observed frequency f' and the source frequency f is calculated with:

$$\frac{f'}{f} = \frac{c/\lambda'}{c/\lambda} = \frac{1}{1 + \frac{dr/dt}{c}} \tag{2.15}$$

The difference between the observed frequency and the source frequency, $(f' - f)$, is called **the Doppler shift**.

If an airplane at altitude h and with a flight speed V is considered as a moving source, then

$$\frac{dr}{dt} = \frac{d}{dt}\sqrt{h^2 + V^2 t^2} = \frac{V^2 r}{t} \tag{2.16}$$

Substituting Equation 2.16 in Equation 2.15, leads to

$$\frac{f'}{f} = \frac{1}{1 + \frac{V^2 t}{rc}} = \frac{1}{1 - M\cos\theta} \tag{2.17}$$

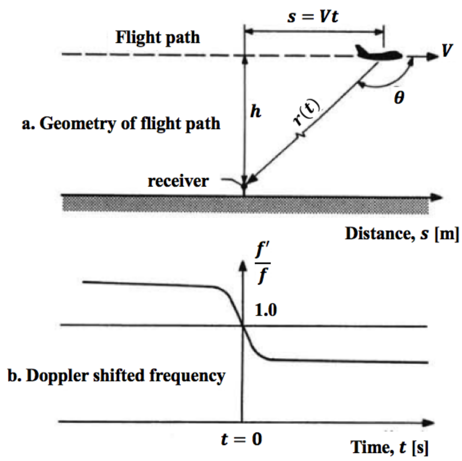

Figure 2.2: Airplane flyover and Doppler Frequency Shift. $t = 0$ coincides with the overhead position and θ is the angle between the velocity vector and the source-observer line [69].

where $r = -Vt/\cos\theta$ respects the geometrical relation and the Mach number is expressed as $M = V/c$. The denominator of the right-hand side of Equation 2.17 is called Doppler factor.

Figure 2.2 illustrates the airplane flyover together with the Doppler shifted frequency [69].

In the end, if a source is moving away from the receiver, the sound is perceived with a lower frequency. The opposite results, if the source is approaching. The evaluations of this effect in terms of observed frequency can be performed using Equation 2.13, Equation 2.14 and Equation 2.15 [64].

2.3.2. Convective amplification

The effect of convective amplification can be retrieved in the change of the sound level. If the source is moving away from the receiver, the sound level is decreased by the square of the Doppler factor. An opposite outcome is obtained, if the source is going towards the observer. Equation 2.18 expresses this proportionality [60]

$$p(r,t) \propto (1 - M\cos(\theta))^{-2} \tag{2.18}$$

2.4. Fourier Transform and Sound Spectrum

In reality, sound is composed by multiple pressure variations, i.e. different tones with different frequencies. Thus, using the Fourier theorem, the acoustic signal can be considered as a combination of sinusoidal waves and each of these can be described with Equation 2.1 [29]. The frequency components and their proportions in the signal are then determined with a Fourier transform. The final result is the sound spectrum, where for each frequency the corresponding energy content is depicted. This procedure allows to move from time domain to frequency domain.

The triggering reason to perform a frequency analysis is to investigate the dominant noise source. The Fourier transform and the Inverse Fourier Transform for a pressure sound, $p(t)$, can be described with [23]

$$P(f) = \int_{-\infty}^{+\infty} p(t) e^{-i2\pi f t} dt \tag{2.19}$$

$$p(t) = \int_{-\infty}^{+\infty} P(f) e^{i2\pi f t} df \tag{2.20}$$

Equation 2.19 and 2.20 are denoted as Fourier integral pair [62]. From these expressions, the **power spectral density** can be defined

$$S(f) = \lim_{T\to\infty} \frac{\left|P(f)^2\right|}{T} \tag{2.21}$$

Since a unit frequency interval is considered, $S(f)$ does not provide a measure of the finite sound intensity. In order to yield that, an integration over a finite frequency interval must be performed [69].

2.4.1. Tonal and broadband sound

Different sound spectra correspond to different types of sound [64]. Figure 2.3 and Figure 2.4 illustrate the time series and the frequency spectrum for a periodic sound and for a broadband sound, respectively.

If a periodic pressure signal is analyzed, a large number of discrete frequency components can be retrieved, which are related to the nominal frequency as integral multiples [69]. The resulting graph in the frequency domain is a **line spectrum**. Example of this category is the noise emitted by a propeller.

On the other hand, if the sound is random or broadband, the sound pressure waveforms do not repeat over the time domain and the pressure fluctuations are randomly. The frequency analysis leads to a **continuous spectrum** where the frequency components of the signal vary among a wide range [29]. A particular random sound is the white noise.

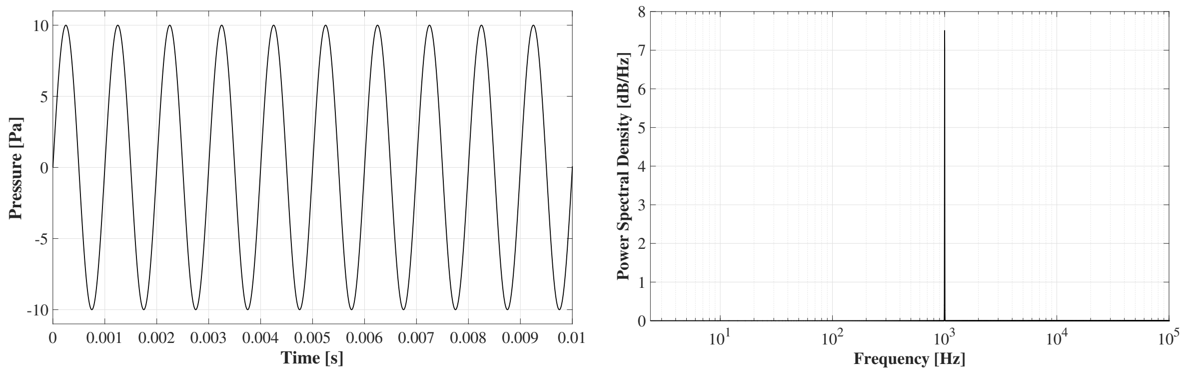

Figure 2.3: Time series and frequency spectrum for a periodic sound. The signal analyzed is a tone at f = 1000 Hz.

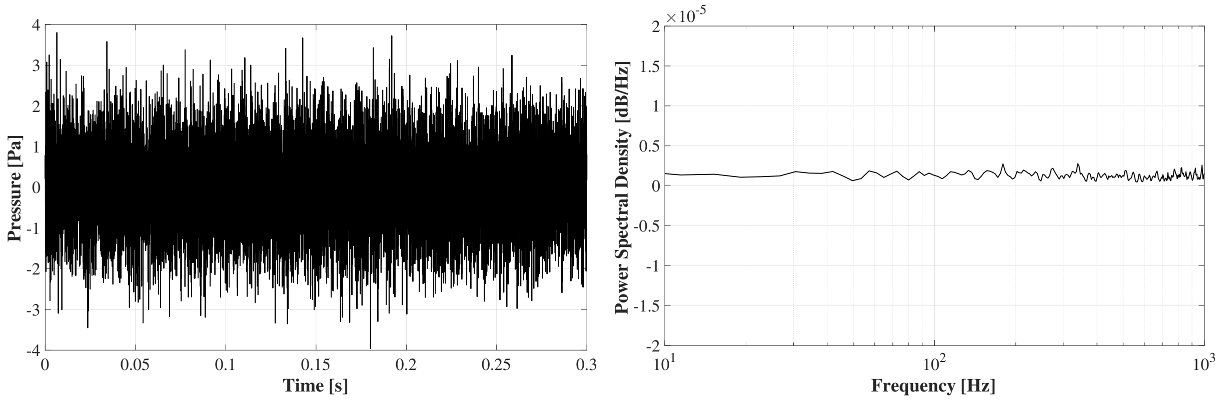

Figure 2.4: Time series and frequency spectrum for a broadband sound. The signal analyzed is white noise.

2.4.2. Frequency bands for the sound spectrum

Two kinds of frequency band can be applied in the representation of sound spectrum [64]:

1. **Constant bands**, used if high frequency resolution is needed. For example, if a pure tone is analyzed.

2. **Proportional bands**, like octaves or one-third octaves, adopted for noise measurements.

These bandwidths lead to different spectral shapes and levels, as it can be noticed from Figure 2.5. Here, the sound spectrum for the white noise is plotted for two different frequency bands: octaves, on the left-side, and one-third octaves, on the right-side.

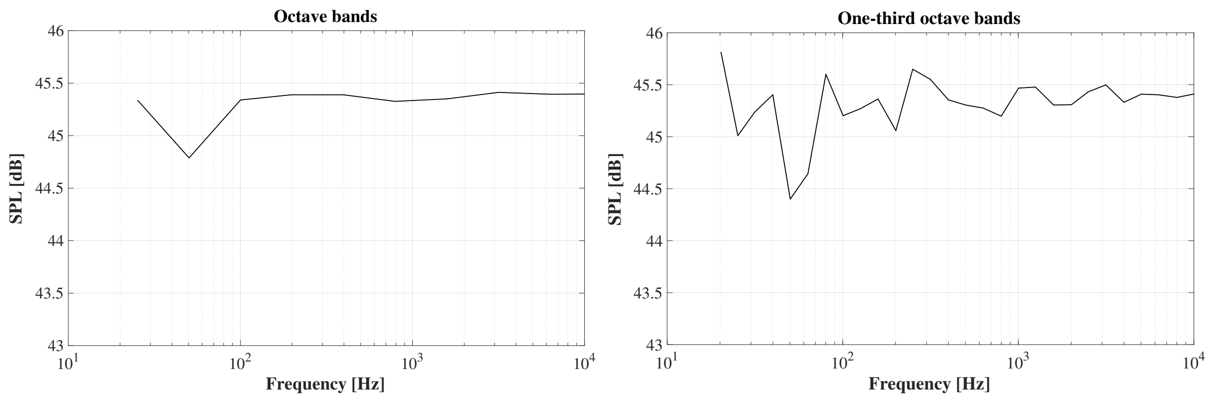

Figure 2.5: Sound spectrum for the white noise, applying octave bands (left-side) and one-third octave bands (right-side).

As regards the octave bands, the upper limit of the bandwidth is twice the lower limit. The nominal frequency, f_n, describes each octave band and results from the geometric mean of the upper and lower frequency limits (i.e. f_U and f_L respectively), as [29]:

$$\log f_n = \frac{1}{2}[\log f_L + \log f_U] \Leftrightarrow \log f_n = \sqrt{f_L f_U} \tag{2.22}$$

Using a narrower band, as the one-third octave, more detailed information about the noise can be obtained.

Within a specific frequency band, the SPL is denoted as **Pressure Band Level** (PBL) [69].

$$\mathrm{PBL} = 10\log\left(\frac{S(f)\Delta f}{p_{ref}^2}\right) = \mathrm{PSL} + 10\log\Delta f \tag{2.23}$$

in which, PSL represents the **Pressure Spectrum Level**. This quantity is the SPL in 1 Hz band centered in a specific frequency. It is also the decibel value for the power spectral density, $S(f)$ [79]. In the current work, the PSL is also referred as Power Spectral Density (PSD).

The Overall Sound Pressure Level (OSPL) is often used to evaluate the total noise emitted by a sound source and it is calculated adding the PBL's (SPL's) over f_i, with $i = 1, \cdots, n$ the band number, as

$$\mathrm{OSPL} = 10\log\sum_{i=1}^{n} 10^{\frac{\mathrm{SPL}(f_i)}{10}} \tag{2.24}$$

This can be translated in the integration of the total power over the frequency spectrum.

In the time domain, the OSPL is expressed as

$$\mathrm{OSPL} = 20\log\left(\frac{p_e}{p_{ref}}\right) \tag{2.25}$$

with p_e the effective pressure.

When the A-weighting filter is applied, the overall A-weighting sound pressure level (OASPL) is obtained as [79]

$$\mathrm{OASPL} = 10\log\sum_{i=1}^{n} 10^{\frac{\mathrm{SPL}(f_i)+\Delta L_A(f_i)}{10}} \tag{2.26}$$

with $\Delta L_A = -145.528 + 98.262\log f - 19.509(\log f)^2 + 0.975(\log f)^3$ and measured in dBA. The A-weighting filter is often used because it provides a good measure of the perceived noise level [69].

2.4.3. Discrete Fourier Transform

However, since most of acoustic signals are defined only for discrete time steps, the Discrete Fourier Transform (DFT) has to be used. For a number of samples, L_s, the complex pressure amplitude for the signal measured by the microphone m, $p_m(f_b)$, is calculated as follows:

$$p_m(f_b) = \frac{2}{L_s}\sum_{l=1}^{L_s} \tilde{p}_{m,l} e^{-2\pi i f_b l \Delta t} \tag{2.27}$$

where $\tilde{p}_{m,l}$ is the discretization of p_m and b is the frequency index.

2.4.4. Fast Fourier Transform

In order to efficiently perform DFT and to reduce the computational time, Equation 2.27 is evaluated through the Fast Fourier Transform (FFT) for each of the frequency component of the acoustic signal, which are [77]

$$f_b = \frac{b}{L\Delta t} \quad \text{with} \quad b = 1, \cdots, \frac{L}{2} - 1 \tag{2.28}$$

Δt is the sample interval in seconds.

2.4.5. Aliasing

According to the **Nyquist criterion**, the sample frequency has to be at least twice the maximum frequency of the sound [16].

In Equation 2.28, the upper limit for the frequency is $f_{L/2} = 1/2\Delta t$, which gives a sampling frequency of

$$f_s = \frac{1}{\Delta t} \tag{2.29}$$

If the signal is under sampled, aliasing occurs. Figure 2.6 compares adequate and inadequate sampling, showing that during aliasing the under sampled signal is at a lower frequency than the original signal. Thus, an incorrect representation of the sound is obtained.

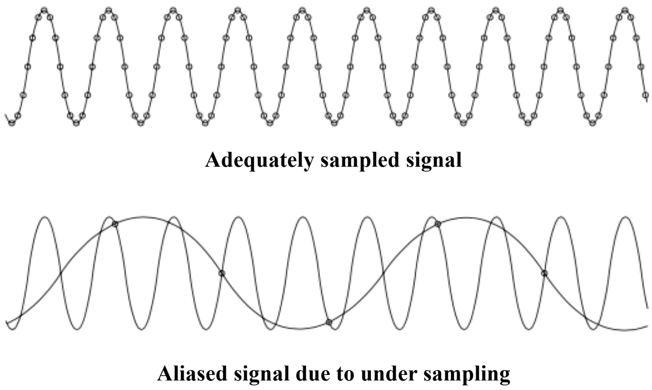

Figure 2.6: Sampling of the signal [16]. On the top, the signal adequately sampled is shown. Instead, on the bottom, aliasing occurs for under sampling.

3
Wind turbine noise

Technological developments in the field of wind energy have led to several improvements in the aerodynamic performance of wind turbines. However, the noise emitted by these devices remains one of the most important obstacles for their siting [52]. For wind turbines, it is possible to distinguish between mechanical and aerodynamic noise sources. The first one results from the motion of the mechanical components while the latter is caused by the interaction of the airflow with the blades. In modern wind turbines, the aerodynamic noise is dominant [22]. Therefore, the present research is mainly focused on aerodynamic noise sources.

The first section of the current Chapter defines the mechanical noise while the second one assesses the different aerodynamic sound sources. The last section is dedicated to the methods used for noise modelling.

3.1. Mechanical noise

The dynamic response of electrical and mechanical equipment in a wind turbine generates mechanical noise [65].

For small wind turbines, the mechanical noise sources are caused by [70]:

1. the rotation of the generator;

2. the yaw correction movement, which appears only for downwind turbine;

3. the furling movement[1].

In addition, in small wind turbines, the absence of a gearbox for the generator reduces the magnitude of the emitted sound, which is mainly tonal, even though some broadband components can appear [63]. These considerations and the high rotational speed of the turbine explain why the contribution of mechanical sound sources is very small compared to the aerodynamic ones in a small wind turbine.

3.2. Aerodynamic noise

Aerodynamic noise can be divided in [60]:

1. **Blade-wake interaction noise**;

2. **Inflow-turbulence noise or leading edge-interaction noise**;

3. **Airfoil-self noise**.

[1]The furling motion is an overspeed protection method. The rotor of the small wind turbine rotates out of the flow [101].

The aerodynamic interaction between the blades and the flow around the tower causes low-frequency[2] noise [22]. Figure 3.1 depicts this phenomenon, where the streamlines represent the flow upstream of the tower. When the blade passes through this region, it generates an unsteady lift and consequently tonal noise. This type of sound source is less relevant for turbines with an upwind configuration, for which the distance between the blade and the tower is larger. In fact, in this case, the wind field interacts first with the rotor and then with the tower [38].

The inflow-turbulence noise mechanism is shown in Figure 3.2, where the incoming atmospheric turbulence interacts with the blade [65]. This type of aerodynamic source is produced by surface pressure disturbances at the leading edge and appears for a distortion of the vortices impinging on it [44]. Since the inflow hitting the blade is turbulent, the size of these eddies with respect to the chord length affects noise generation [2]. In the case of eddies larger than the chord, sound is radiated at low frequency and depends on the sixth power of the Mach number, M^6. Under opposite conditions, the sound source behaves as a quadrupole and scales with the Mach number as M^5. Oerlemans et al. [54] demonstrated that isolated airfoils for small wind turbines show the latter trend.

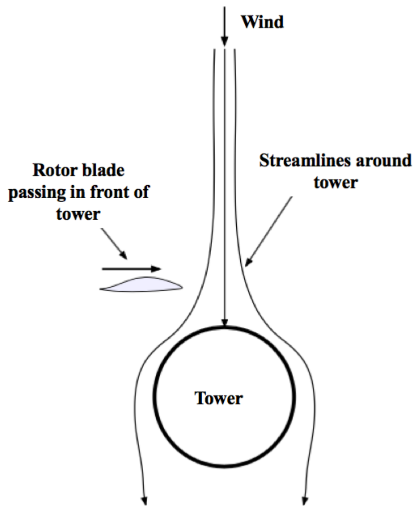

Figure 3.1: Interaction between the tower and the blade [22].

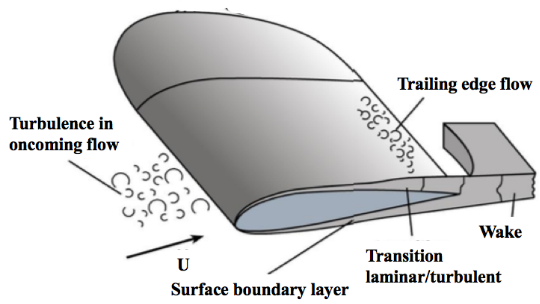

Figure 3.2: Inflow-turbulence noise [58].

The airfoil self-noise is the third source of aerodynamic noise. During the operation of the wind turbine, air flows along the blade. The viscous interaction between the fluid and the airfoil surface leads to the development of a boundary layer. The turbulence generated in this layer and in the near wake interacts with the blade, generating noise [13]. Different flow conditions can occur, influenced not only by the angle of attack but also by the Reynolds number [90]:

$$Re = \frac{UL_c}{\nu} \tag{3.1}$$

with U the free-stream velocity, L_c the airfoil chord and ν the kinematic viscosity of the fluid.

Following these considerations, five airfoil self-noise mechanisms can be highlighted [13]:

1. Laminar Boundary Layer - Vortex Shedding Noise (LBL-VS);
2. Turbulent Boundary Layer - Trailing Edge Noise (TBL-TE);
3. Separation-Stall Noise (SS);
4. Trailing Edge Blunt - Vortex Shedding Noise (TEB-VS);

[2]The frequency range for low frequency noise is between 20 Hz and 100 Hz [22].

5. Tip Noise (TP).

3.2.1. Laminar Boundary Layer - Vortex Shedding noise

At low Reynolds number (lower than 50,000), the boundary layer on the airfoil is laminar. Going from low to moderate values of Re (50,000 to 500,000), small fluctuations appear, which represent the first step in the transition to a turbulent boundary layer [71]. These unsteady disturbances, called Tollmien–Schlichting or T-S waves, are amplified over a separation bubble layer, which might be present at the trailing edge of the blade.

In order to understand the emission of LBL-VS noise, three correlated phenomena are analyzed and depicted in Figure 3.3 [13]:

1. **Separation bubble**;

2. **Vortex roll-up**;

3. **Acoustic feedback**.

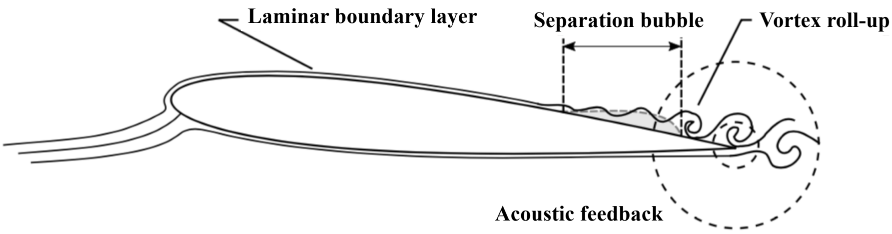

Figure 3.3: Laminar Boundary Layer-Vortex Shedding Noise [13]. The separation bubble, the vortex roll-up and the acoustic feedback are shown.

The main cause of the separated shear layer is an adverse pressure gradient, which generally corresponds to a negative gradient of the velocity at the boundary layer edge, u_e [4]. Since the transition from laminar to turbulent takes place downstream of the separation region, the flow has enough energy to overcome the adverse pressure gradient and to consequently reattach upstream the trailing edge. This type of flow is named as laminar separation bubble and its representation is provided in Figure 3.4 [32]. The dividing streamline is located between the separation point of the shear layer and the reattachment point. In this way, the recirculating flow is not in contact with the separated flow. With Reynolds numbers lower than 50,000, the reattachment of the flow fails, leading to the stall of the blade (i.e. the lift decreases while the drag increases) [55].

During transition, boundary layer instabilities appear in the form of T-S waves [24]. The overall mechanism induces surface pressure perturbations, which generate acoustic waves at the trailing edge [3]. The consequent scattering and upstream diffusion of these sound waves induce the generation of new instabilities. The characteristics of this phenomenon lead to a periodic vortex shedding process.

Looking at the noise spectrum for a NACA0012 in Figure 3.5, it is possible to identify not only a dominant tone, the so-called primary tone with frequency $f_{n,max}$ [6], but also n multiple secondary tones, with frequencies $f_{n,tone}$ proportional to $U^{0.85}$. Even if at the beginning $f_{n,max}$ follows the trend of $f_{n,tone}$, a jump to a higher frequency has been assessed, which results in a ladder-type structure of the acoustic spectrum [61]. Moreover, a broadband component is observed with a centre frequency $f_{s,center}$, caused by either the presence of incoherent eddies or by the scattering of the pressure sound waves at the trailing edge, as studied by Arbey and Bataille [4]. On average, $f_{n,max}$ follows the behaviour of $f_{s,center}$ and depends on the power of the free stream velocity, i.e. $U^{1.5}$. As a consequence, according to the expression of the Reynolds number, an increase of Re leads to a decreasing primary tone [7].

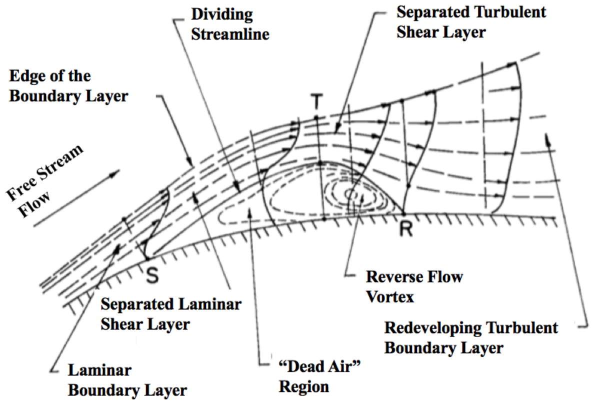

Figure 3.4: Laminar separation bubble layer [32].
The separation point of the laminar shear layer is indicated with the letter S while the reattachment point of the flow with the letter R. The transition point between laminar and turbulent layer is depicted with the letter T.

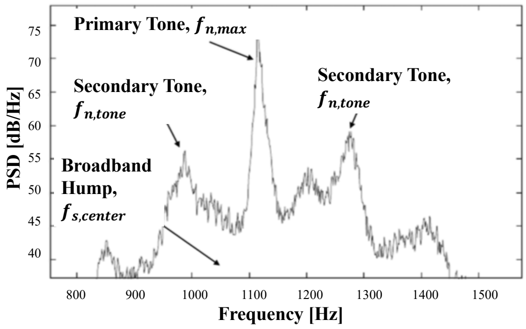

Figure 3.5: Acoustic spectrum for a NACA0012 airfoil at zero angle of attack and a Reynolds number of 75,000 [6].

These peaks occur due to an aeroacoustics feedback mechanism between the trailing edge noise and the T-S waves. Several studies and investigations have been performed to fully understand this feedback loop [21, 57, 81]. However, the physics behind this phenomenon is out of the scope of the current work.

According to Sandberg [71], the values of Re for the flow around blades of small wind turbines are small enough for the development of laminar separation bubbles shedding vortices. As a result, the LBL-VS noise represents one of the most important noise source for these devices.

LBL-TE noise can be prevented by tripping the blades of the wind turbine, leading to a fixed laminar-turbulent transition.

3.2.2. Turbulent Boundary Layer - Trailing Edge noise

At high Reynolds number (i.e. larger than 500,000), the development of a turbulent boundary layer over the airfoil occurs. As these turbulent eddies pass over the sharp trailing edge, they scatter into acoustic pressure waves [13]. TBL-TE noise is produced, representing the most common noise mechanism for large-scale wind turbines [35].

At the trailing edge, the current flow conditions do not allow the generation of periodic phenomena. Thus, large-scale events, like vortical structures, appear randomly arranged and the emitted noise is mainly characterized by a broadband component [27]. In the proximity of the wind turbine, an observer perceives this sound as a "swishing" sound at the blade passing frequency (BPF). The received noise is heard as varying in time and in amplitude due to the Doppler effect and to the convective amplification [46].

Expected values of TBL-TE noise range between 500 Hz and 2000 Hz and, as demonstrated by Oerlemans et al. in their experiments, a louder noise is produced on the outer part of the blade [60].

Figure 3.6 summarizes the phenomena for the TBL-TE noise emission.

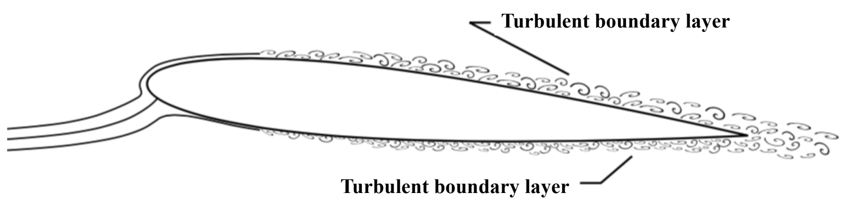

Figure 3.6: Turbulent Boundary Layer-Trailing Edge Noise [13].

3.2.3. Separation - Stall noise

When an airfoil at high angle of attack is investigated, a condition of deep stall is encountered on the suction side [99]. Under this condition, the shear layer separates far upstream, enhancing the creation of vortices. Due to the large length scale of the mechanism, the noise is emitted at low frequency [13].

Higher angles of attack imply that the TBL-TE noise is not anymore the dominant sound source. In fact, due to the consequent stall, the blades are not working properly. The separation-stall noise results the major contribution, increasing the noise by 10 dB compared to the TBL-TE generated at low angles of attack [13]. Follows that, during the optimal operation of a wind turbine, this type of sound source is not produced.

Figure 3.7 shows how a boundary layer separation noise develops while Figure 3.8 gives a representation of a deep stall occurrence.

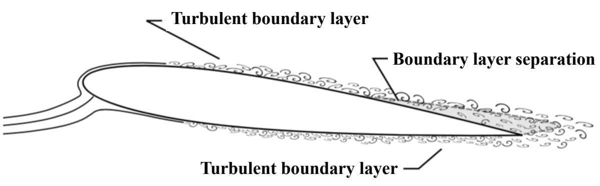

Figure 3.7: Boundary Layer Separation noise [13].

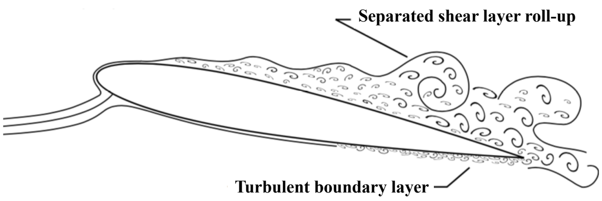

Figure 3.8: Large-scale separation (i.e. deep stall) [13].

3.2.4. Trailing Edge Blunt - Vortex Shedding noise

For a sharp trailing edge, the dominant noise source is represented by the LBL-VS noise, when a laminar instability occurs, or by the TBL-TE noise, when higher Reynolds number enhances a turbulent boundary layer. A different situation is experienced, when a blunt trailing edge is examined. Here, the bluntness leads to the development of a large scale vorticity process in the recirculating flow region. A roll-up of the shed vortices is generated in the near-wake and in the wake region over the trailing edge [12]. Figure 3.9 summarizes the overall phenomena.

The fixed thickness of the blunt edge and the presence of the free-stream velocity determine a narrowband trend in the emitted sound. Under these conditions, the flow along the blade is characterized by a large spanwise correlation and a tonal component can be recognized in the noise spectra [10]. In the case of a bluntness length equivalent to the boundary layer thickness at the trailing edge, the TEB-VS noise is the dominant sound source. Thus, the geometry of the blade influences the intensity of the noise. A necessary condition for the emission of a TEB-VS noise is the following [13]:

$$\frac{h_t}{\delta_l^*} \geq 1 \tag{3.2}$$

being h_t the thickness of the trailing edge and δ_l^* the boundary layer displacement thickness.

With a proper design of the wind turbine, and especially of the trailing edge, the TEB-VS propagation can be prevented. This is the reason why for the current research, the TEB-VS noise will not be assessed.

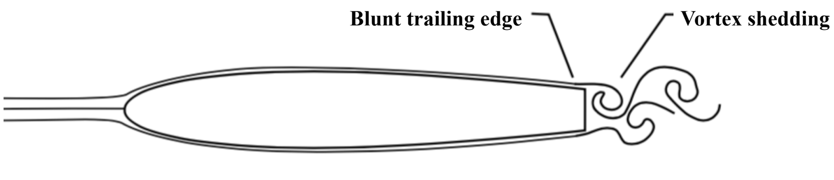

Figure 3.9: Trailing Edge Blunt-Vortex Shedding Noise [13].

3.2.5. Tip noise

Because of the finite length of the blade, a vorticity field is formed at the tip. In this region, the interaction between the stronger vortex at the pressure side and the weaker vortex at the suction side leads to an increasing pressure gradient, which turns into a rotational flow along the airfoil. These turbulent and unsteady vortices cause the generation of tip noise [13]. In Figure 3.10, it is possible to see the formation and the development of a tip vortex structure. The vortices merge downstream at the trailing edge.

According to Casalino et al. [15], the noise level increases in the chordwise direction because the vortex strength continuously enhances. In addition, the overall sound is characterized by a tonal component, with a decreasing dominant noise frequency as the vortex size increases.

On the basis of the experimental studies conducted by Doolan et al. [22], this sound source has a great contribution in the aerodynamic noise produced by wind turbines. Fundamental in this propagation is the influence of the blade geometry as well as of the angle of attack. However, the use of a reverse twist or wingtip on the airfoil leads to a tip noise reduction [54].

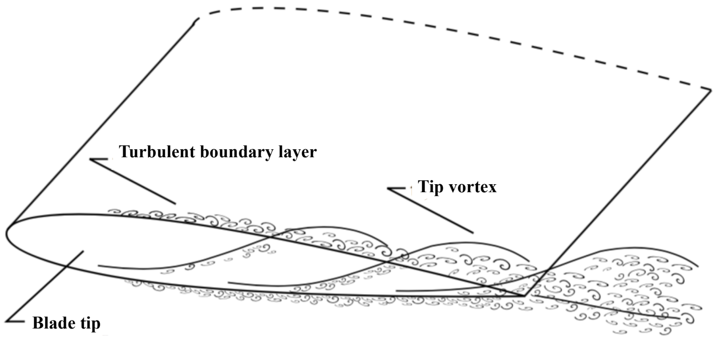

Figure 3.10: Vortex generated at the tip [13].

3.3. Prediction models

Since aeroacoustics measurements will be performed, it is important to compare the experimental results with reliable airfoil noise models. Several methods have been investigated and can be classified as:

1. **Theoretical methods**, where the basic principles for noise prediction are introduced;
2. **Semi-empirical methods**, where analytical scaling rules and empirical data are used;
3. **Numerical methods**, where the sound is calculated using a combination of Computational Fluid Dynamics and Computational Aeroacoustics.

3.3.1. Theoretical methods

According to Howe [35, 36], various theoretical models for trailing edge noise can be identified:

- based on Lighthill's acoustic analogy;
- based on the solution of linearized hydroacoustic equations, like the one developed by Amiet [2, 3];
- *ad hoc* models that make use of empirically determined source distributions.

All the above-mentioned theories achieve the same conclusion: the scattering process, determined by the pressure fluctuations at the sharp edge of the airfoil, leads to an increase in the radiated sound power, corresponding to a M^5- scaling law [71]. This dependence is clearly shown in Figure 3.11, where the power law for trailing edge noise emissions is compared with the data measured for straight and serrated trailing edges. For both cases, the experimental results follow the trend of the 5th power law, proving the relation between the

SPL and the freestream velocity [5].

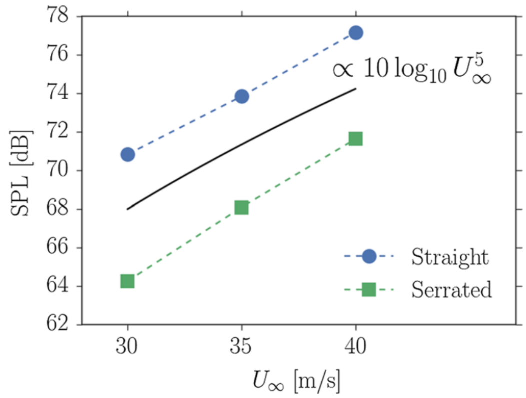

Figure 3.11: The 5th power law dependence of the sound power with the flow speed is represented by the black straight line. The blue and the green lines show the measured data for the straight and the serrated edges, respectively [5].

The main difference between the theoretical models regards how the flow is modelled at the interaction with the edge of the blade. In the first category, a turbulent flow is assumed while in the other two the sound field is related to the pressure disturbances on or near the edge of the blade [35].

Lighthill's acoustic analogy represents the starting point in aeroacoustics modelling. Lighthill [47] investigated the sound radiated in a free turbulent space, with a characteristic length of the eddies δ_c, a velocity U and a flow density ρ. Assuming the sound generation and the sound propagation as two separated mechanisms [14], the aerodynamic noise is derived from the Navier-Stokes equations. Follows that the radiated sound intensity I is proportional to

$$I \sim \rho\, U^3\, M^5\, \frac{\delta_c^2}{R^2} \tag{3.3}$$

where M is the Mach number ($M = U/c$) and R is the distance from the receiver. Here, a quadrupole distribution of the source is adopted [47].

For wind turbines, solid boundaries affect the emitted sound. Thus, it is important to take into account their effects, especially for low flow velocities. Curle makes use of a static surface, with length l_s, and proposes the following scaling rule for the sound intensity in the hypothesis of a compact surface (i.e. Helmholtz number He $= k\, l_s \ll 1$) [19]

$$I \sim \rho\, U^3\, M^3\, \frac{l_s^2}{R^2}\, \frac{L_b}{l_s} \tag{3.4}$$

with L_b, span of the blade.

The compactness of the surface allows to scale the sound intensity with the free stream velocity as U^6. Now, the sound source is approximated as a dipole distribution because the propagation time is very small compared to the wavelength of the acoustic wave.

Comparing Equation 3.3 and Equation 3.4, it is evident that the presence of a surface leads to a louder noise at low Mach number and high Reynolds number. The drawbacks of Curle model is that when non-compact surfaces or high frequencies are assessed, the dipole term cannot be evaluated through a dimensional analysis [26].

Ffowcs-Williams et al. [26, 27] extended the Lighthill theory with the introduction of moving non-compact surfaces and provided an analytical solution in the so-called FH-W model. Splitting the domain into the surface and the surrounding flow, the analogy describes entirely the radiation of acoustic waves from a moving source immersed in a fluid. For a turbulent boundary layer thickness δ_l, passing the trailing edge of a blade with a span L_b, the radiated sound intensity results in

$$I \sim \rho\, U^3\, M^2\, \frac{{\delta_l}^2}{R^2}\, \frac{L_b}{\delta_l}\, \sin^2(\kappa/2) \tag{3.5}$$

with ρ the density of the flow, U the flow velocity and κ the directivity angle of the source. The term $\sin^2(\kappa/2)$ represents the directivity factor, which equals 1 for an observer perpendicular to the trailing edge surface (i.e. $\kappa = 180$ degree) [13]. The sound pressure depends on the fifth power of the flow velocity (i.e. U^5) as well as on the characteristic scale of the flow (i.e. δ_l).

In this case, the acoustic waves are radiated towards the upstream direction and the source is approximated as a combined distribution of monopole and dipole. As already discovered by Curle, a dipole is a more efficient radiator when solid boundaries play a role. Its contribution is known as **thickness noise**, since a fluid displacement is caused by the moving surface. Instead, the monopole contribution is called **loading noise** because the acceleration of the moving noise source introduces a force over the fluid [11].

The analyzed noise emitted from the interaction between a scattering plane and a moving fluid represent the basis for both the semi-empirical and numerical models.

3.3.2. Semi-empirical methods

In the aeroacoustics field, the BPM (i.e. Brooks, Pope and Marcolini) model is the most adopted semi-empirical method. On the basis of the scaling laws previously described, the authors provided a quantitative measure of the SPL for all the five airfoil-self noise mechanisms.

The normalization form of the 1/3-octave SPL ($\mathrm{SPL}_{1/3}$) used in the model is the following [13]:

$$\mathrm{Scaled\,SPL}_{1/3} = \mathrm{SPL}_{1/3} - 10\log_{10}\left(M^5\,\frac{\delta_l^*\,L_b}{R^2}\right) = \mathrm{F(St)} + K \tag{3.6}$$

with $\mathrm{SPL}_{1/3} = \mathrm{OSPL} + \mathrm{F(St)}$.

The scaling term $\mathrm{Scaled\,SPL}_{1/3}$ is a function of the Mach number, M^5, the boundary layer displacement thickness, δ_l^*, the span length of the blade, L_b and the distance between the observer and the edge of the airfoil, R. The characteristics of the acoustic spectrum are represented by the second and the third term on the right-hand side of Equation 3.6. F(St) determines the shape of the spectrum and is subject to the ratio between the Strouhal number (i.e. $\mathrm{St} = f\,\delta_l^*\,/\,U$) and its maximum value (i.e. $\mathrm{St_{peak}} = f_{\mathrm{peak}}\,\delta_l^*\,/\,U$). In general, this factor gives information about the frequency components of the SPL in the spectrum. Instead, K[3] is an empirical constant and determines the peak values of St [13].

Applying the normalization to the TBL-TE noise for zero angle of attack, the resulting SPL emitted depends on two characteristic factors of the airfoil: the pressure and the suction side.

$$\mathrm{SPL_{TBL\text{-}TE}} = 10\log_{10}(10^{\mathrm{SPL}_p/10} + 10^{\mathrm{SPL}_s/10}) \tag{3.7}$$

where $\mathrm{SPL_{TBL\text{-}TE}}$ is the SPL for the TBL-TE noise, SPL_p is the SPL at the pressure side and SPL_s is the SPL at the suction side. According to Brooks et al. [13], each side of the airfoil generates TBL-TE noise independently from the other.

For non-zero angle of attack, the total TBL-TE and the separation noise ($\mathrm{SPL_{total}}$) is computed as

$$\mathrm{SPL_{total}} = 10\log_{10}(10^{\mathrm{SPL}_\alpha/10} + 10^{\mathrm{SPL}_p/10} + 10^{\mathrm{SPL}_s/10}) \tag{3.8}$$

SPL_α is the noise dependent on the angle of attack and accounts for boundary layer separation [13].

[3] The values for K can be find in the Appendix A of "*Airfoil Self-Noise and Prediction*" [13].

For $\alpha \leq$ 12.5 degree, the factors in Equation 3.8 are expressed as:

$$\mathrm{SPL}_p = 10\log\left(\frac{\delta^*_{l,p}\, M^5\, Lb\, \bar{D}_H}{R^2}\right) + \mathrm{F}_1\left(\frac{\mathrm{St}_p}{\mathrm{St}_1}\right) + (K_1 - 3) + \Delta K_1 \tag{3.9}$$

$$\mathrm{SPL}_s = 10\log\left(\frac{\delta^*_{l,s}\, M^5\, Lb\, \bar{D}_H}{R^2}\right) + \mathrm{F}_1\left(\frac{\mathrm{St}_s}{\mathrm{St}_1}\right) + (K_1 - 3) \tag{3.10}$$

$$\mathrm{SPL}_\alpha = 10\log\left(\frac{\delta^*_{l,s}\, M^5\, Lb\, \bar{D}_H}{R^2}\right) + \mathrm{F}_2\left(\frac{\mathrm{St}_s}{\mathrm{St}_2}\right) + K_2 \tag{3.11}$$

While for $\alpha \geq$ 12.5 degree

$$\mathrm{SPL}_p = -\infty \qquad \text{and} \qquad \mathrm{SPL}_s = -\infty \tag{3.12}$$

$$\mathrm{SPL}_\alpha = 10\log\left(\frac{\delta^*_{l,s}\, M^5\, Lb\, \bar{D}_l}{R^2}\right) + \mathrm{F}_1^{'}\left(\frac{\mathrm{St}_s}{\mathrm{St}_2}\right) + K_2 \tag{3.13}$$

Here, $\delta^*_{l,p}$ and $\delta^*_{l,s}$ indicate the boundary layer displacement thickness at the pressure side and at the suction side, respectively. $\bar{D}_H$ and $\bar{D}_l$ represent the directivity functions while F_1, $\mathrm{F}_1^{'}$ and F_2 define the spectral shape functions. K_1 and K_2 are constants. For their detailed formulation, the reader is referred to the Appendix B of "*Airfoil Self-Noise Prediction*" [13].

The Strouhal numbers in Equations 3.9, 3.10, 3.11 and 3.13 are defined as:

$$\mathrm{St}_p = \frac{f\,\delta^*_{l,p}}{U} \qquad \text{and} \qquad \mathrm{St}_s = \frac{f\,\delta^*_{l,s}}{U} \tag{3.14}$$

$$\mathrm{St}_1 = 0.02\, M^{-0.6} \tag{3.15}$$

$$\mathrm{St}_2 = \mathrm{St}_1 \times \begin{cases} 1 & (\alpha < 1.33^\circ) \\ 10^{0.0054\,(\alpha-1.33)^2} & (1.33^\circ \leq \alpha \leq 12.5^\circ) \\ 4.72 & (12.5^\circ < \alpha) \end{cases} \tag{3.16}$$

Considering the LBL-VS noise, no semi-empirical methods are present in literature. This is because the general mechanism is very complex and the trend of multiple tones in the narrowband range is unpredictable. However, some guidelines can be outilined from the experiments perfomed by Brooks et al. [13] leading to the following scale expression:

$$\mathrm{SPL}_{\text{LBL-VS}} = 10\log_{10}\left(\frac{\delta_{l,p}\, M^5\, L_b\, \bar{D}_\mathrm{H}}{R^2}\right) + \mathrm{F}_3\left(\frac{\mathrm{St}^{'}}{\mathrm{St}^{'}_{\text{peak}}}\right) + \mathrm{F}_4\left[\frac{R_e}{R_{e,0}}\right] + \mathrm{F}_5\,(\alpha) \tag{3.17}$$

with $\delta_{l,p}$ the boundary layer thickness at the pressure side. The sound pressure level for the LBL-VS noise, indicated as $\mathrm{SPL}_{\text{LBL-VS}}$, shows a dependence on the boundary layer parameters (i.e. $\delta_{l,p}$ and L_b) as well as on the Reynolds and Mach number.

$R_{e,0}$ is a reference Reynolds number, dependent on the angle of attack as follows:

$$R_{e,0} = \begin{cases} 10^{\,0.125\alpha\,+\,4.978} & \alpha \leq 3.0 \\ 10^{\,0.125\alpha\,+\,4.978} & 3.0 < \alpha \end{cases} \tag{3.18}$$

For the Strouhal numbers, their definitions are provided below:

$$\mathrm{St}' = \frac{f\,\delta_{l,p}}{U} \tag{3.19}$$

$$\mathrm{St}'_{\mathrm{peak}} = \mathrm{St}'_1 \times 10^{-0.04\alpha} \qquad \text{with} \qquad \mathrm{St}'_1 = \begin{cases} 0.18 & (R_e \leq 1.3 \times 10^5) \\ 0.001756\,R_e^{0.3931} & (1.3 \times 10^5 < R_e \leq 4.0 \times 10^5)) \\ 0.28 & (4.0 \times 10^5 < R_e) \end{cases} \tag{3.20}$$

Three spectral shape functions are applied in Equation 3.17 [13]:

1. F_3 determines the shape of the acoustic spectrum as the ratio between the Strouhal number and its maximum value;
2. F_4 defines the peaked scale level of the shape curve. It depends on the Reynolds number;
3. F_5 introduces the angle dependence for the shape curve.

For their complete formulation, the interested reader is referred to "*Airfoil Self-Noise Prediction*" [13].

The SPL for the tip-vortex noise (SPL_{TP}) is computed as:

$$SPL_{TP} = 10\log_{10}\left(\frac{M^5\,(1\,+\,0.036\,\alpha_{\mathrm{tip}})^3\,L_{TP}{}^2\,\bar{D}_H}{R^2}\right) - 30.5(\log \mathrm{St}''\,+\,0.3)^2 + 126 \tag{3.21}$$

with L_{TP} the span wise extent of the vortex at the trailing edge and α_{tip} the tip angle of attack [13].

The second term on the right side of Equation 3.21 provides the spectral shape, with corresponds to a parabolic fit with a peak of the Strouhal number at 0.5. As regards the Strouhal number, it is calculated with

$$\mathrm{St}'' = \frac{f\,L_{TP}}{U(1\,+\,0.036\,\alpha_{\mathrm{tip}})} \tag{3.22}$$

For the TEB-VS noise, Brooks et al. [13] proposed the existence of semi-empirical models. As mentioned in Chapter 3.2.4, the TEB-VS noise is relevant when the magnitude of the trailing edge thickness is comparable with the boundary layer displacement thickness [10]. Under such condition, the $SPL_{TEB\text{-}VS}$ can be predicted similarly to the $SPL_{LBL\text{-}VS}$ and to the $SPL_{TBL\text{-}TE}$

$$SPL_{TEB\text{-}VS} = 10\log_{10}\left(\frac{h_t\,M^{5.5}\,L_b\,\bar{D}_H}{R^2}\right) + F_6\left(\frac{h_t}{\delta^*_{\mathrm{l,avg}}}\,,\,\Psi\right) + F_7\left(\frac{h_t}{\delta^*_{\mathrm{l,avg}}}\,,\,\Psi\,,\,\frac{\mathrm{St}'''}{\mathrm{St}_{\mathrm{peak}}'''}\right) \tag{3.23}$$

with Ψ, the trailing edge solid scale, and $h_t/\delta^*_{\mathrm{l,avg}}$, the degree of bluntness ($\delta^*_{\mathrm{l,avg}}$ is the average between the boundary layer displacement thickness at the pressure side and at the suction side).

The Strouhal numbers are defined as:

$$\mathrm{St}''' = \frac{f\,h_t}{U} \qquad \text{and} \qquad \mathrm{St}'''_{\mathrm{peak}} = \frac{f_{\mathrm{peak}}\,h_t}{U} \tag{3.24}$$

In their experiments, Brooks et al. [13] demonstrated that a better fitting of the sound level is obtained assuming a dependence on the 5.5 power of the Mach number. In addition, the fitting of the function F_7 is performed with only two values of the solid angle (i.e. 0 degree and 14 degree). The acoustic spectrum is determined from the functions F_6 and F_7. The first one gives information about the peak levels while the second one specifies the shape of the spectrum. For the complete derivation of these functions, the reader is referred to "*Airfoil Self-Noise prediction*" [13].

3.3.3. Numerical methods

Next to theoretical and semi-empirical methods, numerical simulations are used to investigate the sound emitted by a wind turbine. The basic idea is to capture the pressure fluctuations in a given region, in order to obtain information about the sound generation. A high spatial resolution is required to correctly detect small pressure disturbances. In this sense, a better approximation of the solution is achieved with a larger series of points per wavelength. The consequent drawbacks result in time-demanding and expensive calculations as well as in a limited range of frequencies measured.

Generally, these computational methodologies are distinguished in two main categories [18]:

1. **Direct**, which evaluate compressible flow equations to simultaneously determine the propagation of the sound and the fluid dynamic of the source.

2. **Hybrid**, which assess the flow and the sound separately. To predict the noise propagation, it is assumed that only the flow can alter the sound emission while the acoustic waves do not modify the flow dynamic [94]. Therefore, these techniques are mainly adopted for flows at low Mach numbers.

However, in the current research numerical methods will not be employed for the noise assessment of small wind turbines.

4

Beamforming techniques

The current Chapter presents the two beamforming algorithms used in this project. The first section describes the conventional beamforming for both the time domain and frequency domain formulations. Then, the ROtating Source Identifier is presented. The last section defines the most important quantities to evaluate the beamforming accuracy.

4.1. Conventional Beamforming

Conventional beamforming (CB) together with microphone phased arrays have been widely used for the localization of sound sources in wind tunnels and flight tests [76].

An array consists of a large number of microphones and records the signals emitted by one or several sources. Afterwards, these sound pressures are processed with the beamforming algorithm, which is able to amplify the sound coming from a specific point as well as attenuate any noise coming from other directions [77].

The basic idea is to consider a two-dimensional discretised scan plane, containing J points, where potential sources are expected. In the case of a wind turbine, the scan grid corresponds to the plane of rotation. Figure 4.1 illustrates this configuration, where $\vec{x_m}$ and $\vec{\xi}_j$ represent the coordinates of microphone m and of the scan point j, respectively. Instead, $\vec{r}_{m,j}$ is the distance between microphone m and the scan point j. Its module is equal to

$$\vec{r}_{m,j} = \left|\vec{x_m} - \vec{\xi}_j\right| \tag{4.1}$$

Then, the travel time from each possible source position to the microphones is computed. To take into account the different travel times, the signal emitted from a specific position is determined by delaying or advacing the recorded signals at the microphones. Consequently, the resulting sound pressures are summed to obtain the reconstructed signal. This is why Conventional Beamforming is also called delay-and-sum.

CB can be applied in the time domain as well as in the frequency domain. The main difference in the two formulations is how the signals are delayed. In the first case, the signals are delayed in time, while in the second one, the signals are delayed in phase. For both techniques, the results are plotted in an acoustic image. If the sound pressure field is modelled as a monopole source[1] and all the microphone signals are used, this plot depicts the contributions of each sound sources and their corresponding positions. Figure 4.2 presents the source map for a time-domain CB applied to a simulated point source emitting tonal sound at 1500 Hz with SPL = 100 dB. The rotational speed corresponds to 6.67 Hz and the distance from the array is 1.5 m. An array of 64 microphones, a scan grid of 2 x 2 m^2 with a total of 25000 scan points[2] and a time snapshot of 0.3 s are employed. The radius of rotation is 0.5 m. From the plot, it can be clearly seen the trajectory followed by

[1]The monopole source is a sound source that emits sound equally in all the directions [69].
[2]50 scan points are used in the x an y direction, which lead to a total of 25000 scan points.

the source as well as the SPL emitted.

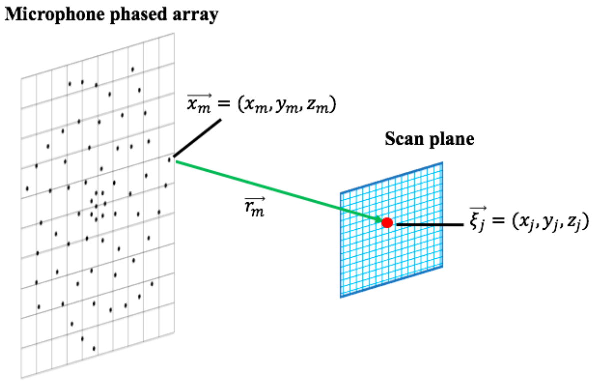

Figure 4.1: The array of 64 microphones and the scan plane of the sound source, used in CB, are shown.

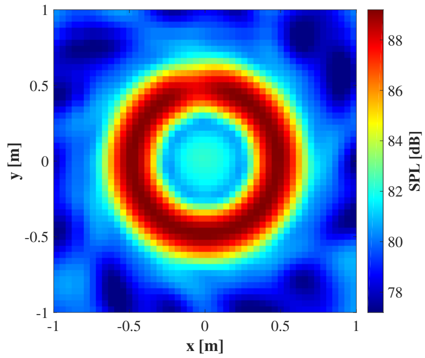

Figure 4.2: Time-domain CB applied to a simulated point source with f = 1500 Hz and SPL = 100 dB.

The simplicity and robustness of CB are limited by the large number of side lobes (i.e. local peaks in the source map where no sound sources are present), as well as by the Rayleigh limit [3] for the array spatial resolution and by a low dynamic range (i.e. the difference between the highest side lobe and the main lobe, expressed in dB [91]).

4.1.1. Time domain

When Conventional Beamforming is performed in the time domain, the main focus is on the time delays between the emission of the sound signal at the source and the received signals at each microphone. This process can be decoupled into two steps, illustrated in Figure 4.3 [42]:

1. **Synchronization**
2. **Weight-and-sum**

For the first one, the time delay is computed from the distance between the grid points on the scan plane and the microphones as

$$\Delta t_{m,j} = \frac{\|\vec{r}_{m,j}\|}{c} \tag{4.2}$$

in which, $\Delta t_{m,j}$ is the time delay between the sound source at scan point j and the microphone m.

Then, this quantity is used to advance or delay each sensor output. As a result, all the signals coming from a desired direction are synchronized.

Next step is to weight and sum all the synchronized signals to obtain a reconstructed sound signal, $p_j(t)$, for a scan point j. It can be expressed as [103]

$$p_j(t) = \frac{1}{M'} \sum_{m=1}^{M'} w_{m,j}\, p_m(t + \Delta t_{m,j}) \tag{4.3}$$

where M' is the total number of microphones placed on the array, $p_m(t)$ is the pressure signal recorded by the microphone m and $w_{m,j}$ is the weight factor.

Even if the microphones have different distances from the source plane, the use of the weight factor guarantees that all the microphones have the same influence on the final output [23]. The weight factor is calculated

[3]The Rayleigh limit will be discussed in Chapter 4.3.1

as

$$w_{m,j} = \frac{\|\vec{r}_{m,j}\|}{r_0} \tag{4.4}$$

The reference distance from the source, r_0, leads to a better comparison between the signals and it is assumed equal to 1 meter.

Knowing the output sound signal, the Sound Pressure Level (SPL) can be computed using Equation 2.7. All the steps are performed for each scan locations. The final result is illustrated in a source map, which includes the coordinates of the position together with the values of SPL.

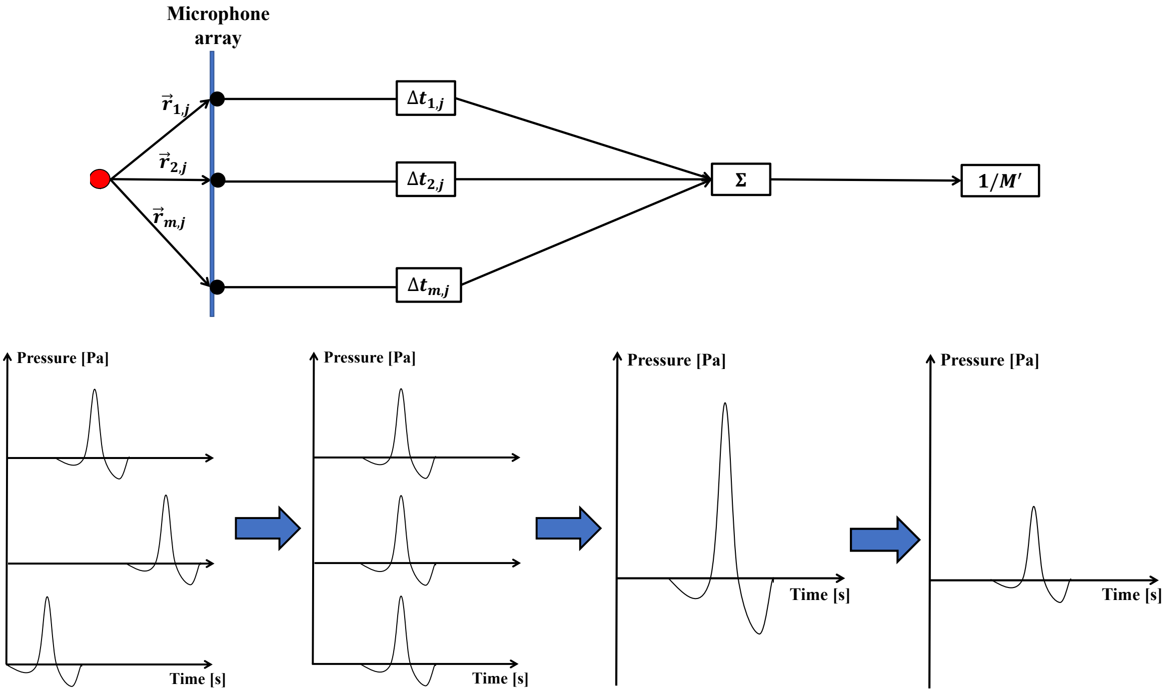

Figure 4.3: Overview of the Conventional Beamforming in the time domain. The synchronization of the signals as well as the weight-and-sum are here presented. The red point represents the sound source.

4.1.2. Frequency domain

If Conventional Beamforming is applied in the frequency domain, the microphone signals are delayed in phase. In comparison with the time-domain CB, a frequency analysis is performed and lower computational times are achieved [59].

The pressure signal received by microphone m and the acoustic pressure on the scan point $\vec{\xi}_0$, $p_{\vec{\xi}_0}(t)$, are linked by

$$p_{\vec{\xi}_0}(t) = \frac{r_{m,0}}{r_0} p_m(t + \Delta t_{m,0}) \tag{4.5}$$

where $r_{m,0}$ and $\Delta t_{m,0}$ represent respectively the distance and the time delay between microphone m and the scan point $\vec{\xi}_0$.

Applying the Fourier transform to Equation 4.5, this results to

$$P_{\vec{\xi}_0}(f) = \frac{r_{m,0}}{r_0} P_m(f) e^{2\pi i f \Delta t_{m,0}} \tag{4.6}$$

After the transformation of the pressure signal in the frequency domain, the reconstructed signal can be evaluated with two different methods.

The first one follows the same steps performed in the time-domain CB and the procedure is repeated for every frequency and for every scan point [42]. The phases of each signals are adjusted (i.e. delayed or advanced), to consider the phase delays caused by the different microphone-to-source distances. The resulting pressures are summed and divided for the number of the microphones in the array, leading to

$$P_{\vec{\xi}_0}(f) = \frac{1}{M'} \sum_{m=1}^{M'} \frac{r_{m,0}}{r_0} P_m(f) e^{2\pi i f \Delta t_{m,0}} \tag{4.7}$$

for a scan point located in $\vec{\xi}_0$. Since in reality acoustic signals are not continuous, DFT is applied as explained in Section 2.4.3.

The second method is fully described in [77]. For its application, Equation 4.7 has to be rearranged

$$P_m(f) = \frac{r_0}{r_{m,j}} P_{\vec{\xi}_j}(f) e^{-2\pi i f \Delta t} \tag{4.8}$$

for a general scan point *j*.

Then, the pressure vector, $\vec{P}(f)$, measured by M' microphones and converted in the frequency domain, can be expressed with:

$$\vec{P}(f) = \begin{pmatrix} P_1(f) \\ P_2(f) \\ \vdots \\ P_{M'}(f) \end{pmatrix} \tag{4.9}$$

$\vec{P}(f)$ can be translated in the scan plane using the steering vector $\vec{g}$. This quantity is used to identify at which scan point the sound source is located by steering from each microphone towards each scan point. Its components, g_m, are defined for every microphone m and for every scan point $\vec{\xi}_j$ as

$$g_m(f, \vec{\xi}_j) = \frac{r_0}{r_{m,j}} e^{-2\pi i f \Delta t_{m,j}} \tag{4.10}$$

In this way, the shifts in phase and the changes in amplitude between the source and the microphone array are taken into account [80]. Knowing the measured pressure vector, the acoustic pressure amplitude, on the scan plane position *j* and at the frequency *f*, results from the following minimization:

$$J_j = \left\| \vec{P} - P_{\vec{\xi}_j}(f) \vec{g}_j \right\|^2 \tag{4.11}$$

The aim of frequency-domain CB is to estimate the value of $P_{\vec{\xi}_j}(f)$ that better matches the measured value of the pressure amplitude, $\vec{P}$. The solution of this problem can be expressed as:

$$\hat{P}_{\vec{\xi}_j}(f) = \frac{\vec{g}_j^{\,*} \vec{P}}{\|\vec{g}_j\|^2} \tag{4.12}$$

where * indicates the complex conjugate transposition.

In order to compute the SPL, effective pressure is determined, as follows:

$$p_e = \frac{\left| \hat{P}_{\vec{\xi}_j}(f) \right|}{\sqrt{2}} \tag{4.13}$$

Generally, source auto-powers are considered

$$B_j = p_e^2 = \frac{1}{2}\left|\hat{P}_{\vec{\xi}_j}(f)\right| = \frac{1}{2}\hat{P}_{\vec{\xi}_j}(f)\hat{P}^*_{\vec{\xi}_j}(f) = \frac{1}{2}\frac{\vec{g_j}^*\vec{P}}{\|\vec{g_j}\|^2}\left(\frac{\vec{g_j}^*\vec{P}}{\|\vec{g_j}\|^2}\right)^* = \frac{1}{2}\frac{\vec{g_j}^*\vec{P}\vec{P}^*\vec{g_j}}{\|\vec{g_j}\|^4} \tag{4.14}$$

If the Cross Spectral Matrix $\vec{C} = \vec{P}\vec{P}^*$ is introduced, Equation 4.14 can be written as

$$B_j = \frac{1}{2}\frac{\vec{g_j}^*\vec{C}\vec{g_j}}{\|\vec{g_j}\|^4} \tag{4.15}$$

If this procedure is repeated for every scan point j, the two-dimensional acoustic image is determined, where all the possible source locations are depicted [77].

4.1.3. Conventional Beamforming without auto-spectra

Often in wind tunnel measurements, microphone auto-powers have higher values compared to the corresponding cross-power, which means that the main diagonal of $\vec{C}$ prevails on the off-diagonal components [75]. This phenomenon is caused by:

1. **Pressure disturbances of hydrodynamic nature**;
2. **Loss of coherence**.

With respect to the first, if a microphone is located in the wind, it will measures not only acoustic pressures but also hydrodynamic pressure, caused by the turbulent boundary layer surrounding the microphone. However, since wind noise is incoherent[4] for every microphone, this effect is only taken into account by the auto-power diagonal. On the other hand, when the sound propagates through a turbulent medium, different travel spaces lead to different deformations. The phase deformation between two microphones is contained only in the cross-powers elements, which result to have a lower value than in the non-deformed case. This is the reason why, if the loss of coherence is significant, the auto-power dominates on the cross-power.

In these cases, in order to improve the resolution and to suppress background noise, auto-powers are not considered in the beamforming algorithm. The minimisation problem is now expressed as:

$$J = \left\|\vec{C} - \vec{B}\vec{g}\vec{g^*}\right\|^2 \tag{4.16}$$

where $\vec{B}$ is computed for all the scan points, j.

4.2. ROtating Source Identifier

ROtating Source Identifier (ROSI) is a beamforming technique used to identify a specific rotating sound source [82]. It has been developed on airplanes flying over and, recently, on wind turbines [78].

The main difference with Conventional Beamforming is the rotation of the scan plane, which follows the movement of the sound source. As it can be seen from Figure 4.4, the vector position of the scan point $\vec{\xi}_j$ depends on an additional variable: the time. Knowing the rotational speed of the source, $\vec{\Omega}$, it is possible to determine the locations in time of all the grid points.

The rotation of the sound source in a uniform flow does not represent any limitations for ROSI [78]. Therefore, this beamforming technique has been adopted to assess a small upwind turbine in the Open Jet Facility at TU Delft University. Placing the microphone array out-of-flow, the acoustic signals are then determined from the analysis of the microphone recordings.

To take into account the presence of a moving frame, de-Dopplerisation is performed [78]. For every source

[4]Two sound waves are defined coherent if they have a constant difference in phase and the same waveform (e.g. sinusoidal) [100].

position, the received time at the microphone is calculated, leading to a time history reconstruction of the received signal. Since microphone is sampled for each of these emission times, the Doppler effect is removed (Equation 2.15). Then, summing all de-Dopplerized signals recorded by all the microphones in the array, the strength of the sound source localized in the specific grid point is increased, while the contributions from other directions are contained [37]. If the process is repeated for different grid points, the final result is an acoustic image, which clearly shows the noise peaks instead of a uniform distribution of the noise sources. Figure 4.5 shows the ROSI plot for a simulated point source emitting tonal sound at 1500 Hz with SPL = 100 dB. The rotational speed corresponds to 6.67 Hz and the distance from the array is 1.5 m. An array of 64 microphones, a scan grid of 2 x 2 m^2 with a total of 25000 scan points[5] and a time snapshot of 0.3 s are employed. The radius of rotation is 0.5 m.

After the source locations are determined using this time domain technique, the reconstruction of the power spectrum is performed in the frequency domain. Thus, the Discrete Fourier Transform is applied to the reconstructed source signal for every specific grid point. Follows the calculation of the auto-power spectrum.

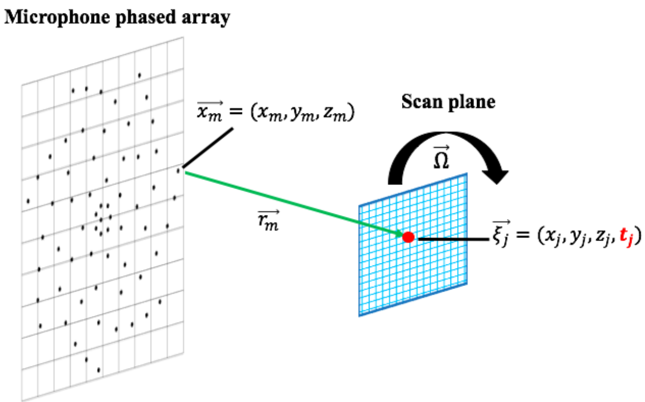

Figure 4.4: The array of 64 microphones and the rotating scan plane of the sound source, applied in ROSI, are shown.

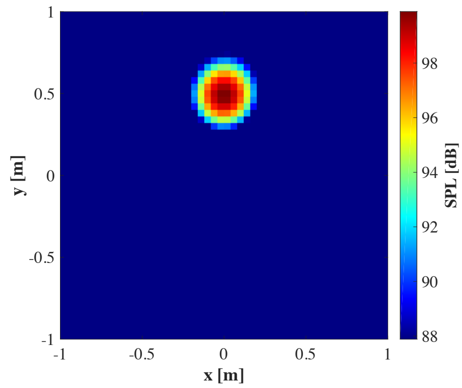

Figure 4.5: ROSI applied to a simulated point source with f = 1500 Hz and SPL =100 dB.

4.3. Array performance

The quality of the acoustic image is an indicator of the array performance. The array resolution is defined as the ability of the array to determine the direction of propagation. It is usually defined in terms of 3 dB down point, i.e. the point located 3 dB below the main peak [88].

Figure 4.6 illustrates two parameters used in the analysis of the source map: the **Main Lobe Width (MLW)** and the **Maximum Side lobe Level (MSL)** [50].

4.3.1. Main Lobe Width and Rayleigh limit

From the acoustic image of Figure 4.6, the sound source can be recognized from the peak position [77]. In particular, the location and the magnitude of the true sound source in the scan plane are described by the main lobe.

To define the Main Lobe Width, an area on the plane at 3 dB below the main lobe's peak is taken. The maximum distance between two points of this contour represents the MLW [88]. This quantity gives information about the spatial resolution of the microphone array: a narrower MLW allows to identify sound sources closely located. However, a distance threshold exists: the Rayleigh limit, R_a, formulated as [51]

[5]50 scan points are used in the x an y direction, which lead to a total of 25000 scan points.

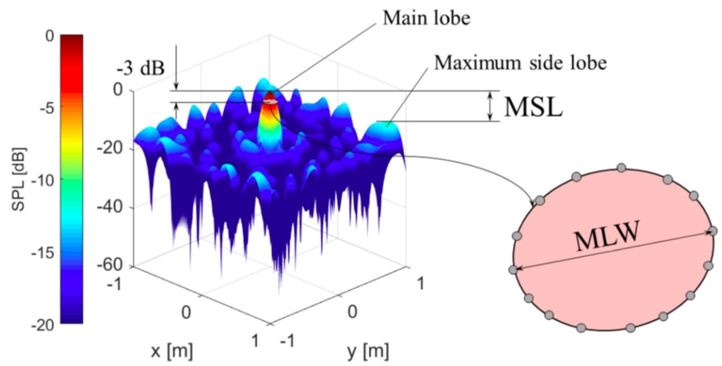

Figure 4.6: Main Lobe Width and Maximum Side lobe Level representation [50].

$$R_a = 1.22 \frac{cY}{Df} \tag{4.17}$$

in which Y measures, in meter, the distance between the microphone phased array and the scan plane of the sound source while D represents the array aperture (also measured in meter).

If the spacing between the sources is below the Rayleigh limit, then the sources are not distinguished like separated.

4.3.2. Maximum Side lobe Level

Other local peaks can appear in the source plot, even if in these regions no sound sources are present [87]. They are called side lobes when their height is less than the main lobe's peak or grating lobes when they have a magnitude comparable with the main lobe. Follows the definition of the Maximum Side lobe Level as the level of the main secondary lobe. This parameter is calculated as the difference in magnitude between the main lobe and the maximum side lobe [45]. The MSL, measured in decibels, indicates how much a true sound source can be misinterpreted.

4.3.3. Window function

Since the acoustic array has a finite number of microphones, the presence of side lobes is unavoidable. However, some techniques have been investigated to optimize the performance of the acoustic array, reducing the side lobe level as low as possible [77].

The most common consists in the use of window functions for the signal analysis. These functions have a continuous spectrum and their amplitude slightly reaches zero outside their interval of definition. A window u_l with $l = 1, \cdots, L_s$ is multiplied to Equation 2.27 as follows [30]:

$$p_m(f_b) = \frac{2}{L_s} \sum_{l=1}^{L_s} u_l \, \tilde{p}_{m,l} e^{-2\pi i f_b l \Delta t} \tag{4.18}$$

When $u_l \equiv 1$, the window is rectangular.

The present work adopts the Hanning window, which has a sinusoidal shape:

$$u_l = \sin^2(\pi \, l / \, L_s) \tag{4.19}$$

In conclusion, first the Hanning window is applied to the time-domain data and then the Discrete Fourier Transform is performed.

5

Experimental set-up

This Chapter describes the set-up of the two experiments carried out in the project. For both experiments, the same array configuration, consisting of 64 microphones, is used (see Figure 5.1).

5.1. Anechoic Tunnel experiment

The first experiment of this research was conducted at the Delft University of Technology anechoic vertical wind tunnel (A-Tunnel). A small-scale rotating structure was built to reproduce the acoustic of a small wind turbine.

5.1.1. Anechoic Tunnel facility

The A-Tunnel is a vertical low turbulence wind tunnel with an open-inflow from below [85]. However, in this experiment no jet-flow was used.

Since the entire chamber is covered with fiberglass wedges, a partial adsorption of sound waves can be obtained. This enables to perform aeroacoustics experiments, preventing the reflections of the sound pressure waves and avoiding any external noise [8]. To record the signals emitted by the test objects, a planar acoustic array of 2 x 2 m^2 was employed. The array consists of 64 G.R.A.S. 40PH free-field microphones with integrated constant current power (CCP) amplifiers [1]. The frequency range of these microphones is between 10 Hz and 20 kHz and a sensitivity of 50 mV/Pa is reached at 250 Hz. The diameter and the length of each microphone correspond to 7 mm and 59.1 mm, respectively. The installed data acquisition system (DAS) contains five National Instruments (NI) PXIe-8370 remote control module and a NI RMC-8354 controller. The connection between each microphone and the DAS is realized through a 10-m long G.R.A.S. AA0028 coaxial cable [1]. Different microphone arrangements and fast re-configuration can be possible because the array is equipped with small holes located in the square lattice. The multi-arm logarithmic spiral configuration applied in the experiment is presented in Figure 5.1.

Figure 5.2 shows the facility where the measurements had be carried out together with the microphone phased array.

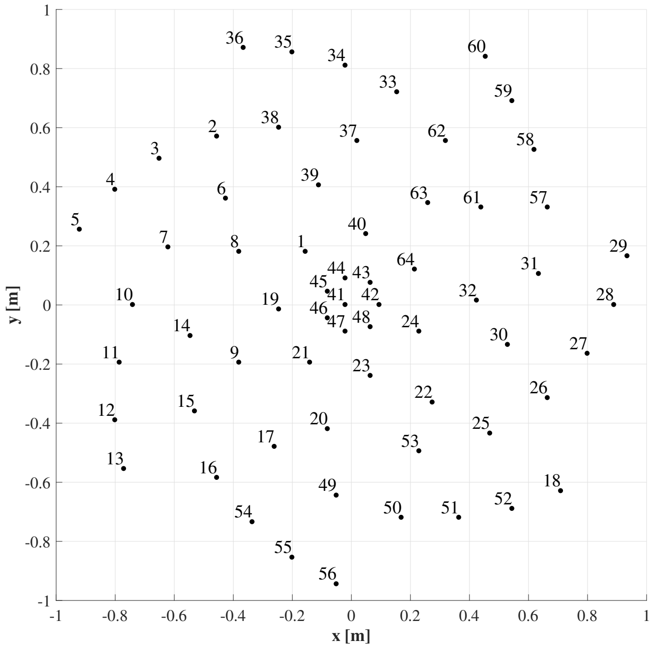

Figure 5.1: Microphone array configuration used in the A-Tunnel experiment. The array is 2 x 2 m^2 and the 64 microphones are arranged in a multi-arm logarithmic spiral configuration.

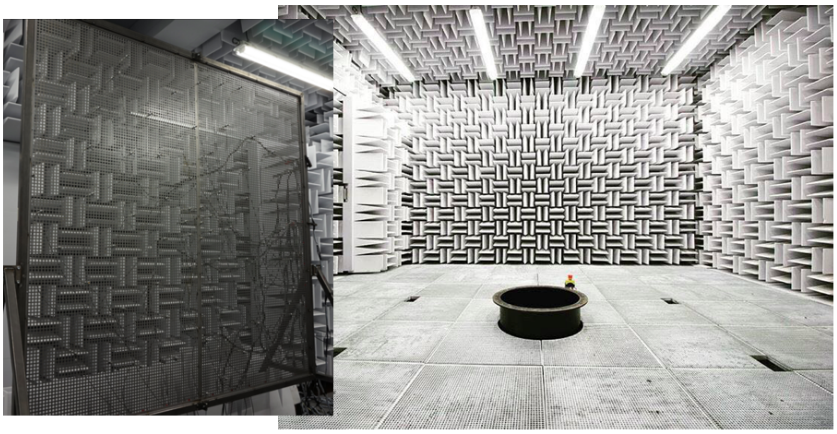

Figure 5.2: Left: the microphone phased array with 64 microphones is shown. Right: the Anechoic Tunnel facility is presented.

5.1.2. Background noise for the A-Tunnel

In a previous experimental campaign [53], an acoustic characterization of the A-Tunnel was performed. However, after these measurements, the facility has been renovated with a new floor. This change may reduce the background noise of the A-Tunnel.

Generally, in a wind tunnel, the driving machines (e.g. the fan), the flow from the nozzle and the interaction of the jet with the collector are the main sources of background noise [72]. For reliable acoustic measurements, a minimal background noise level is required. Specifically, a signal to noise ratio of 10 dB between the sound to measure and the background noise is desired [72].

The levels of background noise at different flow velocities of the tunnel were recorded by the entire array, illustrated in Figure 5.1, and averaged over all the microphones. On the base of other experiments [67, 68], the distance between the microphone array and the center of the nozzle was chosen equal to 1.43 m.

On the left side of Figure 5.3, the background noise spectra for different flow velocities are presented in one-third-octave bands. Also, the case without flow but with the tunnel-system on is included. As expected, the background noise increases with the wind speed. For wind speeds of 10 m/s and of 20 m/s, the spectra show tone peaks at around 315 Hz [53]. The application of acoustic imaging techniques proved that the collector in the ceiling and the wind-tunnel nozzle were the main noise sources at that frequency. In addition, a peak at approximately 700 Hz can be recognized for a flow velocity of 20 m/s. This was due to the cupboard containing the controls of the facility and emitting electronic noise. Since all the sound sources are far away from the test section, their effects are not expected to be relevant for acoustic measurements.

Both the overall background noise levels (OSPL) and the overall A-weighted noise levels (OASPL) are plotted on the right side of Figure 5.3 for a frequency range between 20 Hz and 20 kHz and for different wind speeds. The selected frequency range corresponds to the audible frequency range of a young person [66]. Applying the A-weighted filter, the noise levels are reduced. Especially for higher wind speeds, the noise level decreases up to 25 dB. Another difference in the two curves regards their trend. The OSPL curve follows a logarithmic trend with the wind speed while the OASPL curve has an almost-linear pattern [53].

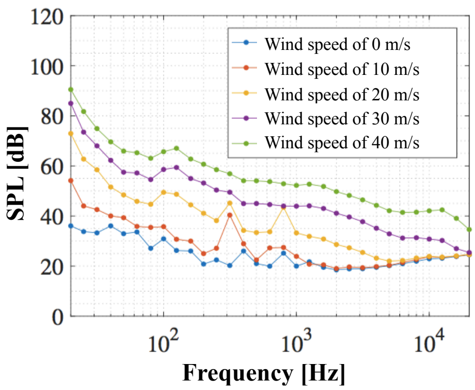

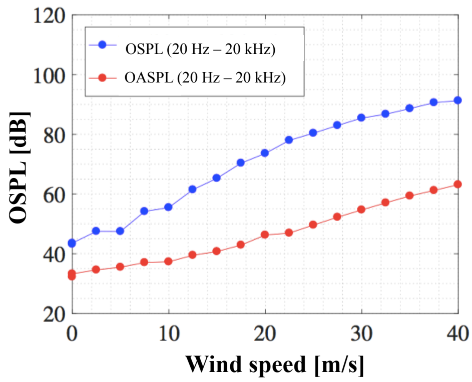

Figure 5.3: Characterization of the background noise for the Anechoic Tunnel. Left: The noise spectra for different wind speeds (i.e. 0 m/s, 10 m/s, 20 m/s, 30 m/s and 40 m/s) in one-third octave bands is presented. Right: The OSPL and the OASPL for different wind speeds (i.e. 0 m/s, 10 m/s, 20 m/s, 30 m/s and 40 m/s) in the frequency range between 20 Hz and 20 kHz are depicted[53].

5.1.3. Sound source

For the experiment, a small-scale rotating source was tested, equipped with four K-50 SQ speakers. These sound sources produced two types of sound: tonal and broadband (i.e. white noise). The pure tone was emitted at two different frequencies, 500 Hz and 1000 Hz. In order to generate and control the signals of the speakers, the following set-up was built, also illustrated in Figure 5.4:

1. Laptop with two MatLab codes to produce the sound;
2. External USB 7.1 Channel Sound Box;
3. USB A-B cable to connect the laptop and the external USB sound card;
4. Eight channel custom amplifier, four tumble switches, four pot-meters (volume) and four jack inputs. Each jack input controls two channels at time (speaker 1 and 2 black channel, speaker 3 and 4 red channel);
5. One jack cable 3.5 mm male-male to connect the external USB sound card with the amplifier, located in the jack port F-out;
6. Custom power supply 12V for the amplifier;
7. Cable with dc jack to connect the eight channel amplifier to the power supply;
8. Four speakers with male cinch connector.

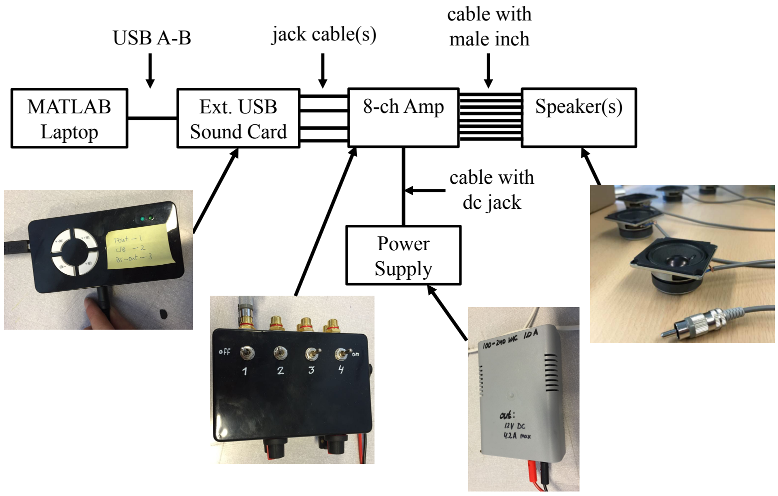

Figure 5.4: Electrical/electronic set-up for the four speakers.

The four speakers were mounted at the tips of a steel tube connected to a DC motor and a slip ring[1]. As it can be seen from Figure 5.5, two speakers were arranged on each radius. The radius of rotation was 0.5 m, while the height of the entire structure was 1.5 m. A power supply gave the input for the rotation of the entire device and an encoder was designed to measure the different rotational speeds tested. In order to distinguish each speaker, different marks were placed on the steel tube. The small-scale structure was located 3.0 m away from the microphone array, aligning the center of rotation of the speakers with the center of the array.

In order to check if the ROSI algorithm recognizes two near sound sources, four set of measurements were taken. The relative distances are shown in Table 5.1. For each of these sets, three rotational velocities were tested: 1 Hz, 2.5 Hz and 4 Hz.

As mentioned before, in the anechoic chamber a small amount of background noise is observed. To analyze how the measurements of the microphone array can be affected by the presence of an external sound source, an additional speaker was used. First, a sound characterization of the object was performed. During this step, the four speakers did not emit any sounds and did not rotate. After that, the external sound source was placed first behind the small-scale prototype (Figure 5.6) and then behind the microphone array.

For each acoustic measurement, a sampling frequency of 50 kHz and a recording time of 40 s were employed.

Measurement number [-]	Distance between the 2 speakers [m]	Distance from the center [m]
1	0.28	0.16
2	0.14	0.30
3	0.33	0.11
4	0	0.37

Table 5.1: Information about the set of measurements performed. The distance between the two sound sources is the distance between the centers of the two speakers on each radius. The distance from the center is the distance from the center of rotation of the device.

[1]The slip ring is an electromechanical device that enables the transmission of both power and electricity from a stationary to a rotating component.

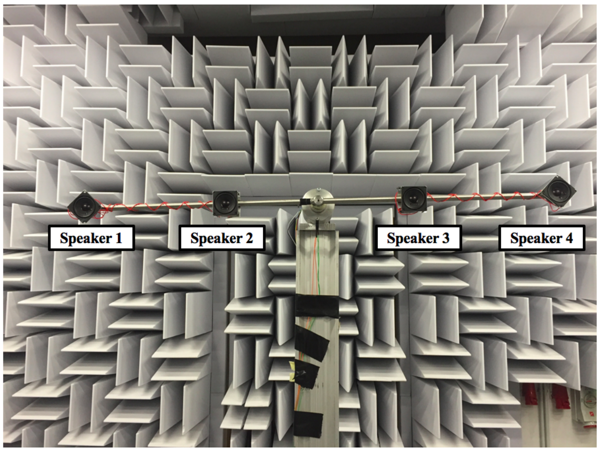

Figure 5.5: Small-scale prototype. The four speakers are labelled.

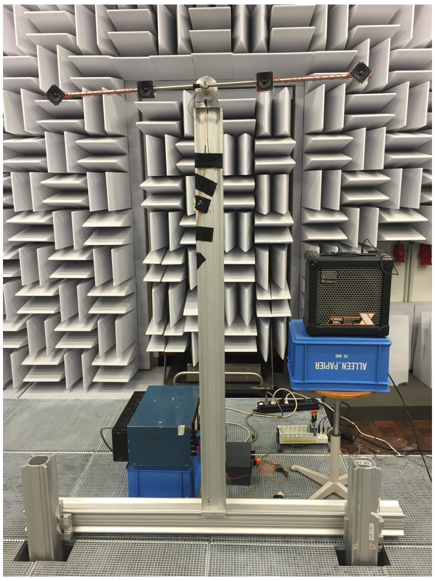

Figure 5.6: Small-scale prototype and an external speaker.

5.2. Open Jet Facility experiment

The second experiment was performed at the Delft Univerisity of Technology Open Jet Facility (OJF). Four different set of blades were tested on the DOD upwind turbine.

5.2.1. Open Jet Facility

The Open Jet Facility is a low speed closed-loop wind tunnel, with an octogonal test section [86]. The equivalent diameter corresponds to 3 m and the ratio between the inlet surface and the outlet surface, the so-called contraction ratio, is equal to 3:1. As a consequence, the stream results uniform with a turbulence intensity of 0.5 % up to 1 m from the noozle exit and lower than 2 % at 6 m from the noozle [49]. The tunnel is powered by a 500 kW fan and the flow velocity reaches its maximum at 34 m/s at the test section [48].

The acoustic array of 2 x 2 m^2 contains 64 POM-2735P-R microphones, arranged in the same configuration of the A-Tunnel experiment (see Figure 5.1). Each microphone has a length of 60 mm and a diameter of 15 mm. The frequency range of these microphones is between 20 Hz and 20 kHz. All the microphones were connected to the data acquisition system (DAS), also called Camera 3 [25]. The array was positioned out-of-flow under the test section of the tunnel. In addition, the array was tilted of 45 degrees.

Figure 5.7 presents the test section of the OJF together with the microphone phased array employed in the measurements. A more detailed representation of the planar array is provided in Figure 5.8.

Figure 5.7: Test section of the Open Jet Facility at TU Delft University. On the bottom, the tilted microphone phased array is presented.

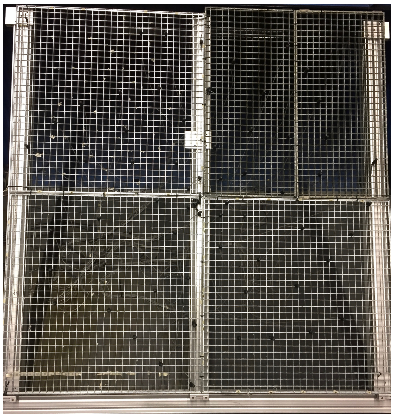

Figure 5.8: The array with 64 microphones arranged in a multi-arm logarithmic spiral configuration.

5.2.2. Background noise for the OJF

During the experimental campaign, the background noise of the OJF was assessed. The noise levels were recorded by the whole array and averaged for all the microphones. As mentioned in Chapter 5.1.2, in a wind tunnel the background noise is mainly caused by the fan, the jet flow from the nozzle and the interaction of the jet with the collector [72].

Figure 5.9 summarizes the results of the noise characterization. On top, the plot shows the noise spectra for different wind speeds (i.e. 5 m/s, 9 m/s, 15 m/s, 25 m/s) in one-third octave bands. As expected, the background noise increases with increasing flow velocities. Several tone peaks can be observed in the spectra:

- for the spectrum corresponding to a wind speed of 5 m/s, the tone peak is at approximately 1.7 kHz;
- for the spectra corresponding to a wind speed of 9 m/s and of 15 m/s, the tone peaks are at about 2.5 kHz. For the spectrum at 15 m/s, another peak can be recognized at 90 Hz;
- for the spectrum corresponding to a wind speed of 25 m/s, the tone peak is at approximately 1.8 kHz;
- for all the spectra, a tone peak occurs at 600 Hz.

In addition, in the range of frequencies where the wind turbine noise is expected, i.e. from 500 Hz to 2000 Hz, the background noise levels are quite high. As it will described in Chapter 7, the background noise is comparable to the sound emitted by the DOD upwind turbine. For that reason, the assessment of the noise for the small wind turbine is compromised.

The bottom plot of Figure 5.9 depicts the OSPL and the OASPL for the background noise. The frequency range is between 20 Hz and 20 kHz and corresponds to the audible frequency range for a young person [66]. Applying the A-weighted filter, a noise reduction of 5 dB can be obtained.

It is important to mention that the background noise measurements were also performed with the tower, the nacelle and the tail fin of the DOD upwind turbine installed. This configuration is illustrated in Figure 5.10. As it can be observed, the rotor is not mounted and the wind turbine is not in operation. The data measured with this geometry will be analyzed in Chapter 7 and further assessments will be provided in Appendix B.

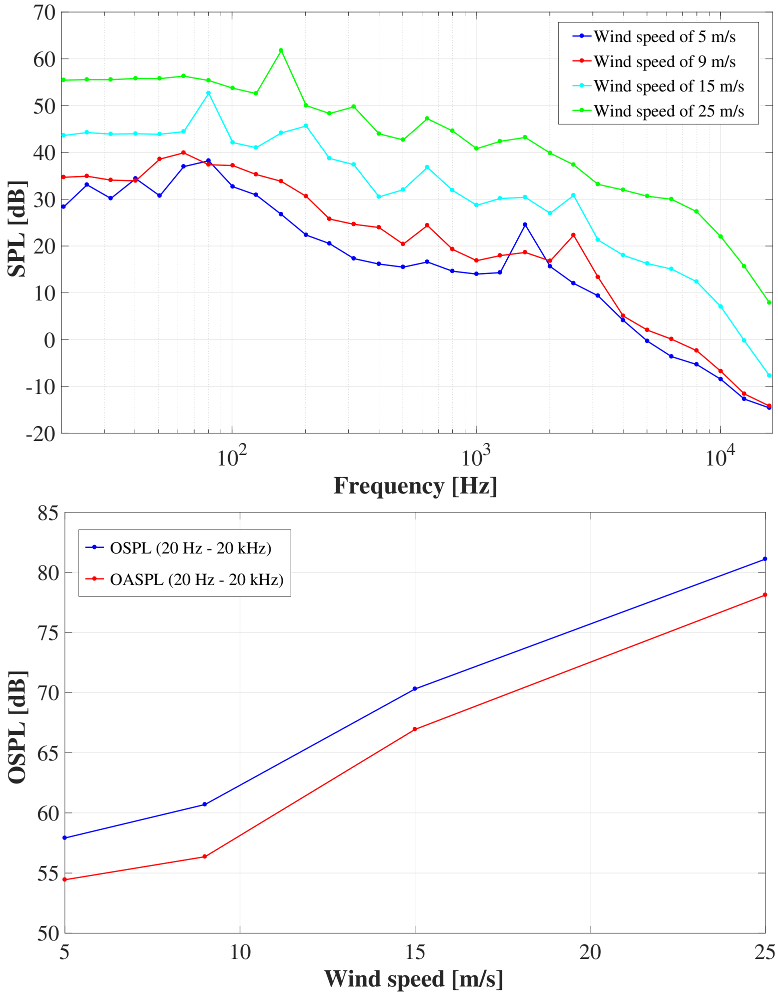

Figure 5.9: Characterization of the background noise for the Open Jet Facility. Top: The noise spectrum for different flow velocities (i.e. 5 m/s, 9 m/s, 15 m/s, 25 m/s) in one-third octave bands is presented. Bottom: The OSPL and the OASPL for different flow velocities (i.e. 5 m/s, 9 m/s, 15 m/s, 25 m/s) in the frequency range between 20 Hz and 20 kHz are depicted.

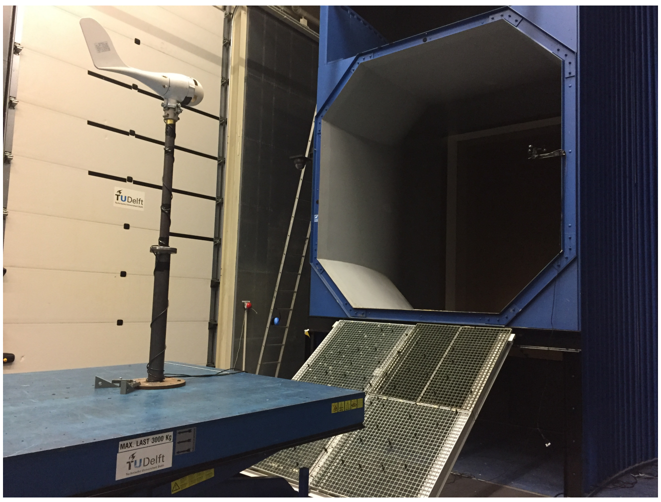

Figure 5.10: Second configuration adopted for the measurement of the OJF background noise. The tower, the nacelle and the tail fin of the DOD upwind turbine are installed. The rotor is not mounted and the wind turbine is not in operation.

5.2.3. DOD upwind turbine

The acoustic measurements were carried out on the small wind turbine, fabricated by the DOD electric company. The horizontal-axis wind turbine has an upwind configuration. The cut-in wind speed, the rated wind speed and the cut-out wind speed correspond to 2.5 m/s, 10 m/s and 25 m/s respectively. The small wind turbine was equipped with a SUN-500G-WAL Grid-Tie inverter. The nacelle of the wind turbine was mounted on a steel tower of 1.8 meter-height. The entire structure was located on a blue table at an height of 1.06 m.

5.2.4. Test matrix

The DOD upwind turbine was tested with four types of blade and at different wind speeds of the tunnel (i.e. 5 m/s, 7 m/s, 9 m/s, 11 m/s and 13 m/s). Through the use of a DC load, it was possible to change the rotational speed of the small wind turbine keeping a constant wind speed. All the blades tested are illustrated in Figure 5.11 while the specifications of the set of measurements performed are given in Table 5.2.

The distance between the center of the microphone array and the center of rotation of the wind turbine was 3 m. The sampling frequency adopted was 50 kHz and the recording time of each measurement was 20 s.

Next to the acoustic measurements, the following wind turbine parameters were recorded: wind speed, power production and rotational speed [60].

Figure 5.11: Four types of blade tested on the DOD small wind turbine during the experiment in the Open Jet Facility. The different blades are presented in the same order as they were tested.

Set of measurements	Number of blades [-]	Rotor diameter [m]	Yaw angle [degree]
1	3	1.66	0
2	3	1.66	30
3	5	1.72	0
4	5	1.72	30
5	5	1.71	0
6	5	2.10	0

Table 5.2: Blades tested on the DOD upwind turbine. The number of blades, the rotor diameter and the yaw angles are shown.

6

Investigation of ROSI uncertainty

In this Chapter, the ROSI uncertainty in the source localization and quantification is assessed using simulations. In particular, simulations are adopted to evaluate the difference between the inputs and the ROSI outputs as well as the agreement between the difference in the beamformed results and the difference in the source levels.

The data sets considered in the current research are the following:

1. A single point sound source, emitting tonal sound;
2. Multiple spatially separated sound sources, emitting tonal sound;
3. Multiple spatially separated sound sources, emitting broadband sound;
4. Distributed line sources, emitting tonal sound;
5. Distributed line sources, emitting broadband sound.

A visualization of the different tested geometries is provided in Figure 6.1. All the sound sources rotate.

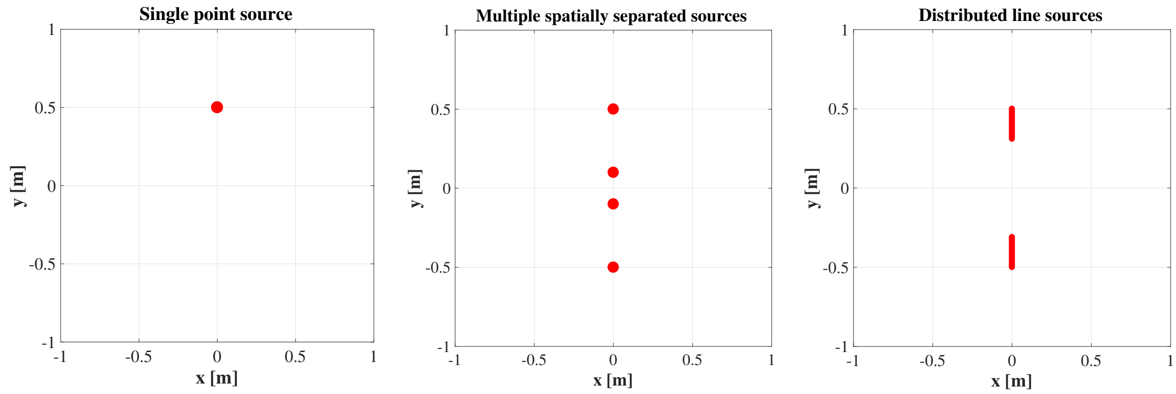

Figure 6.1: Visualization of the different tested geometries. All the sound source rotate. Left: a single point source. Center: multiple spatially separated sources. Right: distributed line sources.

Since measurements are intrinsically imperfect, noise is added to the simulations for a moving point source. Thus, ROSI is investigated under not ideal, but known, conditions.

For the analysis, an array of 64 microphones (see Figure 5.1), with the same configuration employed in the previously described experiments, is used.

In addition, it is important to stress that for the comparison between the inputs and the ROSI outputs, the maximum SPL value is taken and no Source Power Integration[1] over the region of interest is performed, which can have an effect on the results.

First, the simulation model based on ROSI is presented. Then, the five data sets are examined together with an evaluation of how different variables, like the rotational speed, affect the localization and the quantification of the sound source.

6.1. Description of the simulation model

ROSI, discussed in Chapter 4, is the base of this simulation model. Knowing the source pressure at a reference distance (r_0 = 1 m), the algorithm is applied in reverse to determine the pressure at the microphones. The pure tone is simulated as a single frequency cosine wave:

$$p(t) = p_{max}\cos(2\pi f t) \tag{6.1}$$

where $p_{max} = \sqrt{2}p_e$, given that the effective pressure and the SPL are related by Equation 2.7.

The broadband sound is generated through a random number generator, specifically the "randn" function in MatLab. Then, a infinite impulse response (IIR) filter is applied to the signal. In this way, only the frequencies inside the selected band are considered.

The inputs to the model are: the number of sound sources, their velocity vector, their SPL, the frequency of the sound signal or the frequency band if a tone or a broadband are respectively analyzed, the distance from the array and the starting location of the sources.

After the microphone array configuration is loaded, the movement of the source is simulated. Then, for every time step, the distance, $\vec{r}_{m,j}$, from the source current position to each microphone is calculated. With a sound speed of 340 m/s, the time delay is computed using Equation 4.2. Adding the different time delays to the emission time vector, the arrival time at each microphone is obtained and the received acoustic pressure can be determined. Knowing the simulated data recorded by the microphones, ROSI is applied again. The resulting outputs are the source level and the initial location of the sound source. In the case of multiple simulated sources, the sound signals are added together to retrieve the total synthetic pressure. All the steps are summarized in Figure 6.2, where the flow chart of the simulation model is shown.

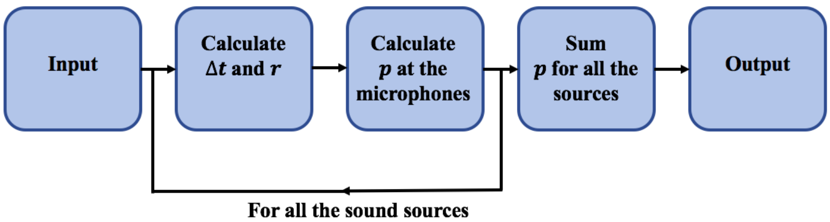

Figure 6.2: Flow chart of the simulation model. The process is performed for all the time steps of the source motion.

[1] Source Power Integration (SPI) is a new acoustic imaging technique. The basic principle is to perform an integration of the source auto-power over the region of interest. As a result, the OSPL for this specific area is determined [77].

6.2. Single rotating sound source

For the investigation of the ROSI estimates, the starting point is a single rotating source emitting tonal sound. The quantification of the source level as well as the source localization are analyzed varying the following parameters:

- the SPL;
- the rotational speed;
- the time snapshot of the input signal;
- the distance from the microphone array;
- the sampling frequency;
- the amount of additional noise.

For all the simulated cases, a scan grid of 2 x 2 m^2 with a total of 25000 scan points[2] has been employed.

6.2.1. Effect of a different SPL

The first simulation consists in one sound source with f = 5000 Hz and a SPL of 30 dB, rotating at 6.67 Hz. The time snapshot corresponds to 1 s and the sampling frequency is 50 kHz. The initial position of the source is (x,y,z) = (0,0.5,3), where y represents the radius of rotation of the source and z the distance between the source and the microphone array. Figure 6.3 depicts the overall configuration, together with the coordinates of the rotating source and the adopted microphone array.

For the second simulation, the single rotating source has a SPL of 60 dB. All the other parameters have been kept equal to the previous case.

Figure 6.4 illustrates the outcomes of the ROSI algorithm. As it can be seen, the initial position of the sound source is correctly retrieved in both examples. Thus, a change in the SPL does not affect the source localization. For the quantification of the source level, the outputs are 29.1770 dB and 59.1770 dB, respectively for the source with a SPL of 30 dB and with a SPL of 60 dB. This proves that the difference in the beamformed results agrees with the difference in the source level (i.e. 30 dB).

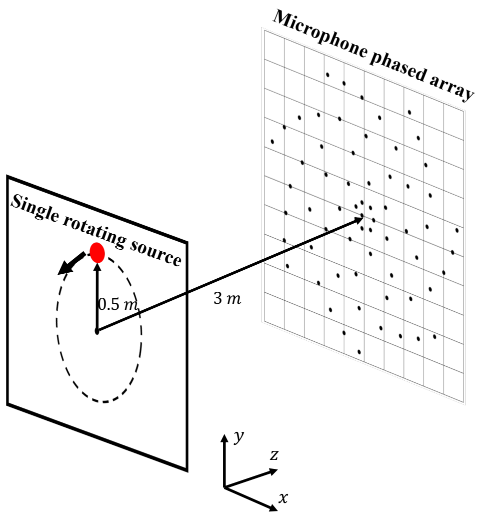

Figure 6.3: Configuration adopted for the simulation of the single rotating source. The multi-arm logarithmic spiral configuration for the microphone array is also illustrated. Initial coordinates of the sound source: (x,y,z) = (0,0.5,3), where x and y are the coordinates of the radius of rotation and z the distance between the source and the array.

[2]50 scan points are used in the x and y direction, which lead to a total of 25000 scan points.

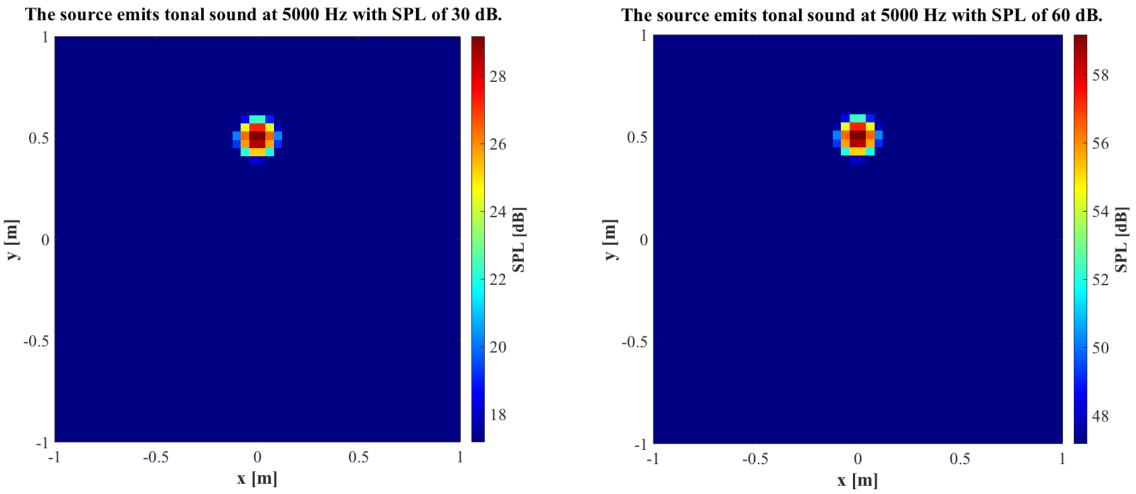

Figure 6.4: Comparison of the ROSI outcome for a sound source rotating at 6.67 Hz and emitting tonal sound at 5000 Hz with SPL of 30 dB (left-side) and with SPL of 60 dB (right-side). The time snapshot is 1 s and the distance between the source and the array is 3 m. An array with 64 microphones (see Figure 5.1) and a scan grid of 2 x 2 m^2 with a total of 25000 scan points are employed.

6.2.2. Effect of the rotational speed

In the simulations, the point source broadcasts tonal sound with a f = 5000 Hz and SPL = 30 dB. The distance between the source and the array is 3 m, the sampling frequency is 50 kHz and the time snapshot is 1 s.

From Figure 6.5, it is possible to deduce that the rotational speed does not affect the computation of the sound level. The ROSI output barely increases with an increasing number of rotations. This can be expected because the scan grid rotates with the same speed of the source, following its movement. The best approximation to the given input is reached with a rotational speed of 6.67 Hz. The SPL values are summarized in Table 6.1.

The rotational speed does not influence the source localization. ROSI is always able to correctly retrieve the initial position of the single rotating source (i.e. (x,y,z) = (0,0.5,3)).

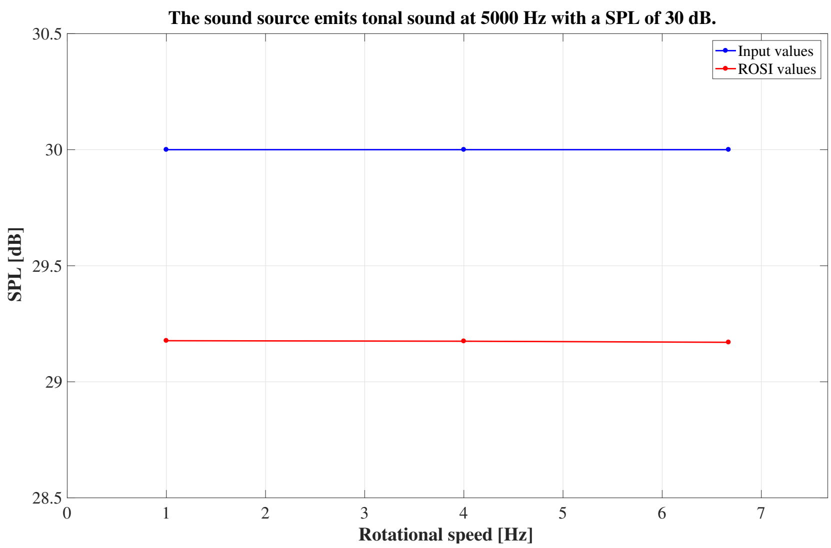

Figure 6.5: Effect of the rotational speed on the estimation of the SPL. The sound source emits tonal sound at 5000 Hz with a SPL of 30 dB. The time snapshot is equal to 1 s. The distance between the point source and the microphone array is 3 m.

Input [dB]	ROSI outputs [dB]		
	RPS = 1 Hz	RPS = 4 Hz	RPS = 6.67 Hz
30	29.18	29.17	29.18

Table 6.1: Comparison of the inputs with the outputs of the ROSI algorithm obtained varying the rotational speed of the point source. The sound source has a f = 5000 Hz and SPL = 30 dB. The distance between the source and the array is 3 m.

6.2.3. Effect of the time snapshot

With respect to the selected time snapshot, in the simulations the point source emits tonal sound with f = 5000 Hz and SPL = 30 dB and rotates at 6.67 Hz. The distance between the source and the array is 3 m and the sampling frequency is 50 kHz.

The selected time snapshot does not play a role in the quantification of the SPL. An increasing time gives slightly better results. Figure 6.6 depicts the trend of the simulations. The ROSI outputs for the SPL are compared with the input in Table 6.2.

Similarly to the case of a variable rotational speed, the location of the simulated source is always determined by ROSI at the time of the sound emission and it corresponds to (x,y,z) = (0,0.5,3).

The change in the time snapshot only affects the computational time of the simulation, because with a longer time the model is performed for a larger number of time samples.

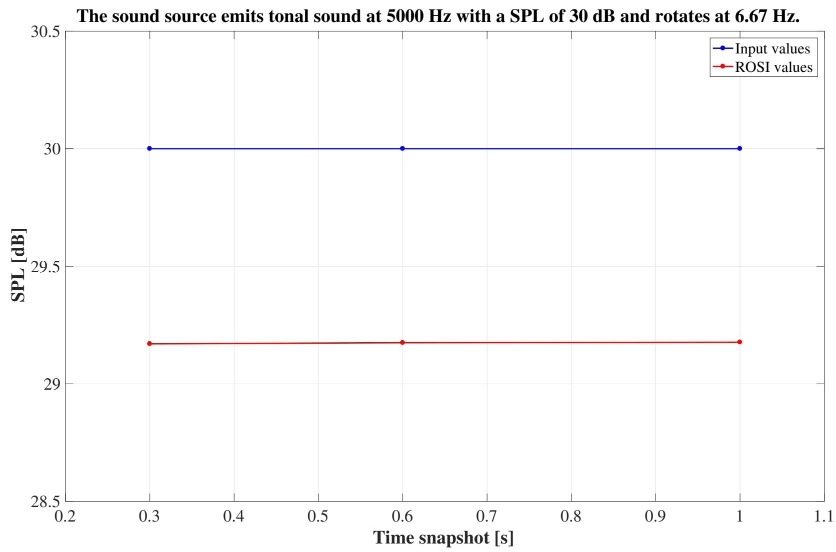

Figure 6.6: Effect of the time snapshot on the estimation of the SPL. The sound source emits tonal sound at 5000 Hz with a SPL of 30 dB and rotates at 6.67 Hz. The distance between the point source and the microphone array is 3 m.

Input [dB]	ROSI outputs [dB]		
	T_s = 0.3 s	T_s = 0.6 s	T_s = 1 s
30	29.17	29.17	29.18

Table 6.2: Comparison of the inputs with the outputs of the ROSI algorithm obtained varying the time snapshot. The sound source has a f = 5000 Hz and SPL = 30 dB. The rotational speed corresponds to 6.67 Hz and the distance between the source and the array is 3 m.

6.2.4. Effect of the distance from the microphone array

Interesting to analyse is how the estimation of the SPL depends on the distance between the rotating point source and the microphone array. Several simulations have been performed with an increasing distance, going from 0.5 m to 15 m. Figure 6.7, Table 6.3 and Table 6.4 present the results for a point source with f = 5000 Hz and SPL of 30 dB. The time snapshot is 1 s and the sampling frequency is 50 kHz. The rotational speed corresponds to 6.67 Hz. As it can be noticed, the difference between the input and the ROSI output is minimum when the sound source is 15 meter far from the array.

The location of the rotating point source does not depend on the distance from the array. The initial position (i.e. (x,y,z) = (0,0.5,3)) is correctly obtained using the ROSI algorithm.

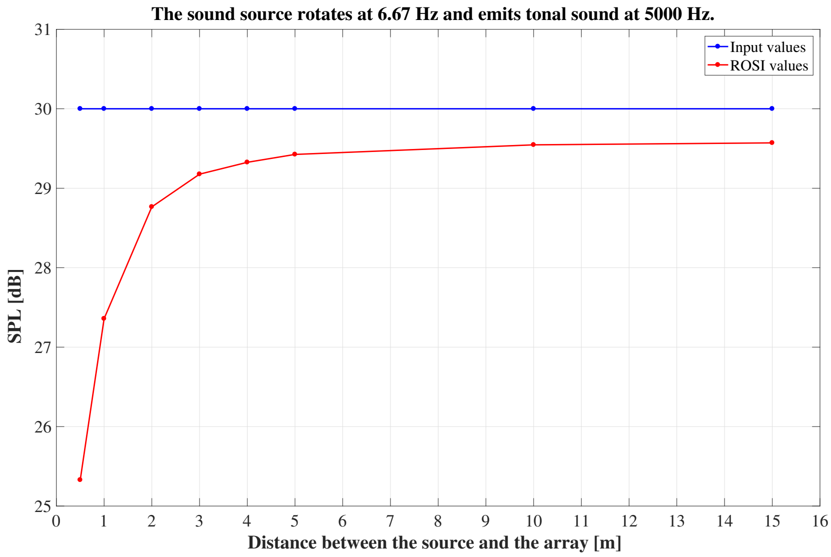

Figure 6.7: Effect of the distance between the source and the microphone array on the estimation of the SPL. The sound source emits tonal sound at 5000 Hz with a SPL of 30 dB and rotates at 6.67 Hz. The time snapshot is equal to 1 s.

Input [dB]	ROSI outputs [dB]			
	z = 0.5 m	z = 1 m	z = 2 m	z = 3 m
30	25.33	27.36	28.77	29.18

Table 6.3: Comparison of the input with outputs of the ROSI algorithm obtained varying the distance between the point source and the microphone array (i.e. 0.5 m, 1 m, 2 m and 3 m). The source has a f = 5000 Hz and SPL = 30 dB. The rotational speed is 6.67 Hz and the time snapshot is 1 s.

Input [dB]	ROSI outputs [dB]			
	z = 4 m	z = 5 m	z = 10 m	z = 15 m
30	29.33	29.43	29.55	29.57

Table 6.4: Comparison of the input with outputs of the ROSI algorithm obtained varying the distance between the point source and the microphone array (i.e. 4 m, 5 m, 10 m and 15 m). The source has a f = 5000 Hz and SPL = 30 dB. The rotational speed is 6.67 Hz and the time snapshot is 1 s.

6.2.5. Effect of the sampling frequency

Fundamental in signal analysis is the choice of the sampling frequency, f_s. As already explained in Chapter 2.4.5, if the signal is under sampled aliasing occurs. Following the Nyquist criterion for a point source with f = 1500 Hz and SPL = 30 dB, two different sampling frequencies have been tested: 5 kHz and 50 kHz. In these simulations, three rotational speeds are considered: 4 Hz, 6.67 Hz, 10 Hz. The distance between the source and the array is 0.5 m and the time snapshot is 1 s. Comparing the results in Figure 6.8 and Table 6.5, a lower sampling frequency leads to a higher difference between the input and the ROSI output, Δ, for the entire range of rotational speeds. An explanation of this trend can be found in Figure 6.9, where the acoustic pressure emitted by the point source is depicted for the two sampling frequencies. The difference in the representation of the signal is clearly visible, proving that the choice of f_s = 50 kHz leads to the best sampling of the signal. In conclusion, ROSI is able to accurately estimate the SPL of the source, only if the correct sample frequency is selected.

Also in this case, the rotational speed does not affect the quantification of the SPL.

As regards the position of the sound source, the ROSI algorithm always retrieves the initial location (i.e. (x,y,z)=(0,0.5,0.5)).

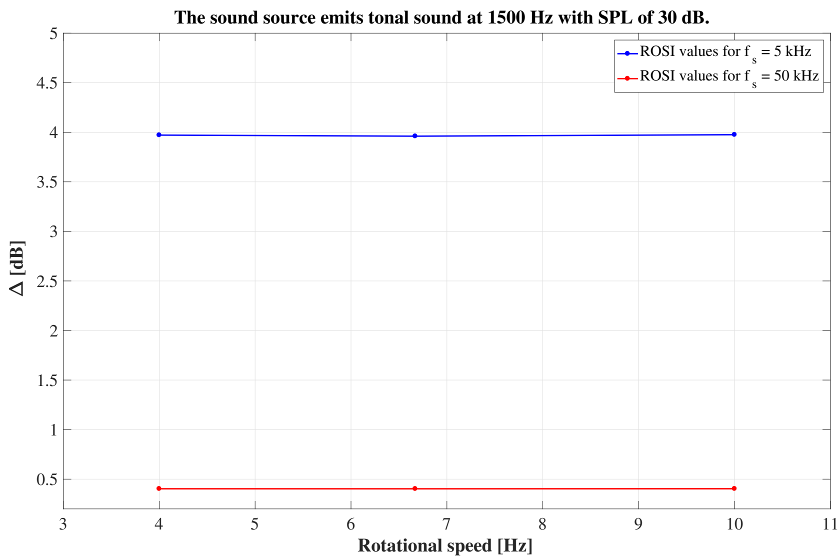

Figure 6.8: Effect of the sampling frequency on the estimation of the SPL. The differences between the input and the ROSI output are plotted as Δ [dB]. The sound source emits tonal sound at 1500 Hz with a SPL of 30 dB. The time snapshot is 1 s and the distance between the source and the array is 0.5 m.

Input [dB]	ROSI outputs [dB] using f_s = 5 kHz			ROSI outputs [dB] using a f_s = 50 kHz		
	RPS = 4 Hz	RPS = 6.67 Hz	RPS = 10 Hz	RPS = 4 Hz	RPS = 6.67 Hz	RPS = 10 Hz
30	26.0285	26.0393	26.0245	29.5971	29.5974	29.5967

Table 6.5: Comparison of the input with outputs of the ROSI algorithm, varying the sampling frequency and the rotational speed. The source emits tonal sound at 1500 Hz with SPL of 30 dB. The time snapshot is 1 s and the distance between the source and the array is 0.5 m.

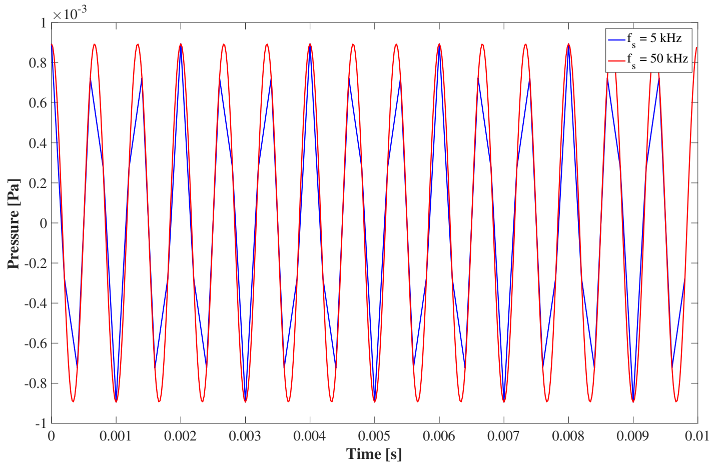

Figure 6.9: Representation of the single frequency cosine wave applying two different sampling frequencies: 5 kHz (red line) and 50 kHz (blue line).

6.2.6. Effect of additional noise

In order to evaluate the influence of imperfect measurements, noise is added to the simulations of a point source with f = 5000 Hz and rotational speed of 6.67 Hz. Six different SNR are considered: 10 db, 5 dB, -2.5 dB, -10 dB, -15 dB and -20 dB. From Figure 6.10, it can be observed the difference between the original tonal sound at 5000 Hz and the signal resulting from the addition of white noise. The comparison is provided for all the employed SNR. As the SNR is decreasing, the signal with added noise (red line) follows a complete different trend with respect to the original one (blue line).

Adopting the same SNR values, a comparison is performed between a single rotating source with SPL = 30 dB and with SPL = 60 dB. Table 6.6 summarizes the outcomes. The differences between the input and the ROSI output are plotted as Δ in Figure 6.11. The two logarithmic trends almost coincide for every SNR, proving that also in this case the difference in the beamformed results agrees with the difference in the source level. This is the reason why only the ROSI plots for a source with SPL = 30 dB are shown in Figure 6.12. Looking at these acoustic images, even if the noise becomes more dominant with a negative SNR, the sound source remains visible. However, a decreasing SNR leads to an overestimation in the SPL.

For all the six data sets, the position of the sound source is correctly determined and it corresponds to the initial one (i.e. (x,y,z) = (0,0.5,3)).

SNR [dB]	Inputs [dB]	ROSI outputs [dB]	Inputs [dB]	ROSI outputs [dB]
10	30	29.3240	60	59.4092
5	30	29.8681	60	59.8575
-2.5	30	31.7956	60	61.9322
-10	30	36.8546	60	66.7755
-15	30	41.419	60	71.0654
-20	30	46.0396	60	76.1846

Table 6.6: Input values vs ROSI values for different SNR. The sound source emits tonal sound at 5000 Hz. Two SPL are considered: 30 dB and 60 dB. The rotational speed is 6.67 Hz and the time snapshot is 1 s. The distance between the source and the array is 3 m.

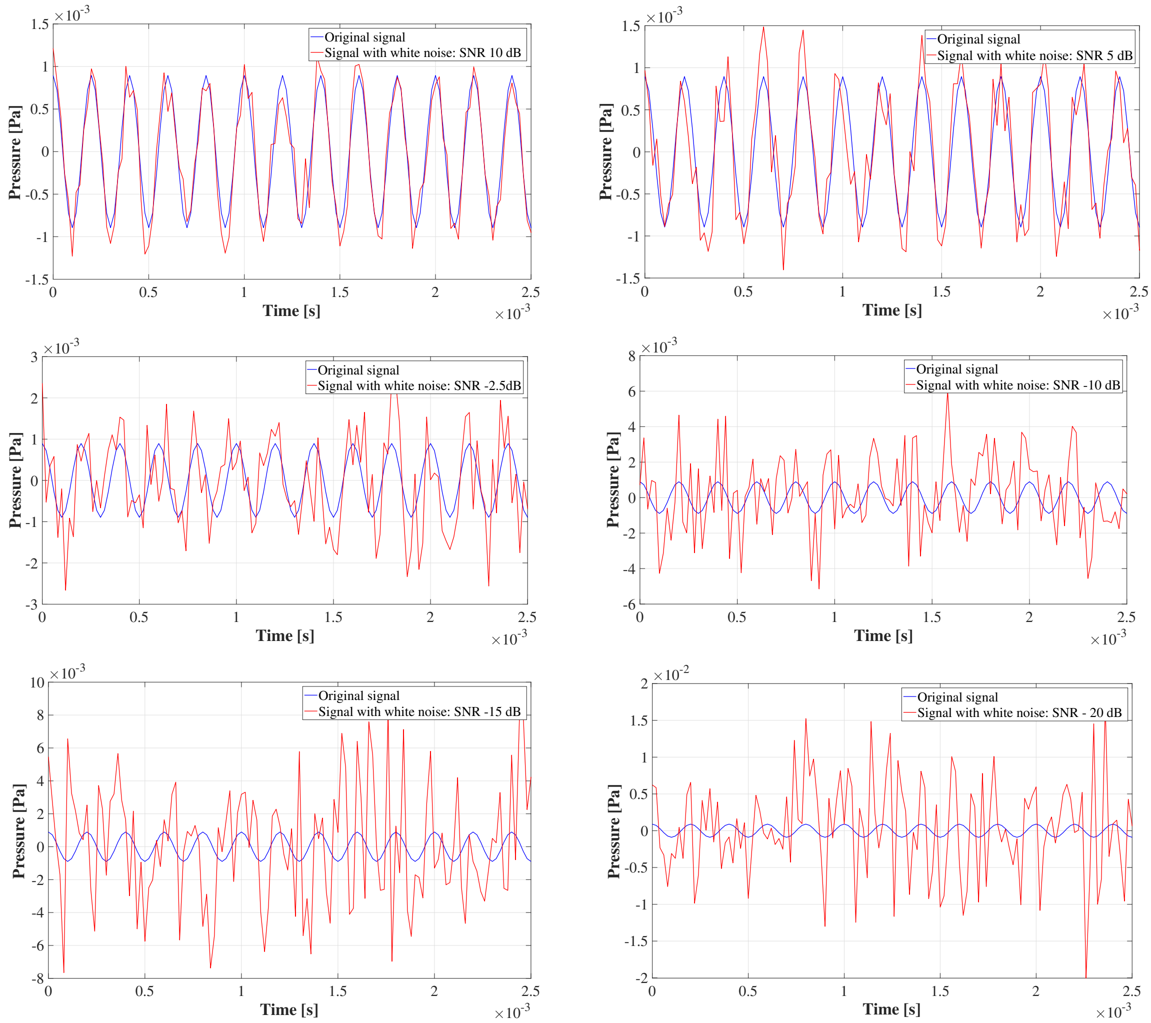

Figure 6.10: Comparison between the tonal sound at f = 5000 Hz (blue) and the signal resulting from the addition of white noise (red). Noise is applied with six decreasing SNR: 10 dB, 5 dB, -2.5 dB, -10 dB, -15 dB, -20 dB. The point source rotates at 6.67 Hz. In this representation, the SPL is 30 dB.

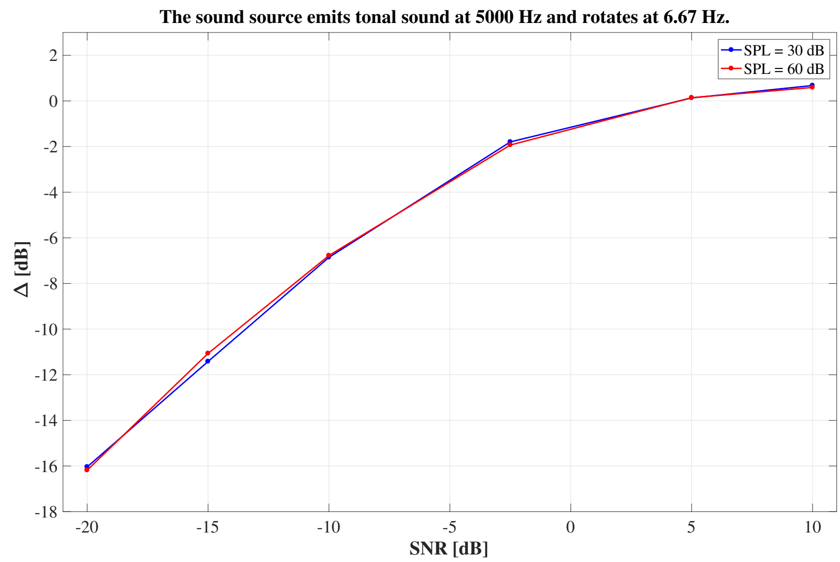

Figure 6.11: Effect of the SNR on the estimation of the SPL. The differences between the input and the ROSI output are plotted as Δ [dB]. The sound source emits tonal sound at 5000 Hz and rotates at 6.67 Hz. Two SPLs are used as inputs: 30 dB (blue) and 60 db (red). The time snapshot is 1 s and the distance between the source and the array is 3 m.

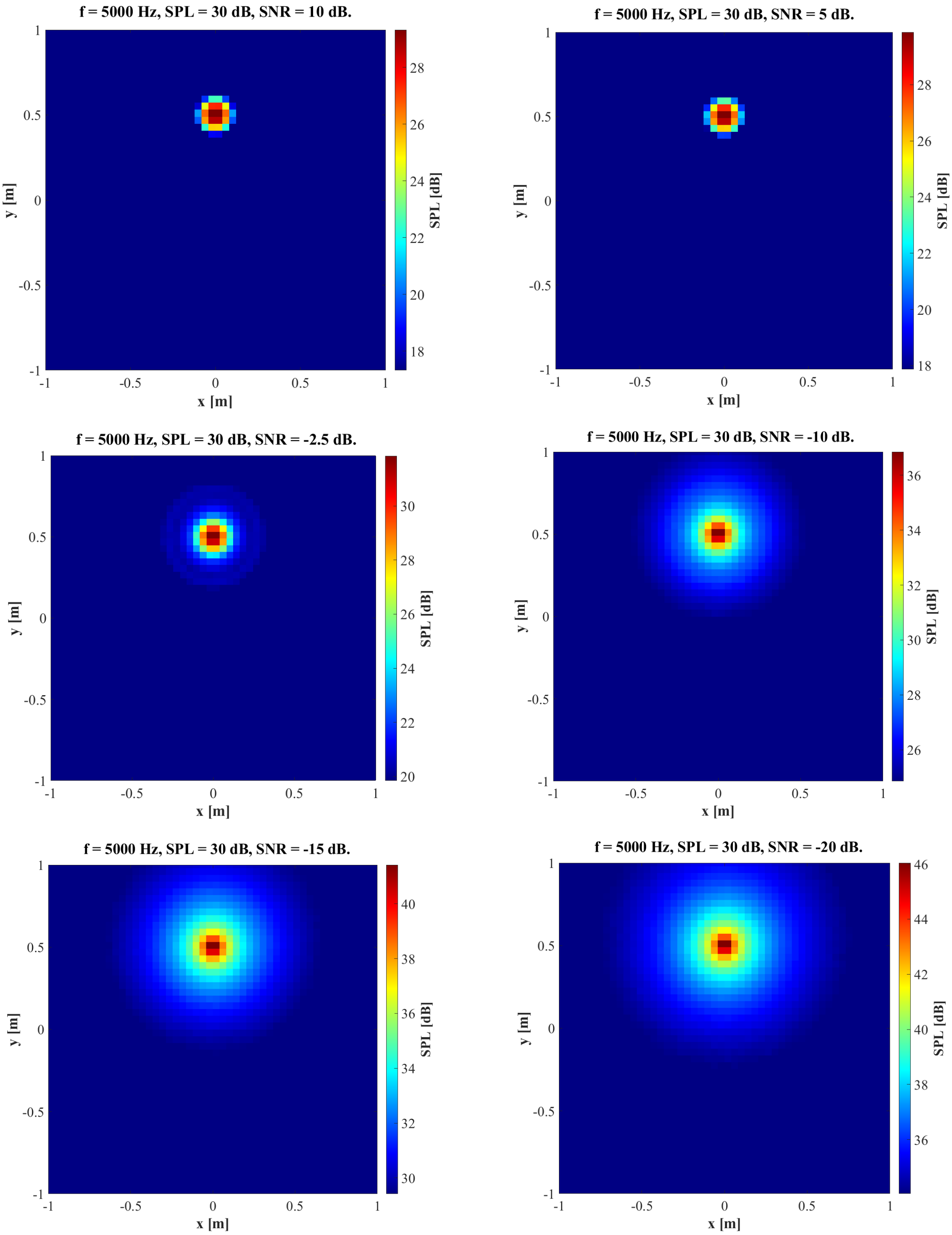

Figure 6.12: Comparison of the ROSI outcomes for a sound source rotating at 6.67 Hz and emitting tonal sound at 5000 Hz with SPL of 30 dB. Noise is applied with six decreasing SNR: 10 dB, 5 dB, -2.5 dB, -10 dB, -15 dB, -20 dB. A scan grid of 2 x 2 m^2 with a total of 25000 scan points is employed.

6.3. Multiple rotating sound sources

The degree of uncertainty increases when multiple sound sources are assessed. The main aim of these simulations is to see if the sound level of each source is correctly retrieved by ROSI.

Four rotating sound sources are investigated with four distinct spatial configurations, denoted as A B, C and D, and at three different distances from the microphone array, z, (i.e. 0.5 m, 1 m and 3 m).

When the sources emit tonal sound several frequencies, f, are simulated: 1500 Hz, 3000 Hz and 5000 Hz.

In Table 6.7, the Rayleigh limits for every combination of the frequency of the tone and distance from the microphone array are presented. The values are computed applying Equation 4.17. If the spacing between the sound sources is below the Rayleigh limit, the algorithm is not able to distinguish the sources as separated. For each configuration, this comparison will be underlined.

Frequency [Hz]	1500			3000			5000		
Distance [m]	0.5	1	3	0.5	1	3	0.5	1	3
Rayleigh limit [m]	0.07	0.19	0.41	0.03	0.07	0.22	0.02	0.04	0.12

Table 6.7: Rayleigh limits obtained from the combination of different frequencies and distances from the array. The values are computed applying Equation 4.17.

If the sources broadcast white noise, the signal is filtered into the following frequency bands: 500 Hz - 2000 Hz and 3500 Hz - 5000 Hz. The first frequency range is chosen because it corresponds to the expected noise range for a small wind turbine. The second band is employed to evaluate the response of the algorithm at high frequencies.

In all the simulations, two different SPL inputs are used: 30 dB and 60 dB. The scope of testing two SPLs for each configuration is to check if the differences in the beamformed results agree with the differences in the sound level. If this is true, ROSI can be used to compare different types of blade or turbine geometry.

In the analysis, an array with 64 microphones (see Figure 5.1), a scan grid of 2 x 2 m^2 with a total of 25000 scan points, a sampling frequency of 50 kHz, a time snapshot of 0.3 s and a rotational speed of 6.67 Hz are employed.

6.3.1. Configuration A

Configuration A is the first configuration tested. Its representation is provided in Figure 6.13. The coordinates of each rotating point source are:

- Source 1 (x,y) = (0,0.5);
- Source 2 (x,y) = (0,0.1);
- Source 3 (x,y) = (0,-0.1);
- Source 4 (x,y) = (0,-0.5);

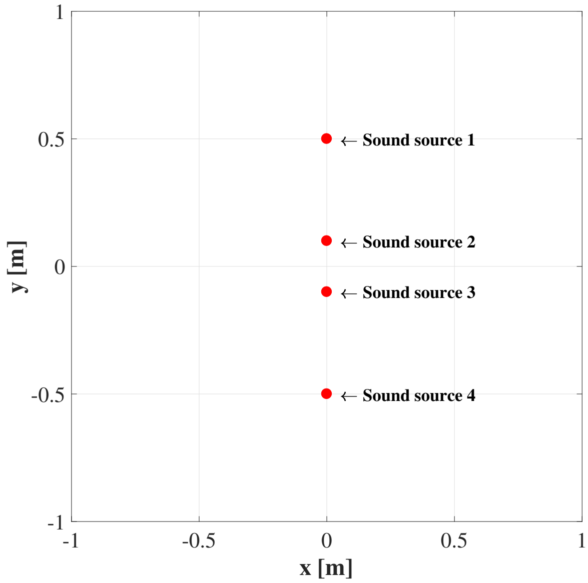

Figure 6.13: Configuration A for four rotating point sources. Coordinates: sound source 1 (x,y) = (0,0.5), sound source 2 (x,y) = (0,0.1), sound source 3 (x,y) = (0,-0.1), sound source 4 (x,y) = (0,-0.5).

The distance between source 1 and source 2 is equal to the distance between source 3 and source 4 and it corresponds to 0.4 m, while the distance between source 2 and source 3 is 0.2 m.

Tonal sound

First, the four rotating sources broadcasting tonal sound are analyzed. In the following cases, the Rayleigh limits are above the spacing between the sources:

- f = 1500 Hz and z = 1 m. The Rayleigh limit is 0.19 m. ROSI does not distinguish source 2 and source 3 as separated sources, while source 1 and source 4 are still visible.
- f = 1500 Hz and z = 3 m. The Rayleigh limit is 0.41 m. The four rotating sources are not visible. The resulting acoustic image is one single lobe.
- f = 3000 Hz and z = 3 m. The Rayleigh limit is 0.21 m. Source 2 and source 3 are not distinguished.

All these considerations are supported by the ROSI plots in Figure 6.14, where only the outcomes for the source with SPL = 30 dB are shown. This is because the differences in the beamformed results agree with the differences in the two SPLs (i.e. 30 dB and 60 dB). As it can be seen, the algorithm yields the initial locations of the sound sources only if they are recognized as separated sources.

Regarding the SPL, its estimation depends on the sound frequency and on the distance from the array adopted. In the evaluation, if the sound sources are not properly identified, their SPLs are not taken into account. For both the SPL inputs, the ROSI outputs are presented in Table 6.8, Table 6.9 and Table 6.10.

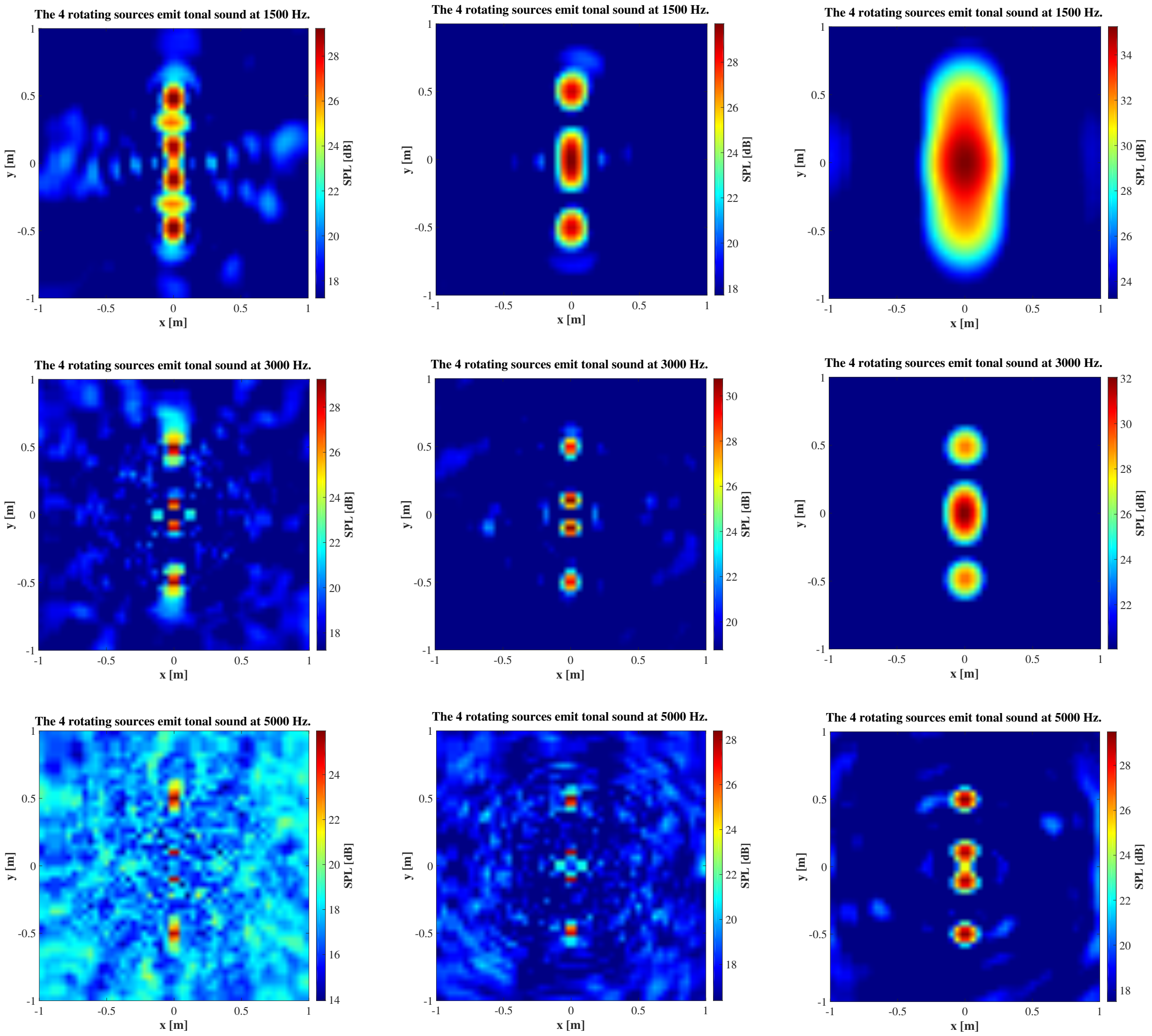

Figure 6.14: Configuration A - Comparison of the ROSI outcomes for four sound sources rotating at 6.67 Hz and emitting tonal sound at: 1500 Hz, 3000 Hz and 5000 Hz. The SPL input is 30 dB for each source. The distance between the source and the array is 0.5 m (left-side), 1 m (center) and 3 m (right-side). A scan grid of 2 x 2 m^2 with a total of 25000 scan points is used.

Inputs [dB]	ROSI outputs [dB] for f = 1500 Hz				ROSI outputs [dB] for f = 3000 Hz				ROSI outputs [dB] for f = 5000 Hz			
	Source 1	Source 2	Source 3	Source 4	Source 1	Source 2	Source 3	Source 4	Source 1	Source 2	Source 3	Source 4
30	29.23	28.77	28.98	29.22	29.23	28.54	28.26	28.84	25.95	25.32	25.38	25.39
60	59.23	58.77	58.98	59.22	59.23	58.54	58.26	58.84	55.95	55.32	55.38	55.37

Table 6.8: Configuration A - Comparison between the input and the ROSI outputs for four rotating sources with different frequencies (i.e. 1500 Hz, 3000 Hz and 5000 Hz) and different SPL (i.e. 30 dB and 60 dB). The distance between the source and the array is 0.5 m.

Inputs [dB]	ROSI outputs [dB] for f = 1500 Hz				ROSI outputs [dB] for f = 3000 Hz				ROSI outputs [dB] for f = 5000 Hz			
	Source 1	Source 2	Source 3	Source 4	Source 1	Source 2	Source 3	Source 4	Source 1	Source 2	Source 3	Source 4
30	28.84	/	/	28.81	29.24	30.75	30.76	29.33	28.39	27.86	27.84	27.48
60	58.84	/	/	58.81	59.24	60.75	60.76	59.33	58.39	57.86	57.84	67.48

Table 6.9: Configuration A - Comparison between the input and the ROSI outputs for four rotating sources with different frequencies (i.e. 1500 Hz, 3000 Hz and 5000 Hz) and different SPL (i.e. 30 dB and 60 dB). The distance between the source and the array is 1 m. For source 2 and source 3 with f = 1500 Hz, the spacing between the sources is below the Rayleigh limit, and the sound sources are not identified as separated sources. Their SPLs are not provided.

Inputs [dB]	ROSI outputs [dB] for f = 1500 Hz				ROSI outputs [dB] for f = 3000 Hz				ROSI outputs [dB] for f = 5000 Hz			
	Source 1	Source 2	Source 3	Source 4	Source 1	Source 2	Source 3	Source 4	Source 1	Source 2	Source 3	Source 4
30	/	/	/	/	29.06	/	/	29.18	29.49	28.93	29.04	29.35
60	/	/	/	/	59.06	/	/	59.18	59.49	58.93	59.04	59.35

Table 6.10: Configuration A - Comparison between the input and the ROSI outputs for four rotating sources with different frequencies (i.e. 1500 Hz, 3000 Hz and 5000 Hz) and different SPL (i.e. 30 dB and 60 dB). The distance between the source and the array is 3 m. For source 1, 2, 3 and 4 with f = 1500 Hz and for source 2 and 3 with f = 3000 Hz, the Rayleigh limit is above the spacing between the sources. The sound sources are not identified as separated sources and their SPLs are not provided.

Broadband sound

As described in Chapter 6.1, if the four rotating sources emit broadband sound, an IIR filter is applied to the signal. Thus, only the frequencies inside the selected band are considered. The ROSI uncertainty is investigated applying two frequency bands: 500 Hz - 2000 Hz and 3500 Hz - 5000 Hz. The two bandwidths are equal and correspond to 1500 Hz.

Also in this case, two SPL inputs are compared: 30 dB and 60 dB. For all the selected frequency bands and distances from the array, the ROSI outcomes are summarized in Table 6.11, Table 6.12 and Table 6.13. Since the differences in the source levels (i.e. 30 dB) agree with the differences in the beamformed results (i.e. 30 dB), only the ROSI plots for the four rotating sources with SPL = 30 dB are illustrated in Figure 6.15. Looking at these acoustic images, it can be noticed that, similarly to the previous simulations, when the distance from the array increases and the sound frequency decreases, the sources are not distinguished as separated. Specifically, the Rayleigh limit is above the spacing between the sound sources when:

- f ranges between 500 Hz and 2000 Hz and z = 1 m. Source 2 and source 3 are not recognized as separated;
- f ranges between 500 Hz and 2000 Hz and z = 3 m. All the four sound sources are not visible and the acoustic image results one single lobe.

If the algorithm does not retrieve the locations of the source, their SPLs are not taken into account. However, when ROSI recognizes the four sources like separated, their initial positions are correctly obtained.

With respect to the SPL, the selected frequency band and the distance from the array affect its estimation. For all the tested distances, z, and for all the frequency bands, the SPL is underestimated.

Inputs [db]	ROSI outputs [dB] Frequency band: 500 Hz - 2000 Hz				ROSI outputs [dB] Frequency band: 3500 Hz - 5000 Hz			
	Source 1	Source 2	Source 3	Source 4	Source 1	Source 2	Source 3	Source 4
30	20.06	19.90	20.11	19.74	18.08	17.90	16.26	18.18
60	50.06	49.90	50.11	49.74	48.08	47.90	46.26	48.18

Table 6.11: Configuration A - Comparison between the inputs (i.e. 30 dB and 60 dB) and the ROSI outputs for four rotating sources. The emitted white noise is filtered into different frequency bands (i.e. 500 Hz - 2000 Hz, 3500 Hz - 5000 Hz). The distance between the source and the array is 0.5 m.

Inputs [db]	ROSI outputs [dB] Frequency band: 500 Hz - 2000 Hz				ROSI outputs [dB] Frequency band: 3500 Hz - 5000 Hz			
	Source 1	Source 2	Source 3	Source 4	Source 1	Source 2	Source 3	Source 4
30	20.54	/	/	19.55	19.40	19.45	19.42	19.39
60	50.54	/	/	49.55	49.40	49.45	49.42	49.39

Table 6.12: Configuration A - Comparison between the inputs (i.e. 30 dB and 60 dB) and the ROSI outputs for four rotating sources. The emitted white noise is filtered into different frequency bands (i.e. 500 Hz - 2000 Hz, 3500 Hz - 5000 Hz). The distance between the source and the array is 1 m. If the sound sources are not recognized as separated sources, their SPLs are not provided.

Inputs [db]	ROSI outputs [dB] Frequency band: 500 Hz - 2000 Hz				ROSI outputs [dB] Frequency band: 3500 Hz - 5000 Hz			
	Source 1	Source 2	Source 3	Source 4	Source 1	Source 2	Source 3	Source 4
30	/	/	/	/	19.83	19.54	19.88	19.08
60	/	/	/	/	49.83	49.54	49.88	49.08

Table 6.13: Configuration A - Comparison between the inputs (i.e. 30 dB and 60 dB) and the ROSI outputs for four rotating sources. The emitted white noise is filtered into different frequency bands (i.e. 500 Hz - 2000 Hz, 3500 Hz - 5000 Hz). The distance between the source and the array is 3 m. If the sound sources are not recognized as separated sources, their SPLs are not provided.

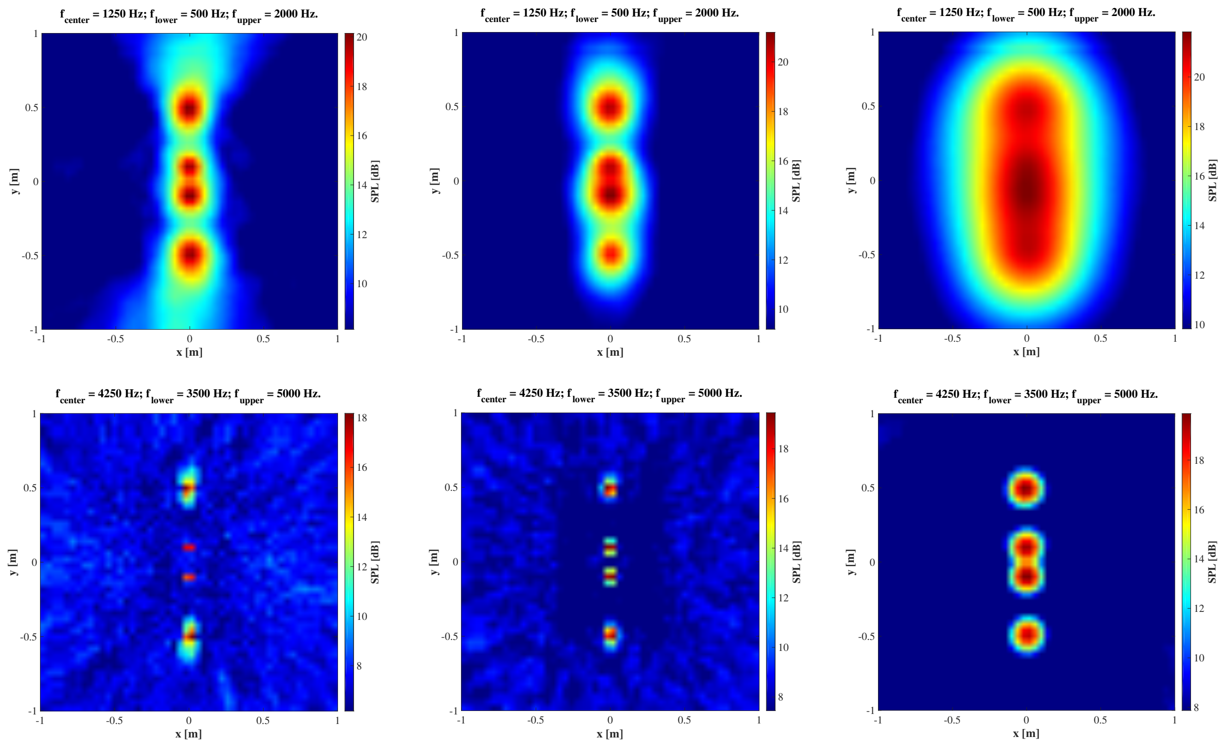

Figure 6.15: Configuration A - Comparison of the ROSI outcomes for four sound sources rotating at 6.67 Hz and emitting white noise. The signal is filtered in the following frequency bands: 500 Hz - 2000 Hz, 3500 Hz - 5000 Hz. The SPL input is 30 dB for each source. The distance between the source and the array is 0.5 m (left-side), 1 m (center) and 3 m (right-side). A scan grid of 2 x 2 m^2 with a total of 25000 scan points is employed.

6.3.2. Configuration B

The second configuration evaluated is configuration B, depicted in Figure 6.16. The coordinates of each rotating point source are:

- Source 1 (x,y) = (0,0.5);
- Source 2 (x,y) = (0,0.2);
- Source 3 (x,y) = (0,-0.2);
- Source 4 (x,y) = (0,-0.5);

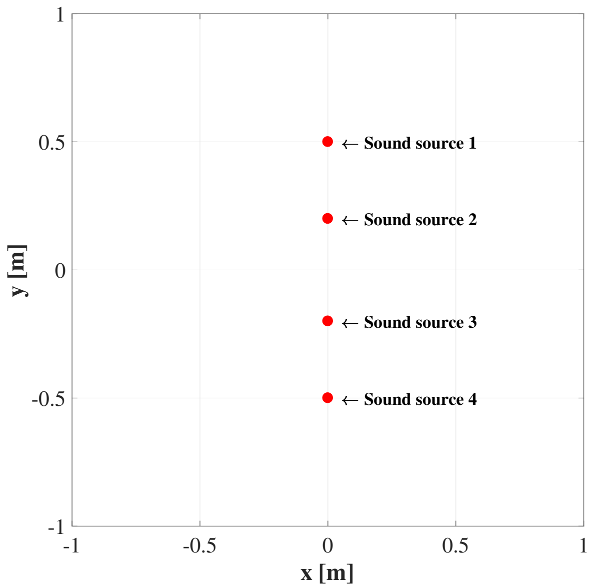

Figure 6.16: Configuration B for four rotating sound sources. Coordinates: source 1 (x,y) = (0,0.5), source 2 (x,y) = (0,0.2), source 3 (x,y) = (0,-0.2), source 4 (x,y) = (0,-0.5).

The distance between source 1 and source 2 is equal to the distance between source 3 and source 4 and it corresponds to 0.3 m, while the distance between source 2 and source 3 is 0.4 m.

Tonal sound

When the sound emitted is a tone, only for f = 1500 Hz and z = 3 m, the Rayleigh limit (i.e. 0.41 m) is above the spacing between the sources. Looking at the ROSI plots in Figure 6.17, it is clear that the algorithm correctly retrieve the initial positions of the point sources only if they are recognized as separated sources. For the same reason explained in section 6.3.1, only the outcomes of the sound source with SPL = 30 dB are shown in Figure 6.17.

The quantification of the SPL is influenced by the sound frequency and the distance from the array employed. All the ROSI outputs for the sources with SPL = 30 dB as well as for the sources with SPL = 60 dB are summarized in Table 6.14, Table 6.15 and Table 6.16. If ROSI does not properly identify the sources as separated, the SPL for that case has not been taken into account in the analysis.

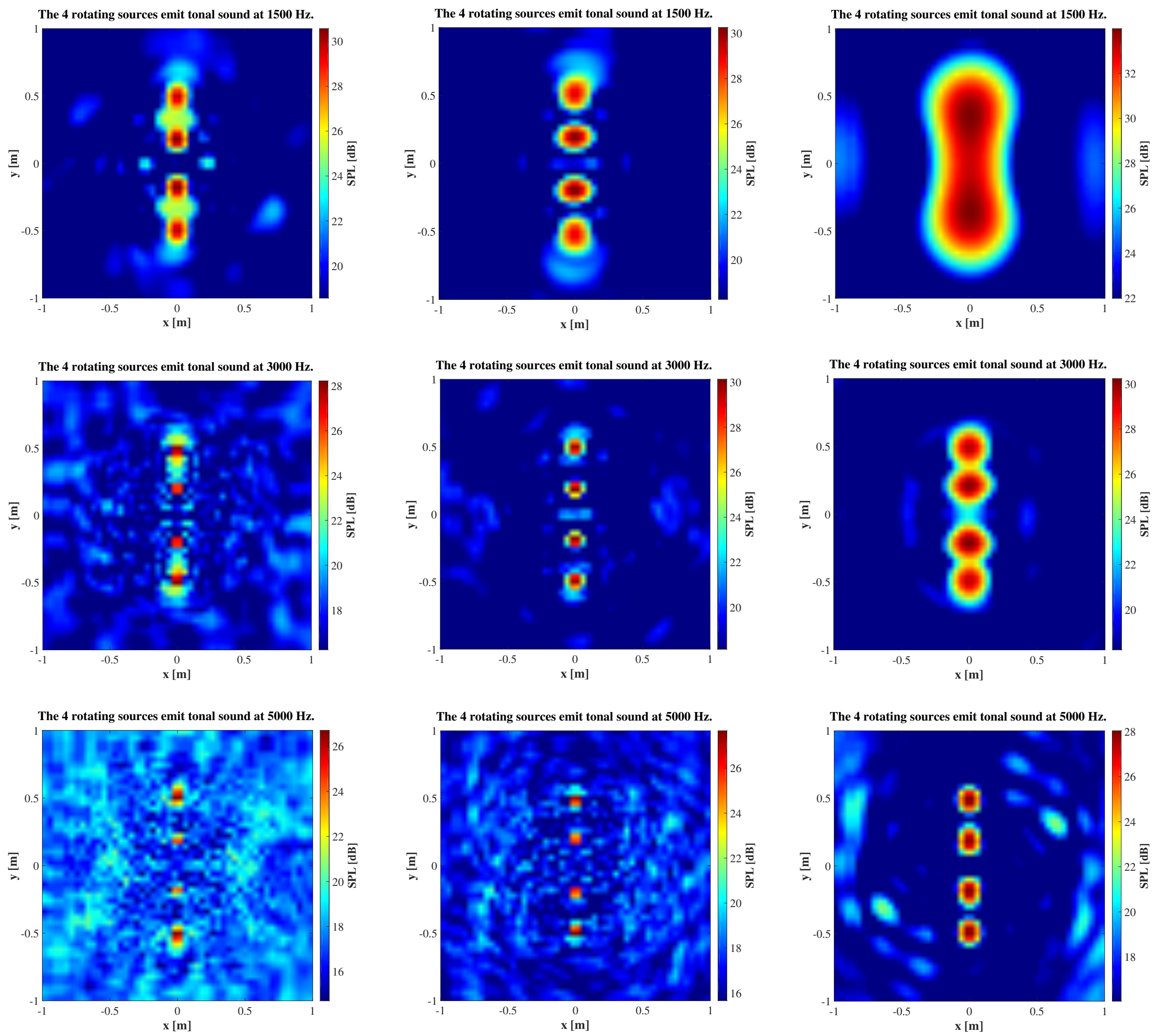

Figure 6.17: Configuration B - Comparison of the ROSI outcomes for four sound sources rotating at 6.67 Hz and emitting tonal sound at: 1500 Hz, 3000 Hz and 5000 Hz. The SPL input is 30 dB for each source. The distance between the source and the array is 0.5 m (left-side), 1 m (center) and 3 m (right-side). A scan grid of 2 x 2 m^2 with a total of 25000 scan points is employed.

Inputs [dB]	ROSI outputs [dB] for f = 1500 Hz				ROSI outputs [dB] for f = 3000 Hz				ROSI outputs [dB] for f = 5000 Hz			
	Source 1	Source 2	Source 3	Source 4	Source 1	Source 2	Source 3	Source 4	Source 1	Source 2	Source 3	Source 4
30	29.66	30.53	30.56	29.81	28.06	26.28	26.61	28.23	26.70	24.36	24.15	26.67
60	59.66	60.53	60.56	59.81	58.06	56.28	56.61	58.23	56.70	54.36	54.15	56.67

Table 6.14: Configuration B - Comparison between the inputs and the ROSI outputs for four rotating sources with different frequencies (i.e. 1500 Hz, 3000 Hz and 5000 Hz) and different SPL (i.e. 30 dB and 60 dB). The distance between the source and the array is 0.5 m.

Inputs [dB]	ROSI outputs [dB] for f = 1500 Hz				ROSI outputs [dB] for f = 3000 Hz				ROSI outputs [dB] for f = 5000 Hz			
	Source 1	Source 2	Source 3	Source 4	Source 1	Source 2	Source 3	Source 4	Source 1	Source 2	Source 3	Source 4
30	28.97	30.09	30.25	28.84	29.75	30.13	29.99	29.79	27.31	25.53	25.92	27.66
60	58.97	60.09	60.25	58.84	59.75	60.13	59.99	59.79	57.31	55.53	55.92	57.66

Table 6.15: Configuration B - Comparison between the inputs and the ROSI outputs for four rotating sources with different frequencies (i.e. 1500 Hz, 3000 Hz and 5000 Hz) and different SPL (i.e. 30 dB and 60 dB). The distance between the source and the array is 1 m.

Inputs [dB]	ROSI outputs [dB] for f = 1500 Hz				ROSI outputs [dB] for f = 3000 Hz				ROSI outputs [dB] for f = 5000 Hz			
	Source 1	Source 2	Source 3	Source 4	Source 1	Source 2	Source 3	Source 4	Source 1	Source 2	Source 3	Source 4
30	/	/	/	/	29.56	29.81	29.99	29.41	28.03	27.87	28.01	27.92
60	/	/	/	/	59.56	59.81	59.99	59.41	58.03	57.87	58.01	57.92

Table 6.16: Configuration B - Comparison between the inputs and the ROSI outputs for four rotating sources with different frequencies (i.e. 1500 Hz, 3000 Hz and 5000 Hz) and different SPL (i.e. 30 dB and 60 dB). The distance between the source and the array is 3 m. For source 1, 2, 3 and 4 with f = 1500 Hz, the spacing between the sources is below the Rayleigh limit and the sound sources are not identified as separated sources. Their SPLs are not provided.

Broadband sound

For the four rotating sources broadcasting white noise, all the ROSI outputs are summarized in Table 6.17, Table 6.18 and Table 6.19. As it can be observed, the difference in the source levels (i.e. 30 dB) always agree with the difference in the beamformed results (i.e. 30 dB). This is why only the ROSI plots for the sources with SPL = 30 dB are shown in Figure 6.18. As discussed for Configuration A, when a large distance from the array and a low frequency are adopted, the algorithm does not recognize the point sources as separated. In particular, only for the frequency 500 Hz - 2000 Hz and z = 3 m, the Rayleigh limit is above the spacing between the sources. The resulting SPLs are not taken into account in the analysis. With respect to the localization of the sources, ROSI is able to correctly retrieve their initial positions only if the sources are distinguished as separated.

Inputs [db]	ROSI outputs [dB] Frequency band: 500 Hz - 2000 Hz				ROSI outputs [dB] Frequency band: 3500 Hz - 5000 Hz			
	Source 1	Source 2	Source 3	Source 4	Source 1	Source 2	Source 3	Source 4
30	19.56	19.50	19.61	19.55	19.00	16.17	16.57	18.75
60	49.56	49.50	49.11	49.55	49.00	46.17	46.57	48.75

Table 6.17: Configuration B - Comparison between the inputs (i.e. 30 dB and 60 dB) and the ROSI outputs for four rotating sources. The emitted white noise is filtered into different frequency bands (i.e. 500 Hz - 2000 Hz, 3500 Hz - 5000 Hz). The distance between the source and the array is 0.5 m.

Inputs [db]	ROSI outputs [dB] Frequency band: 500 Hz - 2000 Hz				ROSI outputs [dB] Frequency band: 3500 Hz - 5000 Hz			
	Source 1	Source 2	Source 3	Source 4	Source 1	Source 2	Source 3	Source 4
30	21.12	21.09	19.77	20.58	18.34	18.14	17.27	19.61
60	51.12	51.09	49.77	50.58	48.34	48.14	47.27	49.61

Table 6.18: Configuration B - Comparison between the inputs (i.e. 30 dB and 60 dB) and the ROSI outputs for four rotating sources. The emitted white noise is filtered into different frequency bands (i.e. 500 Hz - 2000 Hz, 3500 Hz - 5000 Hz). The distance between the source and the array is 1 m.

Inputs [db]	ROSI outputs [dB] Frequency band: 500 Hz - 2000 Hz				ROSI outputs [dB] Frequency band: 3500 Hz - 5000 Hz			
	Source 1	Source 2	Source 3	Source 4	Source 1	Source 2	Source 3	Source 4
30	/	/	/	/	19.14	19.26	19.87	18.98
60	/	/	/	/	49.14	49.26	49.87	48.98

Table 6.19: Configuration B - Comparison between the inputs (i.e. 30 dB and 60 dB) and the ROSI outputs for four rotating sources. The emitted white noise is filtered into different frequency bands (i.e. 500 Hz - 2000 Hz, 3500 Hz - 5000 Hz). The distance between the source and the array is 3 m. If the sound sources are not recognized as separated sources, their SPLs are not provided.

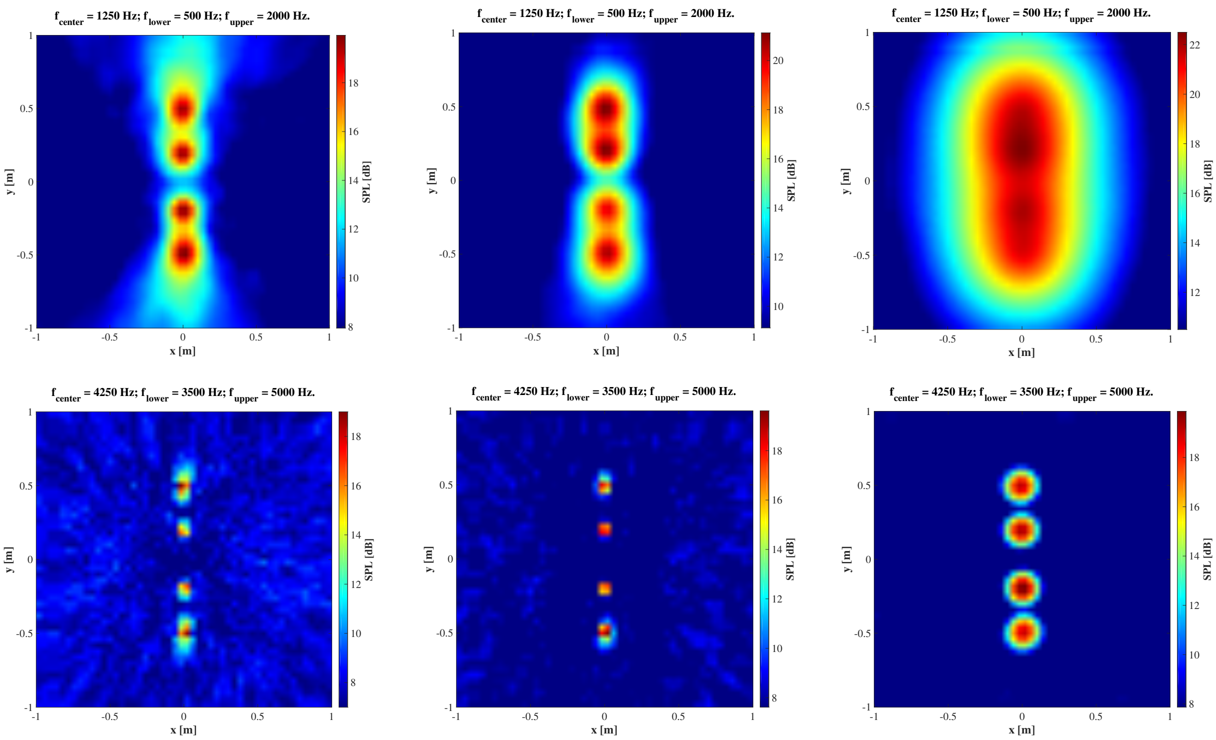

Figure 6.18: Configuration B - Comparison of the ROSI outcomes for four sound sources rotating at 6.67 Hz and emitting white noise. The signal is filtered in the following frequency bands: 500 Hz - 2000 Hz, 3500 Hz - 5000 Hz. The SPL input is 30 dB for each source. The distance between the source and the array is 0.5 m (left-side), 1 m (center) and 3 m (right-side). A scan grid of 2 x 2 m^2 with a total of 25000 scan points is employed.

6.3.3. Configuration C

The third configuration adopted for the four rotating sources is configuration C, presented in Figure 6.19. Here, the coordinates of each sound source are:

- Source 1 (x,y) = (0,0.5);
- Source 2 (x,y) = (0,0.3);
- Source 3 (x,y) = (0,-0.3);
- Source 4 (x,y) = (0,-0.5);

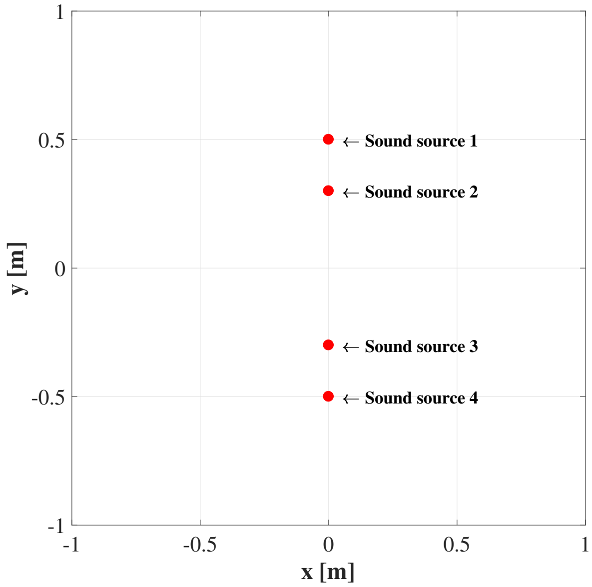

Figure 6.19: Configuration C for four rotating sound sources. Coordinates: source 1 (x,y) = (0,0.5), source 2 (x,y) = (0,0.3), source 3 (x,y) = (0,-0.3), source 4 (x,y) = (0,-0.5).

The distance between source 1 and source 2 equals the distance between source 3 and source 4 and it corresponds to 0.2 m, while the distance between source 2 and source 3 is 0.6 m.

Tonal sound

For the rotating sources emitting tonal sound, the Rayleigh limits are above the spacing between the point sources, in the following cases:

- f = 1500 Hz and z = 1 m. The Rayleigh limit is 0.19 m. ROSI does not distinguish source 1 and source 2 as separated sources and it is not possible to state if one source or two sources are present. The same occur for source 3 and source 4, located on the other side of the radius of rotation.
- f = 1500 Hz and z = 3 m. The Rayleigh limit is 0.41 m. Source 1 and source 2 as well as source 3 and source 4 can no longer be recognized from each other.
- f = 3000 Hz and z = 3 m. The Rayeleigh limit is 0.21 m. Source 1 and source 2 are not clearly visible. The same occurs for source 3 and source 4.

The ROSI plots in Figure 6.20 summarize all these considerations for the sound source with SPL = 30 dB. Looking at the ROSI outcomes in Table 6.20, Table 6.21 and Table 6.22, it can be observed that the difference in the source levels (i.e. 30 dB) always agree with the difference in the beamformed results (i.e. 30 dB). If ROSI does not properly distinguish the sources as separated, the SPL for that case has not been taken into account. Only if the point sources are identified as single sources, ROSI yields their starting location.

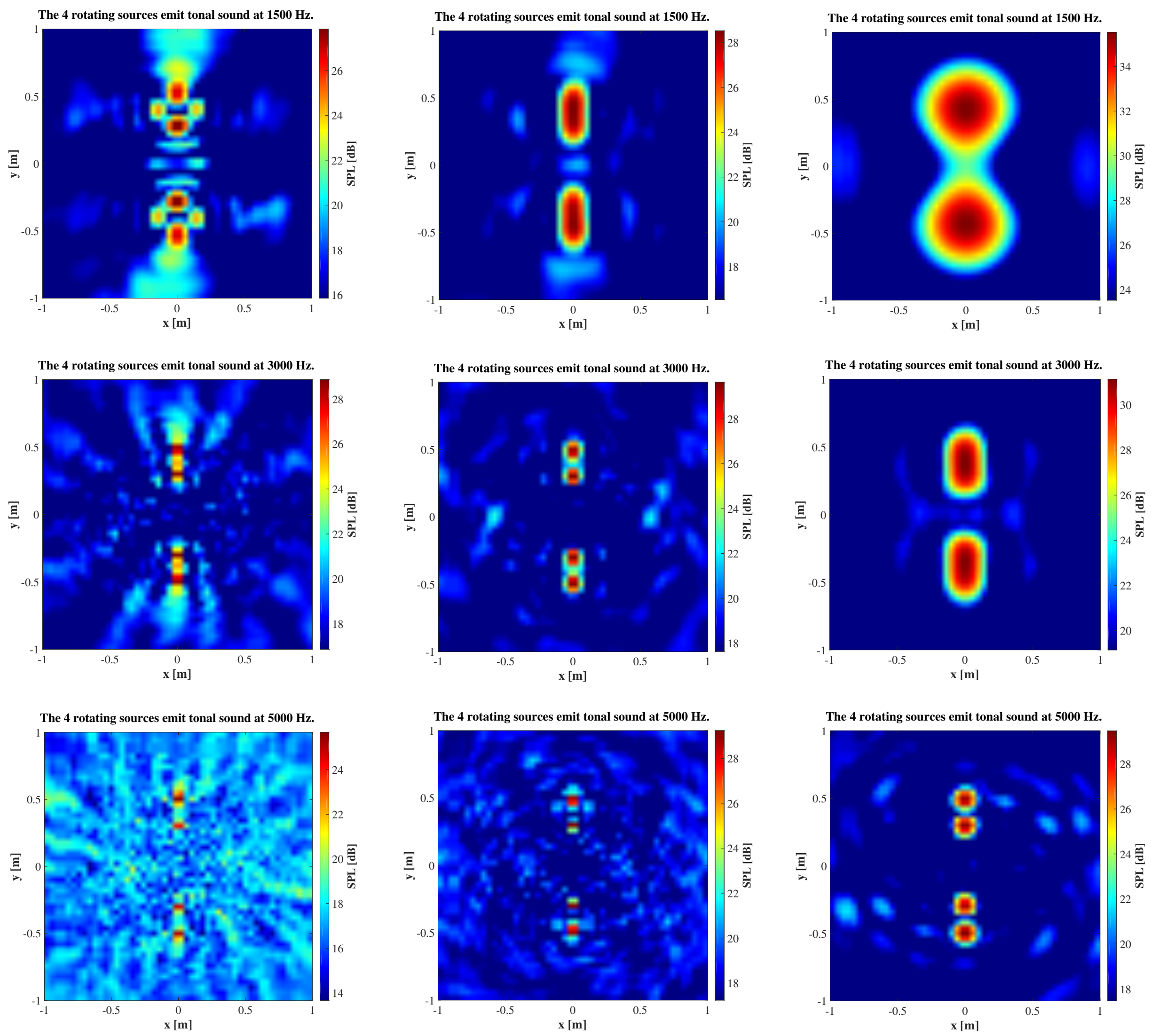

Figure 6.20: Configuration C - Comparison of the ROSI outcomes for four sound sources rotating at 6.67 Hz and emitting tonal sound at: 1500 Hz, 3000 Hz and 5000 Hz. The SPL is 30 dB for each source. The distance between the source and the array is 0.5 m (left-side), 1 m (center) and 3 m (right-side). A scan grid of 2 x 2 m^2 with a total of 25000 scan points is employed.

Inputs [dB]	ROSI outputs [dB] for f = 1500 Hz				ROSI outputs [dB] for f = 3000 Hz				ROSI outputs [dB] for f = 5000 Hz			
	Source 1	Source 2	Source 3	Source 4	Source 1	Source 2	Source 3	Source 4	Source 1	Source 2	Source 3	Source 4
30	26.54	27.85	27.84	26.41	28.52	28.73	28.87	28.57	25.67	24.16	24.74	25.08
60	56.54	57.85	57.84	56.41	58.52	58.73	58.87	58.57	55.67	54.16	54.74	55.08

Table 6.20: Configuration C - Comparison between the inputs and the ROSI outputs for four rotating sources with different frequencies (i.e. 1500 Hz, 3000 Hz and 5000 Hz) and different SPL (i.e. 30 dB and 60 dB). The distance between the source and the array is 0.5 m.

Inputs [dB]	ROSI outputs [dB] for f = 1500 Hz				ROSI outputs [dB] for f = 3000 Hz				ROSI outputs [dB] for f = 5000 Hz			
	Source 1	Source 2	Source 3	Source 4	Source 1	Source 2	Source 3	Source 4	Source 1	Source 2	Source 3	Source 4
30	/	/	/	/	29.28	29.63	29.56	29.49	27.85	28.09	27.98	27.93
60	/	/	/	/	59.28	59.63	59.56	59.49	57.85	58.09	57.98	57.93

Table 6.21: Configuration C - Comparison between the inputs and the ROSI outputs for four rotating sources with different frequencies (i.e. 1500 Hz, 3000 Hz and 5000 Hz) and different SPL (i.e. 30 dB and 60 dB). The distance between the source and the array is 1 m. The distance between the source and the array is 1 m. For source 1, 2, 3 and 4 with f = 1500 Hz, the spacing between the sources is below the Rayleigh limit and the sound sources are not identified as separated sources. Their SPLs are not provided.

Inputs [dB]	ROSI outputs [dB] for f = 1500 Hz				ROSI outputs [dB] for f = 3000 Hz				ROSI outputs [dB] for f = 5000 Hz			
	Source 1	Source 2	Source 3	Source 4	Source 1	Source 2	Source 3	Source 4	Source 1	Source 2	Source 3	Source 4
30	/	/	/	/	/	/	/	/	29.07	29.30	28.89	29.47
60	/	/	/	/	/	/	/	/	59.07	59.30	58.89	59.47

Table 6.22: Configuration C - Comparison between the inputs and the ROSI outputs for four rotating sources with different frequencies (i.e. 1500 Hz, 3000 Hz and 5000 Hz) and different SPL (i.e. 30 dB and 60 dB). The distance between the source and the array is 1 m. The distance between the source and the array is 1 m. For source 1, 2, 3 and 4 with f = 1500 Hz and for source 1,2,3 and 4 with f = 3000 Hz, the spacing between the sources is below the Rayleigh limit and the sound sources are not identified as separated sources. Their SPLs are not provided.

Broadband sound

In this section, ROSI is applied to the four rotating sources emitting broadband sound. The comparisons between the two SPL inputs (i.e. 30 dB and 60 dB) and the ROSI outputs are collected in Table 6.23 for z = 0.5 m, Table 6.24 for z = 1 m and Table 6.25 for z = 3 m. As it can be observed, the difference in the source level always agree with the difference in the beamformed results. This is the reason why, only the ROSI plots for the sources with SPL = 30 dB are presented in Figure 6.21. When the frequency band 500 Hz - 2000 Hz is employed for the filtering, the four sources are not clearly visible and two main lobes can be identified. If the algorithm does not recognize the rotating points as separated, their corresponding SPLs are not taken into account.

Inputs [db]	ROSI outputs [dB] Frequency band: 500 Hz - 2000 Hz				ROSI outputs [dB] Frequency band: 3500 Hz - 5000 Hz			
	Source 1	Source 2	Source 3	Source 4	Source 1	Source 2	Source 3	Source 4
30	/	/	/	/	18.67	18.00	18.29	17.83
60	/	/	/	/	48.67	48.00	48.29	47.83

Table 6.23: Configuration C - Comparison between the inputs (i.e. 30 dB and 60 dB) and the ROSI outputs for four rotating sources. The emitted white noise is filtered into different frequency bands (i.e. 500 Hz - 2000 Hz, 3500 Hz - 5000 Hz). The distance between the source and the array is 0.5 m.

Inputs [db]	ROSI outputs [dB] Frequency band: 500 Hz - 2000 Hz				ROSI outputs [dB] Frequency band: 3500 Hz - 5000 Hz			
	Source 1	Source 2	Source 3	Source 4	Source 1	Source 2	Source 3	Source 4
30	/	/	/	/	18.77	19.18	19.43	19.19
60	/	/	/	/	48.77	49.18	49.43	49.19

Table 6.24: Configuration C - Comparison between the inputs (i.e. 30 dB and 60 dB) and the ROSI outputs for four rotating sources. The emitted white noise is filtered into different frequency bands (i.e. 500 Hz - 2000 Hz, 3500 Hz - 5000 Hz). The distance between the source and the array is 1 m. If the sound sources are not recognized as separated sources, their SPLs are not provided.

Inputs [db]	ROSI outputs [dB] Frequency band: 500 Hz - 2000 Hz				ROSI outputs [dB] Frequency band: 3500 Hz - 5000 Hz			
	Source 1	Source 2	Source 3	Source 4	Source 1	Source 2	Source 3	Source 4
30	/	/	/	/	20.15	20.29	19.54	18.87
60	/	/	/	/	50.15	50.29	49.54	48.87

Table 6.25: Configuration C - Comparison between the inputs (i.e. 30 dB and 60 dB) and the ROSI outputs for four rotating sources. The emitted white noise is filtered into different frequency bands (i.e. 500 Hz - 2000 Hz, 3500 Hz - 5000 Hz). The distance between the source and the array is 3 m. If the sound sources are not recognized as separated sources, their SPLs are not provided.

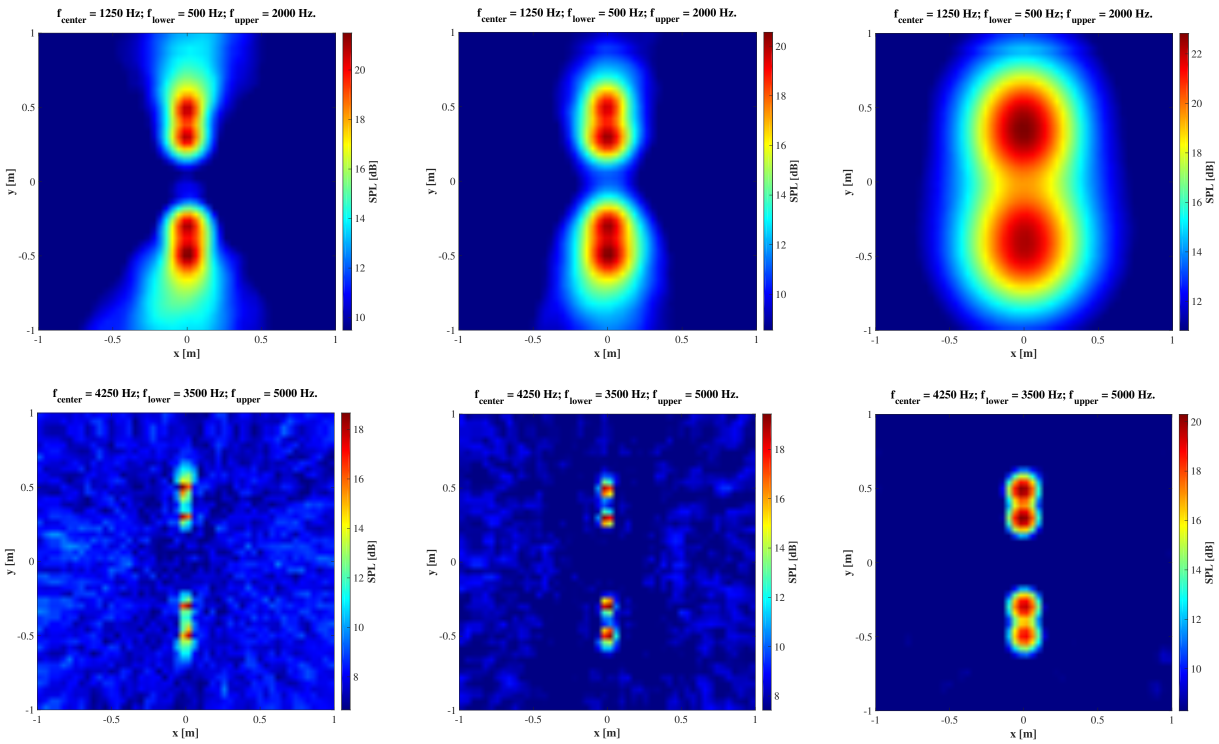

Figure 6.21: Configuration C - Comparison of the ROSI outcomes for four sound sources rotating at 6.67 Hz and emitting white noise. The signal is filtered in the following frequency bands: 500 Hz - 2000 Hz, 3500 Hz - 5000 Hz. The SPL input is 30 dB for each source. The distance between the source and the array is 0.5 m (left-side), 1 m (center) and 3 m (right-side). A scan grid of 2 x 2 m^2 with a total of 25000 scan points is employed.

6.3.4. Configuration D

The last configuration analyzed is configuration D. Its representation is provided in Figure 6.22. The coordinates of the four rotating sources are:

- Source 1 (x,y) = (0,0.5);
- Source 2 (x,y) = (0,0.4);
- Source 3 (x,y) = (0,-0.4);
- Source 4 (x,y) = (0,-0.5).

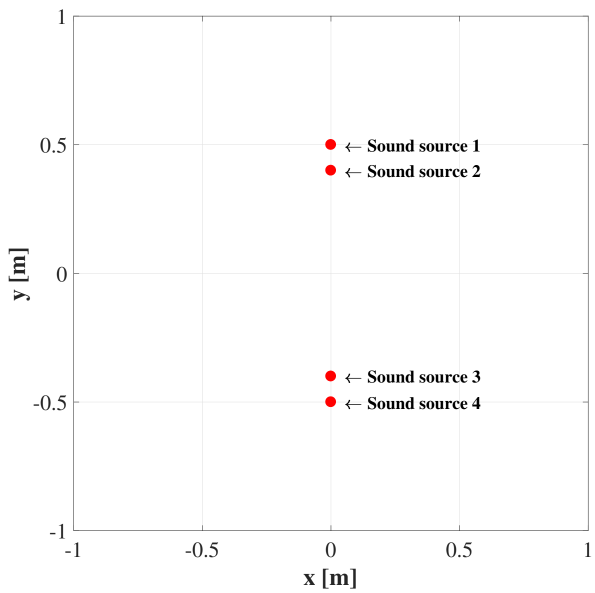

Figure 6.22: Configuration D for four rotating sound sources. Coordinates: source 1 (x,y) = (0,0.5), source 2 (x,y) = (0,0.4), source 3 (x,y) = (0,-0.4), source 4 (x,y) = (0,-0.5).

The distance between source 1 and source 2 is 0.1 m and it is equal to the distance between source 3 and source 4. The distance between source 2 and source 3 corresponds to 0.8 m.

Tonal sound

First, the four rotating sources broadcasting tonal sound are investigated. Except for f = 3000 Hz and z = 0.5 m, for all the other combinations of sound frequency and distance from the array, the resulting Rayleigh limit is above the spacing between the point sources. From the ROSI plots in Figure 6.23, it can be noticed that the algorithm always yields two separated lobes because the spacing between source 2 and source 3 is quite high compared to the entire range of Rayleigh limits. However, ROSI is not able to distinguish the four single rotating sources. As a consequence, for this configuration is not possible to evaluate how the SPL is affected by the different frequencies and by the different distances between the sources and the microphone array.

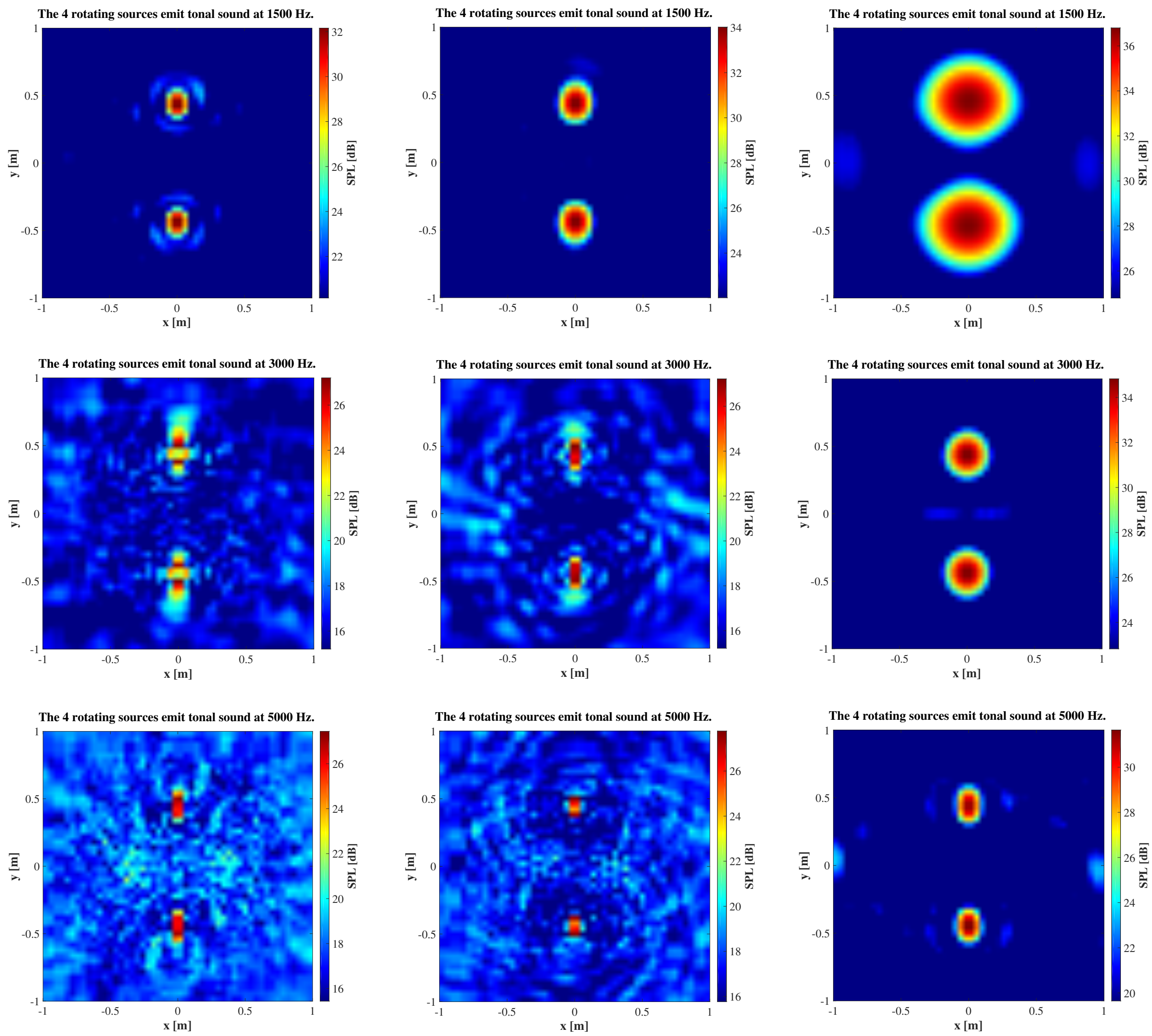

Figure 6.23: Configuration D - Comparison of the ROSI outcomes for a sound source rotating at 6.67 Hz and emitting tonal sound at: 1500 Hz, 3000 Hz and 5000 Hz. The SPL of the source is 30 dB. The distance between the source and the array is 0.5 m (left-side), 1 m (center) and 3 m (right-side).A scan grid of 2 x 2 m^2 with a total of 25000 scan points is employed.

Broadband sound

In this section, the four rotating sources emitting broadband sound are analyzed. Similarly to the tonal sound case, for all the combinations of frequency band and distance from the array, ROSI is not able to distinguish the sources as separated. From Figure 6.24, it can be clearly seen that the algorithm only yields two separated lobes. As a result, for this configuration is not possible to investigate the combined effect of the frequency band and distance from the array on the estimation of the SPL.

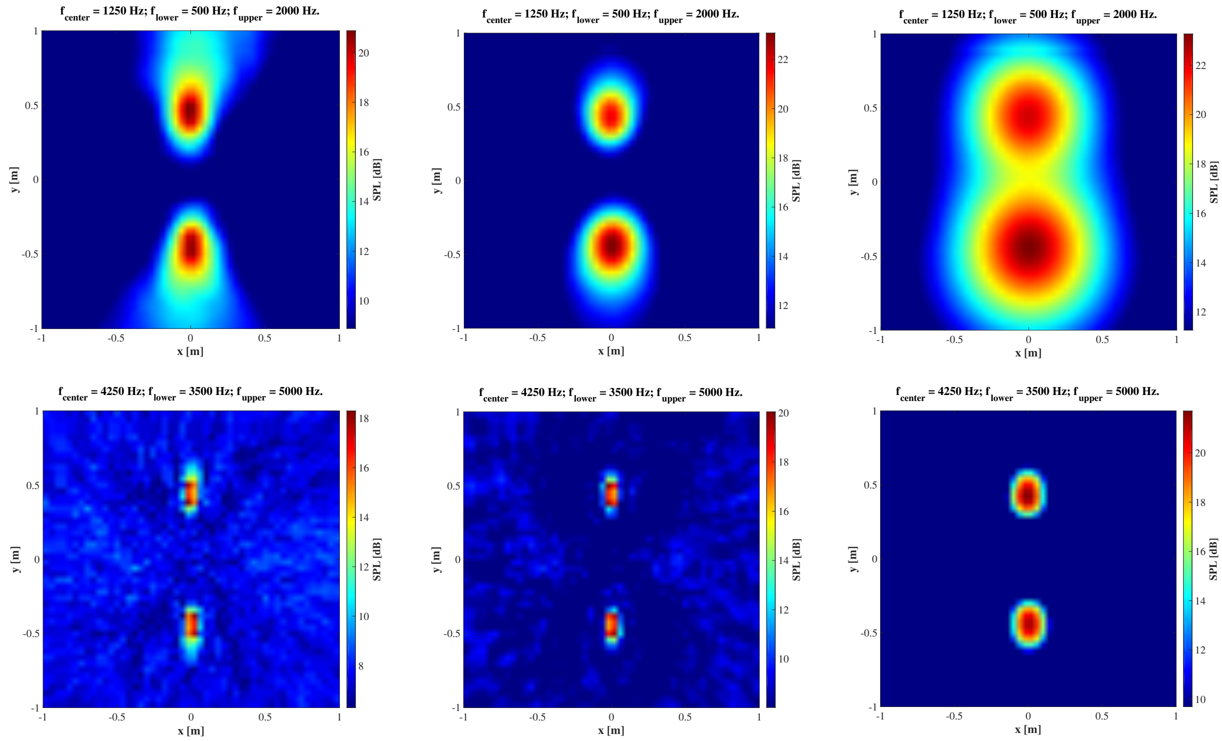

Figure 6.24: Configuration D - Comparison of the ROSI outcomes for four sound sources rotating at 6.67 Hz and emitting white noise. The signal is filtered in the following frequency bands: 500 Hz - 2000 Hz, 3500 Hz - 5000 Hz. The SPL input is 30 dB for each source. The distance between the source and the array is 0.5 m (left-side), 1 m (center) and 3 m (right-side). A scan grid of 2 x 2 m^2 with a total of 25000 scan points is employed.

6.4. Distributed sources

In order to reflect the ROSI application for small wind turbines, the simulations are extended to distributed sources. Employing a radius of rotation of 0.5 m, the following configurations are evaluated:

1. Two line sources consisting of 10 point sources each. The space between these distributed sources is 0.82 m.
2. Two line sources consisting of 20 point sources each. The space between these distributed sources is 0.62 m.

In both cases, the point sources are located at a distance of 0.01 m from each other. Their representation is provided in Figure 6.25.

For the investigation of the ROSI uncertainty, a rotational speed of 6.67 Hz, a time snapshot of 0.3 s, a sampling frequency of 50 kHz, a scan grid of 2 x 2 m^2 with a total of 25000 scan points and a distance from the array of 3 m are adopted.

The point sources broadcast two different sounds: tonal and broadband. In addition, to check if the differences in the beamformed results agree with the differences in the source, two different SPLs are used as inputs: 30 dB and 60 dB.

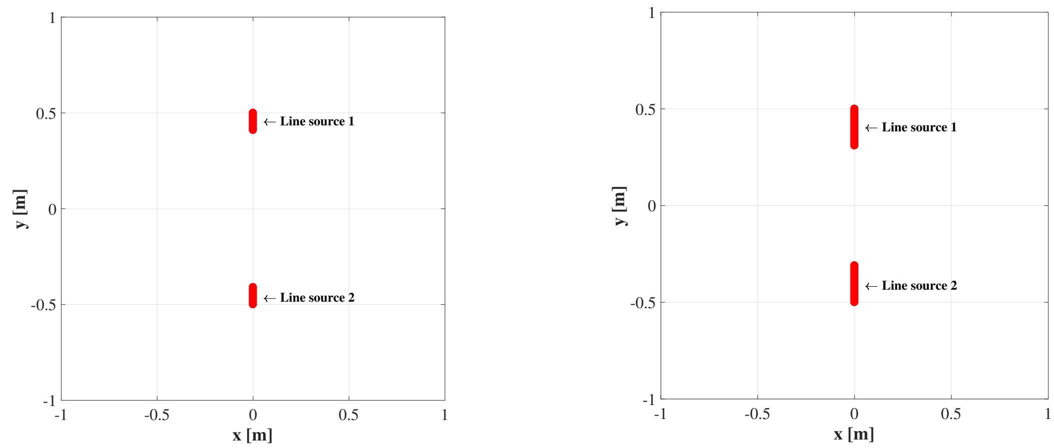

Figure 6.25: Configurations for simulated distributed sources. Left: two line sources with 10 point sources each. The distance between the point sources is 0.01 m. The spacing between the two line sources is 0.82 m. The distance from the array is 3 m. Right: two line sources with 20 point sources each. The distance between the point sources is 0.01 m. The spacing between the two line sources is 0.62 m. The distance from the array is 3 m.

6.4.1. Distributed sources emitting tonal sound

In the simulations, the point sources broadcast tonal sound at two different frequencies: 500 Hz and 5000 Hz. A comparison between the inputs (i.e. 30 dB and 60 dB) and the ROSI outputs is provided in Table 6.26. As it can be observed, the differences in the source levels (i.e. 30 dB) always agree with the differences in the beamformed results (i.e. 30 dB). This proves that the ROSI algorithm can be used to compare different blades or turbine geometries.

Figure 6.26 depicts the ROSI plots for the different distributed sources with SPL = 30 dB.

When f = 500 Hz, the Rayleigh limit (i.e. 1.26 m) is above the spacing between the two line sources for both geometries. As a consequence, ROSI is not able to distinguish the sources as separated and the acoustic images illustrate one single lobe (see the two plots in top row of Figure 6.26). In the analysis, the ROSI outputs are not taken into account.

If f = 5000 Hz, the Rayleigh limit (i.e. 0.12 m) is below the distance between the two line sources and the algorithm yields two separated lobes (see the two plots in the bottom row of Figure 6.26). The locations of the distributed sources are correctly obtained and correspond to the inital ones. However, the SPL values result overestimated.

Inputs [dB]	ROSI outputs [dB]			
	Line source 1 - 10 point sources	Line source 2 - 10 point sources	Line source 1 - 20 point sources	Line source 2 - 20 point sources
30	48.09	48.16	51.59	51.32
60	78.09	78.16	81.59	81.32

Table 6.26: Comparison between the inputs (i.e. 30 dB and 60 dB) and the ROSI outputs for the simulated distributed sources emitting tonal sound with f = 5000 Hz. Second and third columns: line sources with 10 point sources each. Fourth and fifth columns: line sources with 20 point sources each.

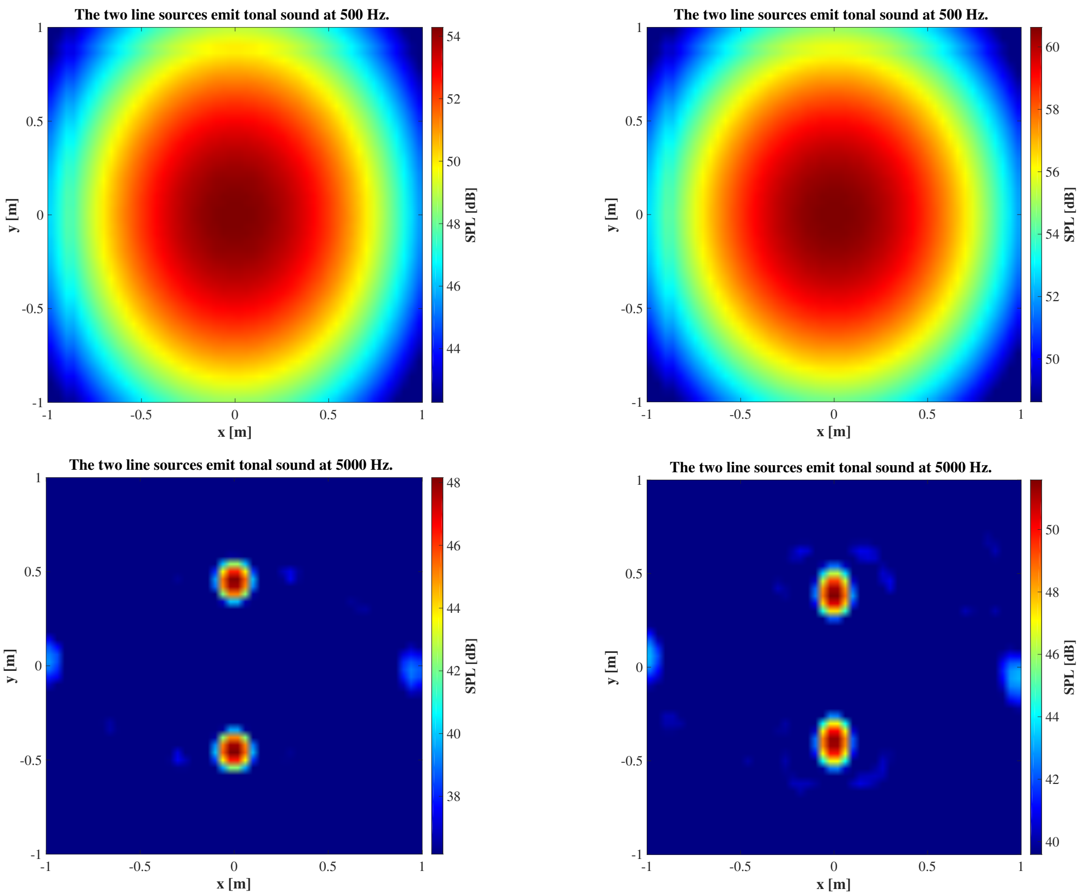

Figure 6.26: ROSI plots for two different distributed sources, emitting tonal sound at f = 500 Hz (first row) and at f = 5000 Hz (second row). The SPL input of each point source corresponds to 30 dB. Left: two line sources with 10 point sources each. Right: two line sources with 20 point sources each. A scan grid of 2 x 2 m^2 with a total of 25000 scan points is employed.

6.4.2. Distributed sources emitting broadband sound

When the distributed sources emit white noise, the signal is analyzed applying a IIR filter. To assess the effect of the frequency in the estimation of the SPL, the aforementioned geometries are tested with two different frequency bands:

- from 500 Hz to 2000 Hz, with a central frequency of 1250 Hz;
- from 3500 Hz to 5000 Hz, with a central frequency of 4250 Hz.

From the results of the simulations, the ROSI performance is in agreement with the Rayleigh limit. In fact, ROSI is able to retrieve the initial positions of the line sources only if the Rayleigh limit is below the spacing between the sources. As it can be observed from Figure 6.27, both the two line sources with 10 point sources each and the two line sources with 20 point sources each are recognized as separated sources when the signal is filtered in the frequency band 3500 Hz - 5000 Hz. Instead, for the range 500 Hz- 2000 Hz, the source localization is affected by the Rayleigh limit and it is not possible to correctly quantify the sound levels.

A comparison between the two SPL inputs (i.e. 30 dB and 60 dB) and the ROSI outputs is performed for the frequency band 3500 - 5000 Hz and the values are summarized in Table 6.27. Since the differences in the source levels (i.e. 30 dB) always agree with the difference in the beamformed results (i.e. 30 dB), the change in the SPL does not affect the ROSI uncertainty. Consequently, ROSI can be used to compare different blades and turbine geometries.

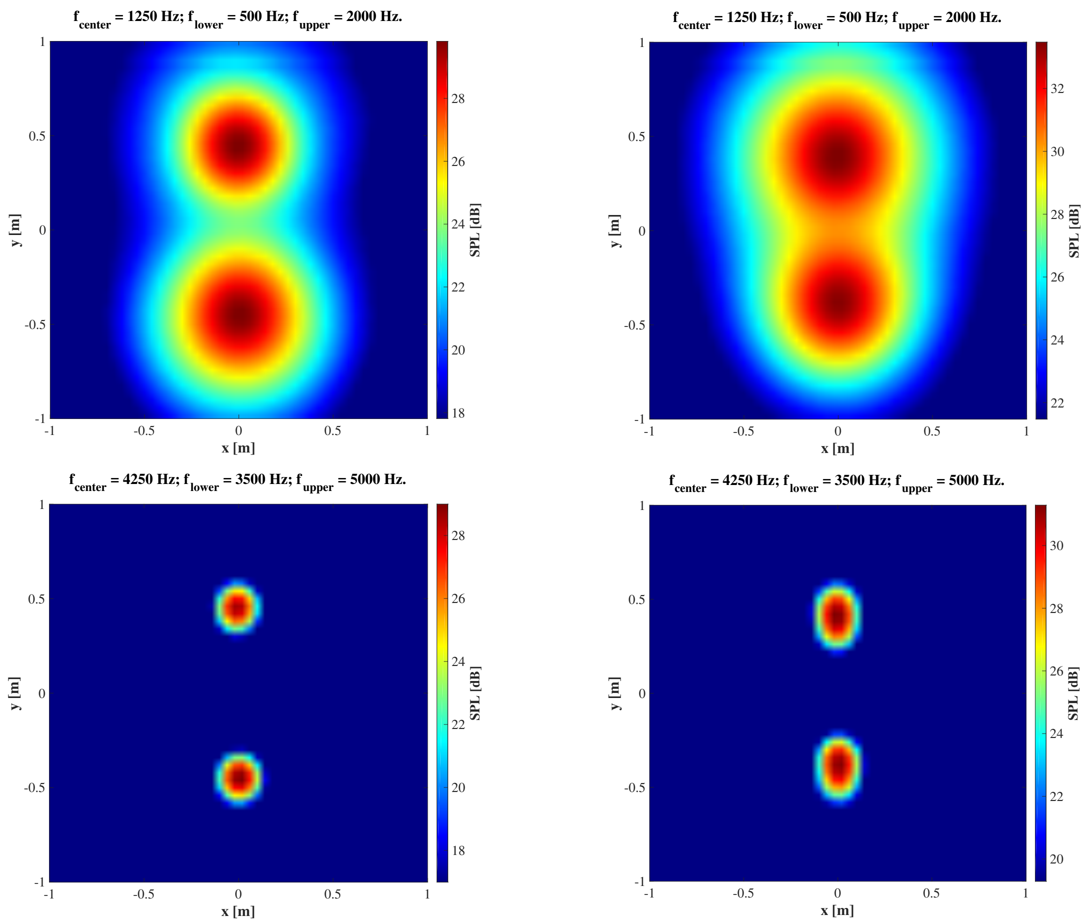

Figure 6.27: ROSI plots for two different distributed sources, emitting broadband sound. Frequency bands used for filtering the signal: 500 Hz - 2000 Hz; 3500 Hz - 5000 Hz. The SPL input of each point source corresponds to 30 dB. Left: two line sources with 10 point sources each. Right: two line sources with 20 point sources each. A scan grid of 2 x 2 m^2 with a total of 25000 scan points is employed.

Inputs [dB]	ROSI outputs [dB]			
	Line source 1 - 10 point sources	Line source 2 - 10 point sources	Line source 1 - 20 point sources	Line source 2 - 20 point sources
30	28.56	29.00	31.29	31.17
60	58.56	59.00	61.29	61.17

Table 6.27: Comparison between the inputs (i.e. 30 dB and 60 dB) and the ROSI outputs for the simulated distributed sources. Second and third columns: line sources with 10 point sources each. Fourth and fifth columns: line sources with 20 point sources each. Frequency band used for filtering the signal: f_{lower} = 3500 Hz, f_{upper} = 5000 Hz and f_{center} = 4250 Hz.

7

Applications of ROSI on experimental data

The Chapter describes the applications of ROSI on the experimental data collected during the research. Two datasets are analyzed:

1. the one measured in the A-Tunnel experiment;
2. the one measured in the OJF experiment.

All the results will be compared with the simulations described in Chapter 6.

7.1. A-Tunnel experimental dataset

For the experimental data recorded in the A-Tunnel at TU Delft University, only the first set of measurements is analyzed in this Chapter[1]. In this case, the distance between speaker 1 and speaker 2 equals the distance between speaker 3 and speaker 4 and it corresponds to 0.28 m, while the distance between speaker 2 and speaker 3 is 0.32 m. The configuration of the four speakers is depicted in Figure 7.1.

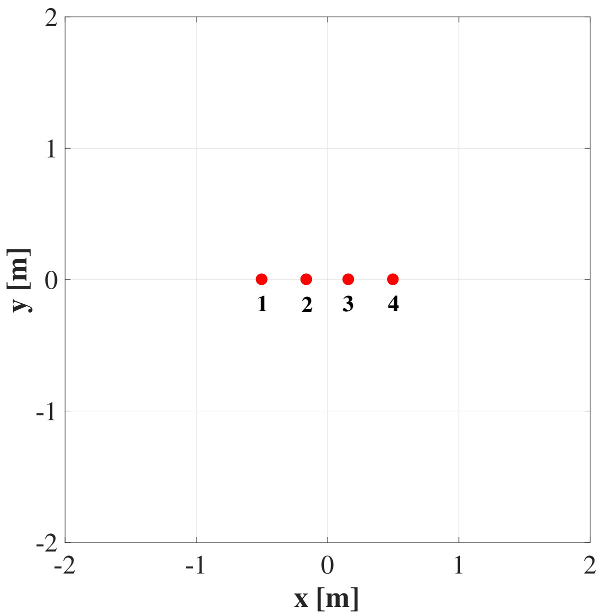

Figure 7.1: Configuration of the four rotating speakers for the first setup tested in the A-Tunnel. Coordinates: sound source 1 (x,y) = (-0.5,0), sound source 2 (x,y) = (-0.16,0), sound source 3 (x,y) = (0.16,0), sound source 4 (x,y) = (0.5,0).

[1] The other measurements are analyzed in Appendix A.

All the acoustic sources broadcast white noise for 40 s. The signal is filtered into two distinct frequency bands: 500 Hz - 2000 Hz and 3500 Hz - 5000 Hz. In addition, three different single frequencies are used for filtering: 1500 Hz, 3000 Hz and 5000 Hz. In this way, all the experimental data will be compared with the simulations of multiple spatially separated sources discussed in Chapter 6. In particular, Configuration B is the best representation of this experimental dataset.

Furthermore, the spacing between the speakers will be compared with the Rayleigh limits for every combination of the selected frequency and distance from the microphone array. As already mentioned, if the spacing between the speakers is below the Rayleigh limit, the algorithm is not able to distinguish the sources as separated. The Rayleigh limits are computed applying Equation 4.17 and the resulting values are presented in Table 7.1.

In the analysis, a sampling frequency of 50 kHz and a scan grid of 4 x 4 m^2 with a total of 40000 scan points[2] are employed. The distance between the center of rotation and the microphone array corresponds to 3 m. The measured data is separated in time blocks of 5000 samples (Δt = 100 ms) and windowed using a Hanning weighting function.

First, Conventional Beamforming is applied to the four stationary speakers emitting white noise. A comparison between the time domain and the frequency domain formulations is provided. Then, for the moving case ROSI is performed. Three different rotational speeds are tested: 1 Hz, 2.5 Hz and 4 Hz.

During the assessment of the data, it was recognized that the center of rotation was slightly displaced on the right (i.e. Xc = 0.16 m, Yc = 0.11 m). Thus, the new coordinates have been updated on the algorithm.

In addition, as explained in Chapter 6, the maximum SPL value is taken and no Source Power Integration over the region of interest is performed, which can have an effect on the results.

Frequency [Hz]	1500	3000	5000
Distance [m]	3	3	3
Rayleigh limit [m]	0.41	0.22	0.12

Table 7.1: Rayleigh limits obtained from the combination of different frequencies and distances from the array. The values are computed applying Equation 4.17.

7.1.1. Stationary case

For the stationary case, the filtered signal is processed with CB both in the time domain and in the frequency domain. All the resulting source maps at the selected frequencies can be found in Figure 7.2, Figure 7.3, Figure 7.4 and Figure 7.5. The SPL outputs for each speaker are summarized in Table 7.2 and Table 7.3, when frequency bands and single frequencies are respectively applied for filtering.

The time domain and frequency domain CB generate similar acoustic images. However, a short computational time is required for the frequency domain beamformer.

When the frequency ranges between 500 Hz and 2000 Hz, both algorithms are not able to distinguish the sources as separated. The same occurs when the selected frequency is 1500 Hz. In these cases, the spacing between the speakers is below the Rayleigh limit. The proper locations of the speakers are identified when the frequency band is 3500 Hz - 5000 Hz and when the single frequency is 5000 Hz. For f = 3000 Hz, only speaker 3 and speaker 4 are clearly separated. In this case, the spacing between the sources is above the Rayleigh limit. However, the difference between these two values is very small and inaccuracy can occur. Looking at the plots, the center of rotation results slightly displaced on the right. In order to obtain reliable results from the application of ROSI, the coordinates of the new center of rotation, (i.e. Xc = 0.16 m, Yc = 0.11 m), will be modified for the moving cases.

[2] 200 scan points are used in the x and y direction, which lead to a total of 40000 scan points.

With respect to the source strength, both methods yield similar SPLs. If the signal is filtered at a single frequency (i.e. 1500 Hz, 3000 Hz and 5000 Hz), the estimated levels decrease of approximately 13 dB.

All the results will be compared with the three moving cases.

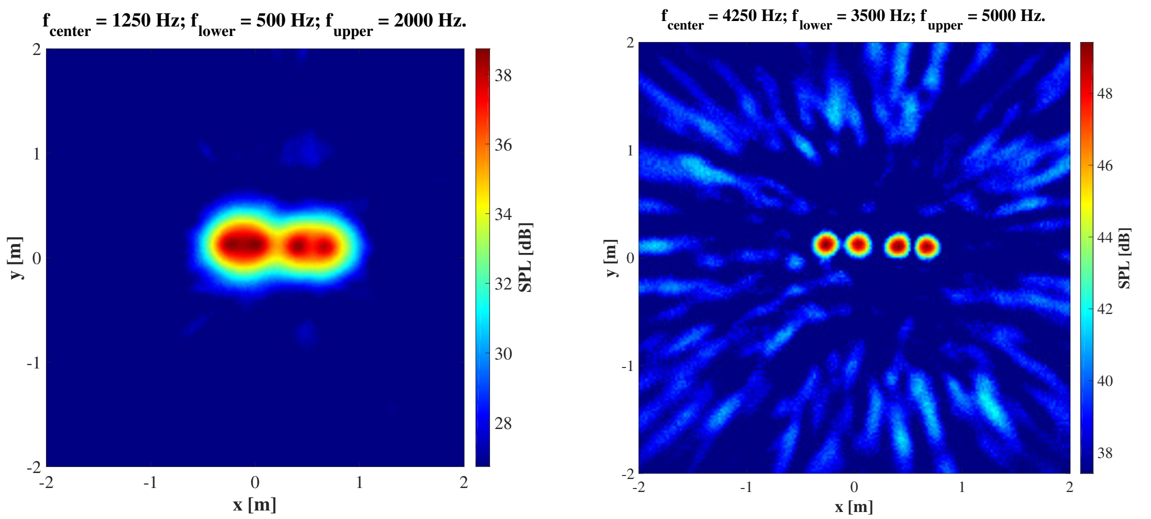

Figure 7.2: Conventional Beamforming in the time domain applied to the four stationary speakers, emitting white noise. The signal is filtered into different frequency bands: 500 Hz - 2000 Hz, 3500 Hz - 5000 Hz. A scan grid of 4 x 4 m^2 with a total of 40000 scan points and a sampling frequency of 50 kHz are employed. The distance from the microphone array is 3 m.

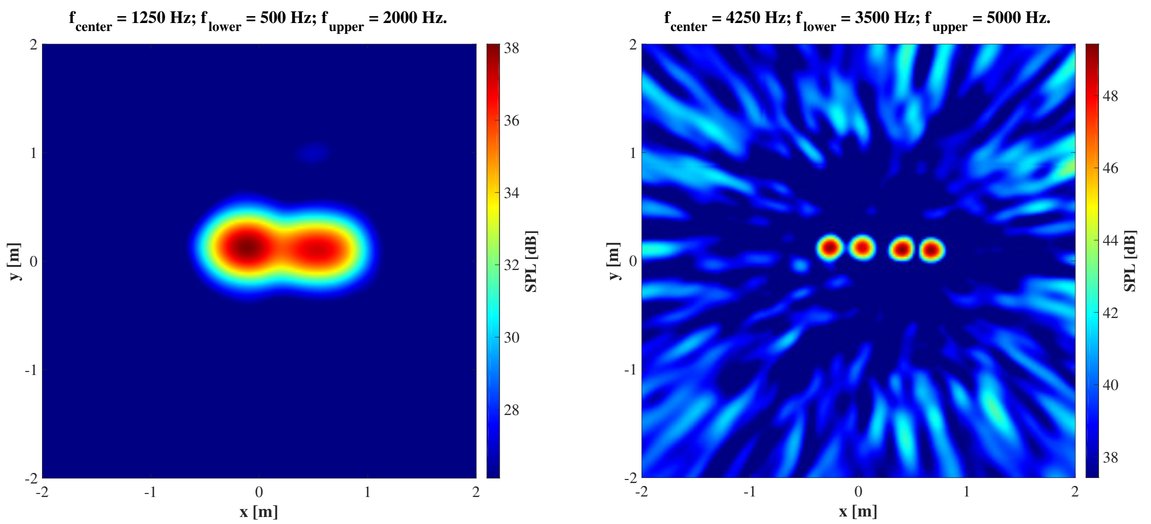

Figure 7.3: Conventional Beamforming in the frequency domain applied to the four stationary speakers, emitting white noise. The signal is filtered into different frequency bands: 500 Hz - 2000 Hz, 3500 Hz - 5000 Hz. A scan grid of 4 x 4 m^2 with a total of 40000 scan points and a sampling frequency of 50 kHz are employed. The distance from the microphone array is 3 m.

Frequency bands [Hz]	500 - 2000				3500 - 5000			
Speaker numbers [-]	1	2	3	4	1	2	3	4
CB outputs - time domain [dB]	/	/	/	/	49.42	48.87	49.34	49.20
CB outputs - frequency domain [dB]	/	/	/	/	49.25	48.57	49.43	49.31

Table 7.2: Comparison between the SPL outputs applying CB in the time domain and the SPL outputs applying CB in the frequency domain to the four stationary speakers. The signal emitted is white noise and it is filtered into different frequency bands (i.e. 500 Hz - 2000 Hz, 3500 Hz - 5000 Hz). If the sound sources are not distinguished as separated sources, their SPLs are not provided.

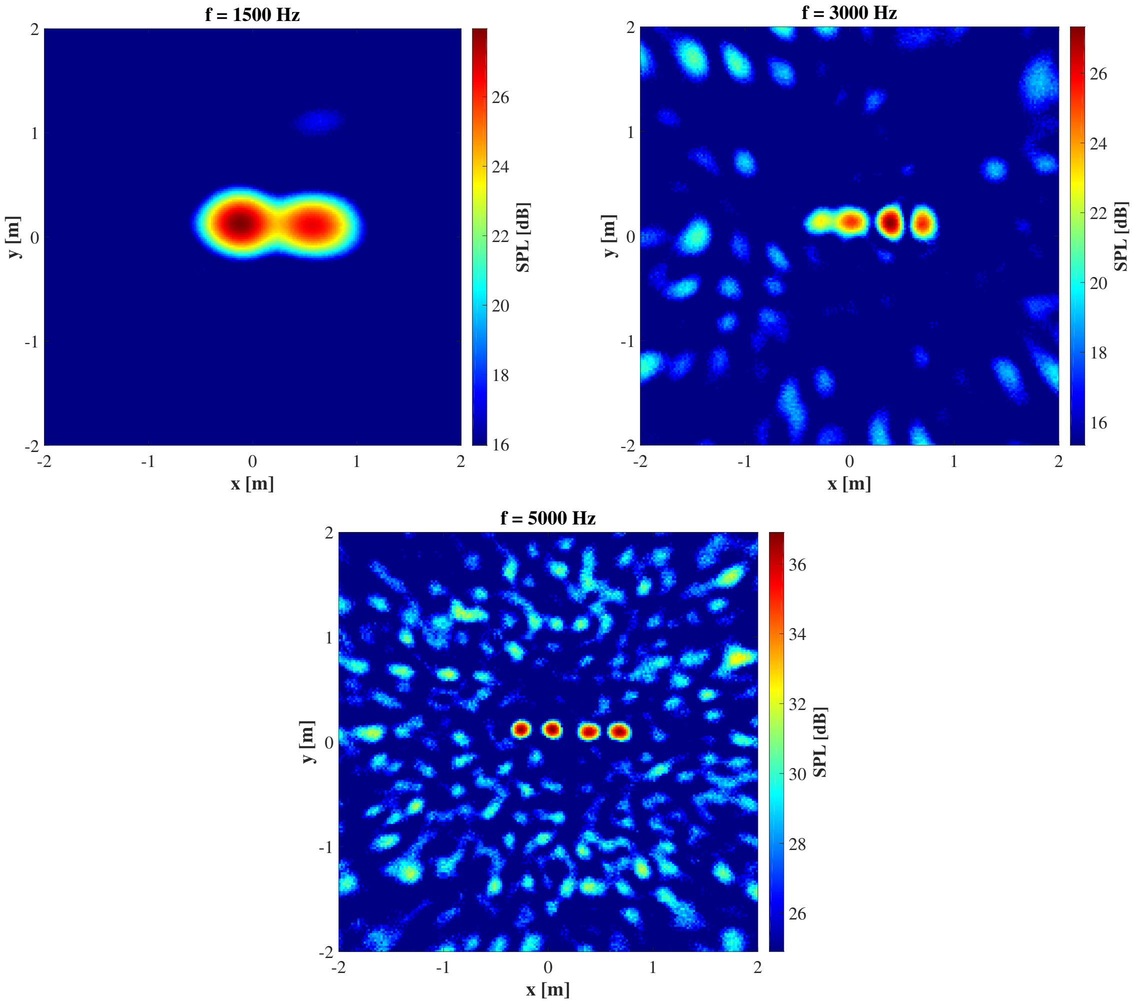

Figure 7.4: Conventional Beamforming in the time domain applied to the four stationary speakers emitting white noise. For the filtering of the signal, three different single frequencies are used: 1500 Hz, 3000 Hz and 5000 Hz. A scan grid of 4 x 4 m^2 with a total of 40000 scan points and a sampling frequency of 50 kHz are employed. The distance from the microphone array is 3 m.

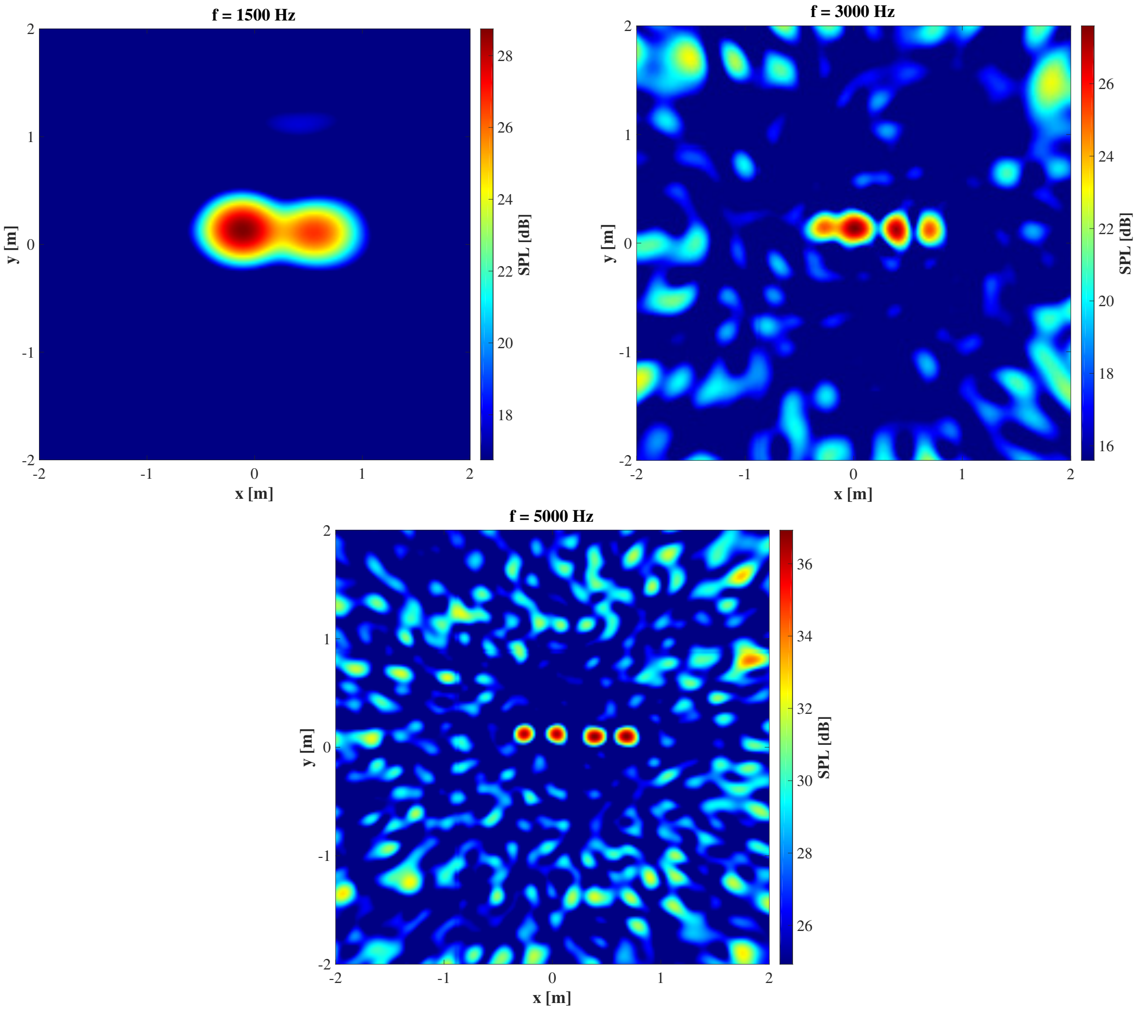

Figure 7.5: Conventional Beamforming in the frequency domain applied to the four stationary speakers emitting white noise. For the filtering of the signal, three different single frequencies are used: 1500 Hz, 3000 Hz and 5000 Hz. A scan grid of 4 x 4 m^2 with a total of 40000 scan points and a sampling frequency of 50 kHz are employed. The distance from the microphone array is 3 m.

Frequency [Hz]	1500				3000				5000			
Speaker numbers [-]	1	2	3	4	1	2	3	4	1	2	3	4
CB outputs - time domain [dB]	/	/	/	/	/	/	27.33	25.64	36.87	36.90	36.36	36.87
CB outputs - frequency domain [dB]	/	/	/	/	/	/	27.18	25.22	36.83	36.92	36.33	36.80

Table 7.3: Comparison between the SPL outputs applying CB in the time domain and the SPL outputs applying CB in the frequency domain to the four stationary speakers. The signal emitted is white noise. For the filtering of the signal, three different single frequencies are used: 1500 Hz, 3000 Hz and 5000 Hz. If the sound sources are not distinguished as separated sources, their SPLs are not provided.

7.1.2. Moving case - rotational speed of 1 Hz

In this section, the four speakers rotate at 1 Hz and emit white noise. ROSI is applied and the resulting acoustic plots are illustrated in Figure 7.6 and in Figure 7.7, when the frequency bands and single frequencies are respectively used for filtering. Table 7.4 and Table 7.5 summarize the ROSI outputs. When the sources are not distinguished as separated, their SPLs are not taken into account.

As in the stationary case, for the frequency band 500 Hz - 2000 Hz and for f = 1500 Hz, the spacing between the speakers is below the Rayleigh limits. Instead, when higher frequencies are employed (i.e. frequency band 3500 Hz - 5000 Hz), the four speakers are clearly visible and ROSI yields their correct locations. Even if for f = 3000 Hz the spacing between the sources is above the Rayleigh limit, the locations of the four speakers is not correctly determined. For f = 5000 Hz, speaker 2 is not identified.

When the frequency band 3500 Hz - 5000 Hz is used, it can be observed a slight underestimation of the SPLs, of approximately 1 dB, compared to the stationary case. This negligible difference may be linked with numerical approximations. On the other hand, when the beamforming is applied at a single frequency, the SPL values for speaker 3 and speaker 4 are similar to the stationary case. In accordance with simulated multiple sources, filtering the signal at a single frequency leads to a better approximation of the source levels.

Frequency bands [Hz]	500 - 2000				3500 - 5000			
Speaker numbers [-]	1	2	3	4	1	2	3	4
ROSI outputs [dB]	/	/	/	/	47.73	47.82	48.82	48.21

Table 7.4: SPL values applying ROSI to the four rotating speakers. The rotational speed corresponds to 1 Hz. The signal emitted is white noise and it is filtered into different frequency bands (i.e. 500 Hz - 2000 Hz, 3500 Hz - 5000 Hz). If the sound sources are not distinguished as separated sources, their SPLs are not provided.

Frequency [Hz]	1500				3000				5000			
Speaker numbers [-]	1	2	3	4	1	2	3	4	1	2	3	4
ROSI outputs [dB]	/	/	/	/	/	/	/	/	32.99	/	36.70	36.87

Table 7.5: SPL values applying ROSI to the four speakers rotating at 1 Hz. The signal emitted is white noise. For the filtering of the signal, three different single frequencies are used: 1500 Hz, 3000 Hz and 5000 Hz. If the sound sources are not distinguished as separated sources, their SPLs are not provided.

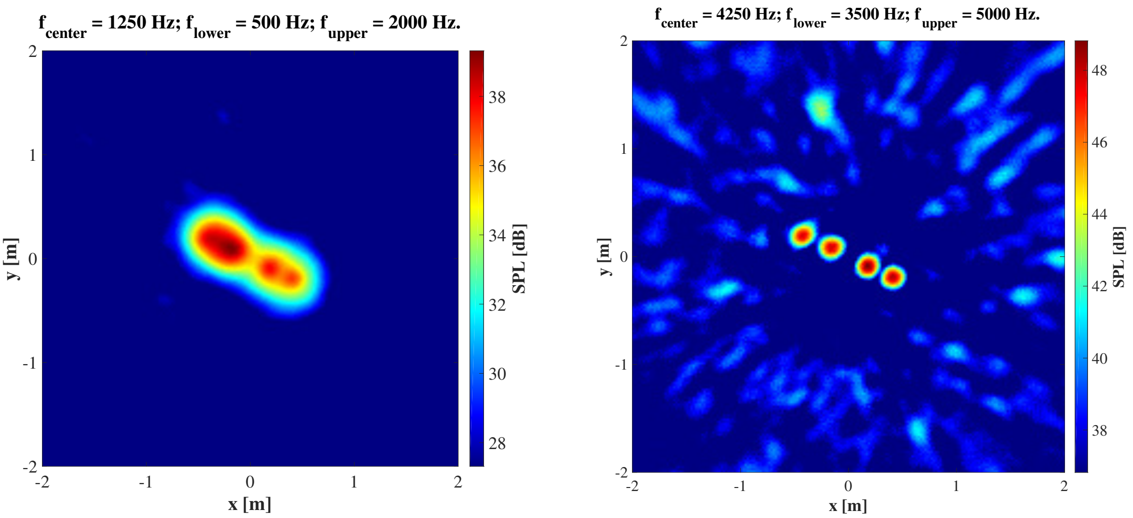

Figure 7.6: ROSI applied to the four speakers rotating at 1 Hz and emitting white noise. The signal is filtered into different frequency bands: 500 Hz - 2000 Hz, 3500 Hz - 5000 Hz. A scan grid of 4 x 4 m^2 with a total of 40000 scan points and a sampling frequency of 50 kHz are employed. The distance from the microphone array is 3 m.

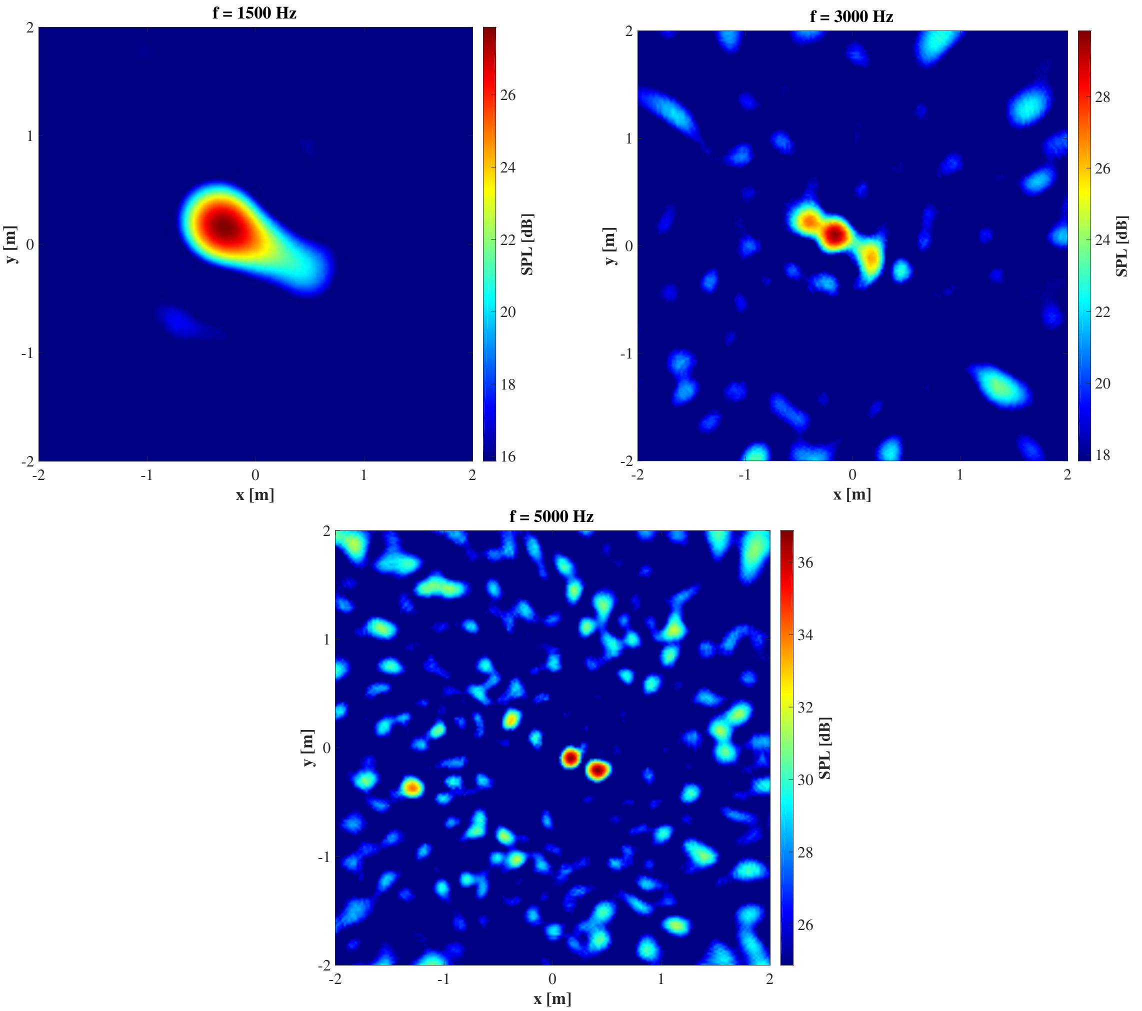

Figure 7.7: ROSI applied to the four speakers rotating at 1 Hz and emitting white noise. For the filtering of the signal, three different single frequencies are used: 1500 Hz, 3000 Hz and 5000 Hz. A scan grid of 4 x 4 m^2 with a total of 40000 scan points and a sampling frequency of 50 kHz are employed. The distance from the microphone array is 3 m.

7.1.3. Moving case - rotational speed of 2.5 Hz

The four sound sources rotate at 2.5 Hz and emit white noise. Figure 7.8 and Figure 7.9 depict the ROSI plots, when the signal is filtered with distinct frequency bands and with single frequencies, respectively. Table 7.6 and Table 7.7 show the results for the SPL.

For this particular measurement, speaker 3 is not detectable neither applying a frequency range of 3500 Hz - 5000 Hz or a frequency of 5000 Hz. As in the previous cases, the spacing between the sources is below the Rayleigh limit for the frequency band 500 Hz - 2000 Hz and for f = 1500 Hz. Thus, ROSI does not recognize the sources as separated.

In the analysis of the SPL, the values retrieved for frequency band 500 Hz -2000 Hz and for f = 1500 Hz are not taken into account. When the initial locations of the rotating speakers is correctly identified, ROSI underestimates the source level. The difference with the stationary case is of approximately 2 dB for the frequency band 3500 Hz - 5000 Hz and of about 5 dB for f = 5000 Hz. For f = 3000 Hz, ROSI yield different SPLs for every speaker. These results can be affected by numerical approximations, since the difference between the spacing of the sources and the Rayleigh limit is very small. By comparing the SPLs with the moving case at 1 Hz, it can be observed that the values are almost the same when the beamforming is applied between 3500 Hz and 5000 Hz. On the other hand, for f = 5000 Hz the difference in the estimation amounts to approximately

6 dB. This is may be linked to the inaccurate operation of speaker 3 during this set of measurements.

Frequency bands [Hz]	500 - 2000				3500 - 5000			
Speaker numbers [-]	1	2	3	4	1	2	3	4
ROSI outputs [dB]	/	/	/	/	47.01	47.63	/	47.07

Table 7.6: SPL values applying ROSI to the four rotating speakers. The rotational speed corresponds to 2.5 Hz. The signal emitted is white noise and it is filtered into different frequency bands (i.e. 500 Hz - 2000 Hz, 3500 Hz - 5000 Hz). If the sound sources are not distinguished as separated sources, their SPLs are not taken into account.

Frequency [Hz]	1500				3000				5000			
Speaker numbers [-]	1	2	3	4	1	2	3	4	1	2	3	4
ROSI outputs [dB]	/	/	/	/	22.58	27.07	/	24.89	32.04	31.92	/	29.03

Table 7.7: SPL values applying ROSI to the four speakers rotating at 2.5 Hz. The signal emitted is white noise. For the filtering of the signal, three different single frequencies are used: 1500 Hz, 3000 Hz and 5000 Hz. If the sound sources are not distinguished as separated sources, their SPLs are not provided.

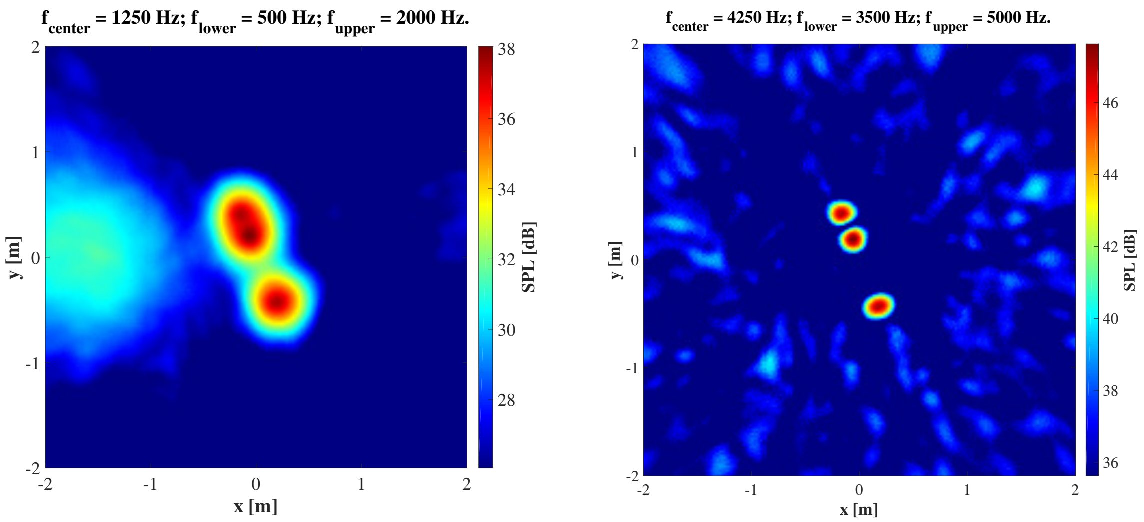

Figure 7.8: ROSI applied to the four speakers rotating at 2.5 Hz and emitting white noise. The signal is filtered into different frequency bands: 500 Hz - 2000 Hz, 3500 Hz - 5000 Hz. A scan grid of 4 x 4 m^2 with a total of 40000 scan points and a sampling frequency of 50 kHz are employed. The distance from the microphone array is 3 m.

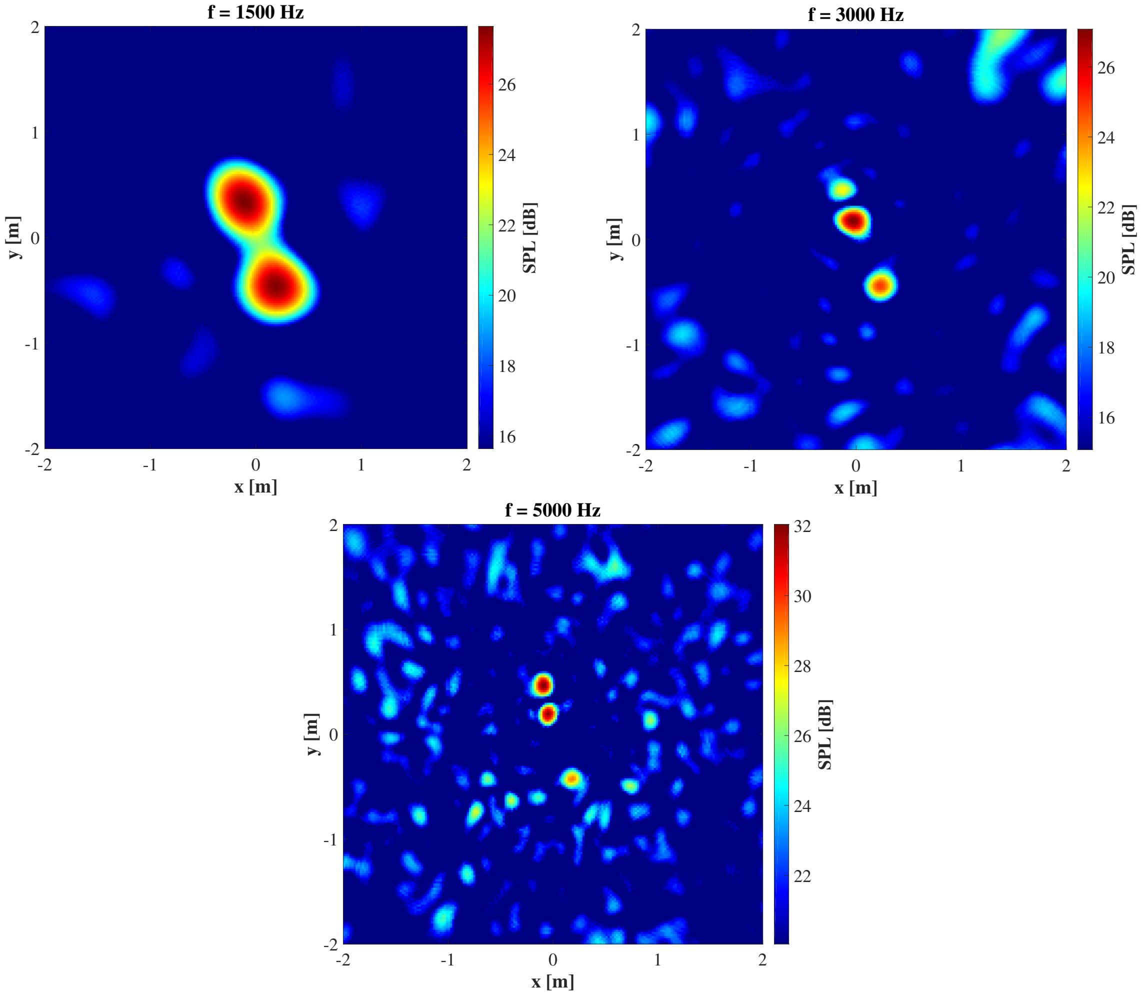

Figure 7.9: ROSI applied to the four speakers rotating at 2.5 Hz and emitting white noise. For the filtering of the signal, three different single frequencies are used: 1500 Hz, 3000 Hz and 5000 Hz. A scan grid of 4 x 4 m^2 with a total of 40000 scan points and a sampling frequency of 50 kHz are employed. The distance from the microphone array is 3 m.

7.1.4. Moving case - rotational speed of 4 Hz

The four sound sources rotate at 4 Hz and emit white noise. For this case, the acoustic images are illustrated in Figure 7.10, if the signal is filtered into distinct frequency bands, and in Figure 7.11, if the signal is filtered at a single frequency. The ROSI outcomes for each speaker are summarized in Table 7.8 and in Table 7.9.

Only for the frequency band 3500 Hz - 5000 Hz and for f = 5000 Hz, ROSI correctly yields the initial locations of the speakers. In contrast with the previous moving cases, all the speakers seem to work properly. For the analysis, only if the sources are distinguished as separated, their corresponding SPLs are taken into account.

For the frequency band 3500 Hz - 5000 Hz, the SPL of speaker 2, speaker 3, speaker 4 result overestimated with respect to the stationary case. For speaker 1, the opposite occurs. As previously explained, the results for f = 3000 Hz are not reliable. At f = 5000 Hz, for speaker 2, 3 and 4 the SPLs differs from the stationary case of approximately 1 dB. Whereas, speaker 1 appears underestimated. By comparing the results obtained with a rotational speed of 1 Hz, the differences in the sound levels amount of approximately 3 dB. This trend can be linked to numerical approximations. In overall, the effect of the rotational speed and of the frequency range on the source quantification reflect the simulations of Chapter 6. Furthermore, the application of ROSI on this experimental dataset confirms that the algorithm is in agreement with the Rayleigh limit.

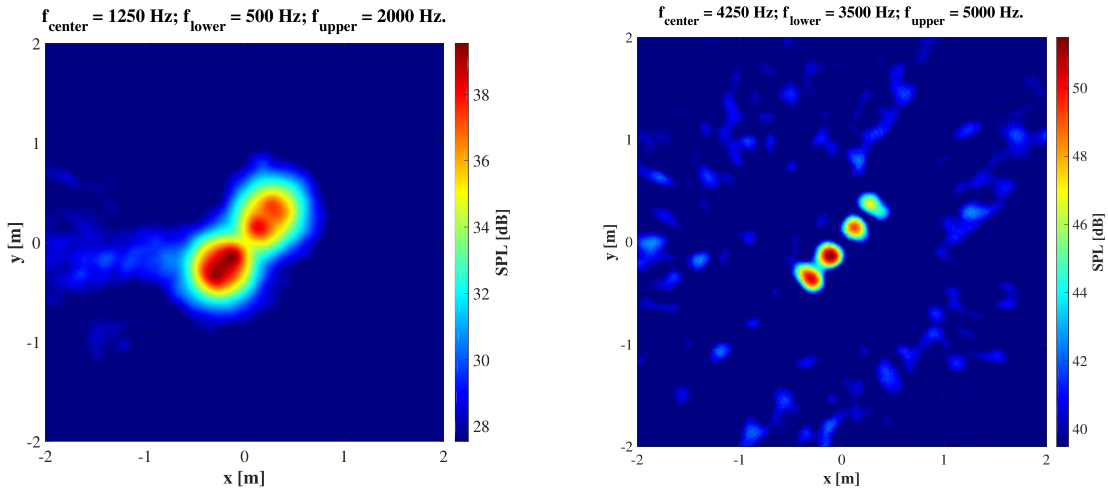

Figure 7.10: ROSI applied to the four speakers rotating at 4 Hz and emitting white noise. The signal is filtered into different frequency bands: 500 Hz - 2000 Hz, 3500 Hz - 5000 Hz. A scan grid of 4 x 4 m^2 with a total of 40000 scan points and a sampling frequency of 50 kHz are employed. The distance from the microphone array is 3 m.

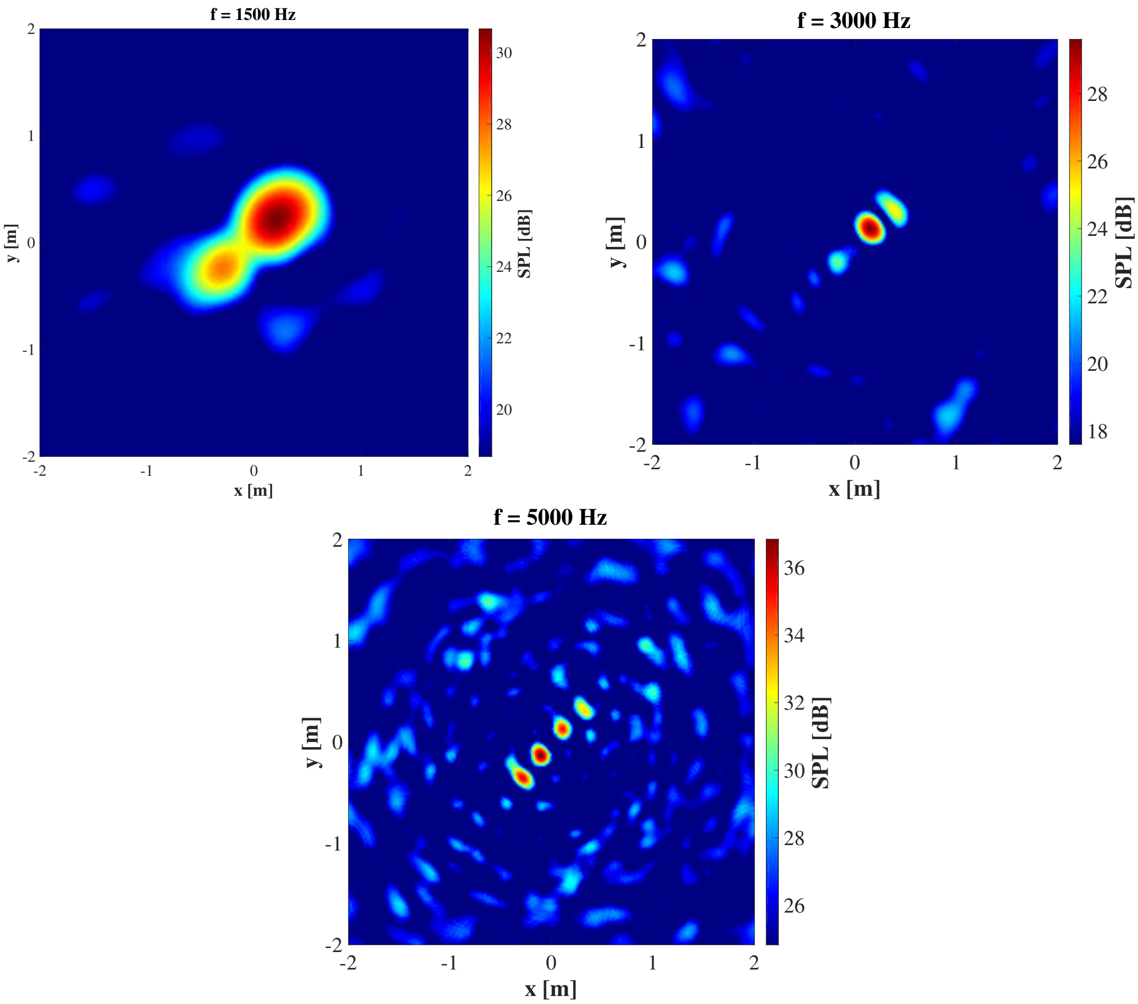

Figure 7.11: ROSI applied to the four speakers rotating at 4 Hz and emitting white noise. For the filtering of the signal, three single frequencies are used: 1500 Hz, 3000 Hz and 5000 Hz. A scan grid of 4 x 4 m^2 with a total of 40000 scan points and a sampling frequency of 50 kHz are employed. The distance from the microphone array is 3 m.

Frequency bands [Hz]	500 - 2000				3500 - 5000			
Speaker numbers [-]	1	2	3	4	1	2	3	4
ROSI outputs [dB]	/	/	/	/	46.86	49.23	51.48	50.45

Table 7.8: SPL values applying ROSI to the four rotating speakers. The rotational speed corresponds to 4 Hz. The signal emitted is white noise and it is filtered into different frequency bands (i.e. 500 Hz - 2000 Hz, 3500 Hz - 5000 Hz). If the sound sources are not distinguished as separated sources, their SPLs are not taken into account.

Frequency [Hz]	1500				3000				5000			
Speaker numbers [-]	1	2	3	4	1	2	3	4	1	2	3	4
ROSI outputs [dB]	/	/	/	/	25.22	29.61	/	/	32.88	35.22	36.83	35.50

Table 7.9: SPL values applying ROSI to the four speakers rotating at 4 Hz. The signal emitted is white noise. For the filtering of the signal, three different single frequencies are used: 1500 Hz, 3000 Hz and 5000 Hz. If the sound sources are not distinguished as separated sources, their SPLs are not taken into account.

7.2. OJF experimental dataset

In this section, the dataset recorded in the OJF experiment is evaluated. As already mentioned in Chapter 5, during the experimental campaign the background noise of the facility was measured at different wind speeds of the tunnel: first, with the empty tunnel and then, with the tower, the nacelle and the tail fin of the wind turbine installed (Figure 5.10). In the range of frequencies where the wind turbine noise is expected (i.e. 500 Hz - 2000 Hz [60]), the background noise levels are quite high and result comparable to the sound emitted by the DOD upwind turbine. Thus, ROSI is not able to correctly localize and quantify the noise emitted by the small wind turbine. An example of this compromised assessment is presented below for the five-bladed DOD wind turbine tested at a wind speed of 9 m/s.

In the analysis, a sampling frequency of 50 kHz and a scan grid of 4x4 m^2 with a total of 40000 scan points are employed. The distance between the center of rotation of the wind turbine and the microphone array corresponds to 3 m. The measured data is separated in time blocks of 25000 samples (Δt = 500 ms) and windowed using a Hanning weighting function.

7.2.1. Five bladed wind turbine - 1

The DOD upwind turbine is tested with five blades. The corresponding rotor diameter is 1.72 m. The yaw angle is set at 0 degree. The wind speed of the tunnel is 9 m/s and the rotational speed of the turbine is 7.1 Hz, which leads to a blade passing frequency (BPF)[3] of 35.5 Hz. The measured power output amounts to 325 W.

Figure 7.12 illustrates the PSD of the OJF background noise at 9 m/s, when the tower, the nacelle and the tail fin of the wind turbine are installed, and the PSD of the five-bladed turbine. Between 500 Hz and 2000 Hz, the two curves almost coincide. However, a small difference can be observed between 700 Hz and 1600 Hz. Thus, the signal is filtered into these two frequency bands and ROSI is applied. The resulting acoustic images are depicted in Figure 7.13. From the source maps, it is not possible to distinguish the five blades of the turbine. The source localization as well as the source quantification of the small wind turbine are compromised by the high levels of background noise.

[3] BPF = (RPM × N_{blades})/60 in which RPM and N_{blades} are respectively the rotational speed and the number of blades of the wind turbine [52].

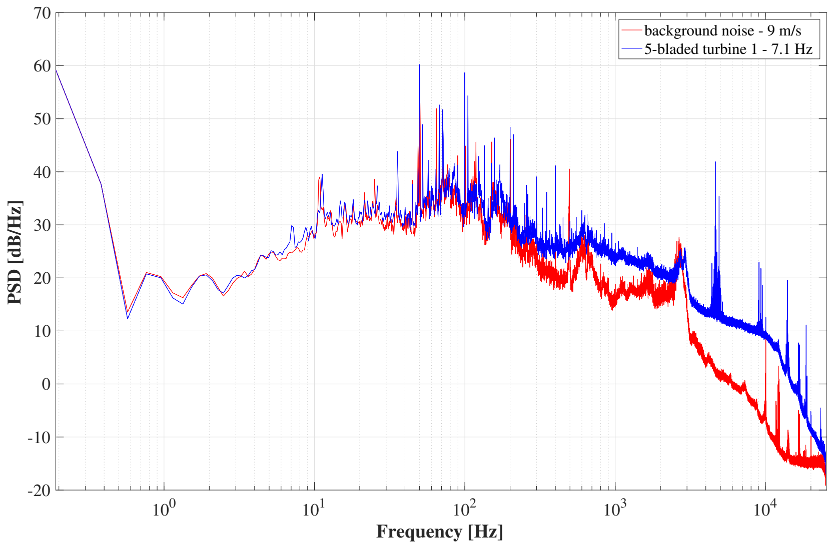

Figure 7.12: Comparison between the PSD of the OJF background noise at 9 m/s (in red) and the PSD of the five-bladed wind turbine (in blue). The measurements for the OJF background noise were carried out with only the tower, the nacelle and the tail fin of the wind turbine installed. The five-bladed wind turbine rotates at 7.1 Hz, which leads to a blade passing frequency of 35.5 Hz. The measured power output amounts to 325 W.

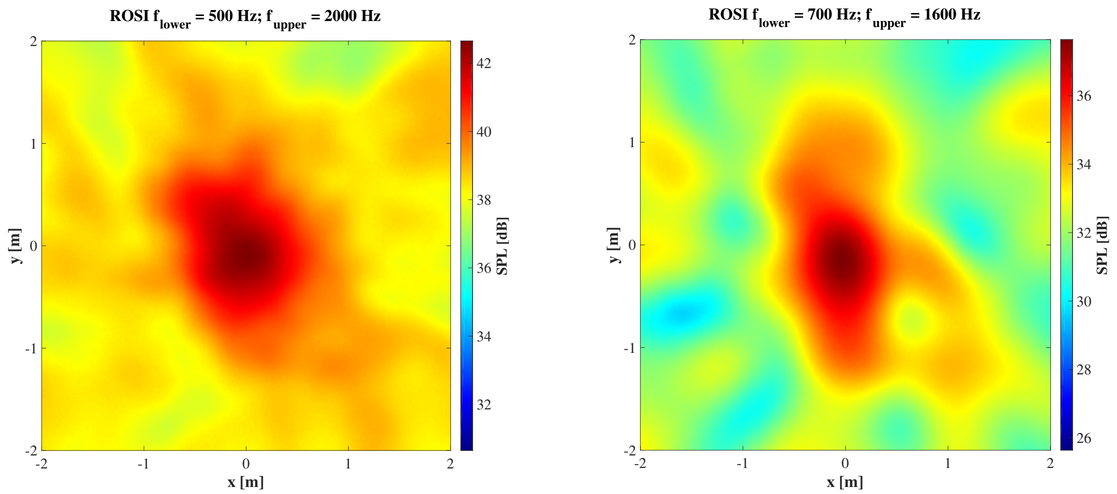

Figure 7.13: ROSI applied to the five-bladed turbine rotating at 7.1 Hz. The wind speed of the tunnel is 9 m/s. The signal is filtered into two different frequency bands: 500 Hz - 2000 Hz and 700 Hz - 1600 Hz. A scan grid of 4x4 m^2 with a total of 40000 scan points and a sampling frequency of 50 kHz are employed. The distance from the microphone array is 3 m.

8 Conclusions and recommendations

The main objective of the research was to assess the noise emitted by a small wind turbine, focusing on the aerodynamic noise sources. The high levels of background noise in the Open Jet Facility did not allow to fulfill this goal. However, the analysis of the ROSI performance was accomplished both with simulations and with the experimental data recorded in the A-Tunnel. All the findings are provided in this Chapter, according to the sub-questions presented in the beginning. In additon, recommendations for future works are drawn.

8.1. Conclusions

What is the ROSI performance for localizing and quantifying rotating sound sources, like small wind turbines?

From the investigation of the ROSI uncertainty, discussed in Chapter 6, several conclusions can be made:

- The differences in the beamformed results always agree with the differences in the source level. Thus, ROSI can be used to compare different blades or turbine geometries.
- The source localization as well as its quantification do not depend neither on the rotational speed of the source or on the length of the analyzed time snapshot. This can be expected because the scan grid rotates with the same speed of the source, following its movement.
- The source quantification is affected by the selected sampling frequency as well as by the additional noise. In the first case, if the signal is not correctly sampled, ROSI is not able to accurately estimate the source level. For the second parameter, a negative SNR leads to an overestimation of the source level. On the other hand, the source localization is independent of the sample frequency and of the added noise.
- The ROSI performance is in agreement with the Rayleigh limit. In fact, if the spacing between the sound sources is below the Rayleigh limit, ROSI does not distinguish the sources as separated. This affects not only the source localization but also the estimation of the SPL.
- When the beamforming is performed at a single frequency, ROSI provides a good estimation of the SPL for multiple spatially separated sources. On the other hand, if the signal is filtered into a frequency band, the ROSI outputs result underestimated with respect to the inputs.
- For distributed sound sources, an opposite trend in the estimation of the SPL can be observed. This may be linked to the larger number of sound sources close together.

Knowing the location of a rotating source in an anechoic environment, is ROSI able to correctly localize and quantify the sound level?

- The application of ROSI on the experimental data confirms that the performance of the algorithm is in agreement with the Rayleigh limit. If the sources are not distinguished as separated, their SPLs are not correctly estimated.
- The rotational speed of the source does not influence the performance of ROSI in the localization and in the quantification of the source level. Since an encoder was employed to measure the rotational speed of the device, at least one cycle of rotation was required to obtain the desired velocity. This is the reason why the locations of the four speakers differ from the stationary case. In addition, a difference can be observed for the three rotational speeds tested. However, by knowing that the rotation of the device was clockwise and by placing a different mark on each speaker, it was always possible to distinguish their positions.

In presence of a non-anechoic environment, is ROSI able to correctly localize and quantify the sound emitted by a small wind turbine?

- The high background noise levels of the OJF do not allow reliable acoustic measurements. As a result, a detailed noise assessment of the wind turbine is not provided and it is not possible to compare the measurement data with the analytical models, present in literature.

8.2. Recommendations

Several improvements for the current study as well as recommendations for future works can be underlined:

- Since for the analysis the maximum SPL value is considered, more accurate results can be achieved applying the Source Power Integration technique over the region of interest. This method is fully described in reference [77].
- In this research, the frequency range was chosen to reflect the noise range emitted by a small wind turbine [58]. A more detailed study is required to determine the optimal frequency range for filtering the signal and for correctly identifying the source level.
- In order to avoid some inaccuracies in the source localization caused by the encoder, a source tracking method, discussed in reference [76], can be applied to determine the rotational speed of the moving object.
- The experiment in the A-Tunnel can be repeated with the four speakers emitting different types of sound at different sound levels. In this way, it will be evaluated if ROSI can quantify different emitted sounds as well as if the differences in the beamformed results agree with the differences in the source level.
- The effect of an additional stationary source on the ROSI performance can be evaluated with a simulated dataset as well as with the experimental dataset measured in the A-Tunnel.
- In the analysis of the OJF dataset, the convection amplification effect as well as the sound propagation path are not taken into account. Since the distance between the wind turbine and the microphone array is small, these parameters do not have a relevant effect on the ROSI estimates. More research is required to assess the ROSI performance when these effects are included in the algorithm.

A

A -Tunnel experiment - further analysis

In this Chapter, the assessment of all the other experimental data recorded in the A-Tunnel is provided.

In the analysis a sampling frequency of 50 kHz and a scan grid of 4 x 4 m^2 with a total of 40000 scan points[1] are employed. The distance between the center of rotation and the microphone array corresponds to 3 m. The measured data is separated in time blocks of 5000 samples (Δt = 100 ms) and windowed using a Hanning weighting function. When the emitted sound is white noise, the signal is filtered into two distinct frequency bands: 500 Hz - 2000 Hz and 3500 Hz - 5000 Hz. For all the set of measurements, the recording time is 40 s.

First, Conventional Beamforming is applied to the four stationary speakers. Then, for the moving cases ROSI is performed. Three different rotational speeds are tested: 1 Hz, 2.5 Hz and 4 Hz.

As explained in Chapter 6 and in Chapter 7, the maximum SPL is taken and no Source Power Integration over the region of interest is performed, which can have an effect on the results. In addition, if the spacing between the sources results below the Rayleigh limit, the resulting SPLs are not provided.

A.1. First set of measurements

For the first set of measurement, the distance between speaker 1 and speaker 2 equals the distance between speaker 3 and speaker 4 and it corresponds to 0.28 m, while the distance between speaker 2 and speaker 3 is 0.32 m. The configuration of the four speakers is provided in Figure 7.1. Two sounds are tested: a tone at 500 Hz and a tone at 1000 Hz. In both cases, the spacing between the speakers is below the Rayleigh limit (for f = 500 Hz, the Rayleigh limit equals 1.24 m, while for f = 1000 Hz, the Rayleigh limit equals 0.62 m.). As a result, neither CB or ROSI can distinguish the source as separated and the resulting SPLs are not provided.

A.1.1. Stationary case

As regards the stationary case, the emitted signal is processed with CB both in the tine domain and in the frequency domain. All the resulting source maps can be found in Figure A.1, for a tone at 500 Hz, and in Figure A.1, for a tone at 1000 Hz.

[1]200 scan points are used in the x and in the y direction, which lead to a total of 40000 scan points.

Tonal sound at 500 Hz

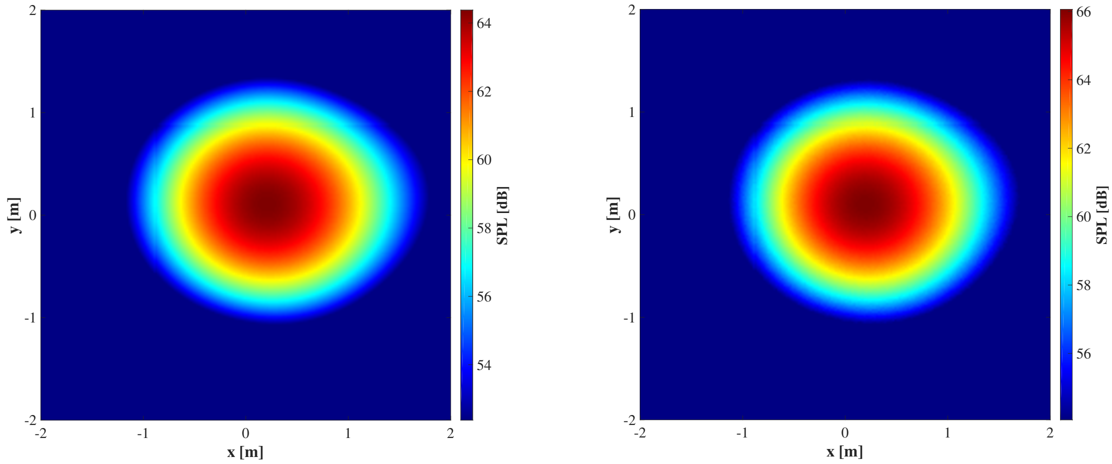

Figure A.1: Left: CB in the frequency domain. Right: CB in the time domain. The stationary four speakers emit tonal sound at 500 Hz. A scan grid of 4 x 4 m^2 with a total of 40000 scan points and a sampling frequency of 50 kHz are employed. The distance from the microphone array is 3 m.

Tonal sound at 1000 Hz

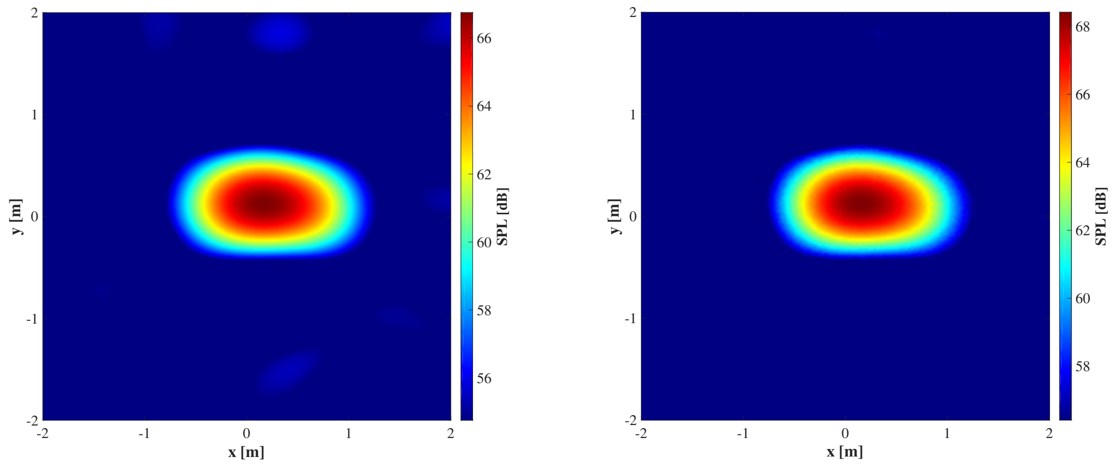

Figure A.2: Left: CB in the frequency domain. Right: CB in the time domain. The stationary four speakers emit tonal sound at 1000 Hz. A scan grid of 4 x 4 m^2 with a total of 40000 scan points and a sampling frequency of 50 kHz are employed. The distance from the microphone array is 3 m.

A.1.2. Moving case - rotational speed of 1 Hz

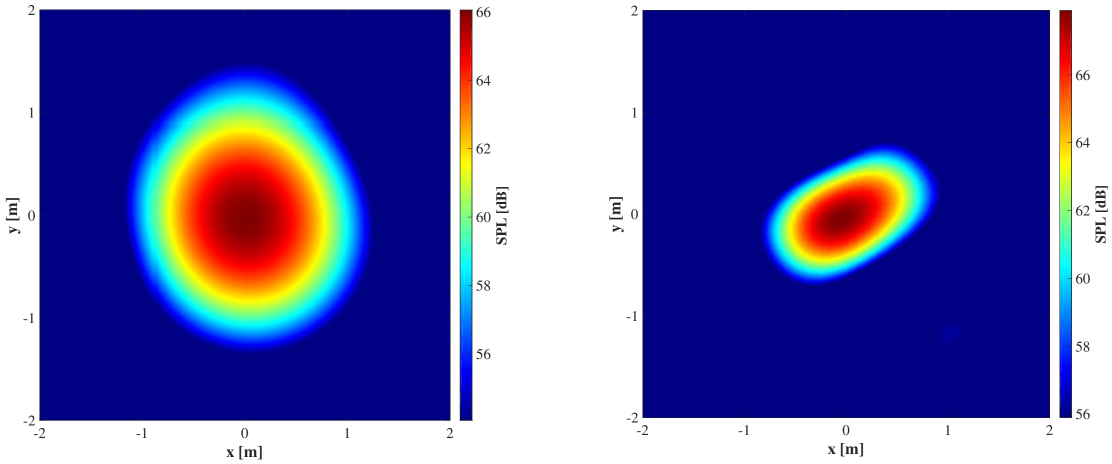

Figure A.3: ROSI applied to the four speakers rotating at 1 Hz. Left: The signal emitted is a tone at 500 Hz. Right: The signal emitted is a tone at 1000 Hz. A scan grid of 4 x 4 m^2 with a total of 40000 scan points and a sampling frequency of 50 kHz are employed. The distance from the microphone array is 3 m.

A.1.3. Moving case - rotational speed of 2.5 Hz

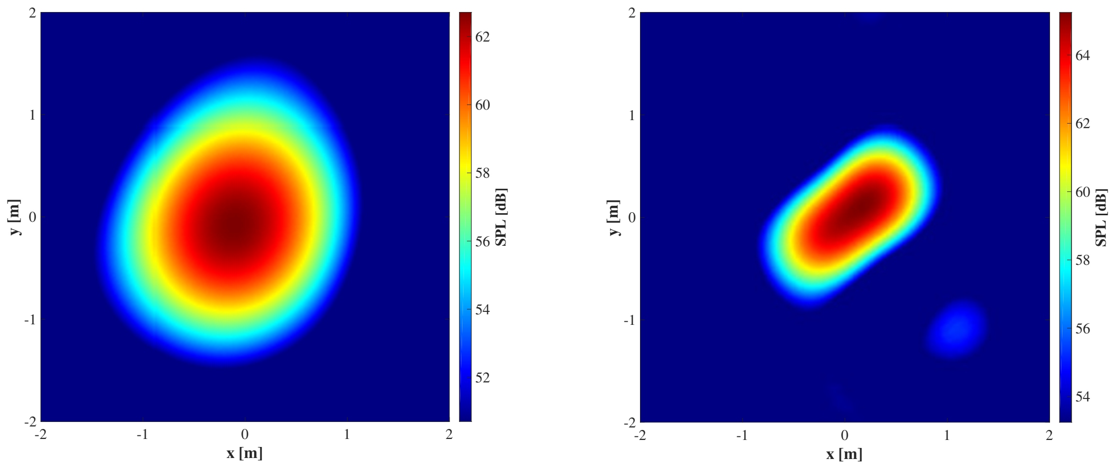

Figure A.4: ROSI applied to the four speakers rotating at 2.5 Hz. Left: The signal emitted is a tone at 500 Hz. Right: The signal emitted is a tone at 1000 Hz. A scan grid of 4 x 4 m^2 with a total of 40000 scan points and a sampling frequency of 50 kHz are employed. The distance from the microphone array is 3 m.

A.1.4. Moving case - rotational speed of 4 Hz

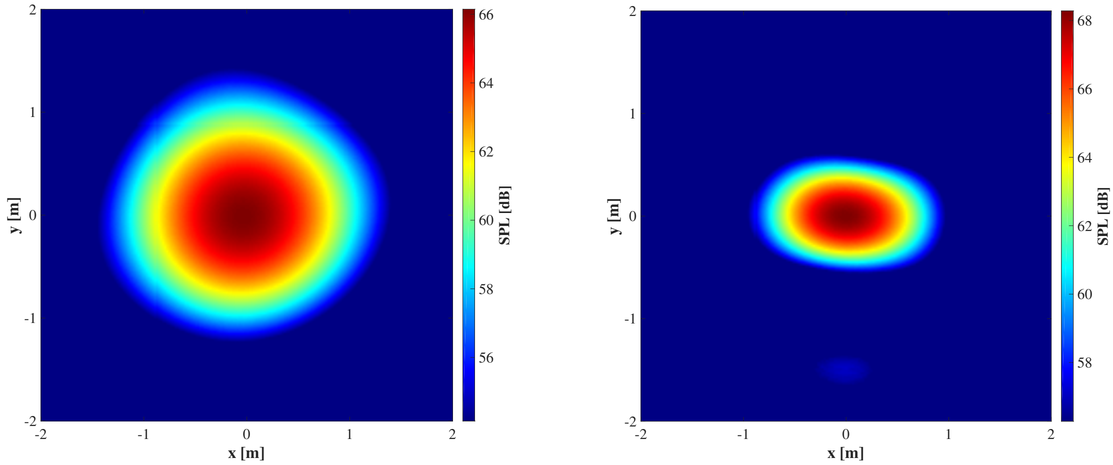

Figure A.5: ROSI applied to the four speakers rotating at 4 Hz. Left: The signal emitted is a tone at 500 Hz. Right: The signal emitted is a tone at 1000 Hz. A scan grid of 4 x 4 m^2 with a total of 40000 scan points and a sampling frequency of 50 kHz are employed. The distance from the microphone array is 3 m.

A.2. Second set of measurements

In this case, the distance between speaker 1 and speaker 2 equals the distance between speaker 3 and speaker 4 and it corresponds to 0.14 m, while the distance between speaker 2 and speaker 3 is 0.60 m. The configuration of the four speakers is depicted in Figure A.6. For this set of measurements, only when the signal is filtered at f = 5000 Hz, the spacing between the sources is above the Rayleigh limit (i.e. 0.12 m) and ROSI can distinguish the sources as separated.

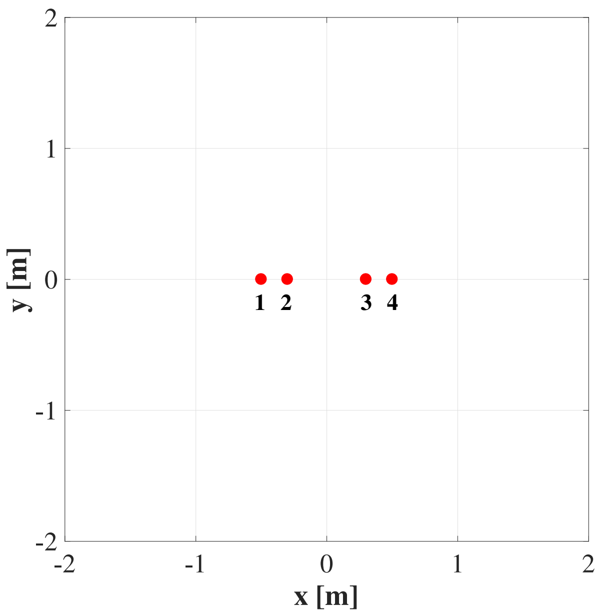

Figure A.6: Configuration of the four rotating speakers for the first setup tested in the A-Tunnel. Coordinates: sound source 1 (x,y) = (-0.5,0), sound source 2 (x,y) = (-0.3,0), sound source 3 (x,y) = (0.3,0), sound source 4 (x,y) = (0.5,0).

A.2.1. Moving case - rotational speed of 1 Hz

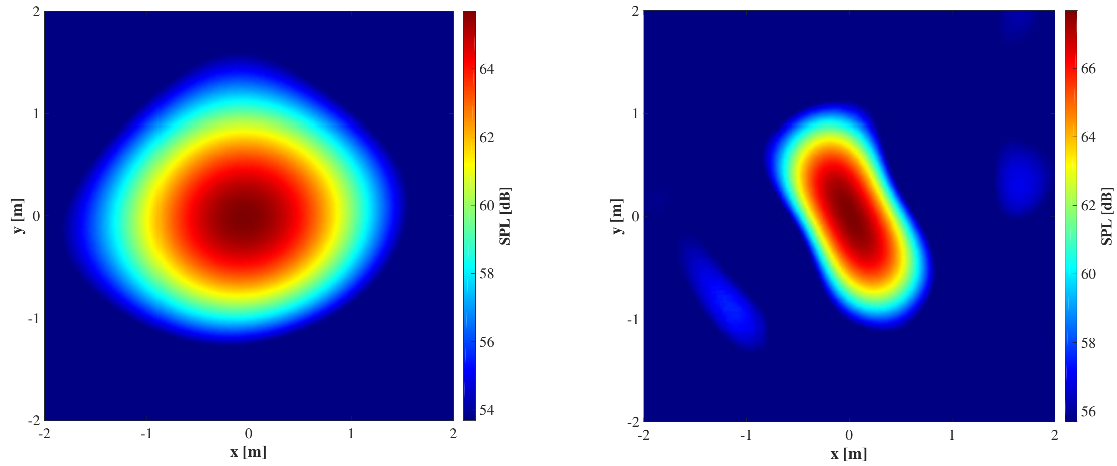

Figure A.7: ROSI applied to the four speakers rotating at 1 Hz. Left: The signal emitted is a tone at 500 Hz. Right: The signal emitted is a tone at 1000 Hz. A scan grid of 4 x 4 m^2 with a total of 40000 scan points and a sampling frequency of 50 kHz are employed. The distance from the microphone array is 3 m.

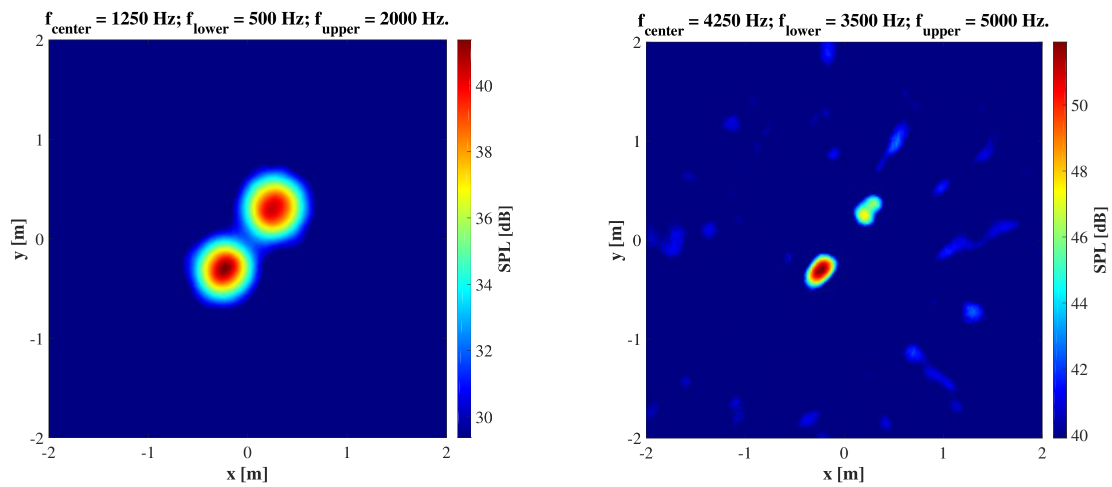

Figure A.8: ROSI applied to the four speakers rotating at 1 Hz and emitting white noise. The signal is filtered into different frequency bands: 500 Hz - 2000 Hz, 3500 Hz - 5000 Hz. A scan grid of 4 x 4 m^2 with a total of 40000 scan points and a sampling frequency of 50 kHz are employed. The distance from the microphone array is 3 m.

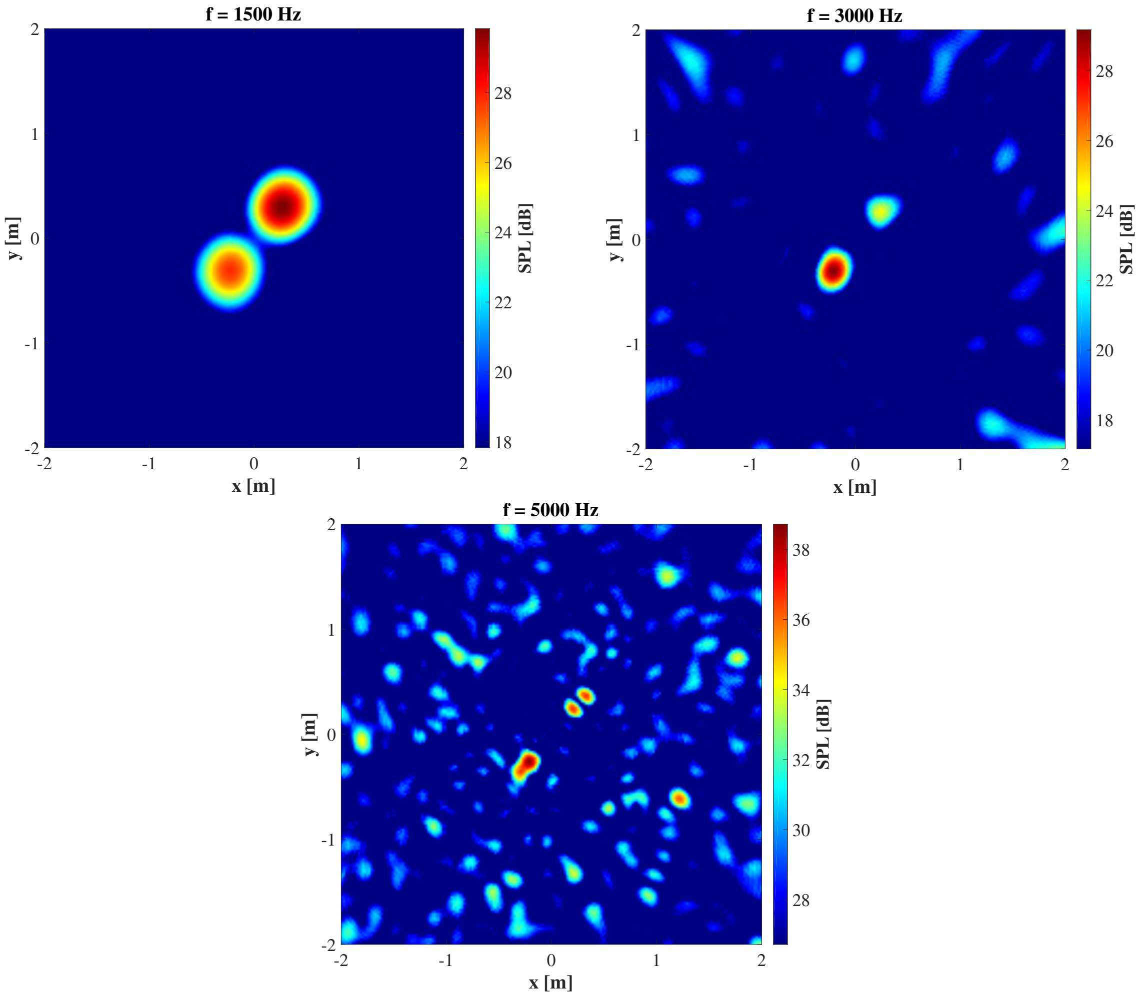

Figure A.9: ROSI applied to the four speakers rotating at 1 Hz and emitting white noise. For the filtering of the signal, three single frequencies are used: 1500 Hz, 3000 Hz and 5000 Hz. A scan grid of 4 x 4 m^2 with a total of 40000 scan points and a sampling frequency of 50 kHz are employed. The distance from the microphone array is 3 m.

Frequency [Hz]	1500				3000				5000			
Speaker numbers [-]	1	2	3	4	1	2	3	4	1	2	3	4
ROSI outputs [dB]	/	/	/	/	/	/	/	/	36.61	36.70	/	/

Table A.1: SPL values applying ROSI to the four speakers rotating at 4 Hz. The signal emitted is white noise. For the filtering of the signal, three different single frequencies are used: 1500 Hz, 3000 Hz and 5000 Hz. If the sound sources are not distinguished as separated sources, their SPLs are not taken into account.

A.2.2. Moving case - rotational speed of 2.5 Hz

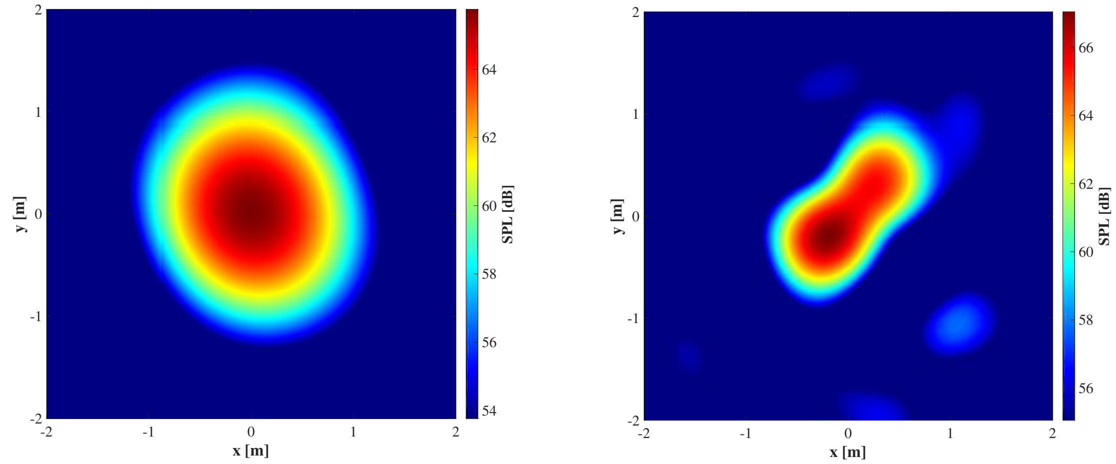

Figure A.10: ROSI applied to the four speakers rotating at 1 Hz. Left: The signal emitted is a tone at 500 Hz. Right: The signal emitted is a tone at 1000 Hz. A scan grid of 4 x 4 m^2 with a total of 40000 scan points and a sampling frequency of 50 kHz are employed. The distance from the microphone array is 3 m.

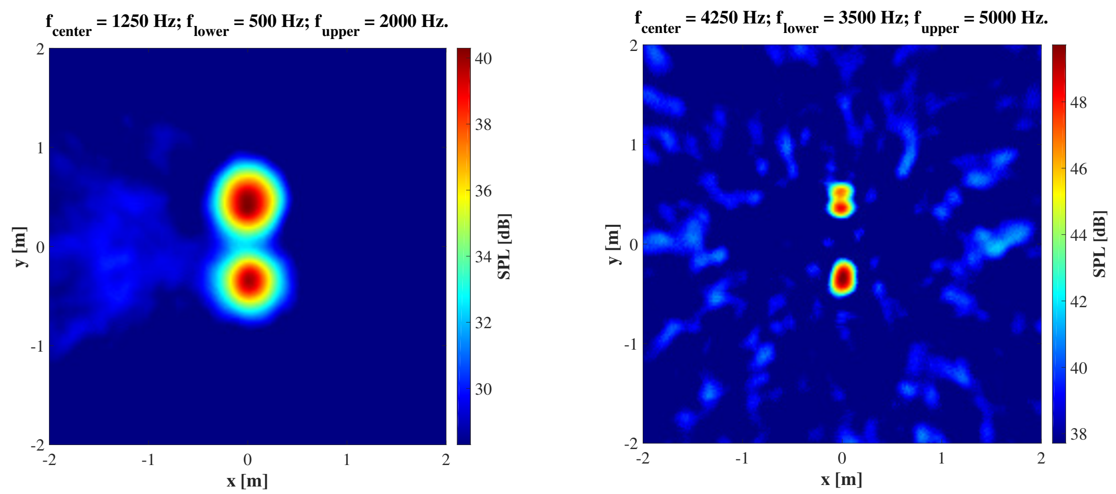

Figure A.11: ROSI applied to the four speakers rotating at 2.5 Hz and emitting white noise. The signal is filtered into different frequency bands: 500 Hz - 2000 Hz, 3500 Hz - 5000 Hz. A scan grid of 4 x 4 m^2 with a total of 40000 scan points and a sampling frequency of 50 kHz are employed. The distance from the microphone array is 3 m.

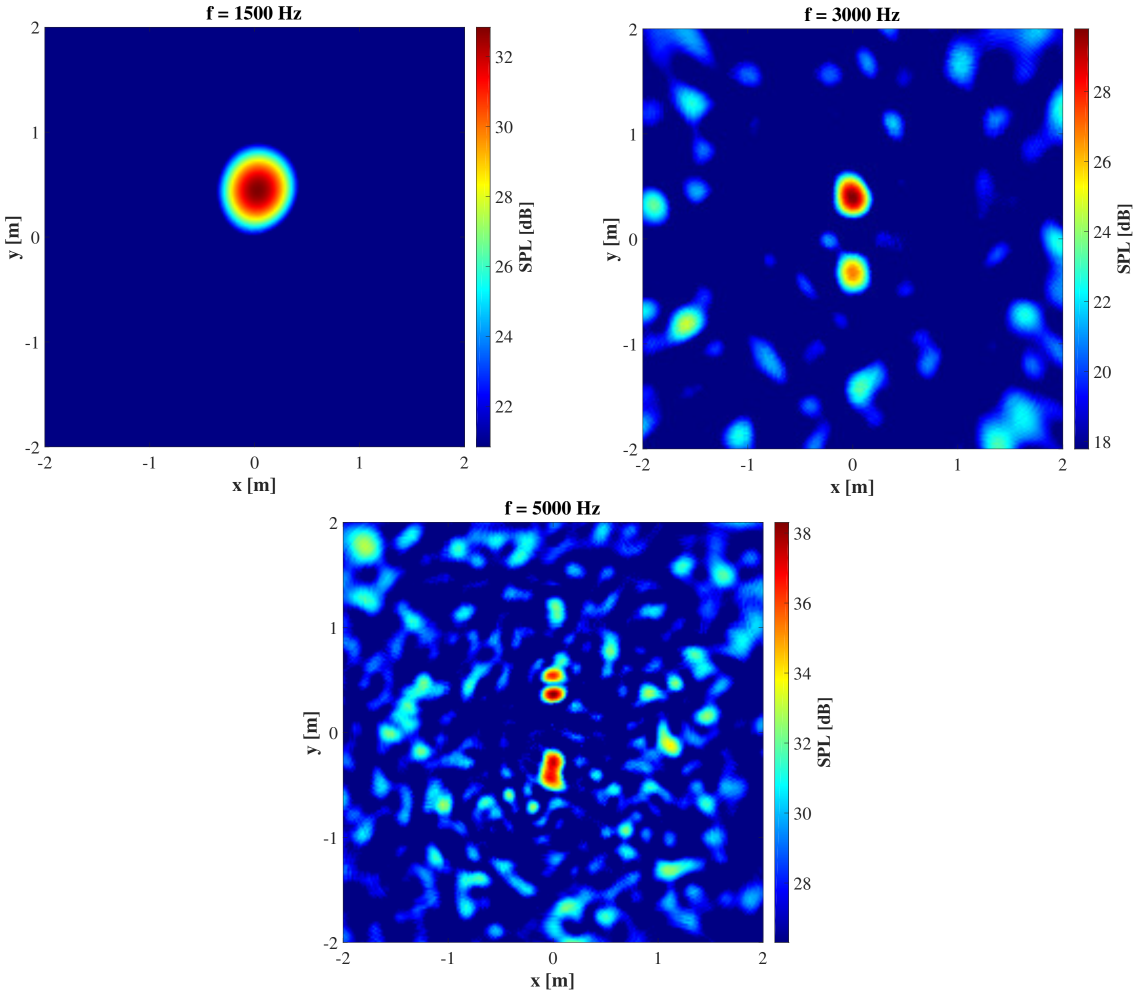

Figure A.12: ROSI applied to the four speakers rotating at 2.5 Hz and emitting white noise. For the filtering of the signal, three single frequencies are used: 1500 Hz, 3000 Hz and 5000 Hz. A scan grid of 4 x 4 m^2 with a total of 40000 scan points and a sampling frequency of 50 kHz are employed. The distance from the microphone array is 3 m.

Frequency [Hz]	1500				3000				5000			
Speaker numbers [-]	1	2	3	4	1	2	3	4	1	2	3	4
ROSI outputs [dB]	/	/	/	/	/	/	/	/	36.55	38.30	/	/

Table A.2: SPL values applying ROSI to the four speakers rotating at 2.5 Hz. The signal emitted is white noise. For the filtering of the signal, three different single frequencies are used: 1500 Hz, 3000 Hz and 5000 Hz. If the sound sources are not distinguished as separated sources, their SPLs are not taken into account.

A.2.3. Moving case - rotational speed of 4 Hz

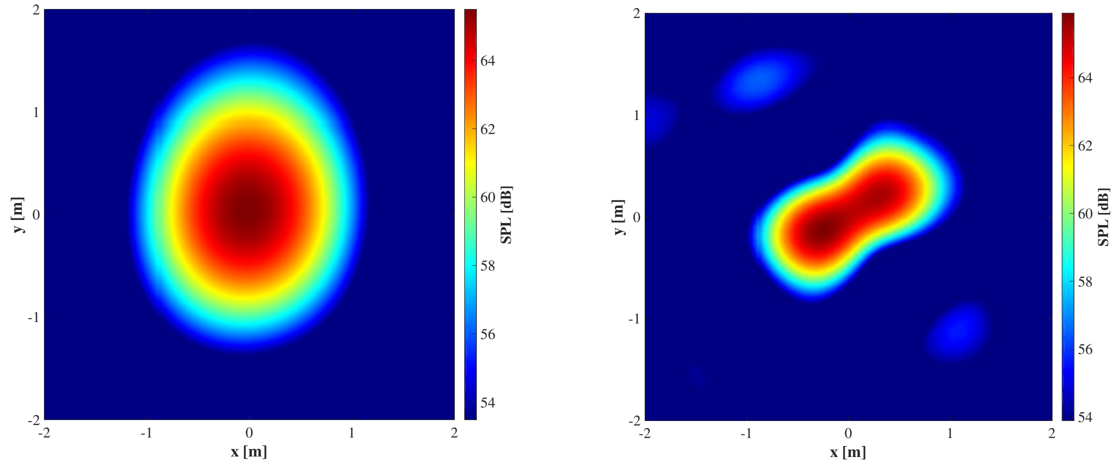

Figure A.13: ROSI applied to the four speakers rotating at 4 Hz. Left: The signal emitted is a tone at 500 Hz. Right: The signal emitted is a tone at 1000 Hz. A scan grid of 4 x 4 m^2 with a total of 40000 scan points and a sampling frequency of 50 kHz are employed. The distance from the microphone array is 3 m.

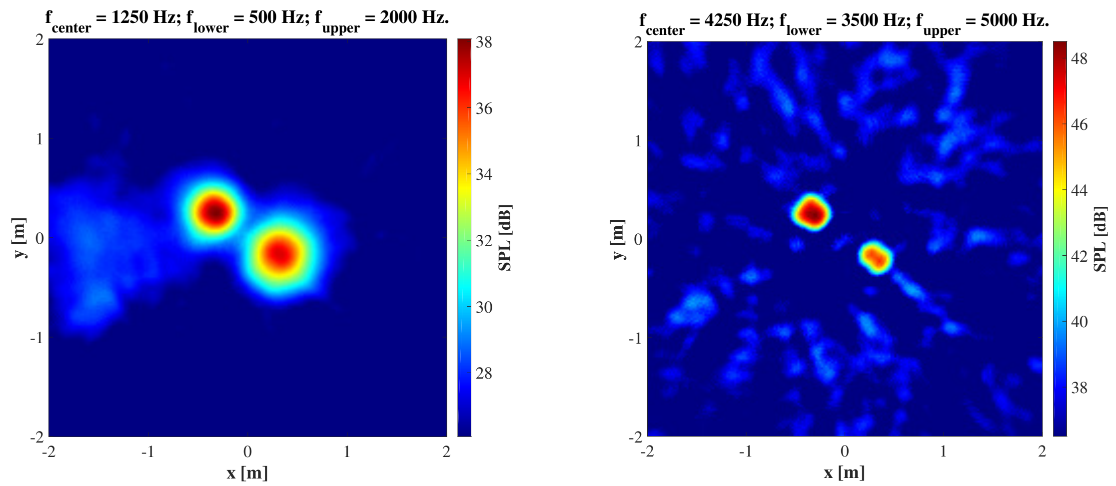

Figure A.14: ROSI applied to the four speakers rotating at 4 Hz and emitting white noise. The signal is filtered into different frequency bands: 500 Hz - 2000 Hz, 3500 Hz - 5000 Hz. A scan grid of 4 x 4 m^2 with a total of 40000 scan points and a sampling frequency of 50 kHz are employed. The distance from the microphone array is 3 m.

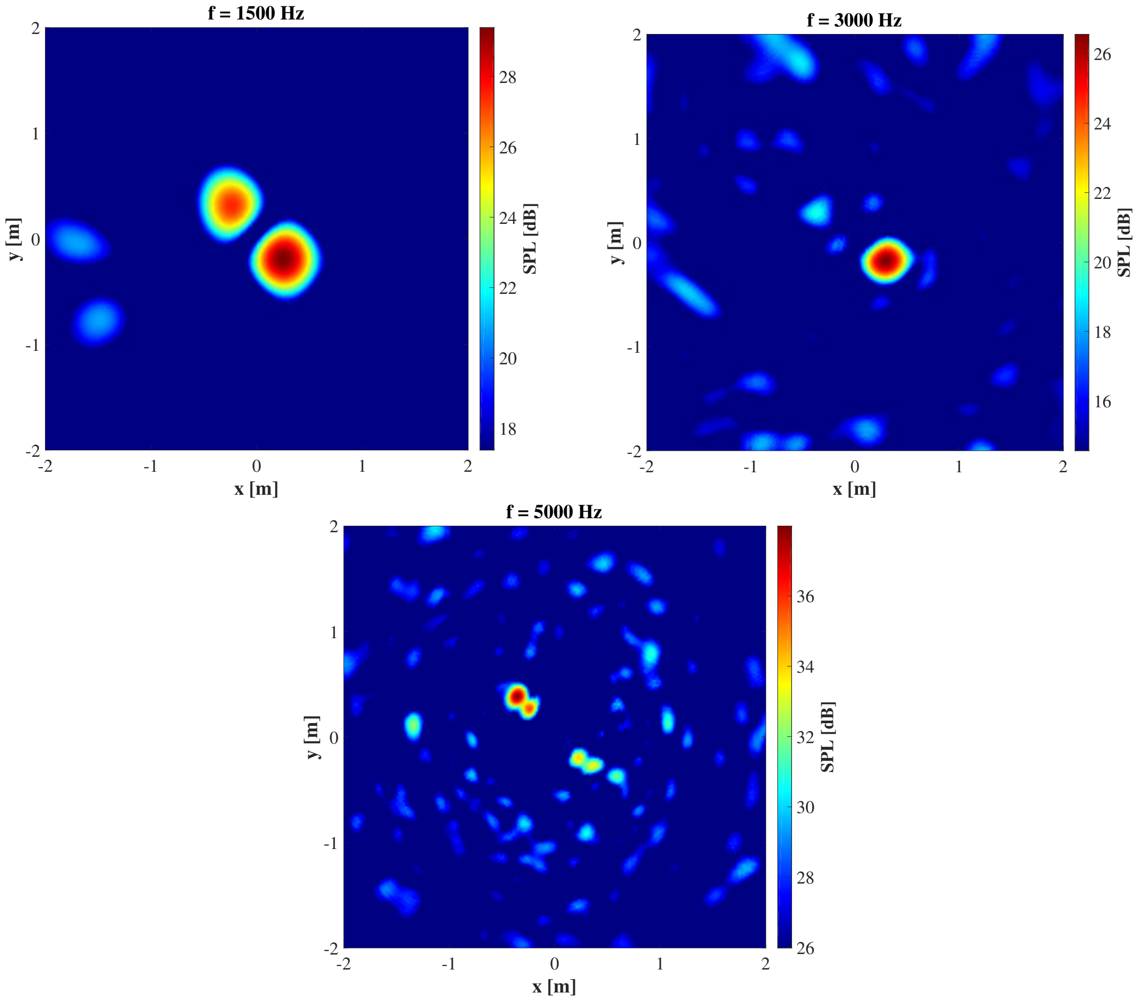

Figure A.15: ROSI applied to the four speakers rotating at 4 Hz and emitting white noise. For the filtering of the signal, three single frequencies are used: 1500 Hz, 3000 Hz and 5000 Hz. A scan grid of 4 x 4 m^2 with a total of 40000 scan points and a sampling frequency of 50 kHz are employed. The distance from the microphone array is 3 m.

Frequency [Hz]	1500				3000				5000			
Speaker numbers [-]	1	2	3	4	1	2	3	4	1	2	3	4
ROSI outputs [dB]	/	/	/	/	/	/	/	/	37.99	35.70	34.09	33.57

Table A.3: SPL values applying ROSI to the four speakers rotating at 4 Hz. The signal emitted is white noise. For the filtering of the signal, three different single frequencies are used: 1500 Hz, 3000 Hz and 5000 Hz. If the sound sources are not distinguished as separated sources, their SPLs are not taken into account.

A.3. Third set of measurements

In this set of measurements, the distance between speaker 1 and speaker 2 equals the distance between speaker 3 and speaker 4 and it corresponds to 0.33 m, while the distance between speaker 2 and speaker 3 is 0.22 m. The configuration of the four speakers is depicted in Figure A.16. Only for f = 500 Hz, f = 1000 Hz and for the frequency band 500 Hz - 2000 Hz, the resulting Rayleigh limit is above the spacing between the sources. Thus, ROSI is not able to distinguish the sources as separated. As a result, their SPLs are not taken into account. For f = 3000 Hz, the distance between speaker 2 and speaker 3 equals the Rayleigh limit at that frequency. This can lead to inaccuracy in the results.

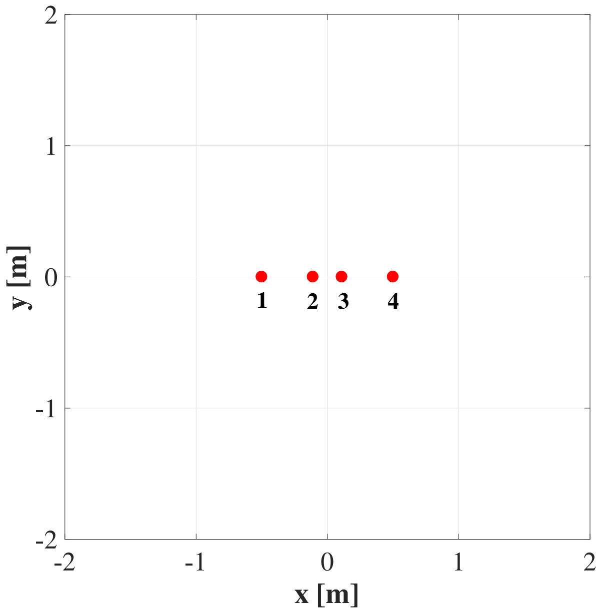

Figure A.16: Configuration of the four rotating speakers for the first setup tested in the A-Tunnel. Coordinates: sound source 1 (x,y) = (-0.5,0), sound source 2 (x,y) = (-0.11,0), sound source 3 (x,y) = (0.11,0), sound source 4 (x,y) = (0.5,0).

A.3.1. Moving case - rotational speed of 1 Hz

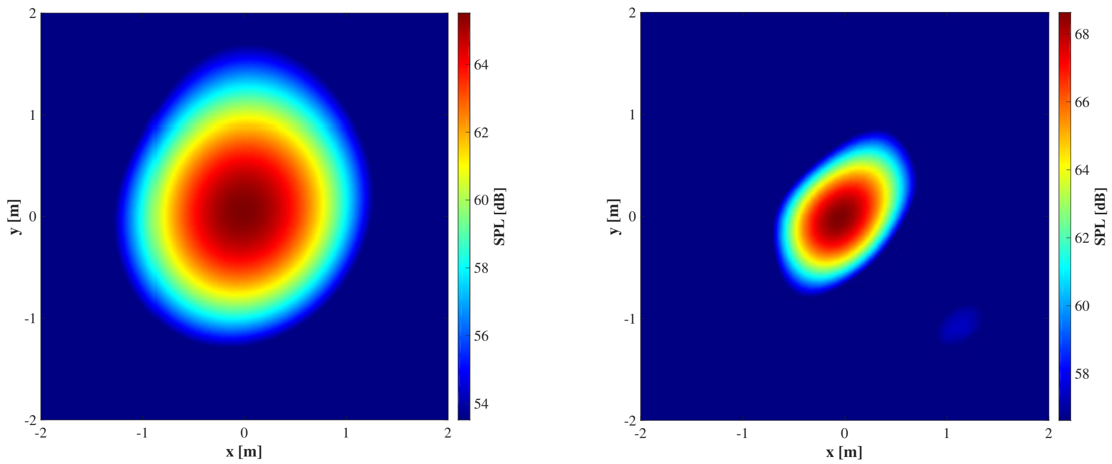

Figure A.17: ROSI applied to the four speakers rotating at 1 Hz. Left: The signal emitted is a tone at 500 Hz. Right: The signal emitted is a tone at 1000 Hz. A scan grid of 4 x 4 m^2 with a total of 40000 scan points and a sampling frequency of 50 kHz are employed. The distance from the microphone array is 3 m.

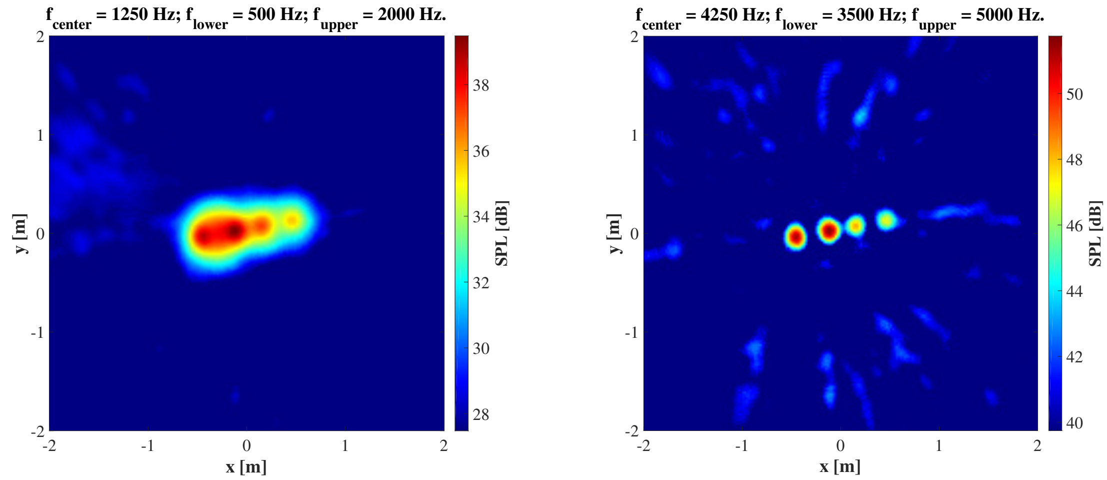

Figure A.18: ROSI applied to the four speakers rotating at 1 Hz and emitting white noise. The signal is filtered into different frequency bands: 500 Hz - 2000 Hz, 3500 Hz - 5000 Hz. A scan grid of 4 x 4 m^2 with a total of 40000 scan points and a sampling frequency of 50 kHz are employed. The distance from the microphone array is 3 m.

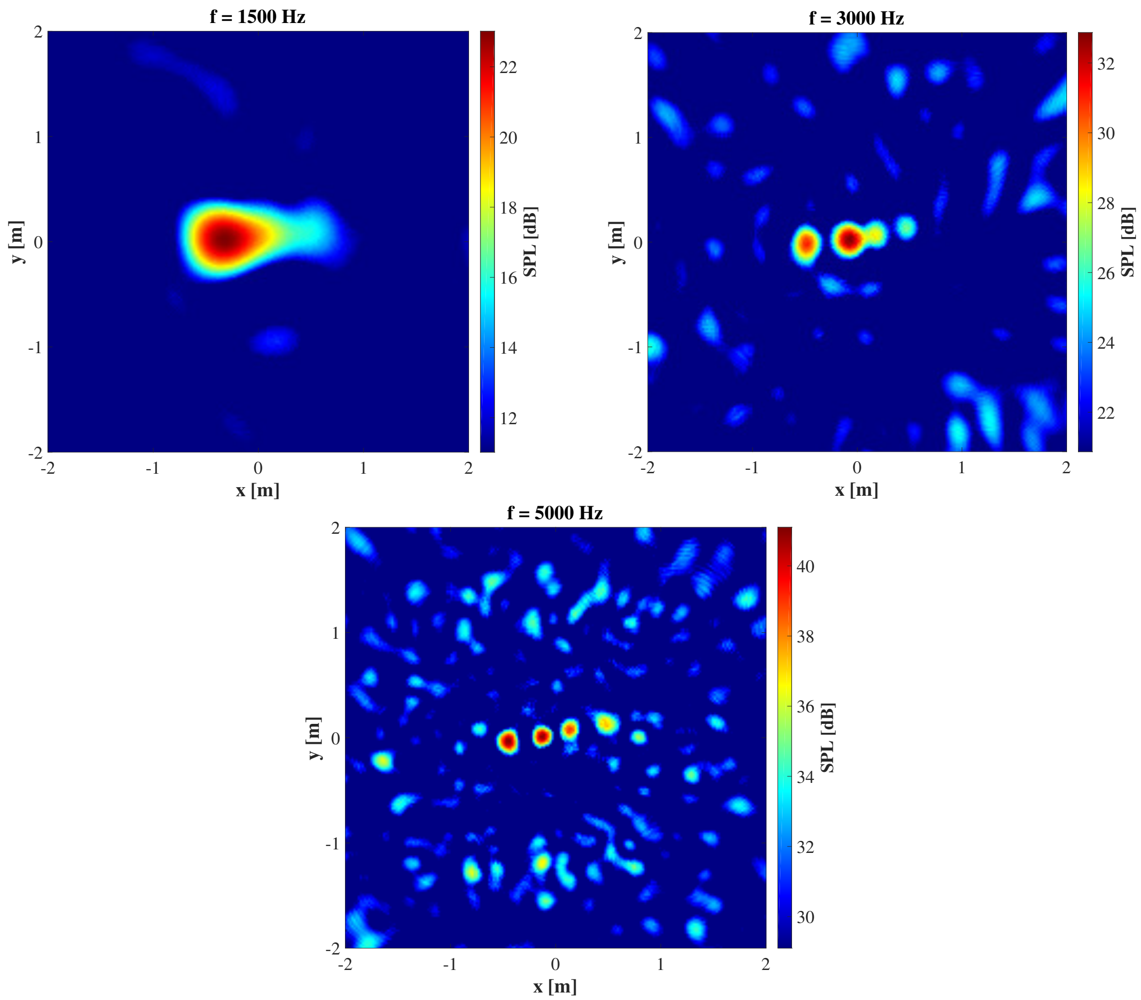

Figure A.19: ROSI applied to the four speakers rotating at 1 Hz and emitting white noise. For the filtering of the signal, three single frequencies are used: 1500 Hz, 3000 Hz and 5000 Hz. A scan grid of 4 x 4 m^2 with a total of 40000 scan points and a sampling frequency of 50 kHz are employed. The distance from the microphone array is 3 m.

Frequency bands [Hz]	500 - 2000				3500 - 5000			
Speaker numbers [-]	1	2	3	4	1	2	3	4
ROSI outputs [dB]	/	/	/	/	51.12	51.74	48.20	46.94

Table A.4: SPL values applying ROSI to the four rotating speakers. The rotational speed corresponds to 1 Hz. The signal emitted is white noise and it is filtered into different frequency bands (i.e. 500 Hz - 2000 Hz, 3500 Hz - 5000 Hz). If the sound sources are not distinguished as separated sources, their SPLs are not taken into account.

Frequency [Hz]	1500				3000				5000			
Speaker numbers [-]	1	2	3	4	1	2	3	4	1	2	3	4
ROSI outputs [dB]	/	/	/	/	30.98	/	/	/	41.10	40.99	38.97	37.49

Table A.5: SPL values applying ROSI to the four speakers rotating at 1 Hz. The signal emitted is white noise. For the filtering of the signal, three different single frequencies are used: 1500 Hz, 3000 Hz and 5000 Hz. If the sound sources are not distinguished as separated sources, their SPLs are not taken into account.

A.3.2. Moving case - rotational speed of 2.5 Hz

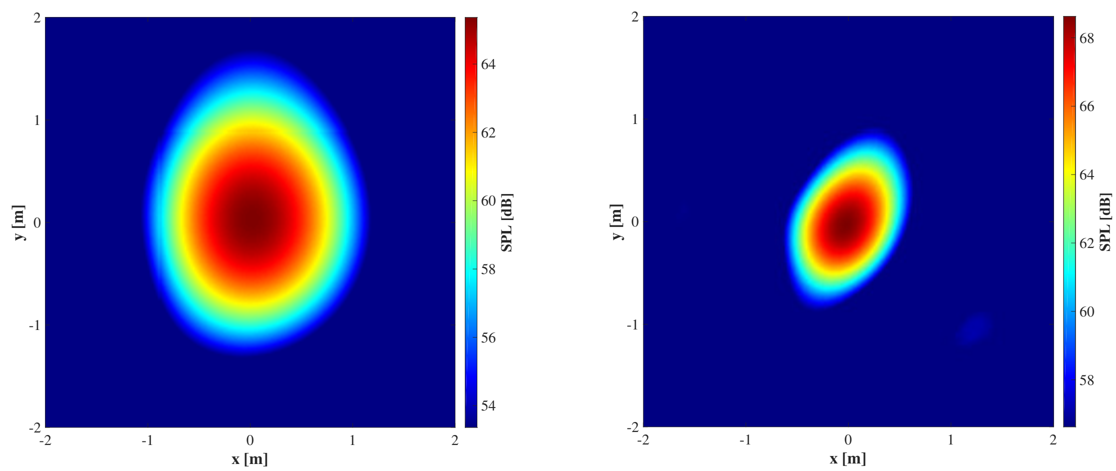

Figure A.20: ROSI applied to the four speakers rotating at 2.5 Hz. Left: The signal emitted is a tone at 500 Hz. Right: The signal emitted is a tone at 1000 Hz. A scan grid of 4 x 4 m^2 with a total of 40000 scan points and a sampling frequency of 50 kHz are employed. The distance from the microphone array is 3 m.

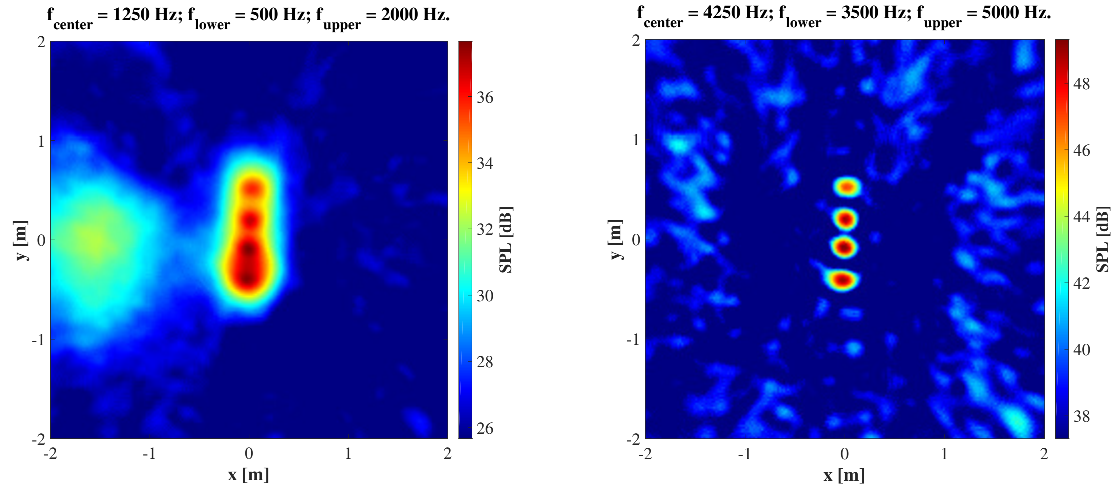

Figure A.21: ROSI applied to the four speakers rotating at 2.5 Hz and emitting white noise. The signal is filtered into different frequency bands: 500 Hz - 2000 Hz, 3500 Hz - 5000 Hz. A scan grid of 4 x 4 m^2 with a total of 40000 scan points and a sampling frequency of 50 kHz are employed. The distance from the microphone array is 3 m.

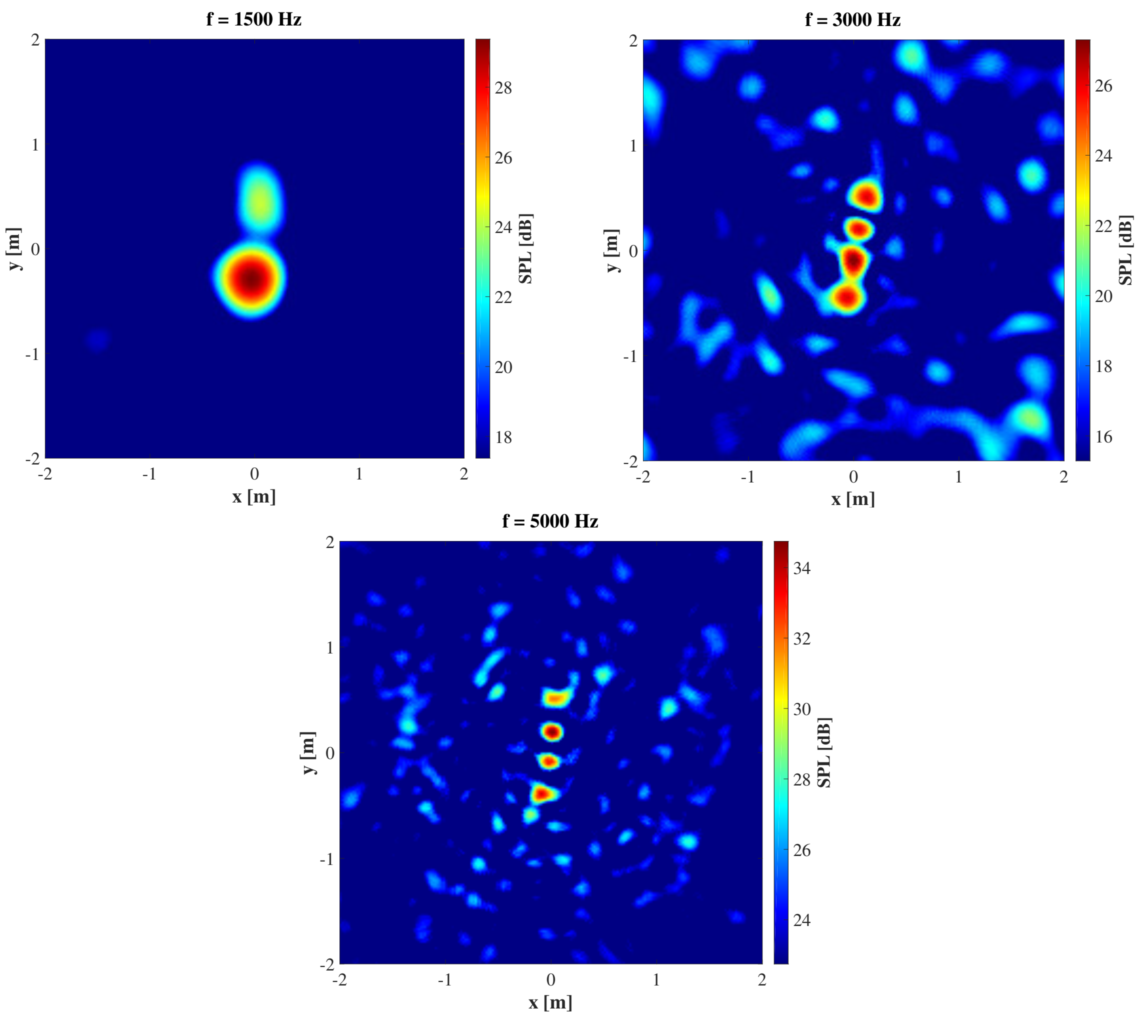

Figure A.22: ROSI applied to the four speakers rotating at 2.5 Hz and emitting white noise. For the filtering of the signal, three single frequencies are used: 1500 Hz, 3000 Hz and 5000 Hz. A scan grid of 4 x 4 m^2 with a total of 40000 scan points and a sampling frequency of 50 kHz are employed. The distance from the microphone array is 3 m.

Frequency bands [Hz]	500 - 2000				3500 - 5000			
Speaker numbers [-]	1	2	3	4	1	2	3	4
ROSI outputs [dB]	/	/	/	/	47.03	48.89	49.31	49.08

Table A.6: SPL values applying ROSI to the four rotating speakers. The rotational speed corresponds to 2.5 Hz. The signal emitted is white noise and it is filtered into different frequency bands (i.e. 500 Hz - 2000 Hz, 3500 Hz - 5000 Hz). If the sound sources are not distinguished as separated sources, their SPLs are not taken into account.

Frequency [Hz]	1500				3000				5000			
Speaker numbers [-]	1	2	3	4	1	2	3	4	1	2	3	4
ROSI outputs [dB]	/	/	/	/	26.13	26.20	27.29	26.14	31.81	34.75	33.01	33.77

Table A.7: SPL values applying ROSI to the four speakers rotating at 2.5 Hz. The signal emitted is white noise. For the filtering of the signal, three different single frequencies are used: 1500 Hz, 3000 Hz and 5000 Hz. If the sound sources are not distinguished as separated sources, their SPLs are not taken into account.

A.3.3. Moving case - rotational speed of 4 Hz

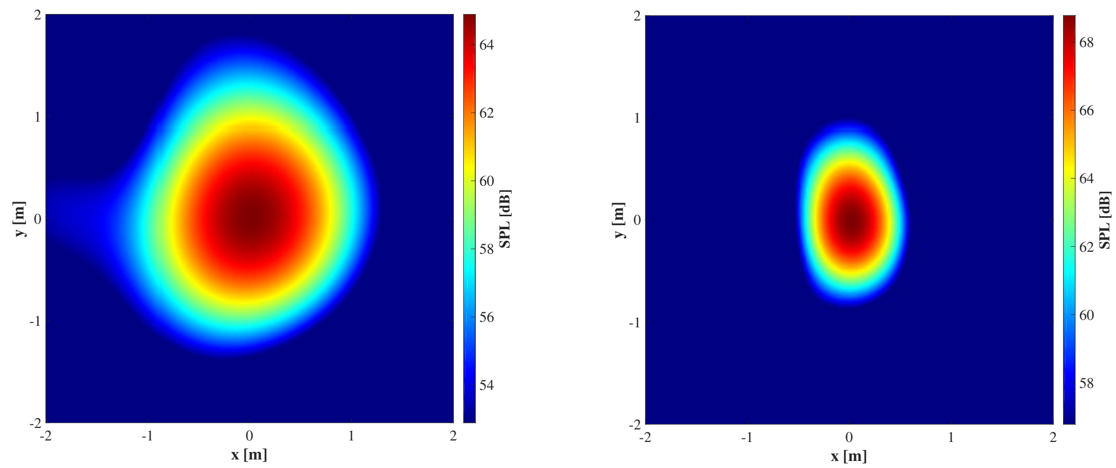

Figure A.23: ROSI applied to the four speakers rotating at 4 Hz. Left: The signal emitted is a tone at 500 Hz. Right: The signal emitted is a tone at 1000 Hz. A scan grid of 4 x 4 m^2 with a total of 40000 scan points and a sampling frequency of 50 kHz are employed. The distance from the microphone array is 3 m.

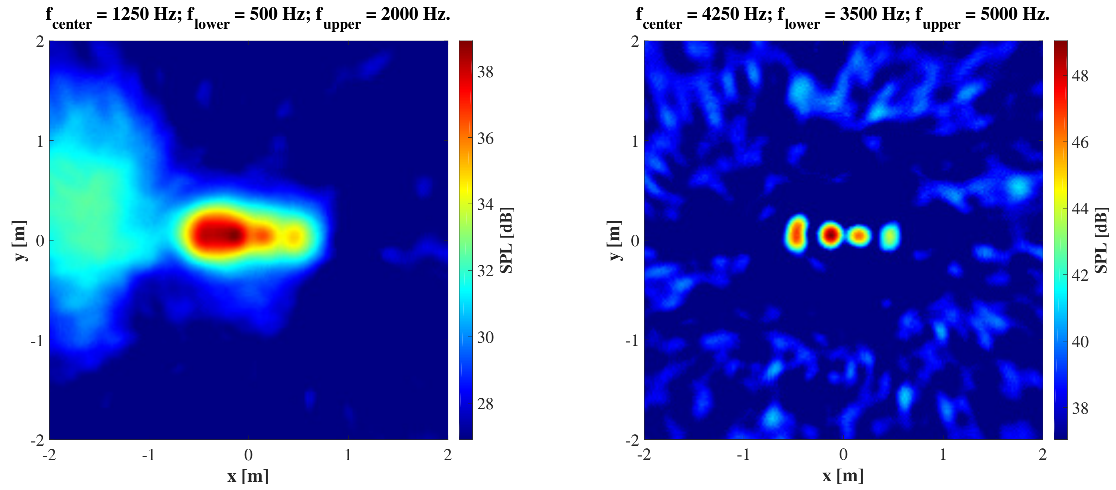

Figure A.24: ROSI applied to the four speakers rotating at 4 Hz and emitting white noise. The signal is filtered into different frequency bands: 500 Hz - 2000 Hz, 3500 Hz - 5000 Hz. A scan grid of 4 x 4 m^2 with a total of 40000 scan points and a sampling frequency of 50 kHz are employed. The distance from the microphone array is 3 m.

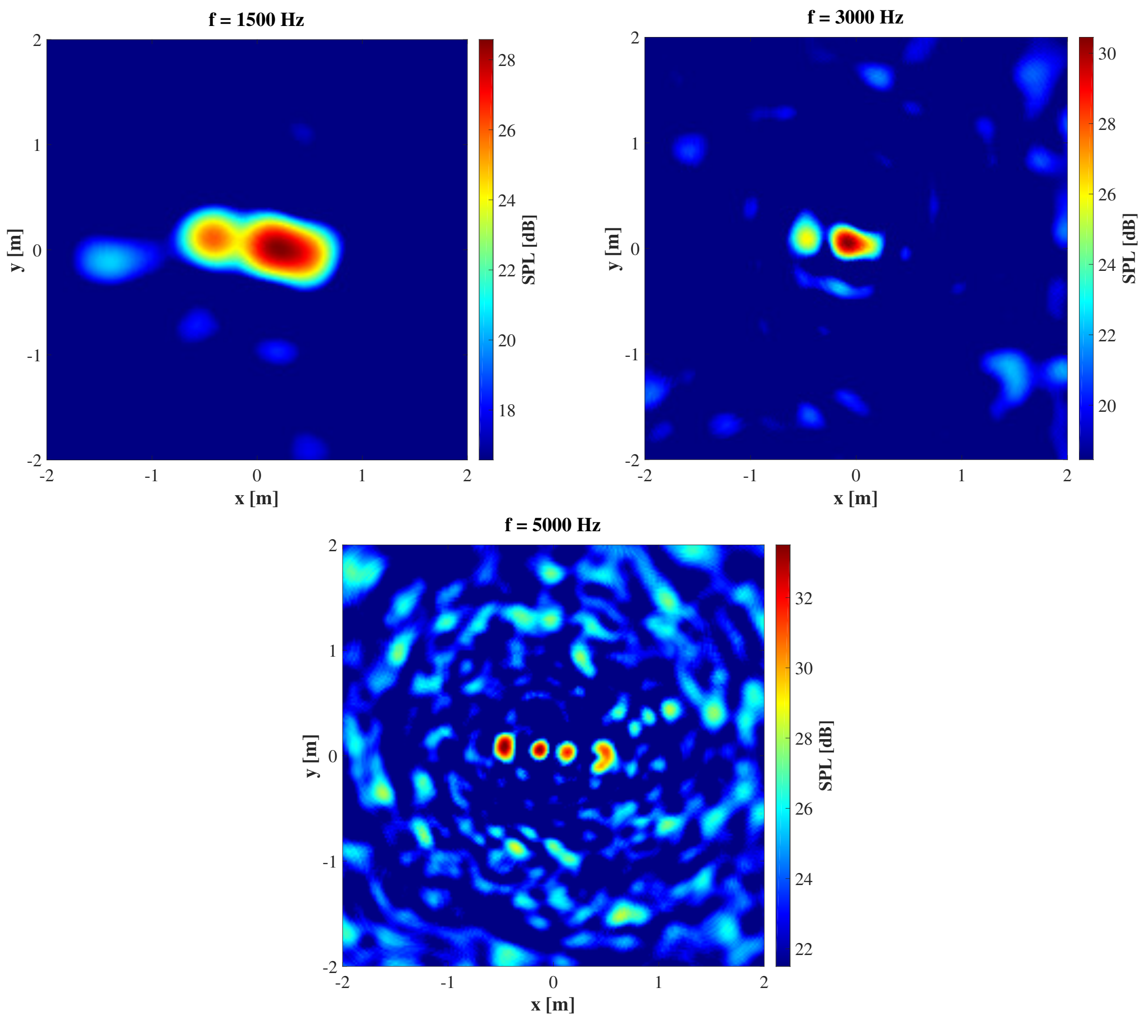

Figure A.25: ROSI applied to the four speakers rotating at 4 Hz and emitting white noise. For the filtering of the signal, three single frequencies are used: 1500 Hz, 3000 Hz and 5000 Hz. A scan grid of 4 x 4 m^2 with a total of 40000 scan points and a sampling frequency of 50 kHz are employed. The distance from the microphone array is 3 m.

Frequency bands [Hz]	500 - 2000				3500 - 5000			
Speaker numbers [-]	1	2	3	4	1	2	3	4
ROSI outputs [dB]	/	/	/	/	46.87	49.04	46.32	43.81

Table A.8: SPL values applying ROSI to the four rotating speakers. The rotational speed corresponds to 4 Hz. The signal emitted is white noise and it is filtered into different frequency bands (i.e. 500 Hz - 2000 Hz, 3500 Hz - 5000 Hz). If the sound sources are not distinguished as separated sources, their SPLs are not taken into account.

Frequency [Hz]	1500				3000				5000			
Speaker numbers [-]	1	2	3	4	1	2	3	4	1	2	3	4
ROSI outputs [dB]	/	/	/	/	/	/	/	/	33.50	33.41	31.98	31.20

Table A.9: SPL values applying ROSI to the four speakers rotating at 4 Hz. The signal emitted is white noise. For the filtering of the signal, three different single frequencies are used: 1500 Hz, 3000 Hz and 5000 Hz. If the sound sources are not distinguished as separated sources, their SPLs are not taken into account.

A.4. Fourth set of measurements

For this set of measurements, the distance between speaker 1 and speaker 2 equals the distance between speaker 3 and speaker 4 and it corresponds to 0 m, while the distance between speaker 2 and speaker 3 is 0.74 m. The configuration of the four speakers is depicted in Figure A.26. For all the tested frequencies, the resulting Rayleigh limit is above the spacing between the sources. Thus, ROSI is not able to distinguish the sources as separated and the outputs for the SPL are not taken into account.

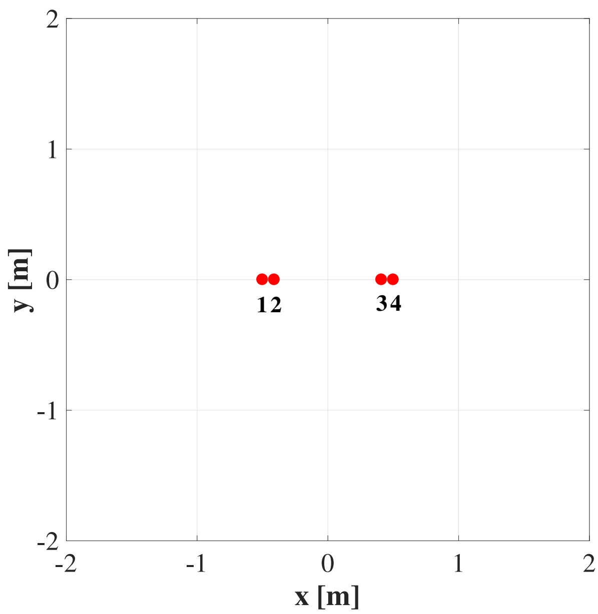

Figure A.26: Configuration of the four rotating speakers for the first setup tested in the A-Tunnel. Coordinates: sound source 1 (x,y) = (-0.5,0), sound source 2 (x,y) = (-0.45,0), sound source 3 (x,y) = (0.45,0), sound source 4 (x,y) = (0.5,0).

A.4.1. Moving case - rotational speed of 1 Hz

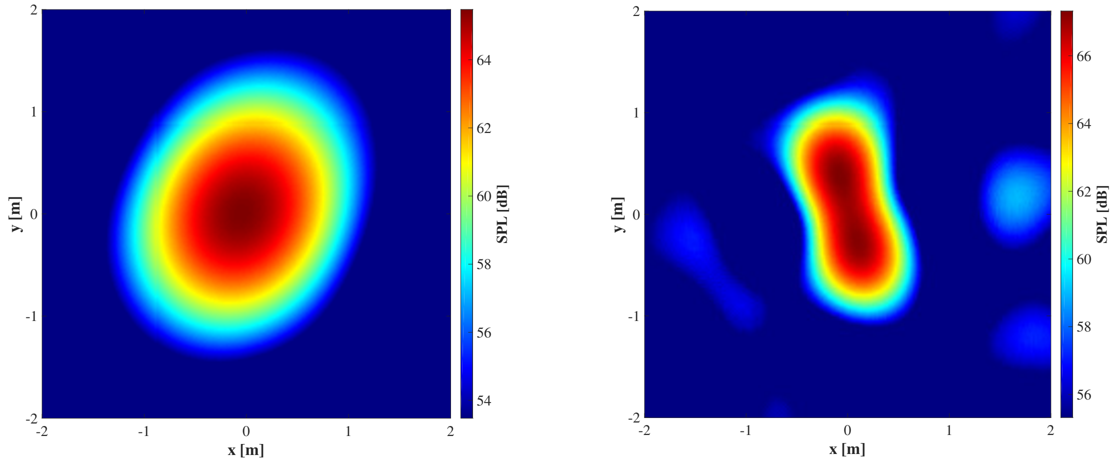

Figure A.27: ROSI applied to the four speakers rotating at 1 Hz. Left: The signal emitted is a tone at 500 Hz. Right: The signal emitted is a tone at 1000 Hz. A scan grid of 4 x 4 m^2 with a total of 40000 scan points and a sampling frequency of 50 kHz are employed. The distance from the microphone array is 3 m.

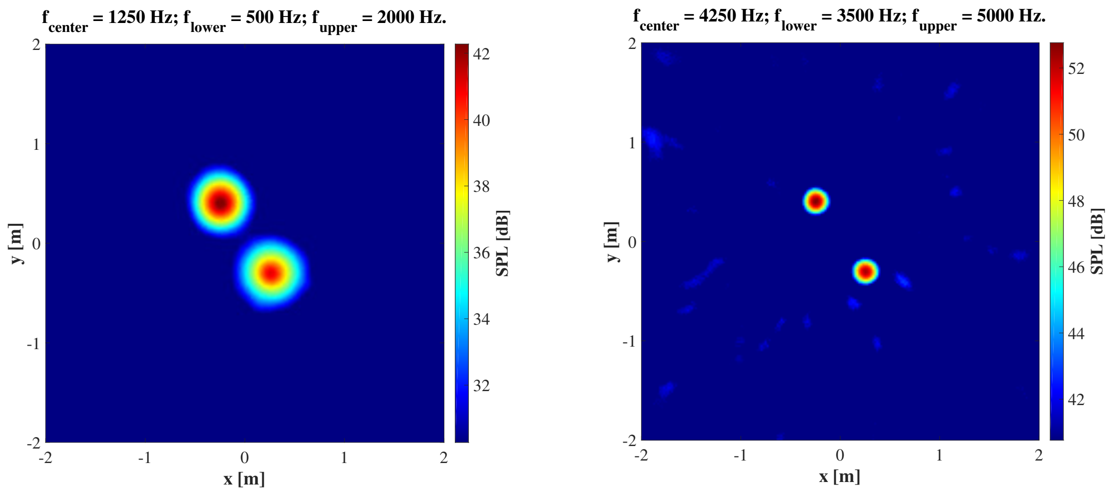

Figure A.28: ROSI applied to the four speakers rotating at 1 Hz and emitting white noise. The signal is filtered into different frequency bands: 500 Hz - 2000 Hz, 3500 Hz - 5000 Hz. A scan grid of 4 x 4 m^2 with a total of 40000 scan points and a sampling frequency of 50 kHz are employed. The distance from the microphone array is 3 m.

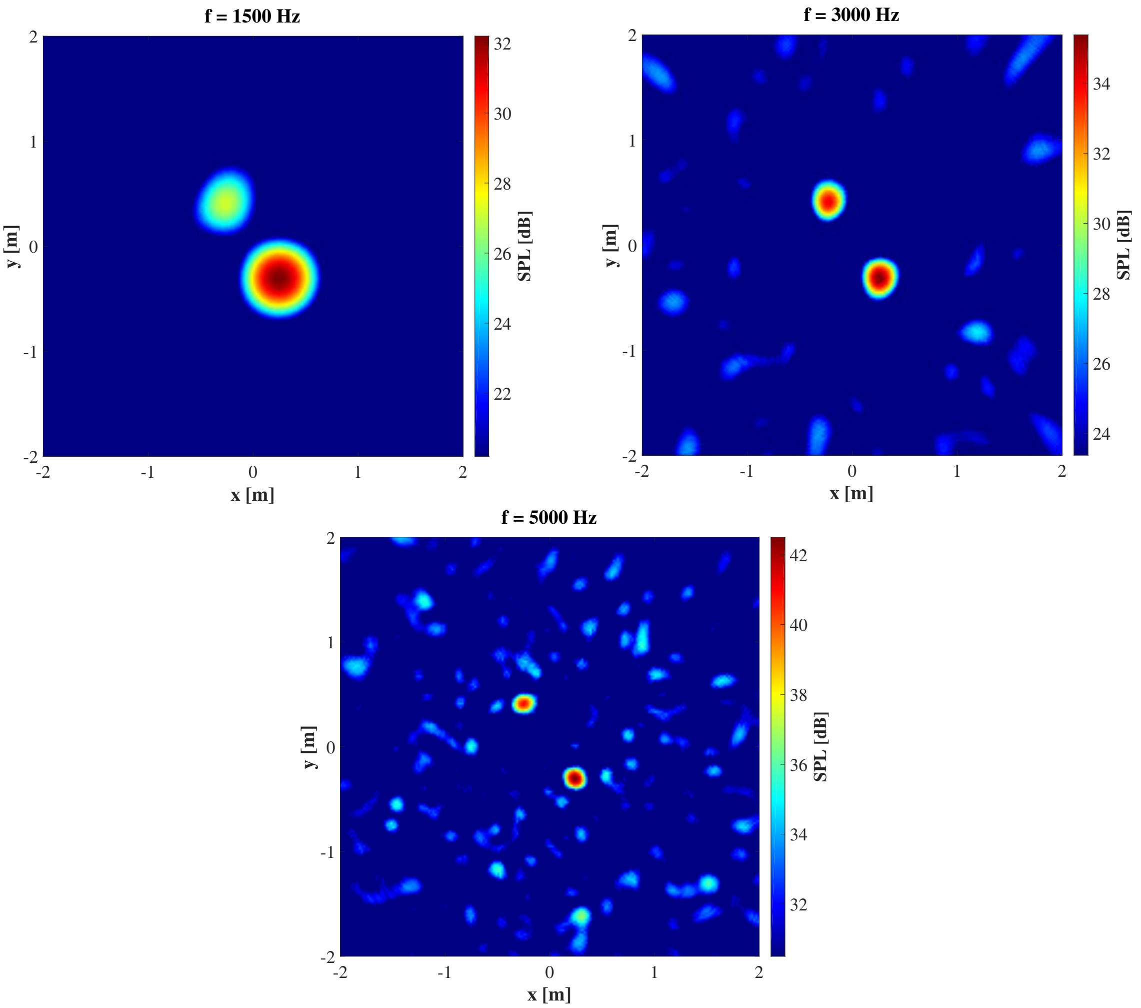

Figure A.29: ROSI applied to the four speakers rotating at 1 Hz and emitting white noise. For the filtering of the signal, three single frequencies are used: 1500 Hz, 3000 Hz and 5000 Hz. A scan grid of 4 x 4 m^2 with a total of 40000 scan points and a sampling frequency of 50 kHz are employed. The distance from the microphone array is 3 m.

A.4.2. Moving case - rotational speed of 2.5 Hz

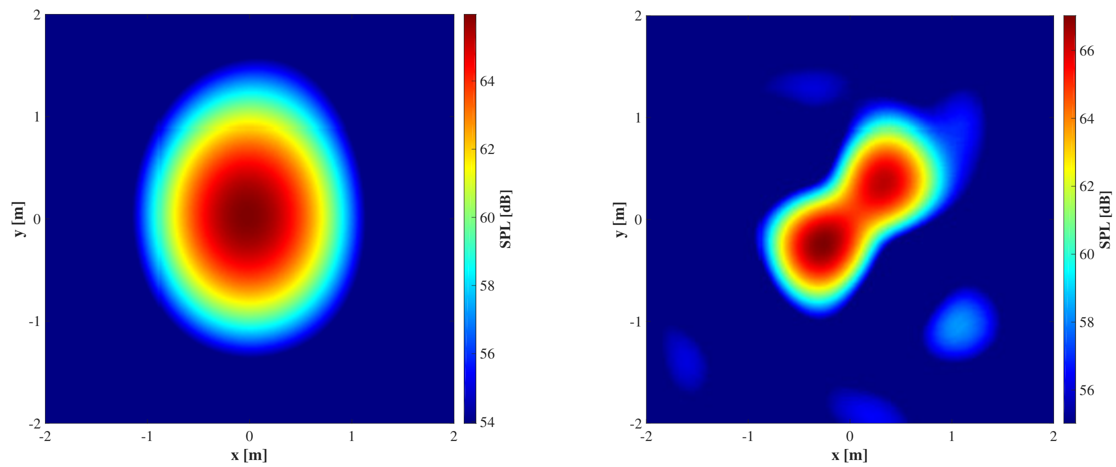

Figure A.30: ROSI applied to the four speakers rotating at 2.5 Hz. Left: The signal emitted is a tone at 500 Hz. Right: The signal emitted is a tone at 1000 Hz. A scan grid of 4 x 4 m^2 with a total of 40000 scan points and a sampling frequency of 50 kHz are employed. The distance from the microphone array is 3 m.

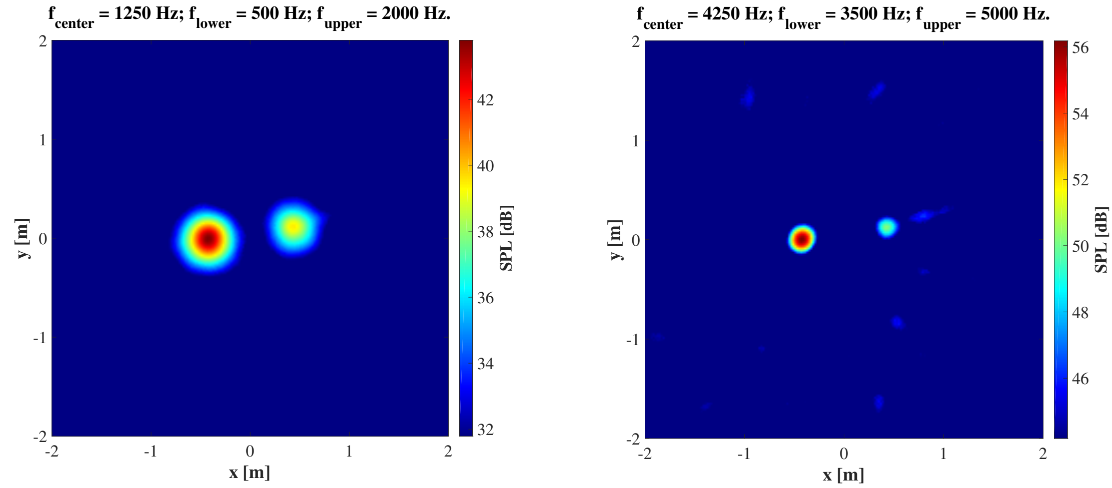

Figure A.31: ROSI applied to the four speakers rotating at 2.5 Hz and emitting white noise. The signal is filtered into different frequency bands: 500 Hz - 2000 Hz, 3500 Hz - 5000 Hz. A scan grid of 4 x 4 m^2 with a total of 40000 scan points and a sampling frequency of 50 kHz are employed. The distance from the microphone array is 3 m.

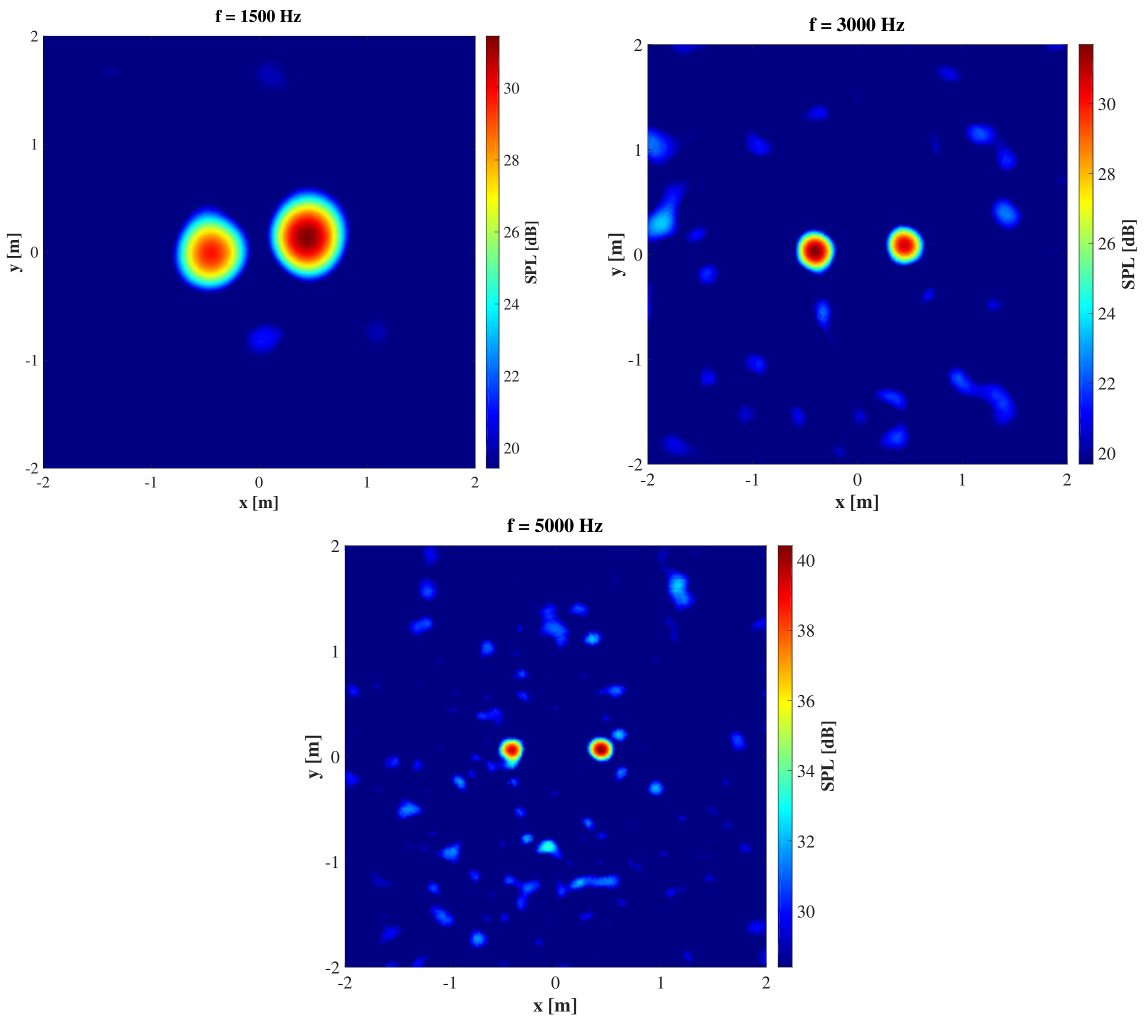

Figure A.32: ROSI applied to the four speakers rotating at 2.5 Hz and emitting white noise. For the filtering of the signal, three single frequencies are used: 1500 Hz, 3000 Hz and 5000 Hz. A scan grid of 4 x 4 m^2 with a total of 40000 scan points and a sampling frequency of 50 kHz are employed. The distance from the microphone array is 3 m.

A.4.3. Moving case - rotational speed of 4 Hz

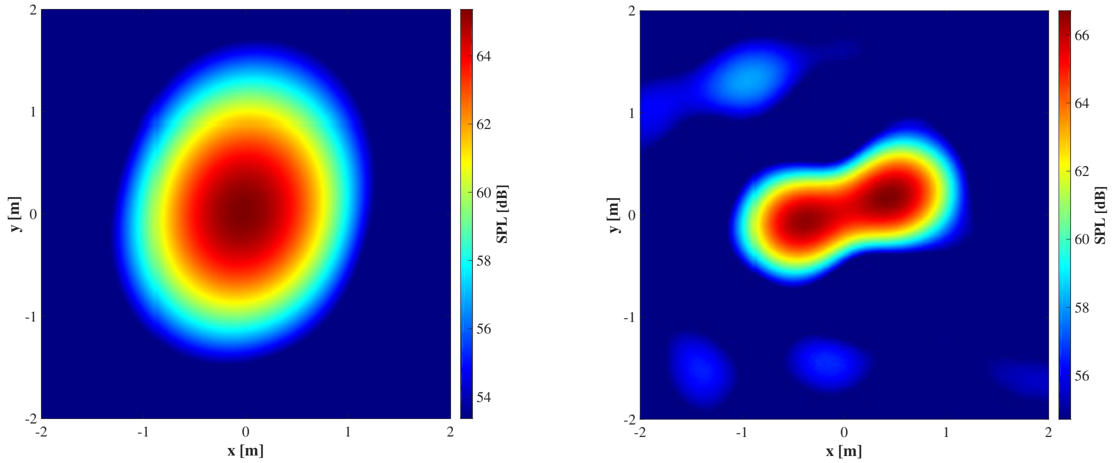

Figure A.33: ROSI applied to the four speakers rotating at 4 Hz. Left: The signal emitted is a tone at 500 Hz. Right: The signal emitted is a tone at 1000 Hz. A scan grid of 4 x 4 m^2 with a total of 40000 scan points and a sampling frequency of 50 kHz are employed. The distance from the microphone array is 3 m.

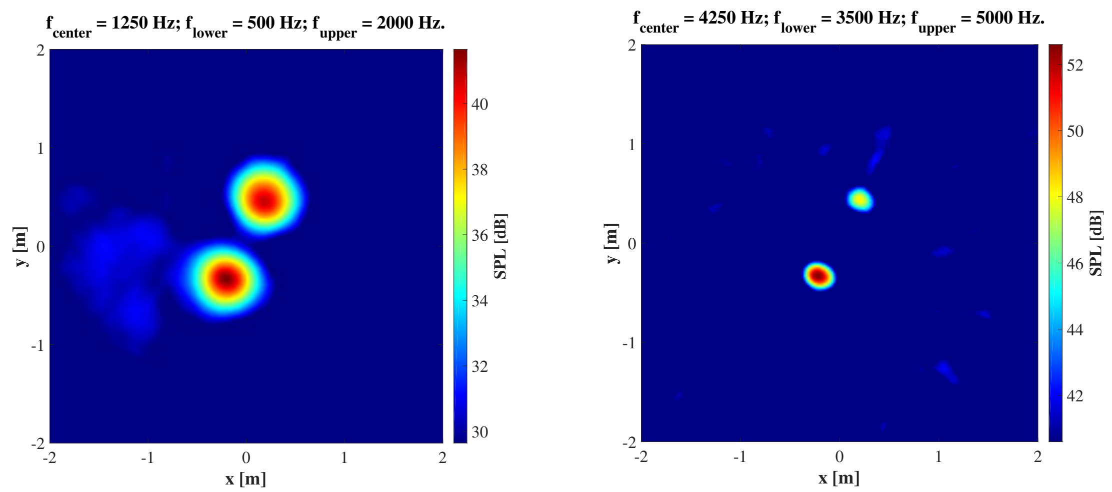

Figure A.34: ROSI applied to the four speakers rotating at 4 Hz and emitting white noise. The signal is filtered into different frequency bands: 500 Hz - 2000 Hz, 3500 Hz - 5000 Hz. A scan grid of 4 x 4 m^2 with a total of 40000 scan points and a sampling frequency of 50 kHz are employed. The distance from the microphone array is 3 m.

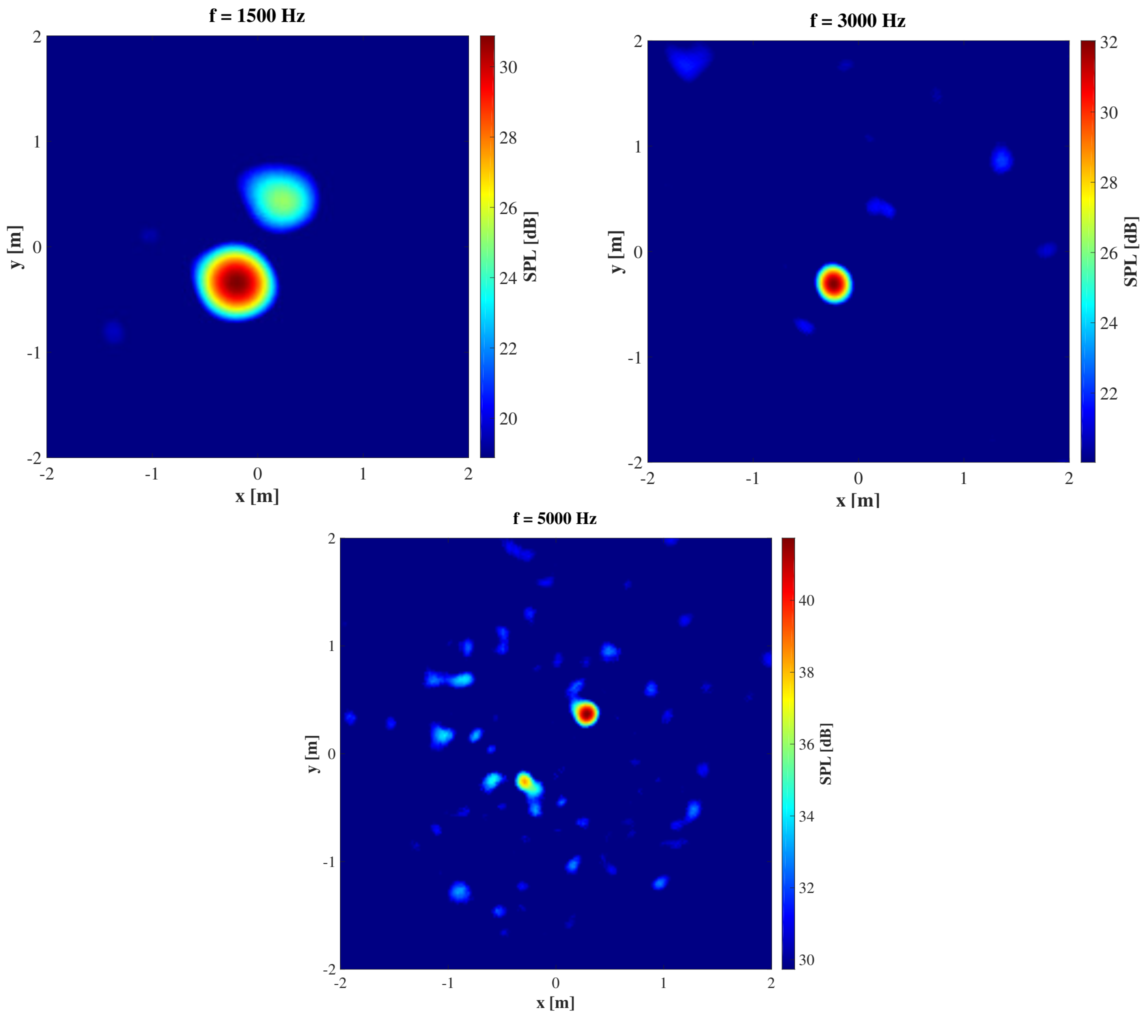

Figure A.35: ROSI applied to the four speakers rotating at 4 Hz and emitting white noise. For the filtering of the signal, three single frequencies are used: 1500 Hz, 3000 Hz and 5000 Hz. A scan grid of 4 x 4 m^2 with a total of 40000 scan points and a sampling frequency of 50 kHz are employed. The distance from the microphone array is 3 m.

B

OJF experiment - further analysis

In this Chapter, other experimental data recorded in the OJF are presented to confirm that the high levels of background noise of the facility do not allow the assessment of the wind turbine noise.

In the analysis, a sampling frequency of 50 kHz and a scan grid of 4 x 4 m^2 with a total of 40000 scan points[1] are employed. The distance between the center of rotation and the microphone array corresponds to 3 m. The measured data is separated in time blocks of 25000 samples (Δt = 500 ms) and windowed using a Hanning weighting function. Following the same steps performed in the A-Tunnel experiment, the data has been evaluated with three beamforming algorithms: CB in the time domain, CB in the frequency domain and ROSI. In this way, it is possible to check if the center of rotation of the wind turbine is in the correct position.

First, the background noise at a wind speed of 5 m/s, 7 m/s and 9 m/s is evaluated, when only the tower, the nacelle and the tail fin of the DOD upwind turbine are installed. The rotor is not mounted and the wind turbine is not in operation. This configuration is illustrated in Figure 5.10 in Chapter 5. CB in the time domain as well as CB in the frequency domain are applied to this dataset. Then, the small wind turbine is tested with different blades and at different wind speeds of the tunnel. For each case, a comparison between the PSD of the background noise and the PSD of the wind turbine is provided together with the acoustic images obtained applying CB in time domain, CB in the frequency domain and ROSI. The resulting source plots are very similar and the reader will recognize how the high levels of background noise do not allow to localize and to quantify the main noise sources in the small wind turbine.

[1]200 scan points are used in the x and in the y direction, which lead to a total of 40000 scan points.

B.1. Wind speed - 5 m/s

In this section, the wind speed of the tunnel is set at 5 m/s. First, the background noise of the facility is evaluated with only the tower, the nacelle and the tail fin of the wind turbine installed. Follows the analysis of the DOD upwind turbine with four different blade configurations.

B.1.1. OJF background noise

For this set of measurement, the wind turbine was not in operation. Figure B.1, Figure B.2 and Figure B.3 present the resulting acoustic images when CB in the time domain and CB in the frequency domain are applied to the experimental data. The signal is filtered into three different frequency bands: 500 Hz - 2000 Hz, 500 Hz - 1000 Hz and 700 Hz - 1000 Hz. As it can be observed, only for the frequency band 500 Hz - 2000 Hz the beamforming algorithms are not able to localize the nacelle. For the other cases, the interaction between the wind and the nacelle results the most dominant noise source and the nacelle can be recognized in the center of the source map.

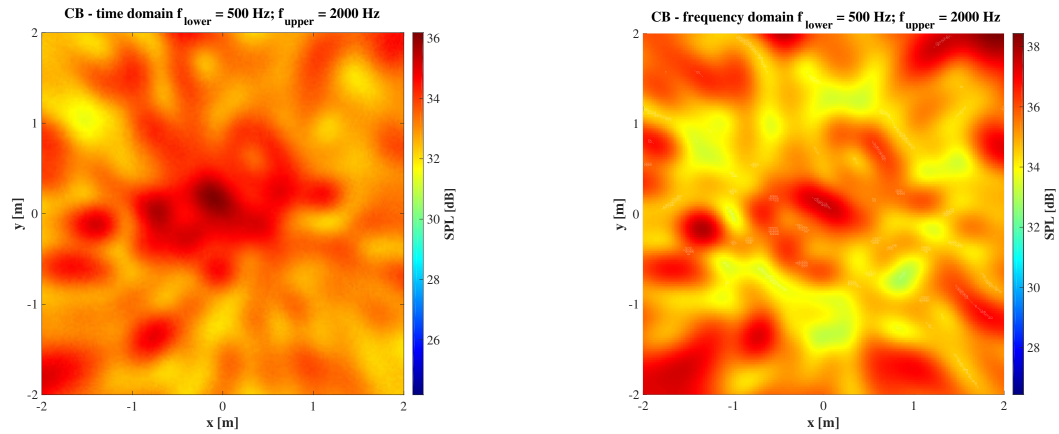

Figure B.1: Left: CB in the time domain. Right: CB in the frequency domain. The signal is filtered into the frequency band: 500 Hz - 2000 Hz. A scan grid of 4x4 m^2 with a total of 40000 scan points and a sampling frequency of 50 kHz are employed. The distance from the microphone array is 3 m.

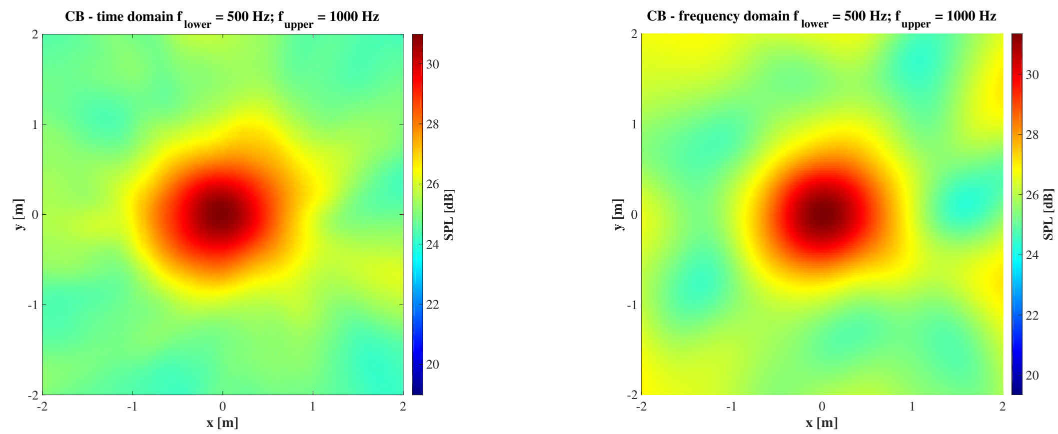

Figure B.2: Left: CB in the time domain. Right: CB in the frequency domain. The signal is filtered into the frequency band: 500 Hz - 1000 Hz. A scan grid of 4x4 m^2 with a total of 40000 scan points and a sampling frequency of 50 kHz are employed. The distance from the microphone array is 3 m.

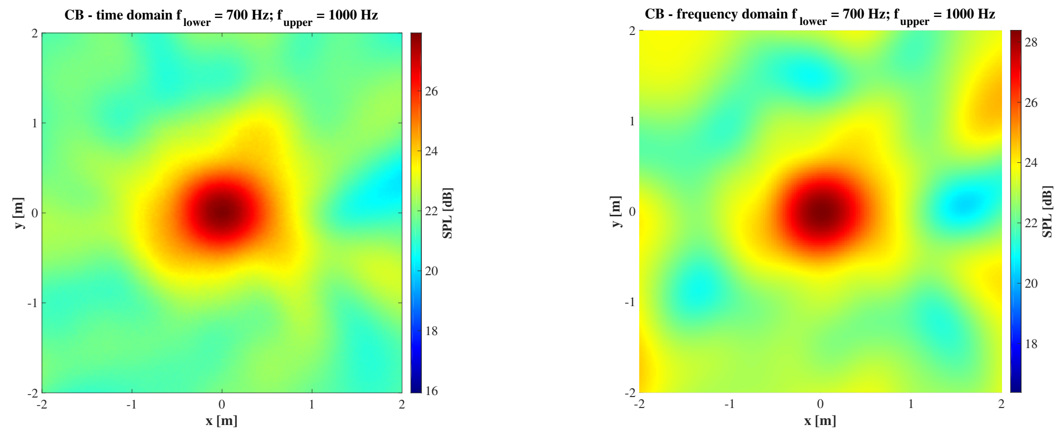

Figure B.3: Left: CB in the time domain. Right: CB in the frequency domain. The signal is filtered into the frequency band: 700 Hz - 1000 Hz. A scan grid of 4x4 m^2 with a total of 40000 scan points and a sampling frequency of 50 kHz are employed. The distance from the microphone array is 3 m.

B.1.2. Three bladed wind turbine

The DOD upwind turbine is tested with three blades. The corresponding rotor diameter is 1.66 m. The yaw angle is set at 0 degree. The wind speed of the tunnel is 5 m/s and the rotational speed of the turbine is 5.4 Hz, which leads to a blade passing frequency (BPF) of 16.2 Hz. The measured power output amounts to 55 W.

Figure B.4 illustrates the PSD of the OJF background noise at 5 m/s, when the tower, the nacelle and the tail fin of the wind turbine are installed, and the PSD of the three-bladed turbine. Between 500 Hz and 2000 Hz, the two curves almost coincide. However, a difference can be observed between 700 Hz and 1000 Hz. By filtering the signal into these two frequency bands, CB in time domain, CB in the frequency domain and ROSI are applied. The resulting acoustic images are depicted in Figure B.5 and in Figure B.6. From the source maps, it is not possible to distinguish the three blades of the turbine. The source localization as well as the source quantification of the small wind turbine are compromised by the high levels of background noise.

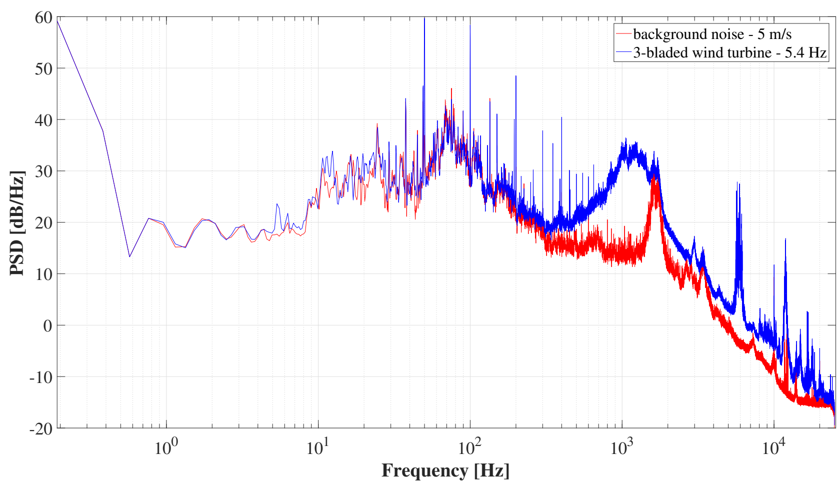

Figure B.4: Comparison between the PSD of the OJF background noise at 5 m/s (in red) and the PSD of the three-bladed wind turbine (in blue). The measurements for the OJF background noise were carried out with only the tower, the nacelle and the tail fin of the wind turbine installed. The three-bladed wind turbine has a rotational speed of 5.4 Hz. The blade passing frequency is 16.2 Hz. The measured power output amounts to 55 W.

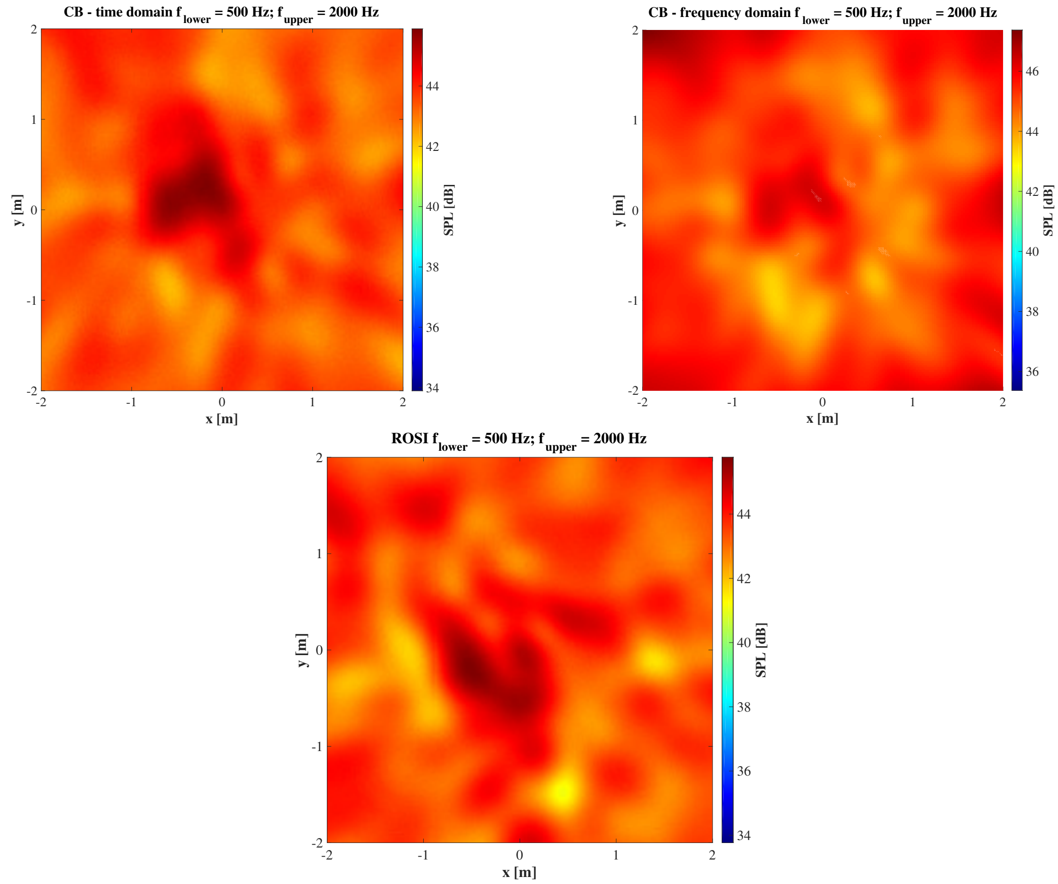

Figure B.5: Left: CB in the time domain. Right: CB in the frequency domain. Center: ROSI. The three-bladed wind turbine rotates at 5.4 Hz. The wind speed of the tunnel is 5 m/s. The signal is filtered into the frequency band 500 Hz - 2000 Hz. A scan grid of 4x4 m^2 with a total of 40000 scan points and a sampling frequency of 50 kHz are employed. The distance from the microphone array is 3 m.

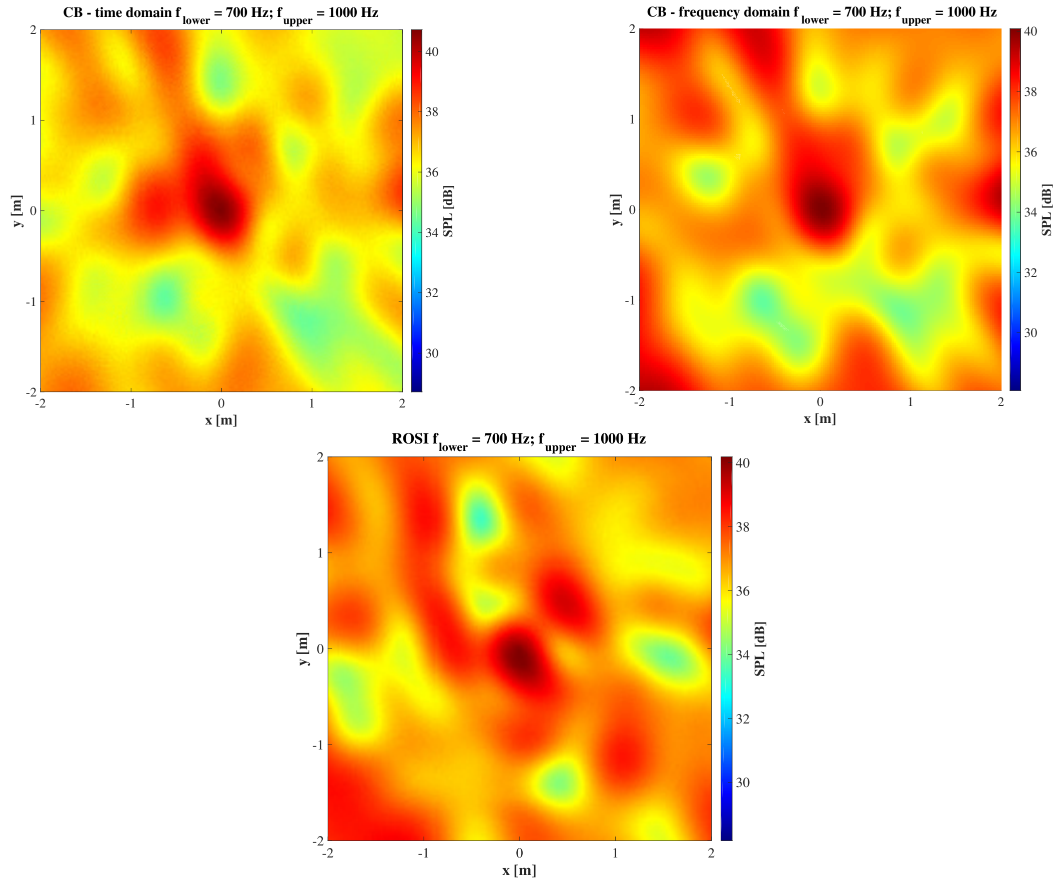

Figure B.6: Left: CB in the time domain. Right: CB in the frequency domain. Center: ROSI. The three-bladed wind turbine rotates at 5.4 Hz. The wind speed of the tunnel is 5 m/s. The signal is filtered into the frequency band 700 Hz - 1000 Hz. A scan grid of 4x4 m^2 with a total of 40000 scan points and a sampling frequency of 50 kHz are employed. The distance from the microphone array is 3 m.

B.1.3. Five bladed wind turbine - 1

The DOD upwind turbine is tested with five blades. The corresponding rotor diameter is 1.72 m. The yaw angle is set at 0 degree. The wind speed of the tunnel is 5 m/s and the rotational speed of the turbine is 5.8 Hz, which leads to a blade passing frequency (BPF) of 29 Hz. The measured power output amounts to 55 W.

Figure B.7 illustrates the PSD of the OJF background noise at 5 m/s, when the tower, the nacelle and the tail fin of the wind turbine are installed, and the PSD of the five-bladed turbine. Between 500 Hz and 2000 Hz, the two curves almost coincide. However, a small difference can be observed between 500 Hz and 1000 Hz. By filtering the signal into these two frequency bands, CB in time domain, CB in the frequency domain and ROSI are applied. The resulting acoustic images are depicted in Figure B.8 and in Figure B.9. From the source maps, it is not possible to distinguish the five blades of the turbine. The source localization as well as the source quantification of the small wind turbine are compromised by the high levels of background noise.

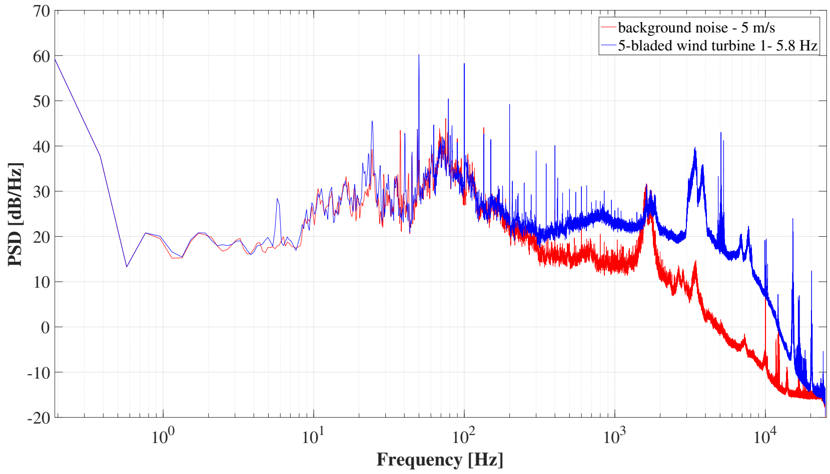

Figure B.7: Comparison between the PSD of the OJF background noise at 5 m/s (in red) and the PSD of the five-bladed wind turbine (in blue). The measurements for the OJF background noise were carried out with only the tower, the nacelle and the tail fin of the wind turbine installed. The five-bladed wind turbine has a rotational speed of 5.8 Hz. The blade passing frequency is 29 Hz. The measured power output amounts to 55 W.

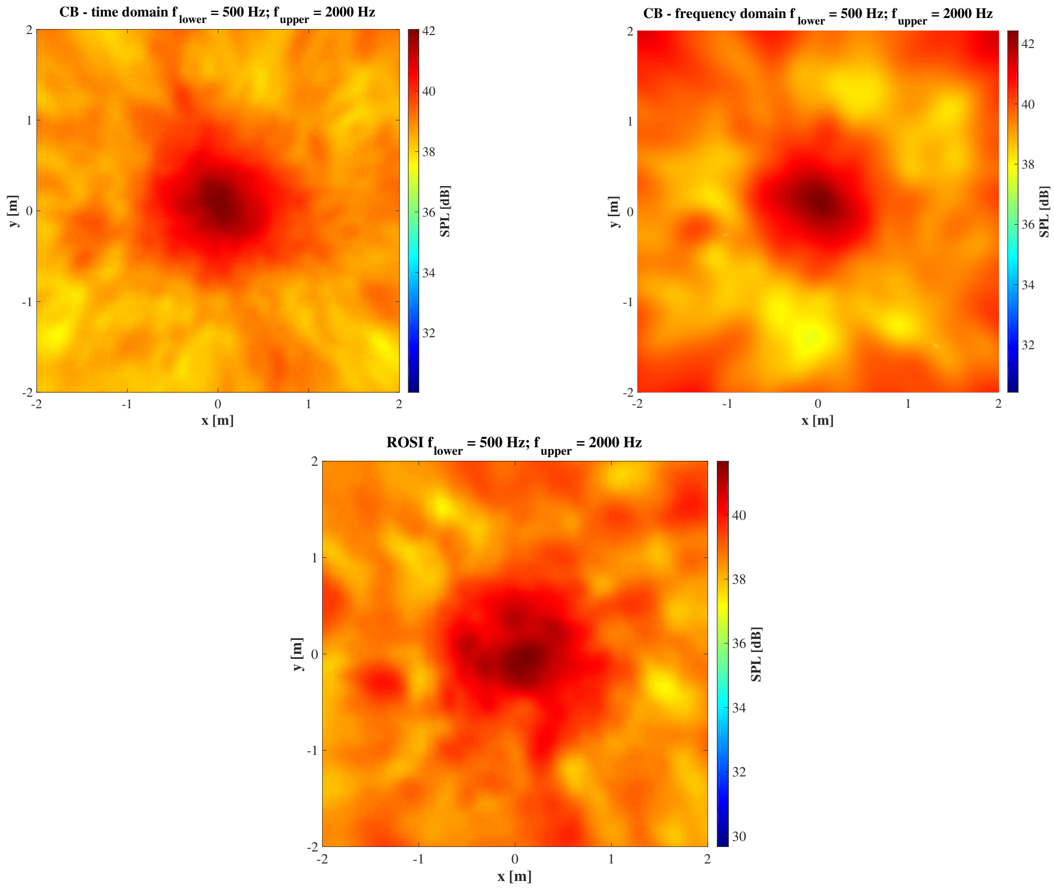

Figure B.8: Left: CB in the time domain. Right: CB in the frequency domain. Center: ROSI. The five-bladed wind turbine rotates at 5.8 Hz. The wind speed of the tunnel is 5 m/s. The signal is filtered into the frequency band 500 Hz - 2000 Hz. A scan grid of 4x4 m^2 with a total of 40000 scan points and a sampling frequency of 50 kHz are employed. The distance from the microphone array is 3 m.

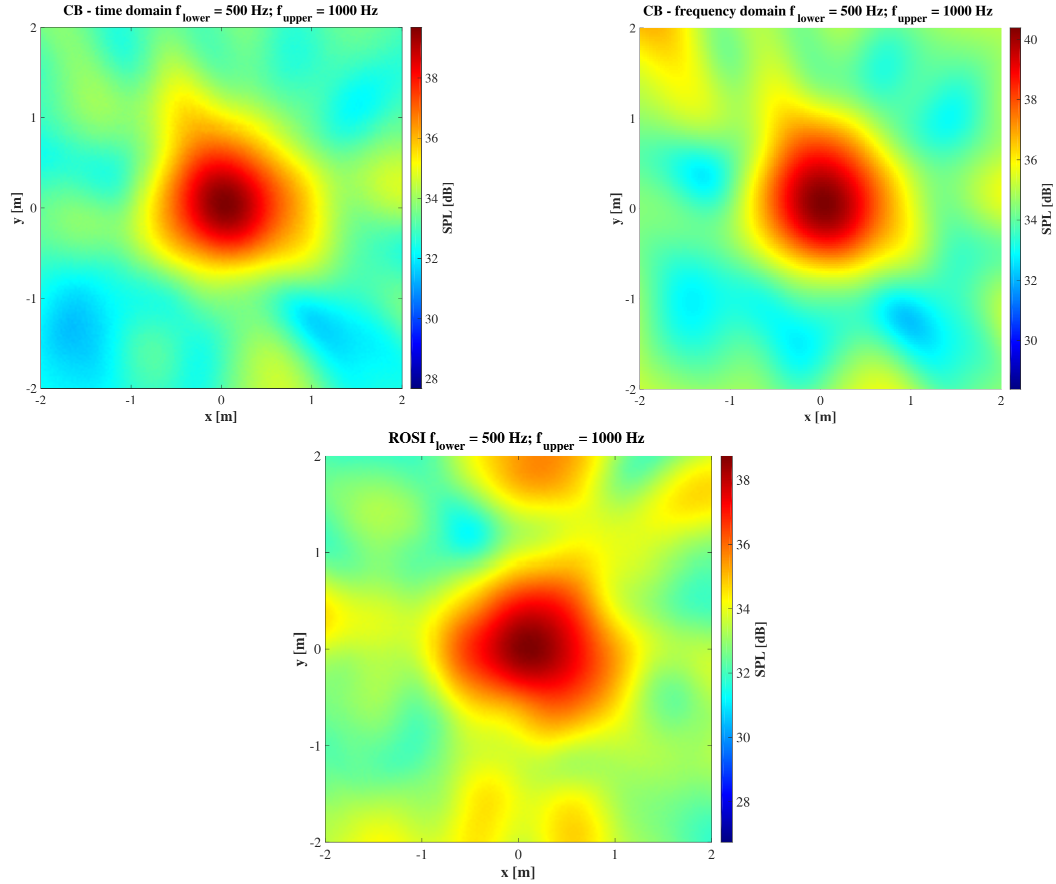

Figure B.9: Left: CB in the time domain. Right: CB in the frequency domain. Center: ROSI. The five-bladed wind turbine rotates at 5.8 Hz. The wind speed of the tunnel is 5 m/s. The signal is filtered into the frequency band 500 Hz - 2000 Hz. A scan grid of 4x4 m^2 with a total of 40000 scan points and a sampling frequency of 50 kHz are employed. The distance from the microphone array is 3 m.

B.1.4. Five bladed wind turbine - 2

The DOD upwind turbine is tested with five blades. The corresponding rotor diameter is 1.71 m. The yaw angle is set at 0 degree. The wind speed of the tunnel is 5 m/s and the rotational speed of the turbine is 5.9 Hz, which leads to a blade passing frequency (BPF) of 29.6 Hz. The measured power output amounts to 55 W.

Figure B.10 illustrates the PSD of the OJF background noise at 5 m/s, when the tower, the nacelle and the tail fin of the wind turbine are installed, and the PSD of the five-bladed turbine. Between 500 Hz and 2000 Hz, the two curves almost coincide. However, a small difference can be recognized between 500 Hz and 1000 Hz. By filtering the signal into these two frequency bands, CB in time domain, CB in the frequency domain and ROSI are applied. The resulting acoustic images are depicted in Figure B.11 and in Figure B.12. From the source maps, it is not possible to distinguish the five blades of the turbine. The source localization as well as the source quantification of the small wind turbine are compromised by the high levels of background noise.

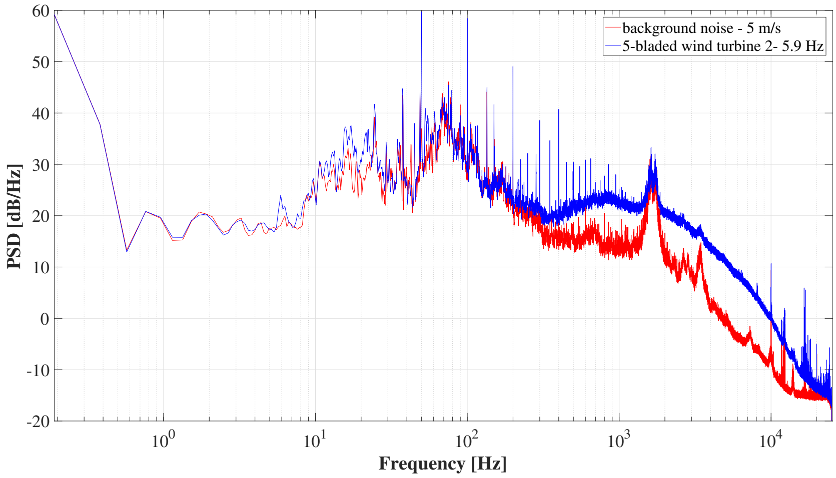

Figure B.10: Comparison between the PSD of the OJF background noise at 5 m/s (in red) and the PSD of the five-bladed wind turbine (in blue). The measurements for the OJF background noise were carried out with only the tower, the nacelle and the tail fin of the wind turbine installed. The five-bladed wind turbine has a rotational speed of 5.9 Hz. The blade passing frequency is 29.6 Hz. The measured power output amounts to 55 W.

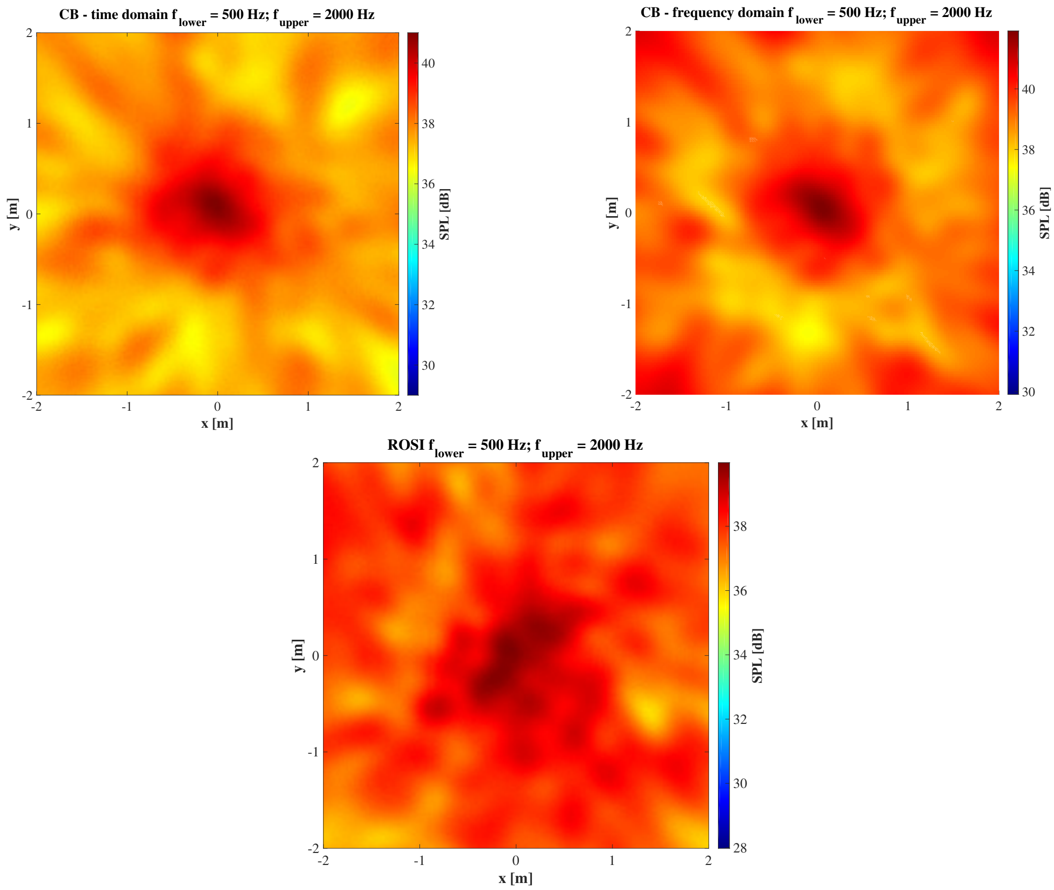

Figure B.11: Left: CB in the time domain. Right: CB in the frequency domain. Center: ROSI. The five-bladed wind turbine rotates at 5.9 Hz. The wind speed of the tunnel is 5 m/s. The signal is filtered into the frequency band 500 Hz - 2000 Hz. A scan grid of 4x4 m^2 with a total of 40000 scan points and a sampling frequency of 50 kHz are employed. The distance from the microphone array is 3 m.

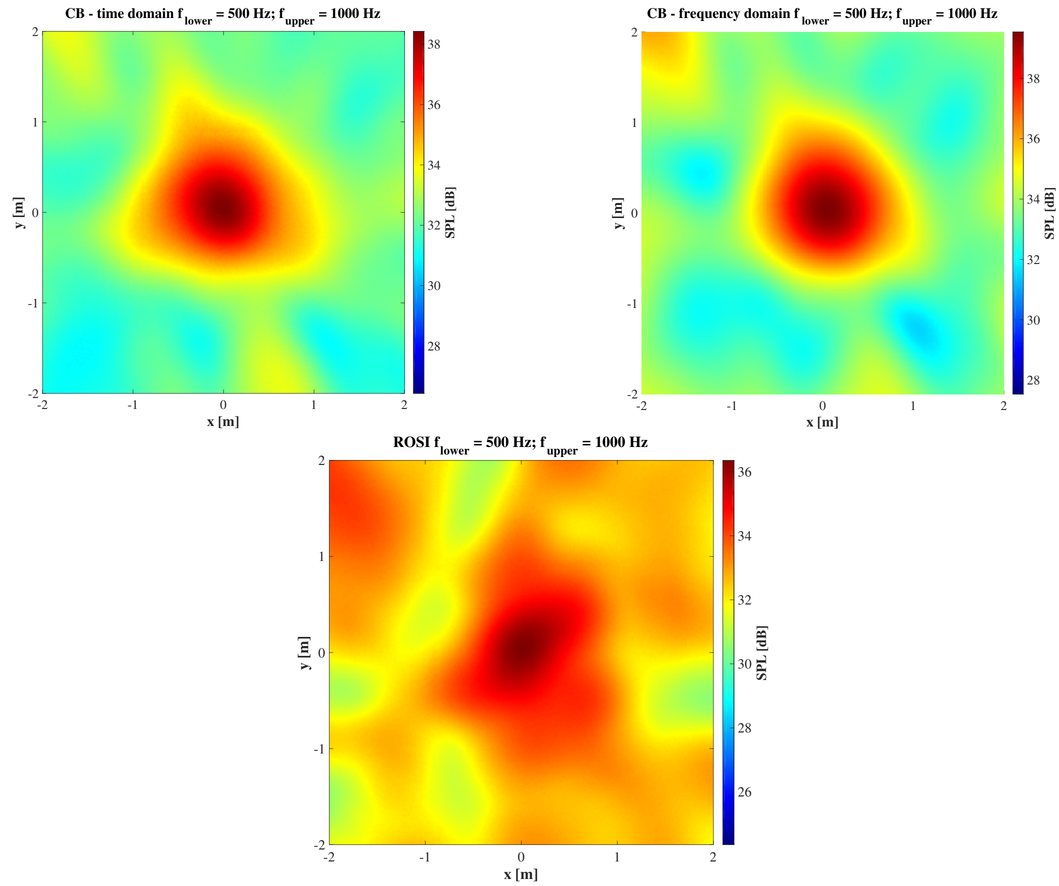

Figure B.12: Left: CB in the time domain. Right: CB in the frequency domain. Center: ROSI. The five-bladed wind turbine rotates at 5.9 Hz. The wind speed of the tunnel is 5 m/s. The signal is filtered into the frequency band 500 Hz - 1000 Hz. A scan grid of 4x4 m^2 with a total of 40000 scan points and a sampling frequency of 50 kHz are employed. The distance from the microphone array is 3 m.

B.1.5. Five bladed wind turbine - 3

The DOD upwind turbine is tested with five blades. The corresponding rotor diameter is 2.10 m. The yaw angle is set at 0 degree. The wind speed of the tunnel is 5 m/s and the rotational speed of the turbine is 5.7 Hz, which leads to a blade passing frequency (BPF) of 28.7 Hz. The measured power output amounts to 58 W.

Figure B.13 illustrates the PSD of the OJF background noise at 5 m/s, when the tower, the nacelle and the tail fin of the wind turbine is installed, and the PSD of the five-bladed turbine. Between 500 Hz and 2000 Hz, the two curves almost coincide. However, a small difference can be recognized between 500 Hz and 1000 Hz. By filtering the signal into these two frequency bands, CB in time domain, CB in the frequency domain and ROSI are applied. The resulting acoustic images are depicted in Figure B.14 and in Figure B.15. From the source maps, it is not possible to distinguish the five blades of the turbine. The source localization as well as the source quantification of the small wind turbine are compromised by the high levels of background noise.

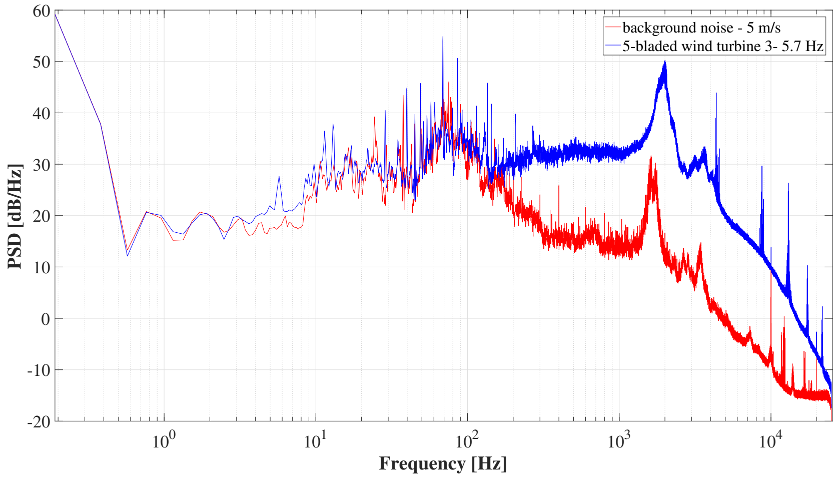

Figure B.13: Comparison between the PSD of the OJF background noise at 5 m/s (in red) and the PSD of the five-bladed wind turbine (in blue). The measurements for the OJF background noise were carried out with only the tower of the wind turbine installed. The five-bladed wind turbine has a rotational speed of 5.7 Hz. The blade passing frequency is 28.7 Hz. The measured power output amounts to 58 W.

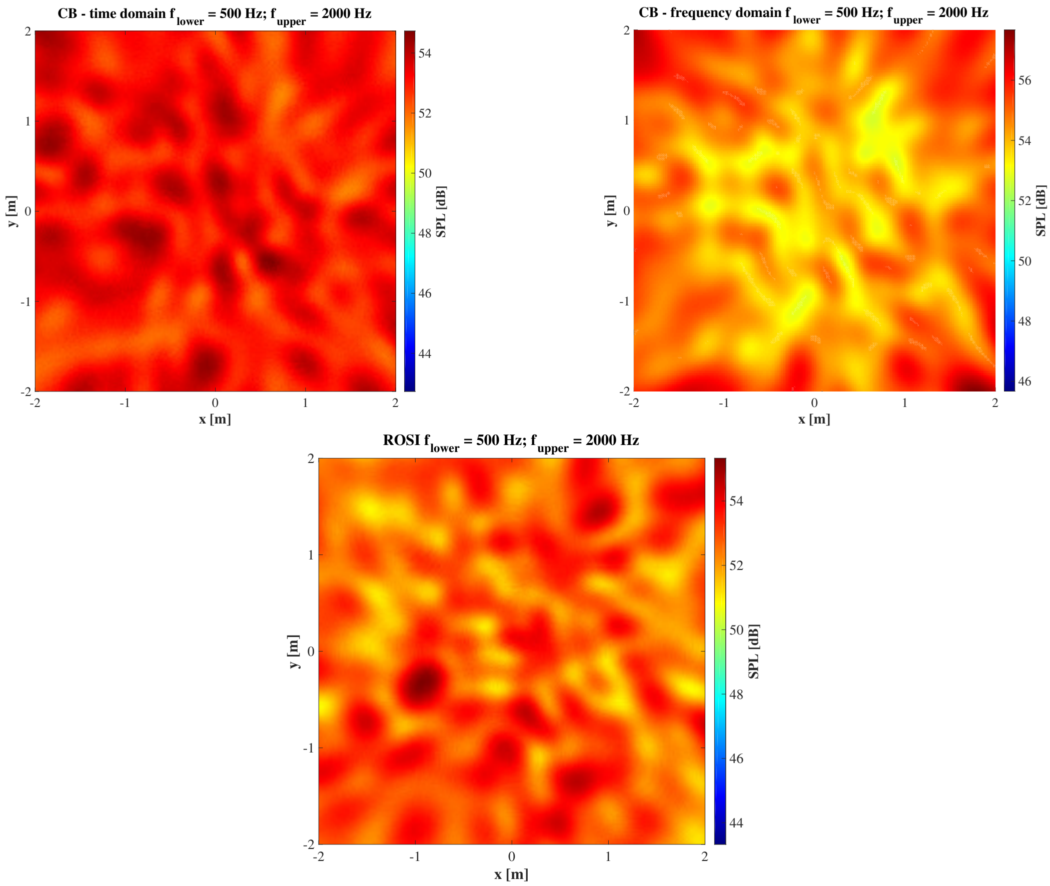

Figure B.14: Left: CB in the time domain. Right: CB in the frequency domain. Center: ROSI. The five-bladed wind turbine rotates at 5.7 Hz. The wind speed of the tunnel is 5 m/s. The signal is filtered into the frequency band 500 Hz - 2000 Hz. A scan grid of 4x4 m^2 with a total of 40000 scan points and a sampling frequency of 50 kHz are employed. The distance from the microphone array is 3 m.

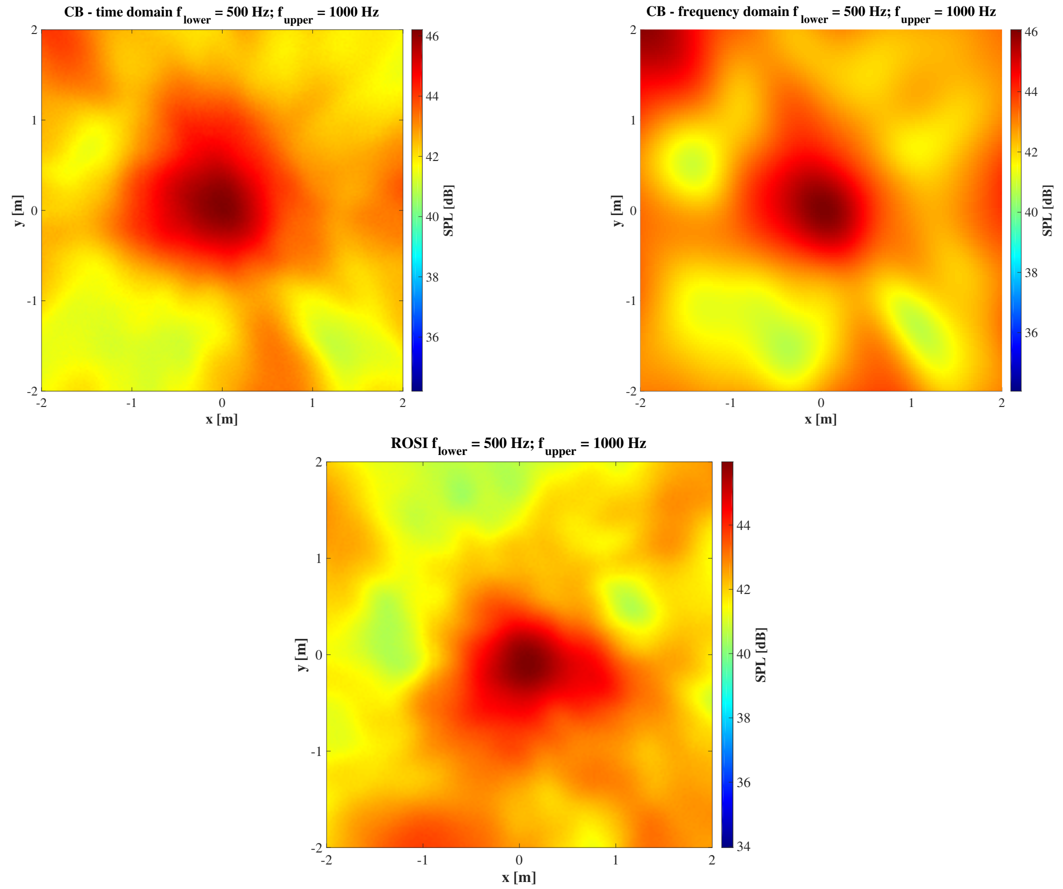

Figure B.15: Left: CB in the time domain. Right: CB in the frequency domain. Center: ROSI. The five-bladed wind turbine rotates at 5.7 Hz. The wind speed of the tunnel is 5 m/s. The signal is filtered into the frequency band 500 Hz - 1000 Hz. A scan grid of 4x4 m^2 with a total of 40000 scan points and a sampling frequency of 50 kHz are employed. The distance from the microphone array is 3 m.

B.2. Wind speed - 7 m/s

In this section, the wind speed of the tunnel is set at 7 m/s. First, the background noise of the facility is evaluated with only the tower, the nacelle and the tail fin of the wind turbine installed. Follows the analysis of the DOD upwind turbine with four different blade configurations.

B.2.1. OJF background noise

For this set of measurement, the wind turbine was not in operation. Figure B.16, Figure B.17 and Figure B.18 present the resulting acoustic images when CB in the time domain and CB in the frequency domain are applied to the experimental data. The signal is filtered into three different frequency bands: 500 Hz - 2000 Hz, 500 Hz - 1000 Hz and 700 Hz - 1000 Hz. As it can be observed, for all the adopted frequency bands the interaction between the wind and the nacelle results the most dominant noise source and the nacelle can be recognized in the center of the source map. However, in the range 500 Hz - 2000 Hz the background noise levels are higher compared to the other cases.

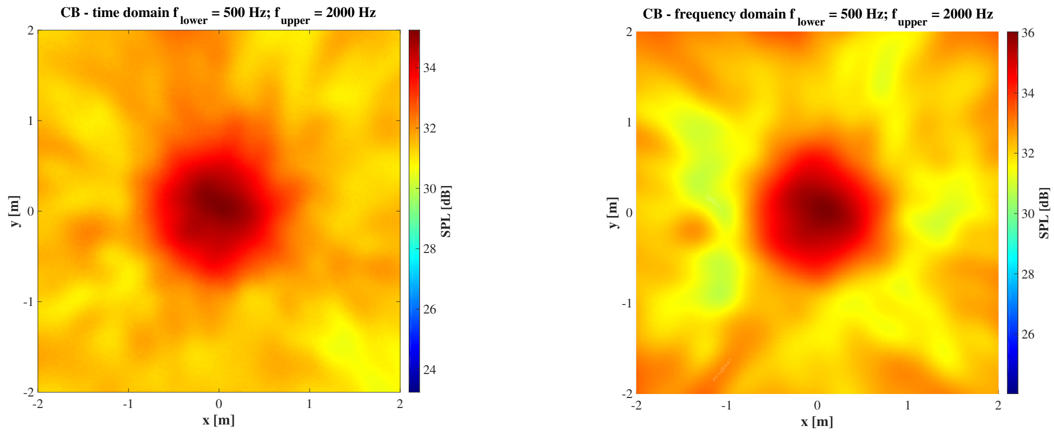

Figure B.16: Left: CB in the time domain. Right: CB in the frequency domain. The signal is filtered into the frequency band: 500 Hz - 2000 Hz. A scan grid of 4x4 m^2 with a total of 40000 scan points and a sampling frequency of 50 kHz are employed. The distance from the microphone array is 3 m.

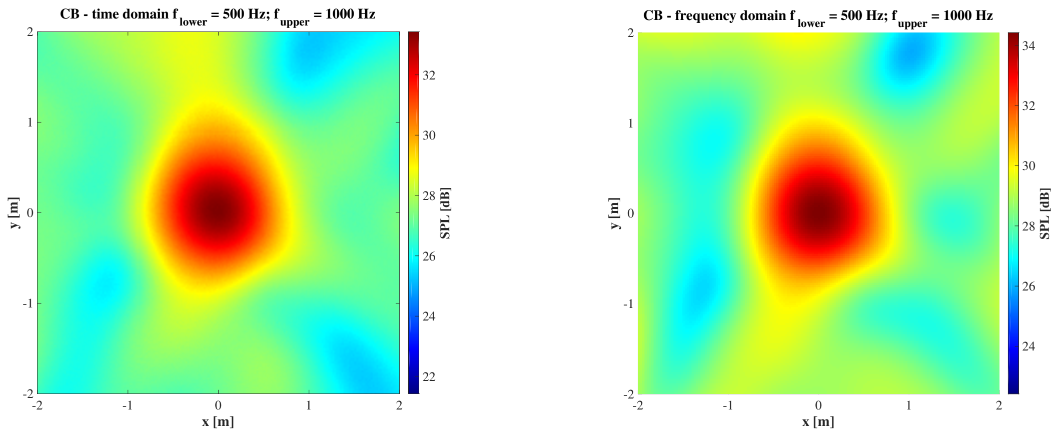

Figure B.17: Left: CB in the time domain. Right: CB in the frequency domain. The signal is filtered into the frequency band: 500 Hz - 1000 Hz. A scan grid of 4x4 m^2 with a total of 40000 scan points and a sampling frequency of 50 kHz are employed. The distance from the microphone array is 3 m.

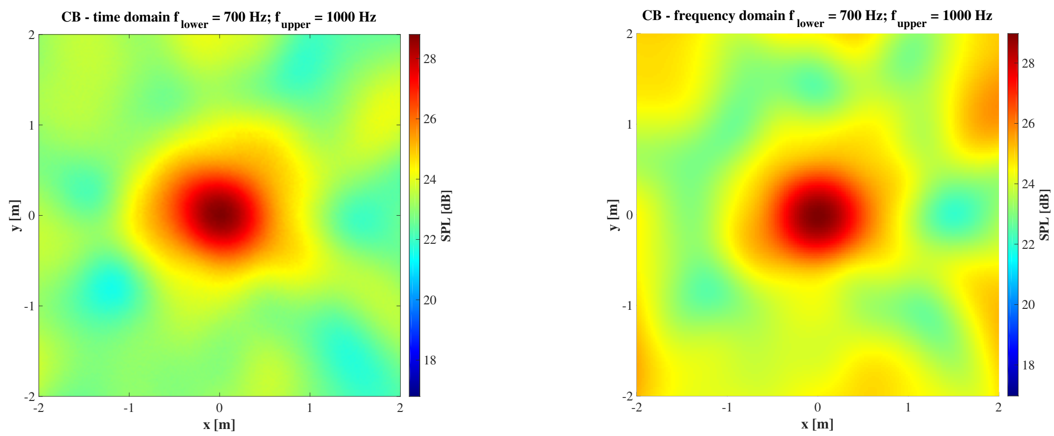

Figure B.18: Left: CB in the time domain. Right: CB in the frequency domain. The signal is filtered into the frequency band: 700 Hz - 1000 Hz. A scan grid of 4x4 m^2 with a total of 40000 scan points and a sampling frequency of 50 kHz are employed. The distance from the microphone array is 3 m.

B.2.2. Three bladed wind turbine

The DOD upwind turbine is tested with three blades. The corresponding rotor diameter is 1.66 m. The yaw angle is set at 0 degree. The wind speed of the tunnel is 7 m/s and the rotational speed of the turbine is 5.1 Hz, which leads to a blade passing frequency (BPF) of 15.4 Hz. The measured power output amounts to 180 W.

Figure B.20 illustrates the PSD of the OJF background noise at 7 m/s, when the tower, the nacelle and the tail fin of the wind turbine are installed, and the PSD of the three-bladed turbine. Between 500 Hz and 2000 Hz, the two curves almost coincide. By filtering the signal into this frequency band, CB in time domain, CB in the frequency domain and ROSI are applied. The resulting acoustic images are depicted in Figure B.19. From the source maps, it is not possible to distinguish the three blades of the turbine. The source localization as well as the source quantification of the small wind turbine are compromised by the high levels of background noise.

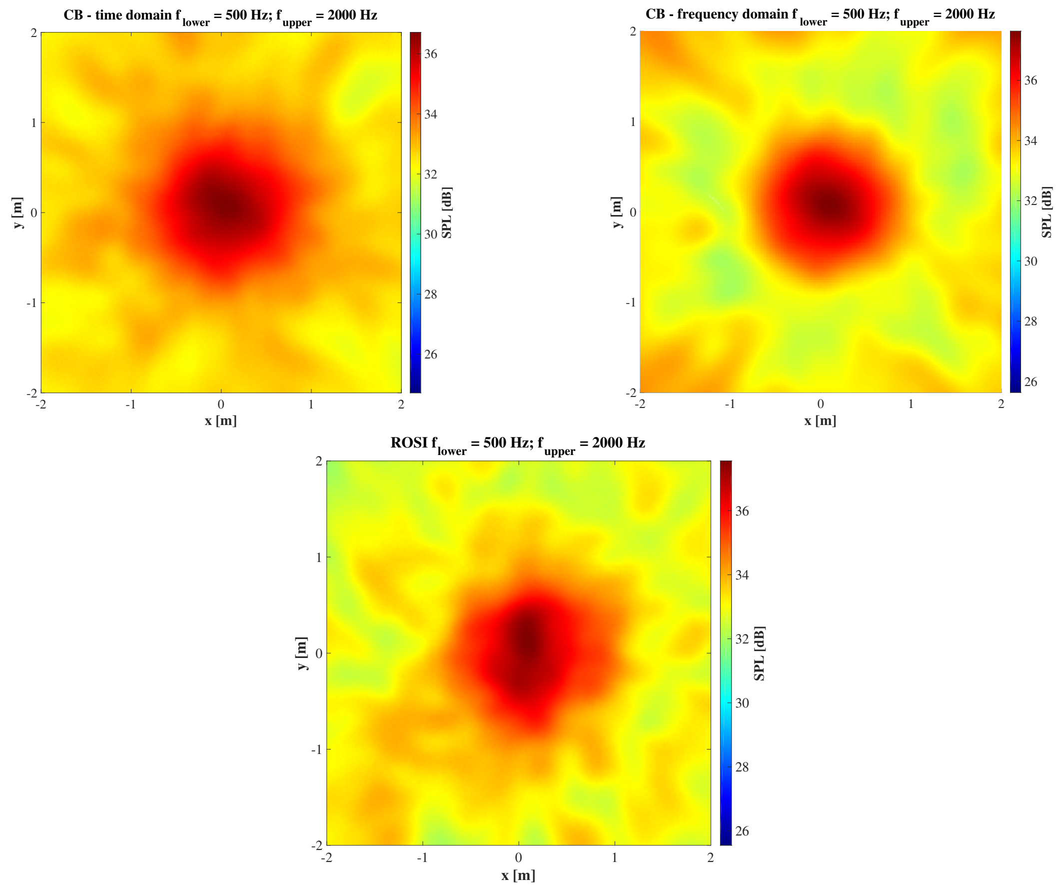

Figure B.19: Left: CB in the time domain. Right: CB in the frequency domain. Center: ROSI. The three-bladed wind turbine rotates at 5.1 Hz. The wind speed of the tunnel is 7 m/s. The signal is filtered into the frequency band 500 Hz - 2000 Hz. A scan grid of 4x4 m^2 with a total of 40000 scan points and a sampling frequency of 50 kHz are employed. The distance from the microphone array is 3 m.

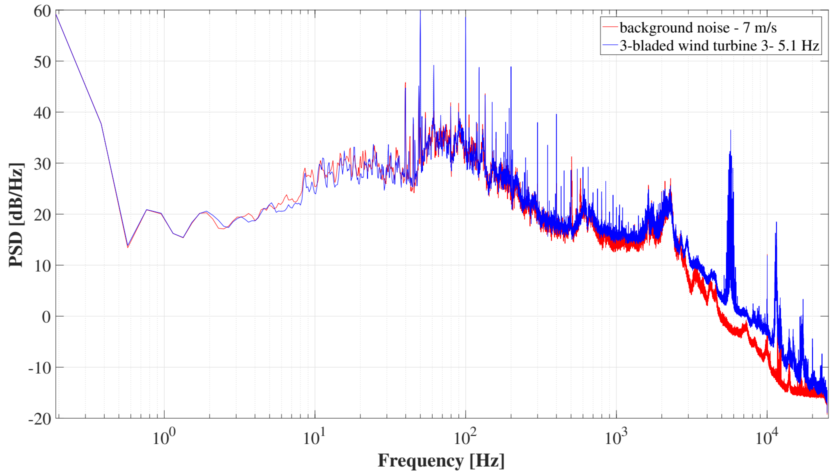

Figure B.20: Comparison between the PSD of the OJF background noise at 7 m/s (in red) and the PSD of the three-bladed wind turbine (in blue). The measurements for the OJF background noise were carried out with only the tower, the nacelle and the tail fin of the wind turbine installed. The three-bladed wind turbine has a rotational speed of 5.1 Hz. The blade passing frequency is 15.4 Hz. The measured power output amounts to 180 W.

B.2.3. Five bladed wind turbine - 1

The DOD upwind turbine is tested with five blades. The corresponding rotor diameter is 1.72 m. The yaw angle is set at 0 degree. The wind speed of the tunnel is 7 m/s and the rotational speed of the turbine is 6 Hz, which leads to a blade passing frequency (BPF) of 30 Hz. The measured power output amounts to 182 W.

Figure B.21 illustrates the PSD of the OJF background noise at 7 m/s, when the tower, the nacelle and the tail fin of the wind turbine are installed, and the PSD of the five-bladed turbine. Between 500 Hz and 2000 Hz, the two curves almost coincide. However, a small difference can be observed between 700 Hz and 1500 Hz. By filtering the signal into these two frequency bands, CB in time domain, CB in the frequency domain and ROSI are applied. The resulting acoustic images are depicted in Figure B.22 and in Figure B.23. From the source maps, it is not possible to distinguish the five blades of the turbine. The source localization as well as the source quantification of the small wind turbine are compromised by the high levels of background noise.

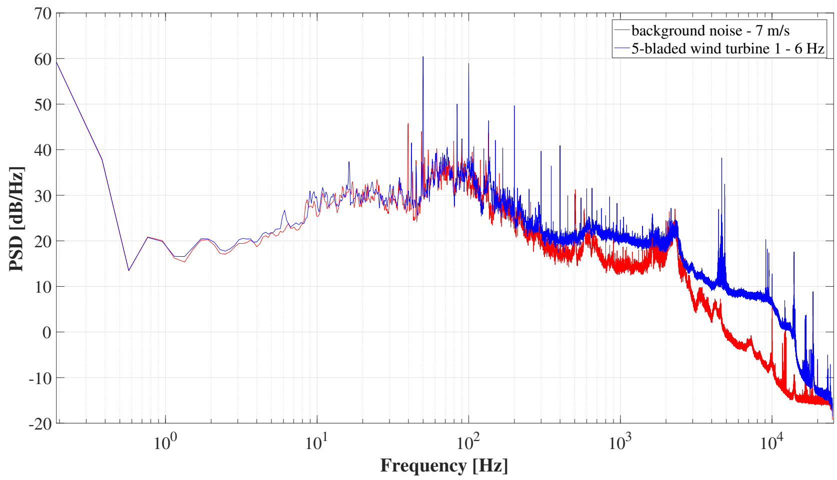

Figure B.21: Comparison between the PSD of the OJF background noise at 7 m/s (in red) and the PSD of the five-bladed wind turbine (in blue). The measurements for the OJF background noise were carried out with only the tower, the nacelle and the tail fin of the wind turbine installed. The five-bladed wind turbine has a rotational speed of 6 Hz. The blade passing frequency is 30 Hz. The measured power output amounts to 182 W.

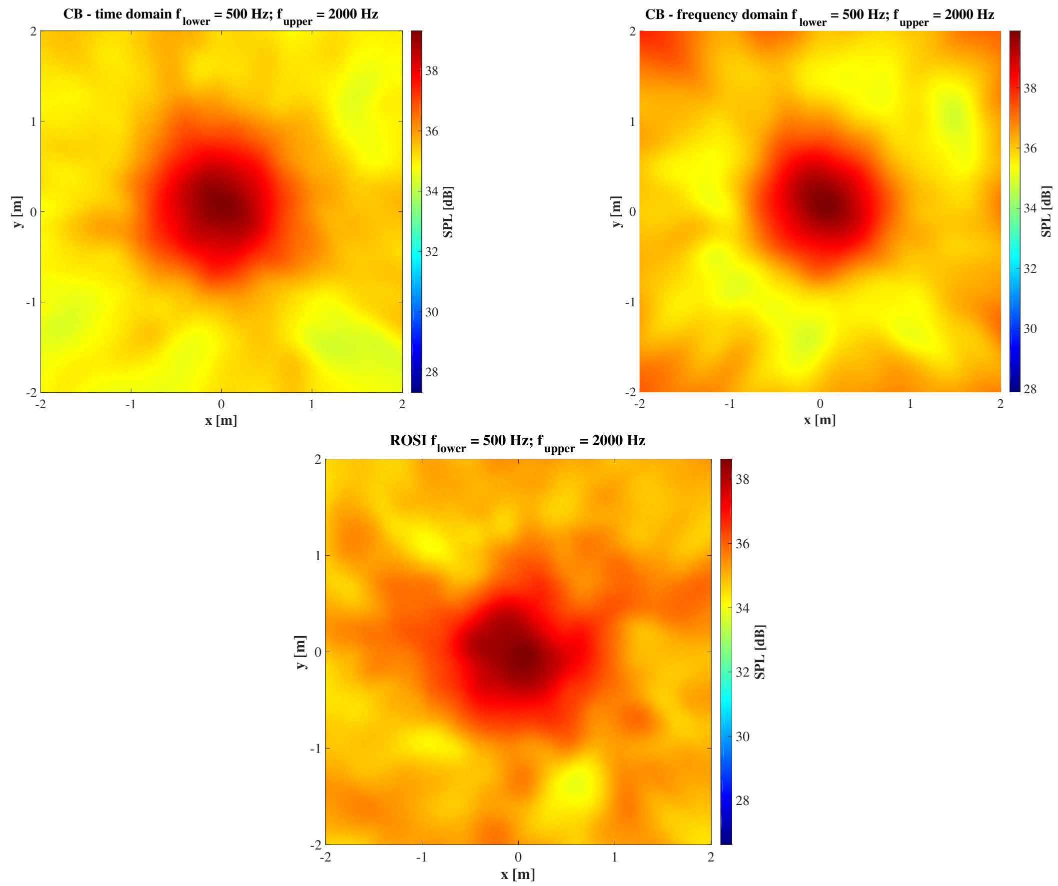

Figure B.22: Left: CB in the time domain. Right: CB in the frequency domain. Center: ROSI. The five-bladed wind turbine rotates at 6 Hz. The wind speed of the tunnel is 7 m/s. The signal is filtered into the frequency band 500 Hz - 2000 Hz. A scan grid of 4x4 m^2 with a total of 40000 scan points and a sampling frequency of 50 kHz are employed. The distance from the microphone array is 3 m.

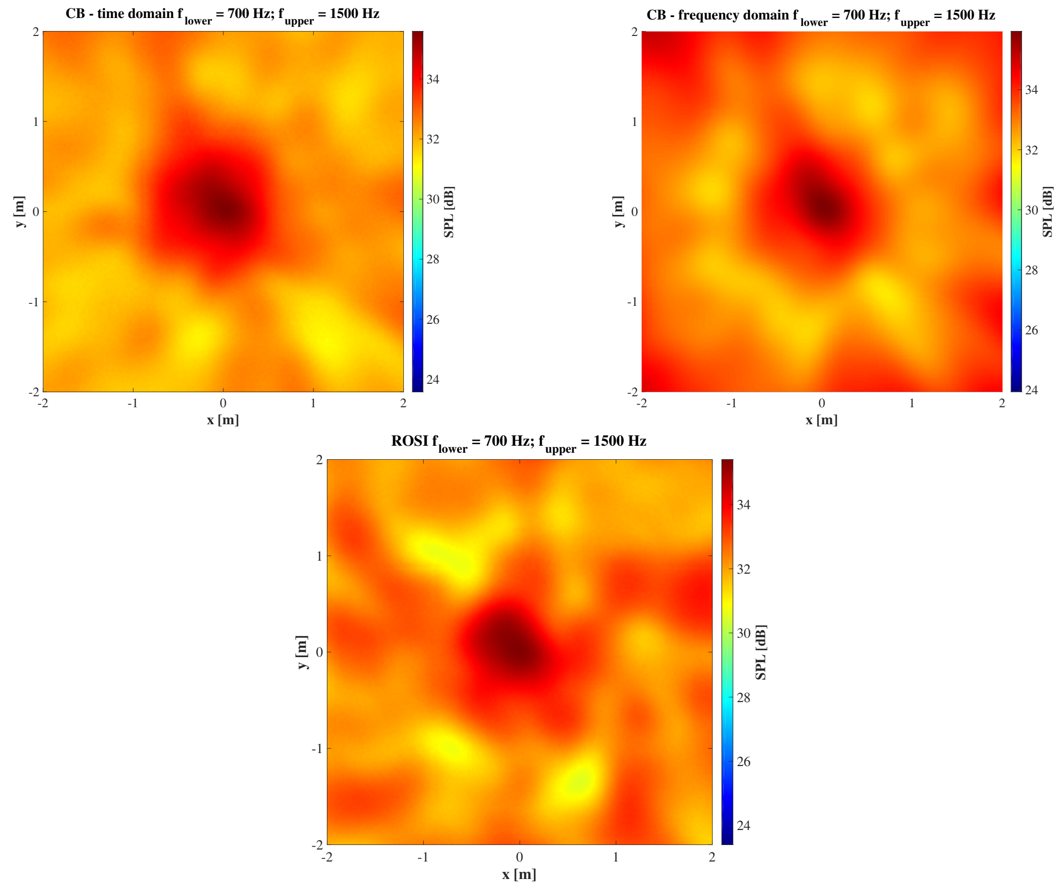

Figure B.23: Left: CB in the time domain. Right: CB in the frequency domain. Center: ROSI. The five-bladed wind turbine rotates at 6 Hz. The wind speed of the tunnel is 7 m/s. The signal is filtered into the frequency band 700 Hz - 1500 Hz. A scan grid of 4x4 m^2 with a total of 40000 scan points and a sampling frequency of 50 kHz are employed. The distance from the microphone array is 3 m.

B.2.4. Five bladed wind turbine - 2

The DOD upwind turbine is tested with five blades. The corresponding rotor diameter is 1.71 m. The yaw angle is set at 0 degree. The wind speed of the tunnel is 7 m/s and the rotational speed of the turbine is 5.9 Hz, which leads to a blade passing frequency (BPF) of 29.5 Hz. The measured power output amounts to 181 W.

Figure B.24 illustrates the PSD of the OJF background noise at 7 m/s, when the tower, the nacelle and the tail fin of the wind turbine are installed, and the PSD of the five-bladed turbine. Between 500 Hz and 2000 Hz, the two curves almost coincide. However, a small difference can be recognized between 700 Hz and 1500 Hz. By filtering the signal into these two frequency bands, CB in time domain, CB in the frequency domain and ROSI are applied. The resulting acoustic images are depicted in Figure B.25 and in Figure B.26. From the source maps, it is not possible to distinguish the five blades of the turbine. The source localization as well as the source quantification of the small wind turbine are compromised by the high levels of background noise.

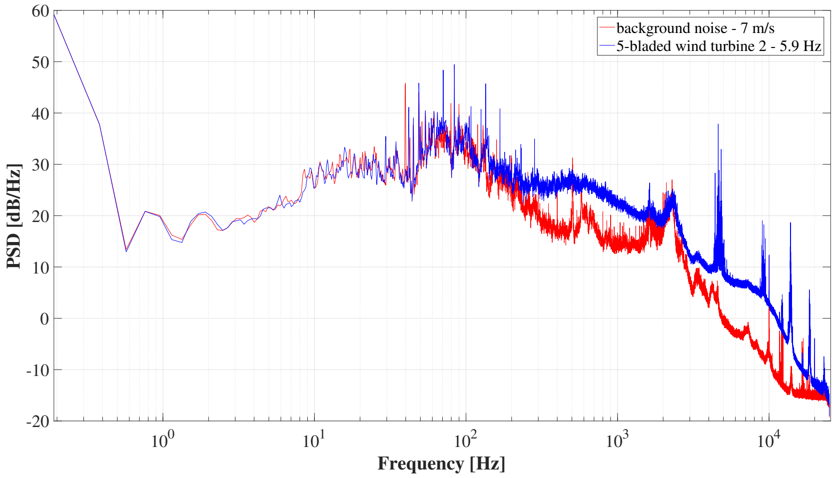

Figure B.24: Comparison between the PSD of the OJF background noise at 7 m/s (in red) and the PSD of the five-bladed wind turbine (in blue). The measurements for the OJF background noise were carried out with only the tower, the nacelle and the tail fin of the wind turbine installed. The five-bladed wind turbine has a rotational speed of 5.9 Hz. The blade passing frequency is 29.5 Hz. The measured power output amounts to 181 W.

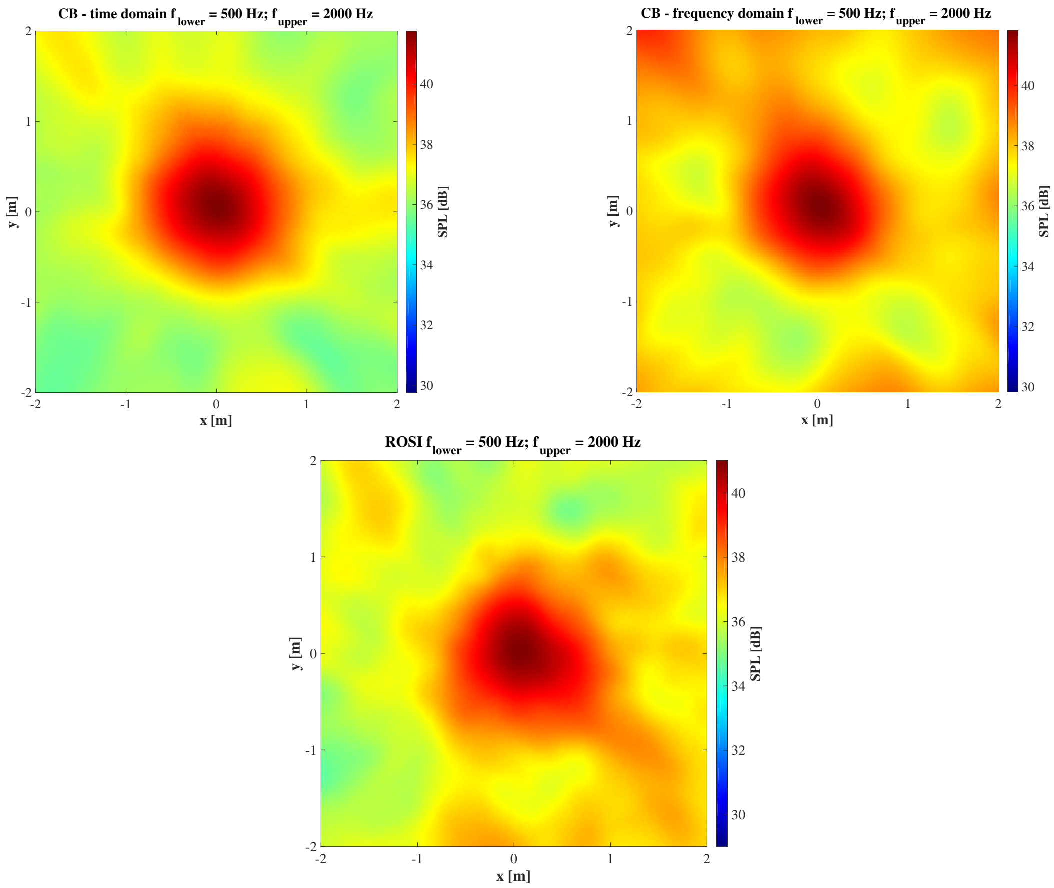

Figure B.25: Left: CB in the time domain. Right: CB in the frequency domain. Center: ROSI. The five-bladed wind turbine rotates at 5.9 Hz. The wind speed of the tunnel is 7 m/s. The signal is filtered into the frequency band 500 Hz - 2000 Hz. A scan grid of 4x4 m^2 with a total of 40000 scan points and a sampling frequency of 50 kHz are employed. The distance from the microphone array is 3 m.

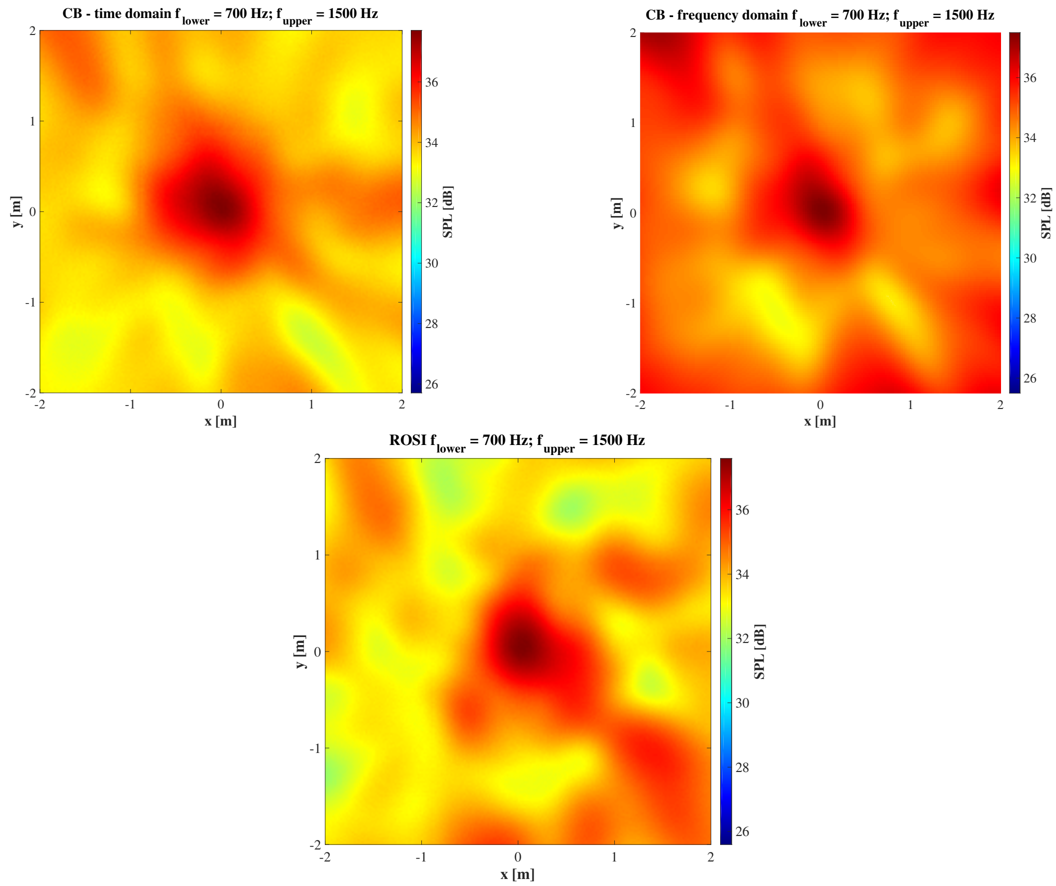

Figure B.26: Left: CB in the time domain. Right: CB in the frequency domain. Center: ROSI. The five-bladed wind turbine rotates at 5.9 Hz. The wind speed of the tunnel is 7 m/s. The signal is filtered into the frequency band 700 Hz - 1500 Hz. A scan grid of 4x4 m^2 with a total of 40000 scan points and a sampling frequency of 50 kHz are employed. The distance from the microphone array is 3 m.

B.2.5. Five bladed wind turbine - 3

The DOD upwind turbine is tested with five blades. The corresponding rotor diameter is 2.10 m. The yaw angle is set at 0 degree. The wind speed of the tunnel is 7 m/s and the rotational speed of the turbine is 4.9 Hz, which leads to a blade passing frequency (BPF) of 24.6 Hz. The measured power output amounts to 180 W.

Figure B.27 illustrates the PSD of the OJF background noise at 7 m/s, when the tower, the nacelle and the tail fin of the wind turbine are installed, and the PSD of the five-bladed turbine. Between 500 Hz and 2000 Hz, the two curves almost coincide. However, a small difference can be recognized between 700 Hz and 1000 Hz as well as between 1400 Hz and 2000 Hz. By filtering the signal into these three frequency bands, CB in time domain, CB in the frequency domain and ROSI are applied. The resulting acoustic images are depicted in Figure B.28, in Figure B.29 and in Figure B.30. From the source maps, it is not possible to distinguish the five blades of the turbine. The source localization as well as the source quantification of the small wind turbine are compromised by the high levels of background noise.

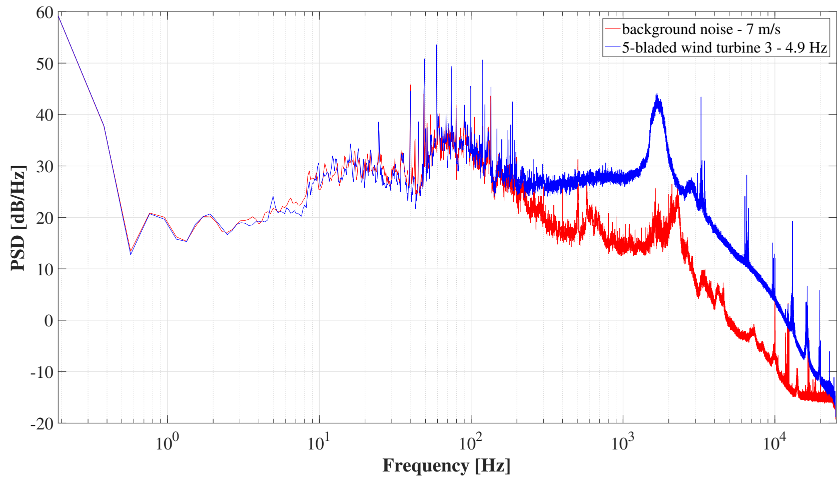

Figure B.27: Comparison between the PSD of the OJF background noise at 7 m/s (in red) and the PSD of the five-bladed wind turbine (in blue). The measurements for the OJF background noise were carried out with only the tower, the nacelle and the tail fin of the wind turbine installed. The five-bladed wind turbine has a rotational speed of 4.9 Hz. The blade passing frequency is 24.6 Hz. The measured power output amounts to 180 W.

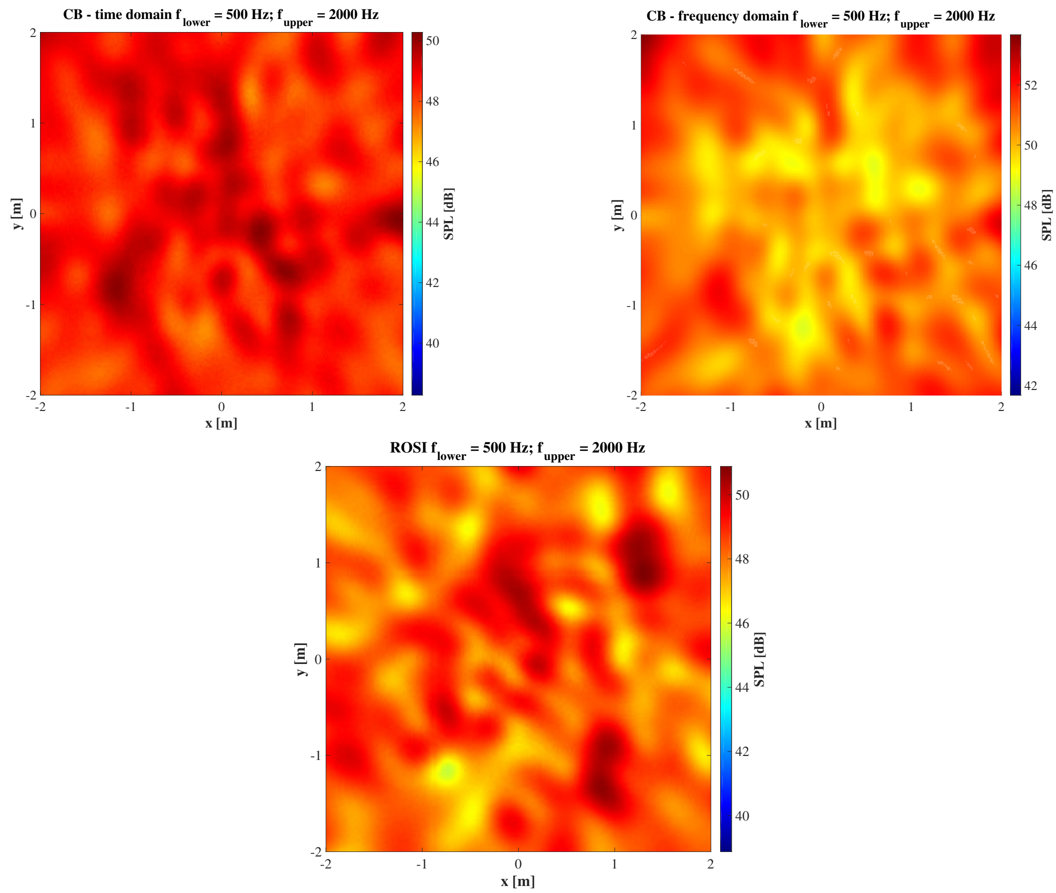

Figure B.28: Left: CB in the time domain. Right: CB in the frequency domain. Center: ROSI. The five-bladed wind turbine rotates at 4.9 Hz. The wind speed of the tunnel is 7 m/s. The signal is filtered into the frequency band 500 Hz - 2000 Hz. A scan grid of 4x4 m^2 with a total of 40000 scan points and a sampling frequency of 50 kHz are employed. The distance from the microphone array is 3 m.

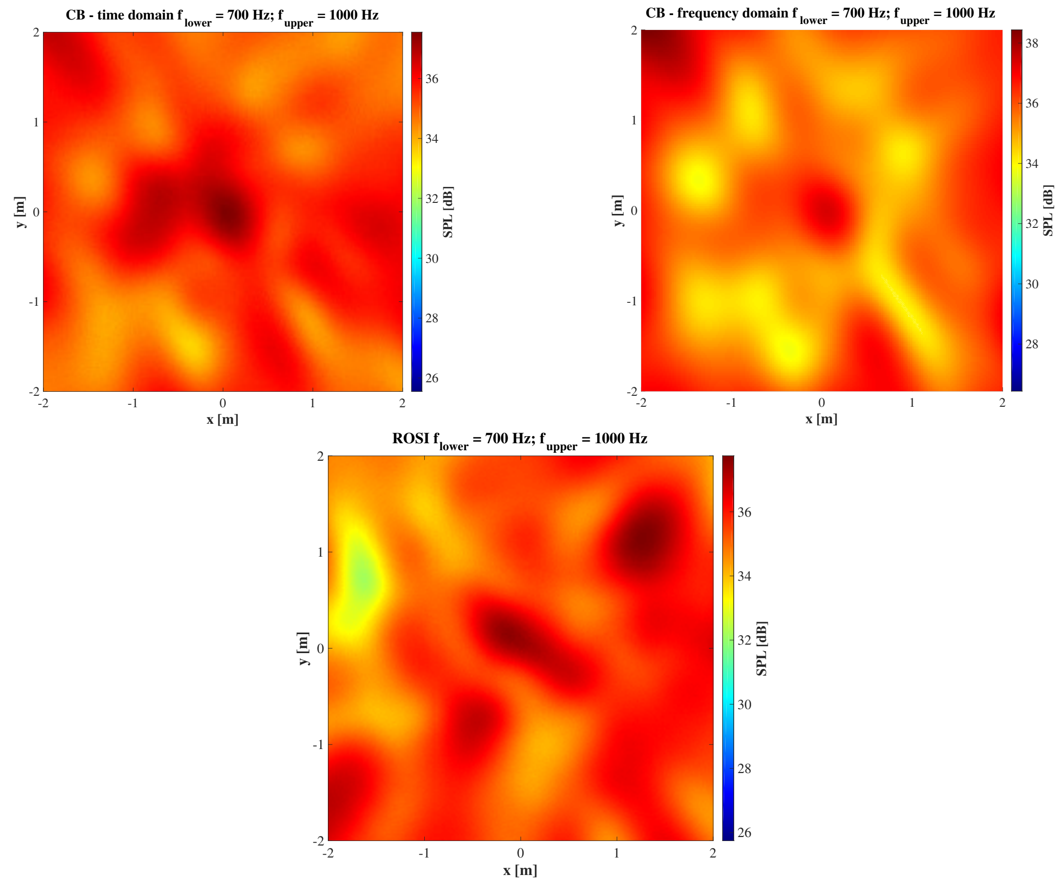

Figure B.29: Left: CB in the time domain. Right: CB in the frequency domain. Center: ROSI. The five-bladed wind turbine rotates at 4.9 Hz. The wind speed of the tunnel is 7 m/s. The signal is filtered into the frequency band 700 Hz - 1000 Hz. A scan grid of 4x4 m^2 with a total of 40000 scan points and a sampling frequency of 50 kHz are employed. The distance from the microphone array is 3 m.

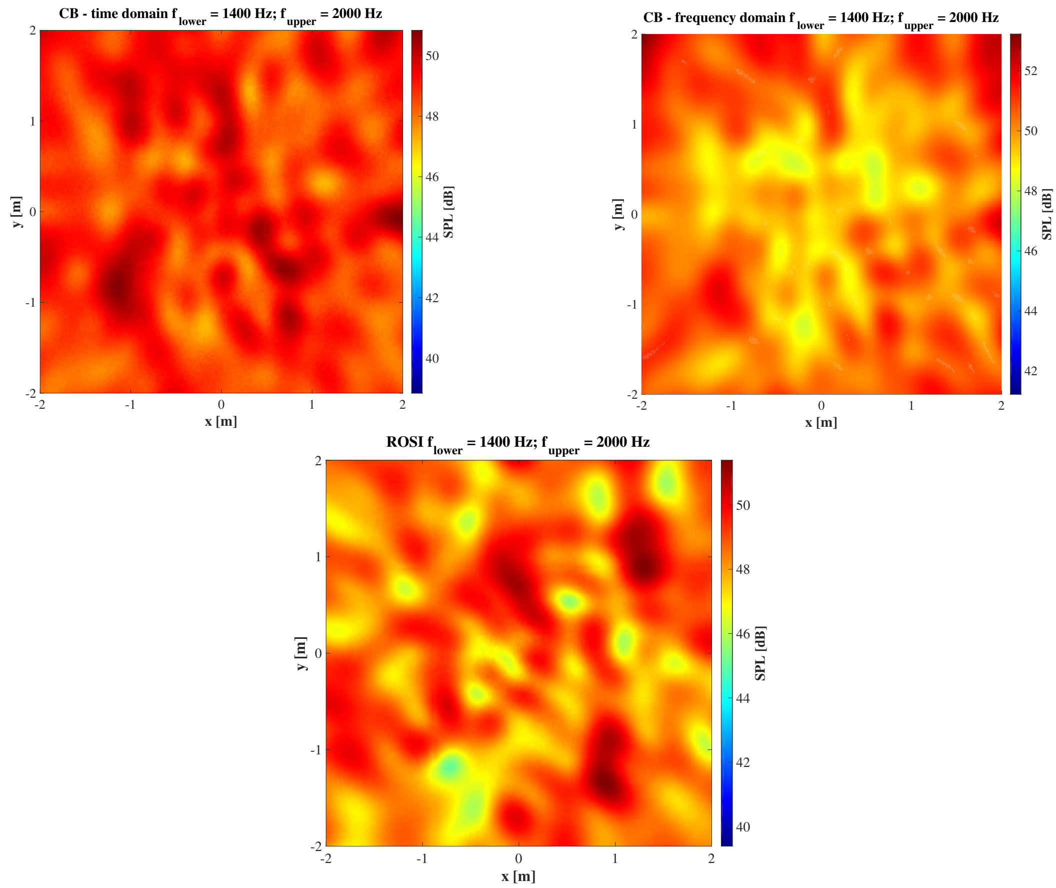

Figure B.30: Left: CB in the time domain. Right: CB in the frequency domain. Center: ROSI. The five-bladed wind turbine rotates at 4.9 Hz. The wind speed of the tunnel is 7 m/s. The signal is filtered into the frequency band 1400 Hz - 2000 Hz. A scan grid of 4x4 m^2 with a total of 40000 scan points and a sampling frequency of 50 kHz are employed. The distance from the microphone array is 3 m.

B.3. Wind speed - 9 m/s

In this section, the wind speed of the tunnel is set at 9 m/s. First, the background noise of the facility is evaluated with only the tower, the nacelle and the tail fin of the wind turbine installed. Follows the analysis of the DOD upwind turbine with four different blade configurations.

B.3.1. OJF background noise

For this set of measurement, the wind turbine was not in operation. Figure B.31, Figure B.32 and Figure B.33 present the resulting acoustic images when CB in the time domain and CB in the frequency domain are applied to the experimental data. The signal is filtered into three different frequency bands: 500 Hz - 2000 Hz, 500 Hz - 1000 Hz and 700 Hz - 1000 Hz. As it can be observed, for all the adopted frequency bands the nacelle is in the center of the source map. Even if the interaction between the wind and the nacelle results one of the most dominant noise source, the background noise levels are very high. In particular, this trend can be recognized for the range 500 Hz - 2000 Hz.

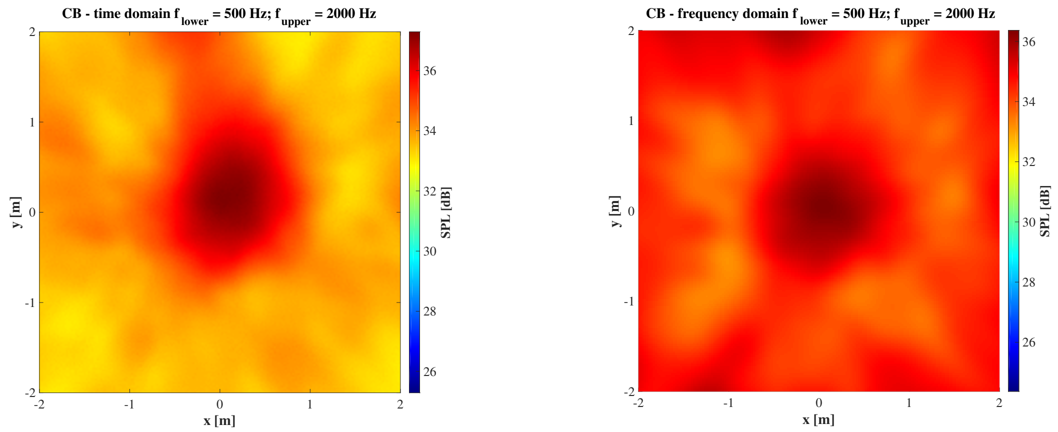

Figure B.31: Left: CB in the time domain. Right: CB in the frequency domain. The signal is filtered into the frequency band: 500 Hz - 2000 Hz. A scan grid of 4x4 m^2 with a total of 40000 scan points and a sampling frequency of 50 kHz are employed. The distance from the microphone array is 3 m.

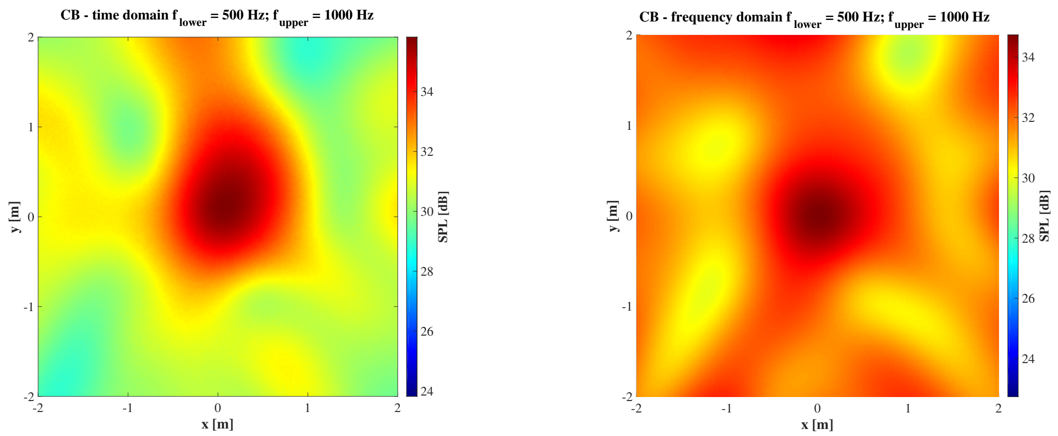

Figure B.32: Left: CB in the time domain. Right: CB in the frequency domain. The signal is filtered into the frequency band: 500 Hz - 1000 Hz. A scan grid of 4x4 m^2 with a total of 40000 scan points and a sampling frequency of 50 kHz are employed. The distance from the microphone array is 3 m.

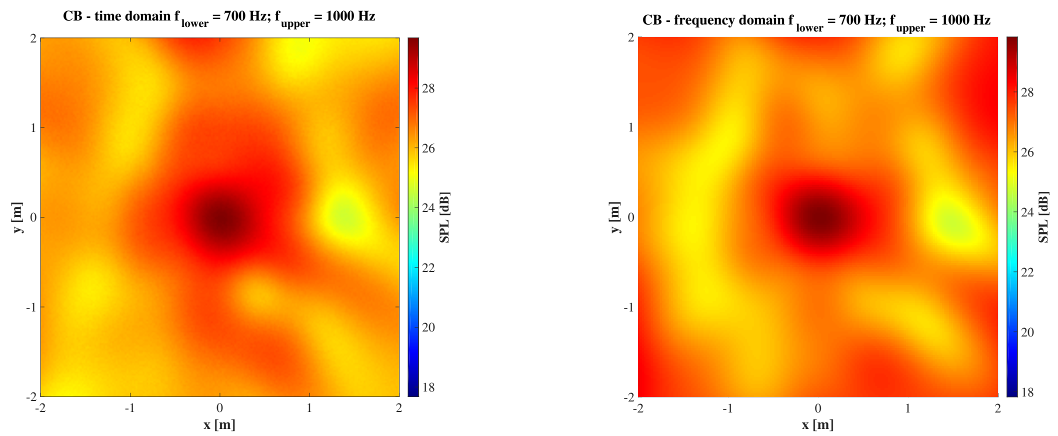

Figure B.33: Left: CB in the time domain. Right: CB in the frequency domain. The signal is filtered into the frequency band: 700 Hz - 1000 Hz. A scan grid of 4x4 m^2 with a total of 40000 scan points and a sampling frequency of 50 kHz are employed. The distance from the microphone array is 3 m.

B.3.2. Three bladed wind turbine

The DOD upwind turbine is tested with three blades. The corresponding rotor diameter is 1.66 m. The yaw angle is set at 0 degree. The wind speed of the tunnel is 9 m/s and the rotational speed of the turbine is 6.4 Hz, which leads to a blade passing frequency (BPF) of 19.2 Hz. The measured power output amounts to 320 W.

Figure B.35 illustrates the PSD of the OJF background noise at 9 m/s, when the tower, the nacelle and the tail fin of the wind turbine are installed, and the PSD of the three-bladed turbine. Between 500 Hz and 2000 Hz, the two curves almost coincide. By filtering the signal into this frequency band, CB in time domain, CB in the frequency domain and ROSI are applied. The resulting acoustic images are depicted in Figure B.34. From the source maps, it is not possible to distinguish the three blades of the turbine. The source localization as well as the source quantification of the small wind turbine are compromised by the high levels of background noise.

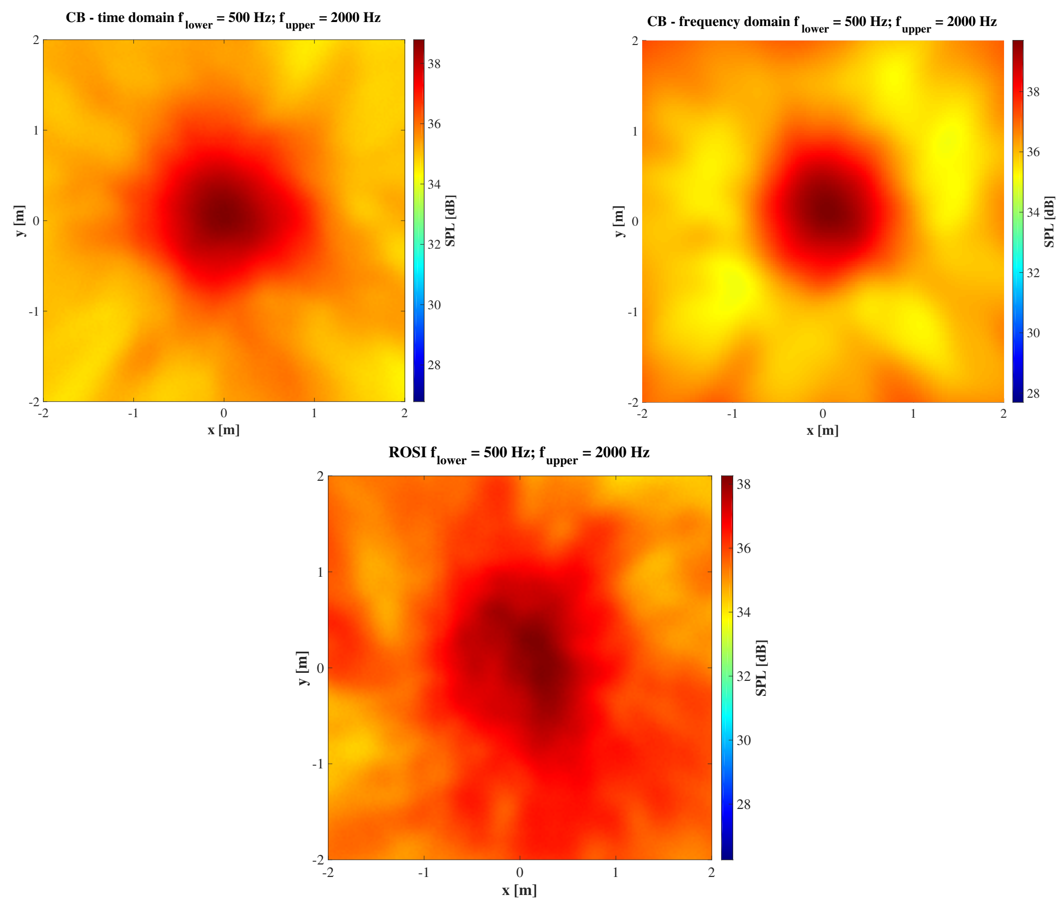

Figure B.34: Left: CB in the time domain. Right: CB in the frequency domain. Center: ROSI. The three-bladed wind turbine rotates at 6.4 Hz. The wind speed of the tunnel is 9 m/s. The signal is filtered into the frequency band 500 Hz - 2000 Hz. A scan grid of 4x4 m^2 with a total of 40000 scan points and a sampling frequency of 50 kHz are employed. The distance from the microphone array is 3 m.

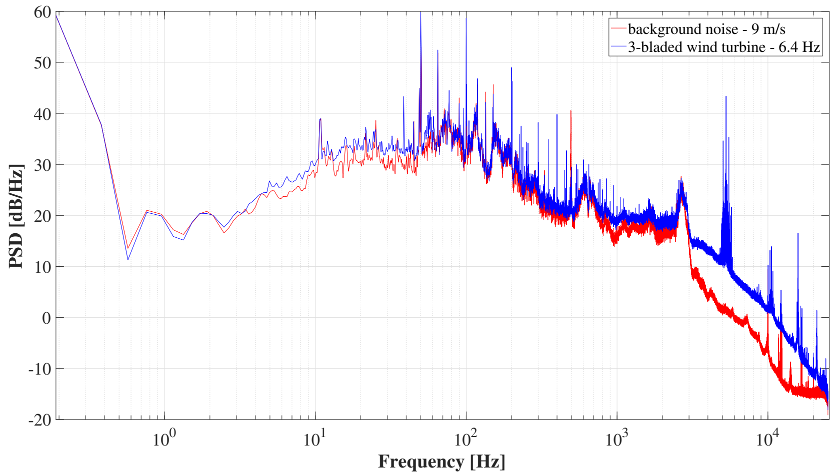

Figure B.35: Comparison between the PSD of the OJF background noise at 9 m/s (in red) and the PSD of the three-bladed wind turbine (in blue). The measurements for the OJF background noise were carried out with only the tower, the nacelle and tail fin of the wind turbine installed. The three-bladed wind turbine has a rotational speed of 6.4 Hz. The blade passing frequency is 19.2 Hz. The measured power output amounts to 320 W.

B.3.3. Five bladed wind turbine - 2

The DOD upwind turbine is tested with five blades. The corresponding rotor diameter is 1.71 m. The yaw angle is set at 0 degree. The wind speed of the tunnel is 9 m/s and the rotational speed of the turbine is 7.2 Hz, which leads to a blade passing frequency (BPF) of 36 Hz. The measured power output amounts to 330 W.

Figure B.36 illustrates the PSD of the OJF background noise at 9 m/s, when the tower, the nacelle and the tail fin of the wind turbine are installed, and the PSD of the five-bladed turbine. Between 500 Hz and 2000 Hz, the two curves almost coincide. However, a small difference can be recognized between 700 Hz and 1000 Hz. By filtering the signal into these two frequency bands, CB in time domain, CB in the frequency domain and ROSI are applied. The resulting acoustic images are depicted in Figure B.37 and in Figure B.38. From the source maps, it is not possible to distinguish the five blades of the turbine. The source localization as well as the source quantification of the small wind turbine are compromised by the high levels of background noise.

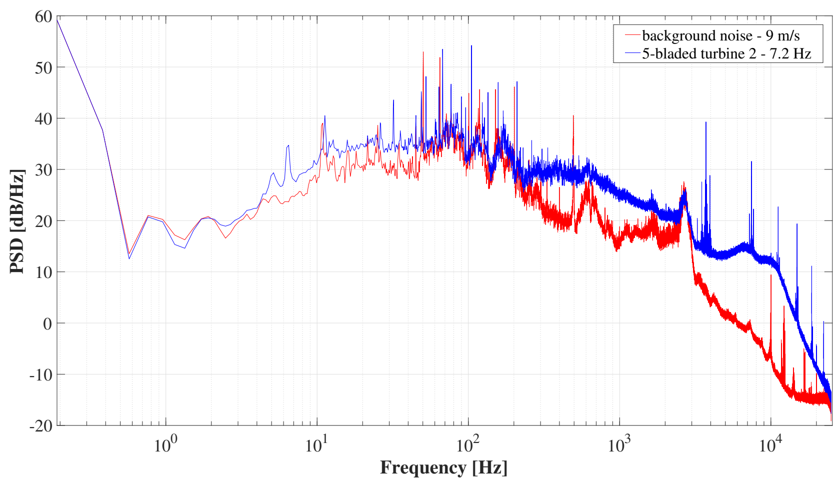

Figure B.36: Comparison between the PSD of the OJF background noise at 9 m/s (in red) and the PSD of the three-bladed wind turbine (in blue). The measurements for the OJF background noise were carried out with only the tower, the nacelle and the tail fin of the wind turbine installed. The five-bladed wind turbine has a rotational speed of 7.2 Hz. The blade passing frequency is 36 Hz. The measured power output amounts to 330 W.

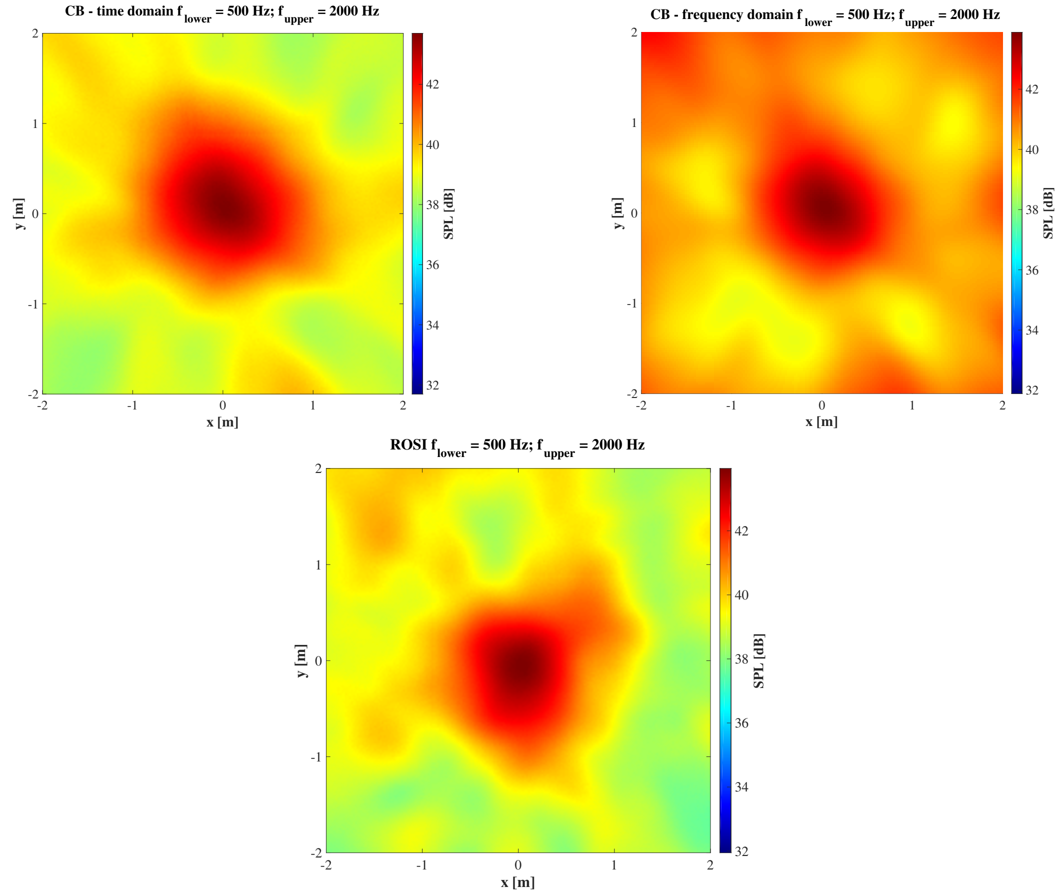

Figure B.37: Left: CB in the time domain. Right: CB in the frequency domain. Center: ROSI. The five-bladed wind turbine rotates at 7.2 Hz. The wind speed of the tunnel is 9 m/s. The signal is filtered into the frequency band 500 Hz - 2000 Hz. A scan grid of 4x4 m^2 with a total of 40000 scan points and a sampling frequency of 50 kHz are employed. The distance from the microphone array is 3 m.

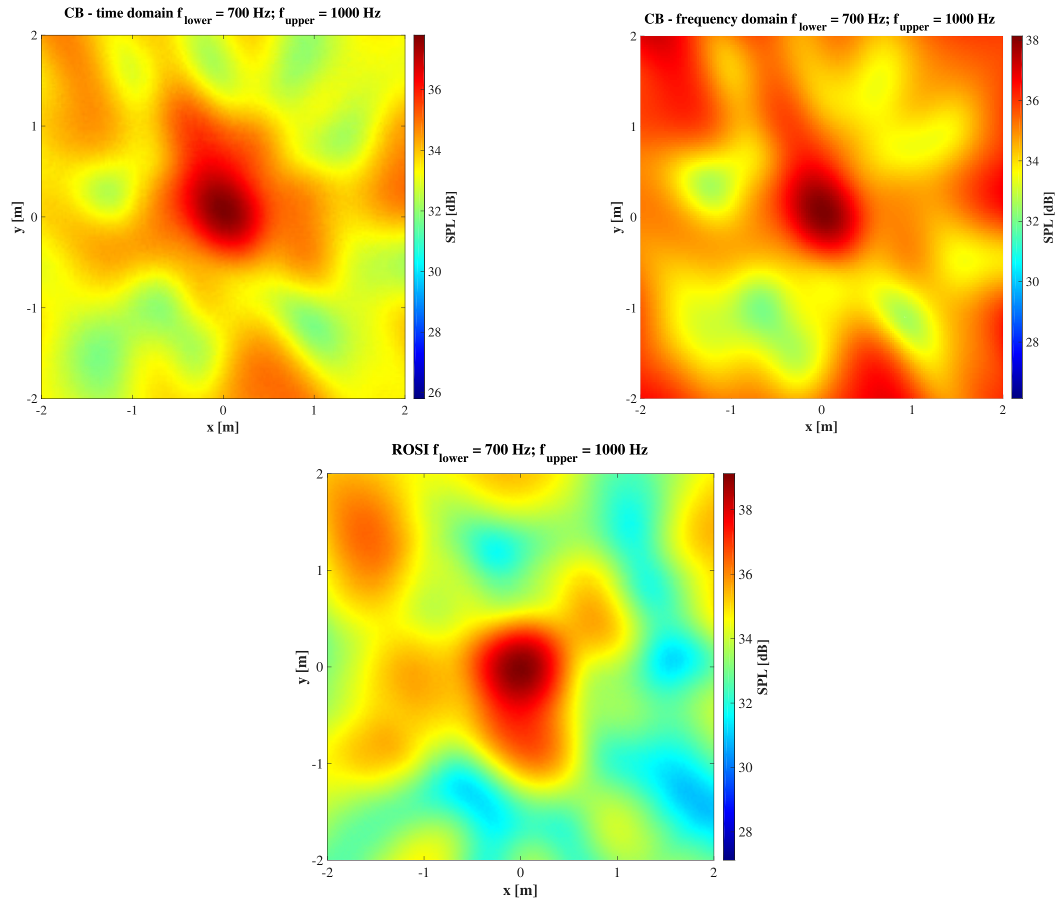

Figure B.38: Left: CB in the time domain. Right: CB in the frequency domain. Center: ROSI. The five-bladed wind turbine rotates at 7.2 Hz. The wind speed of the tunnel is 9 m/s. The signal is filtered into the frequency band 700 Hz - 1000 Hz. A scan grid of 4x4 m^2 with a total of 40000 scan points and a sampling frequency of 50 kHz are employed. The distance from the microphone array is 3 m.

B.3.4. Five bladed wind turbine - 3

The DOD upwind turbine is tested with five blades. The corresponding rotor diameter is 2.10 m. The yaw angle is set at 0 degree. The wind speed of the tunnel is 9 m/s and the rotational speed of the turbine is 6.9 Hz, which leads to a blade passing frequency (BPF) of 34.3 Hz. The measured power output amounts to 330 W.

Figure B.39 illustrates the PSD of the OJF background noise at 9 m/s, when the tower, the nacelle and the tail fin of the wind turbine are installed, and the PSD of the five-bladed turbine. Between 500 Hz and 2000 Hz, the two curves almost coincide. However, a small difference can be recognized between 500 Hz and 1000 Hz. By filtering the signal into these two frequency bands, CB in time domain, CB in the frequency domain and ROSI are applied. The resulting acoustic images are depicted in Figure B.40 and in Figure B.41. From the source maps, it is not possible to distinguish the five blades of the turbine. The source localization as well as the source quantification of the small wind turbine are compromised by the high levels of background noise.

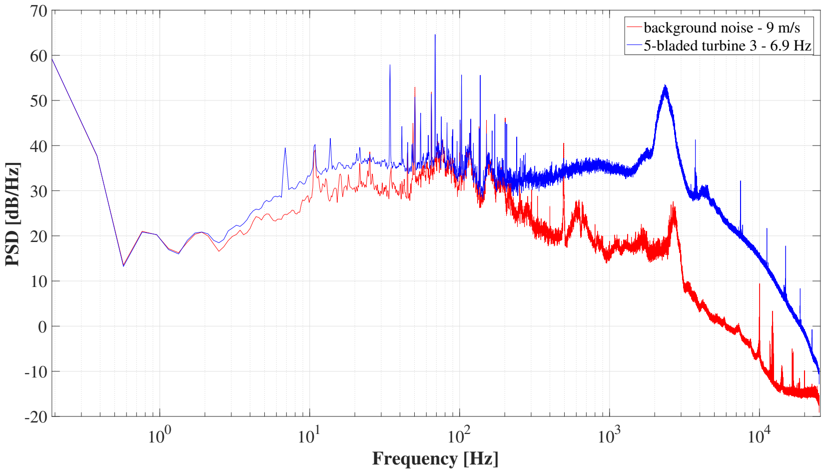

Figure B.39: Comparison between the PSD of the OJF background noise at 9 m/s (in red) and the PSD of the five-bladed wind turbine (in blue). The measurements for the OJF background noise were carried out with only the tower, the nacelle and the tail fin of the wind turbine installed. The five-bladed wind turbine has a rotational speed of 6.9 Hz. The blade passing frequency is 34.3 Hz. The measured power output amounts to 330 W.

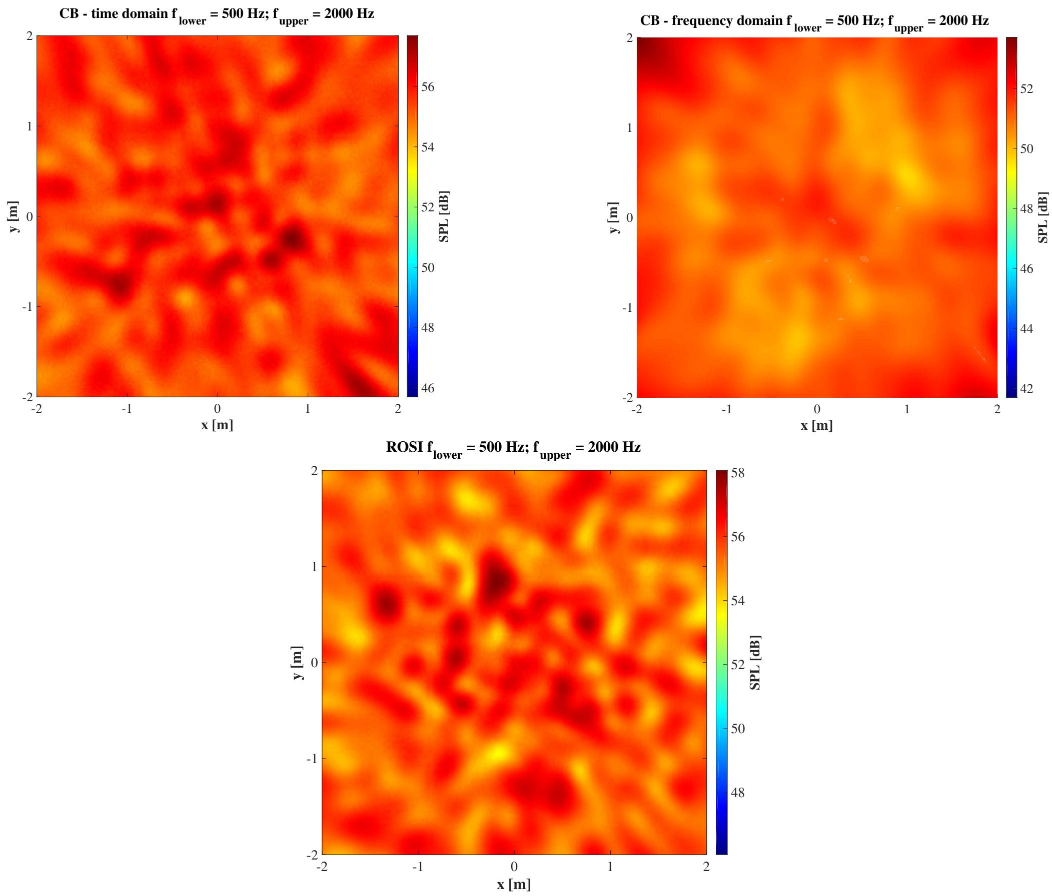

Figure B.40: Left: CB in the time domain. Right: CB in the frequency domain. Center: ROSI. The five-bladed wind turbine rotates at 6.9 Hz. The wind speed of the tunnel is 9 m/s. The signal is filtered into the frequency band 500 Hz - 2000 Hz. A scan grid of 4x4 m^2 with a total of 40000 scan points and a sampling frequency of 50 kHz are employed. The distance from the microphone array is 3 m.

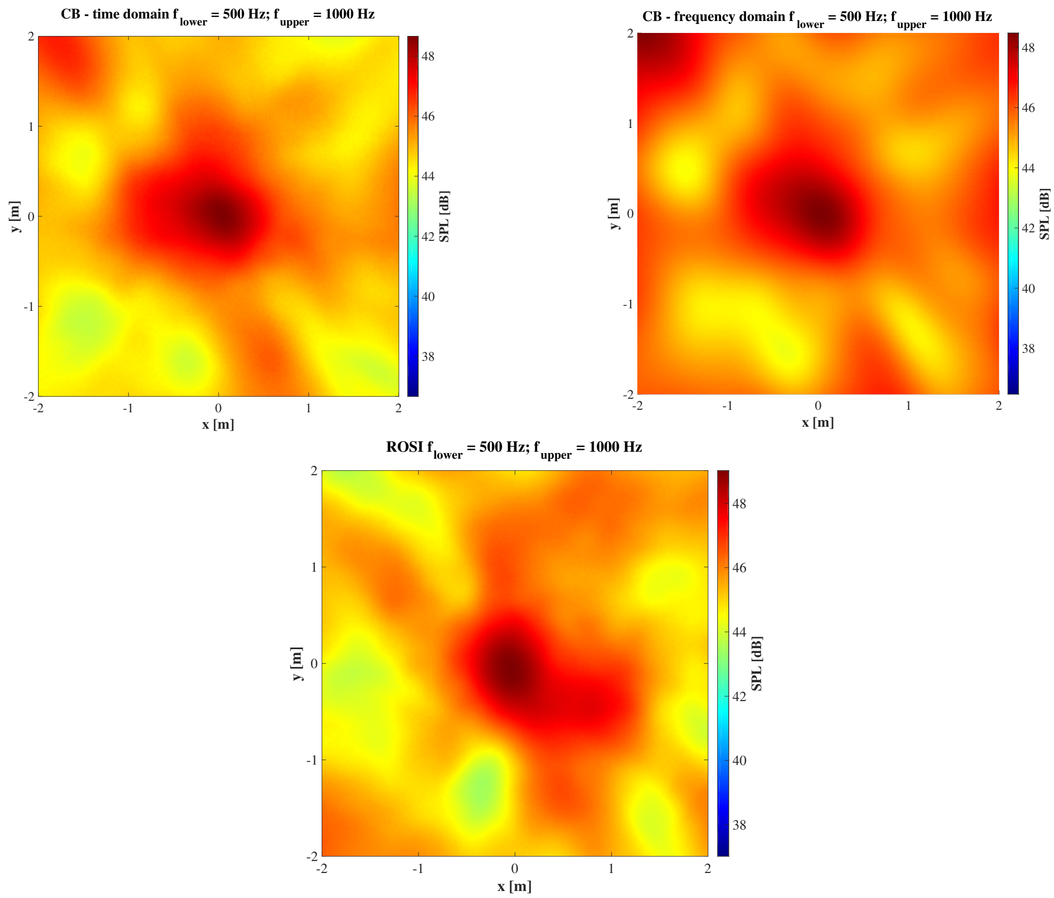

Figure B.41: Left: CB in the time domain. Right: CB in the frequency domain. Center: ROSI. The five-bladed wind turbine rotates at 6.9 Hz. The wind speed of the tunnel is 9 m/s. The signal is filtered into the frequency band 500 Hz - 1000 Hz. A scan grid of 4x4 m^2 with a total of 40000 scan points and a sampling frequency of 50 kHz are employed. The distance from the microphone array is 3 m.

C

In-field experiment

In the research, an additional experiment was performed in-field, specifically on the noise barrier[1] between the road N-470 and the highway A-13 (E-19) in Delft, Netherlands [92]. During the experimental campaign, a small downwind turbine was mounted on top of the noise barrier and acoustic measurements were carried out with a microphone phased array.

First, the experimental set-up is presented. Then, an analysis of the results is provided. Also for this dataset, the high levels of background noise do not allow to localize and to quantify the main noise sources in the wind turbine.

C.1. Experimental set-up

This section illustrates the set-up of the in-field experiment. However, the installation of the downwind turbine on top of the noise barrier is not here described. For further information, the interested reader is referred to the Thesis report of Vilarasau Amoros [92].

C.1.1. Microphone phased array

The acoustic array of 1 x 1 m^2 contains 64 POM-2735P-R microphones, arranged in a multi-arm logarithmic spiral configuration (see Figure C.1). Each microphone has a length of 60 mm and a diameter of 15 mm. The frequency range of these microphones is between 20 Hz and 20 kHz. All the microphones were connected to the data acquisition system (DAS), also called Camera 3 [25]. The array was tilted of approximately 45 degrees and placed on the metal structure shown on the left-side of Figure C.2.

C.1.2. WindLeaf downwind turbine

The acoustic measurements were carried out on the three-bladed small wind turbine, fabricated by the Wind-Challenge company. The horizontal-axis wind turbine has a downwind configuration, which allows to align the rotor to the wind without a yaw drive mechanism. However, in order to have a constant distance from the microphone array, in the measurements the rotor of the turbine was locked in a fixed position, shown on the right-side of Figure C.2. The resulting distance between the center of rotation of the turbine and the center of the array is 2.7 m. The start-up wind speed, the rated wind speed and the cut-out wind speed correspond to 1.5 m/s, 9.5 m/s and 21 m/s respectively. The rated power of the turbine is 0.7 kW and the rotor diameter is 1.7 m [95].

[1]For further information about the noise barrier, the reader is referred to the Thesis report of Vilarasau Amoros [92].

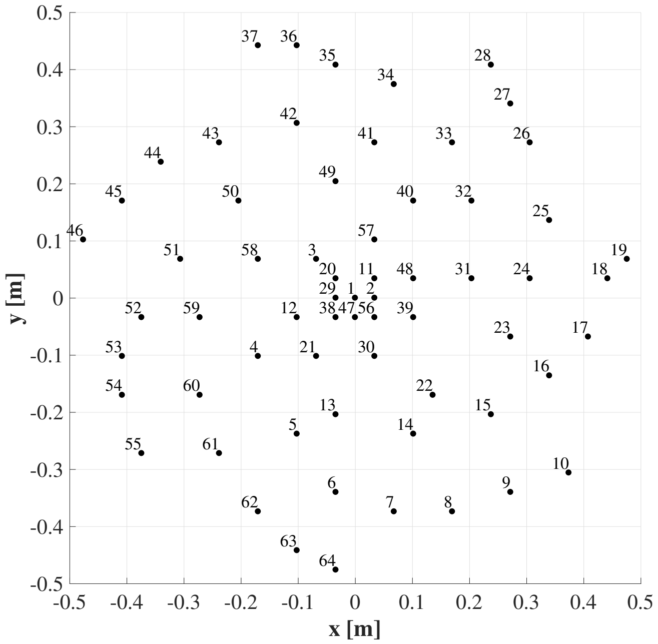

Figure C.1: Microphone array configuration used in the In-Field experiment. The array is 1x1 m^2 and the 64 microphones are arranged in a multi-arm logarithmic spiral configuration.

Figure C.2: Left: Configuration used in the In-Field experiment. The noise barrier and the wind turbine are shown. The microphone array was placed on the metal structure. Right: WindLeaf downwind turbine.

C.2. Results

In the analysis, a sampling frequency of 50 kHz and a scan grid of 4 x 4 m^2 with a total of 40000 scan points[2] are employed. The distance between the center of rotation and the microphone array corresponds to 2.7 m. The measured data is separated in time blocks of 25000 samples (Δt = 500 ms) and windowed using a Hanning weighting function. The signal is filtered into the frequency band 500 Hz - 2000 Hz, where the wind turbine noise is expected [60].

During the campaign, it was not possible to measure neither the background noise or the wind speed. Only one experimental dataset is here assessed. In this case, the rotational speed of the wind turbine is 6.6 Hz. CB in the time domain, CB in the frequency domain and ROSI are applied to the data. The resulting acoustic images are depicted in Figure C.3. As it can be observed, the high levels of background noise, mainly produced by the vehicles on the road, do not allow to correctly localize and quantify the wind turbine noise.

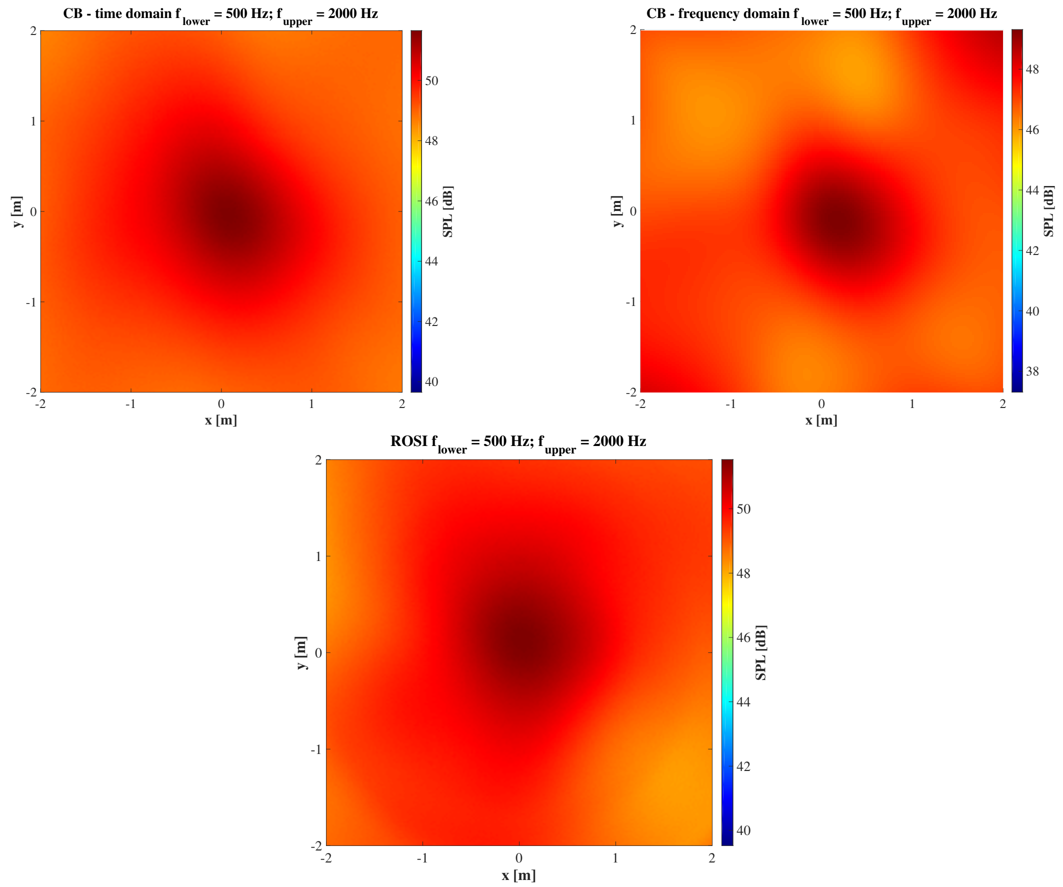

Figure C.3: Left: CB in the time domain. Right: CB in the frequency domain. Center: ROSI. The three-bladed wind turbine rotates at 6.6 Hz. The signal is filtered into the frequency band 500 Hz - 2000 Hz. A scan grid of 4x4 m^2 with a total of 40000 scan points and a sampling frequency of 50 kHz are employed. The distance from the microphone array is 2.7 m.

[2]200 scan points are used in the x and in the y direction, which lead to a total of 40000 scan points.

Bibliography

[1] G.R.A.S. Sound & Vibration – 40PH CCP Free–field array microphone. URL https://www.gras.dk/products/special-microphone/array-microphones/product/178-40ph.

[2] R. K. Amiet. Acoustic radiation from an airfoil in a turbulent stream. *Journal of Sound and Vibration*, 41(4):407–420, 1975.

[3] R. K. Amiet. Noise due to turbulent flow past a trailing edge. *Journal of Sound and Vibration*, 47(3):387–393, 1976. ISSN 10958568. doi: 10.1016/0022-460X(76)90948-2.

[4] H. Arbey and J. Bataille. Noise generated by aifoil profiles placed in a uniform laminar flow. *Journal of Fluid Mechanics*, 134:33–47, 1983.

[5] C. Arce León, R. Merino-Martínez, D. Ragni, F. Avallone, and M. Snellen. Boundary layer characterization and acoustic measurements of flow-aligned trailing edge serrations. *Experiments in Fluids*, 57(12):1–22, 2016. ISSN 07234864. doi: 10.1007/s00348-016-2272-z.

[6] E. Arcondoulis, C. Doolan, and A. Zander. Airfoil noise measurements at various angles of attack and low Reynolds number. *Proceedings of ACOUSTICS*, (November):1–8, 2009. URL http://www.acoustics.asn.au/conference{_}proceedings/AAS2009/papers/p48.pdf.

[7] E. Arcondoulis, C. Doolan, A. Zander, and L. Brooks. A review of trailing edge noise generated by airfoils at low to moderate Reynolds number. *Acoustics Australia/ Australian Acoustic Society*, 38:135–139, 2010.

[8] Ashish. How Are Anechoic Chambers, The Quietest Rooms On Earth, Made?, 2016. URL http://sciabc.us/LRCuU.

[9] M. Bergey. Bergey Windpower's 10 kW Residential Wind Turbine becomes the First Certified Small Wind Turbine in America, 2011.

[10] W.K. Blake. *Mechanics of Flow-Induced Sound and Vibration*. 1986.

[11] K. S. Brentner and F. Farassat. An analytical comparison of the acoustic analogy and Kirchhoff formulation for moving surfaces. *AIAA Journal*, 1998.

[12] T. F. Brooks and T. H. Hodgson. Trailing edge noise prediction from measured surface pressures. *Journal of Sound and Vibration*, 78(1):69–117, 1981.

[13] T. F. Brooks, S. Pope, and M. A. Marcolini. Airfoil Self-Noise and Prediction. *NASA Reference Publication 1218*, pages 1–142, 1989. ISSN 14786095. doi: 10.1080/09524622.2008.9753825. URL http://ntrs.nasa.gov/archive/nasa/casi.ntrs.nasa.gov/19890016302.pdf.

[14] D. Casalino. An advanced time approach for acoustic analogy predictions. *Journal of Sound and Vibration*, 261:583–612, 2003.

[15] D. Casalino, A. Hazir, E. Fares, B. Duda, and M. R. Khorrami. On the Connection Between Flap Side-Edge Noise and Tip Vortex Dynamics. 2015.

[16] M. Cerna and A. F. Harvey. The Fundamentals of FFT-Based Signal Analysis and Measurement. *Spectrum*, 41(July):1–20, 2000. doi: AN-041. URL http://www.electronics.teipir.gr/PersonalPages/papageorgas/download/dsp{_}lab{_}I/MATLAB{_}material/FFT{_}fundamentals.pdf.

[17] CES-admin. 400 Watts 12V OR 24V Wind Turbine with Controller, 2016. URL http://cavite-ecosolutions.com/category/wind-turbine/.

[18] T. Colonius and K. L. Sanjiva. Computational aeroacoustics: progress on nonlinear problems of sound generation. *Progress in Aerospace Sciences*, 40:345–416, 2004.

[19] N. Curle. Influence of Solid Boundaries upon Aerodynamic Sound. *Proceedings of the Royal Society of London. Series A, Mathematical and Physical Sciences*, 231(1187):505–514, 1955.

[20] A. Dalla Riva, J. Hethey, and A. Vitina. IEA Wind TCP Task 26 - Impacts of Wind Turbine Technology on the System Value of Wind in Europe. Technical report, 2017.

[21] G. Desquesnes, M. Terracol, and P. Sagaut. Numerical investigation of the tone noise mechanism over laminar airfoils. *Journal of Fluid Mechanics*, 591:155–182, 2007.

[22] J. Doolan, D. J. Moreau, and L. A. Brooks. Wind turbine noise mechanisms and some concepts for its control. *Acoustics Australia*, 40(1):7–13, 2012. ISSN 08146039.

[23] R. P. Dougherty. Beamforming In Acoustic Testing. In T.J. Mueller, editor, *Aeroacoustic Measurements*, pages 62–97. Berlin, springer edition, 2002. ISBN 3-540-41757-5.

[24] A. V. Dovgal, V. V. Kozlov, and A. Michalke. Laminar boundary layer separation: Instability and associated phenomena. *Progress in Aerospace Sciences*, 30(1):61–94, 1994. ISSN 03760421. doi: 10.1016/0376-0421(94)90003-5.

[25] Aircraft Noise Effects and Climate. Acoustic camera user manual, 2014.

[26] J. E. Ffowcs Williams and L. H. Hall. Aerodynamic sound generation by turbulent flow in the vicinity of a scattering half plane. *Journal of Fluid Mechanics*, 40(4):657–670, 1970.

[27] J. E. Ffowcs Williams and D. L. Hawkings. Sound generation by turbulence and surfaces in arbitray motion. *Philosophical Transactions of the Royal Society of London. Series A, Mathematical and Physical Sciences*, 264(1151):321–342, 1969.

[28] GWEC. Global Wind Report. Annual Market Update 2017. *Global Wind Energy Council*, page 72, 2017.

[29] C. H. Hansen. Fundamentals of Acoustics. pages 1–26, 2003.

[30] F. J. Harris. On the use of windows for harmonic analysis with the discrete Fourier transform. *Proceedings of the IEEE*, 66(1):51–83, 1978. ISSN 0018-9219. doi: 10.1109/PROC.1978.10837. URL http://ieeexplore.ieee.org/lpdocs/epic03/wrapper.htm?arnumber=1455106.

[31] J. P. Harrison. Wind Turbine Noise. *Bulletin of Science, Technology & Society*, 31(4):256–261, 2011. ISSN 0270-4676. doi: 10.1177/0270467611412549. URL http://journals.sagepub.com/doi/10.1177/0270467611412549.

[32] H. P. Horton. Laminar separation bubbles in two and three-dimensional incompressible flow. 1968.

[33] C. Horvath and B. Kocsis. Towards a Doppler effect based beamforming method for rotating coherent noise sources. 2018.

[34] D. Howard and J. Angus. *Acoustic and Psychoacoustics.* 2008.

[35] M. S. Howe. A review of the theory of trailing edge noise. *Journal of Sound and Vibration*, 61(3):4367–465, 1978.

[36] M. S. Howe. Trailing Edge Noise at Low Mach Numbers, Part 2: Attached and separated edge flows. *Journal of Sound and Vibration*, 234(5):761–775, 2000.

[37] G. P. Howell, A. J. Bradley, M. A. Mccormick, and J. D. Brown. De-Dopplerization and acoustic imaging of aircraft flyover noise measurements. *Journal of Sound and Vibration*, 105:151–167, 1986.

[38] H. H. Hubbard and K. P. Shepherd. Wind turbine acoustics. *NASA Technical Paper*, 3057:20320–20377, 1990. ISSN 1845642058. doi: 10.2495/978-1-84564. URL http://ntrs.nasa.gov/archive/nasa/casi.ntrs.nasa.gov/19910007366.pdf.

[39] IEC. Wind turbines – Part 2: Design requirements for small wind turbines. 2006. URL https://webstore.iec.ch/p-preview/info{_}iec61400-2{%}7Bed2.0{%}7Den{_}d.pdf.

[40] ISO. ISO:12001 Acoustics — Noise emitted by machinery and equipment — Rules for the drafting and presentation of a noise test code.

[41] A. KC, J. Whale, and T. Urmee. Urban wind conditions and small wind turbines in the built environment: A review. *Renewable Energy*, 131:268–283, 2018. ISSN 09601481. doi: 10.1016/j.renene.2018.07.050. URL https://linkinghub.elsevier.com/retrieve/pii/S0960148118308474.

[42] W. Kellermann. *Microphone Array Signal Processing*, volume 2. 2009. ISBN 9783540786115. doi: 10.1007/978-3-642-11130-3. URL http://link.springer.com/content/pdf/10.1007/978-3-540-78612-2.pdf.

[43] M. Kerscher, J. Heimann, C. Puhle, K. Oeckel, C. Friebe, and R. Krause. Application of rotational beamforming algorithms on fast rotating sound sources. 2018.

[44] J. W. Kim, S. Haeri, and P. F. Joseph. On the reduction of aerofoil-turbulence interaction noise associated with wavy leading edges. *Journal of Fluid Mechanics*, 792:526–552, 2016.

[45] F. Le Courtois, J. Thomas, F. Poisson, and J. Pascal. Genetic optimisation of a plane array geometry for beamforming. Application to source localisation in a high speed train. *Journal of Sound and Vibration*, 371:78–93, 2016.

[46] S. Lee, S. Lee, and S. Lee. Numerical modeling of wind turbine aerodynamic noise in the time domain. *Acoustical Society of America*, 133(2), 2013.

[47] M. J. Lighthill. On Sound Generated Aerodynamically. I. General Theory. *Proceedings of the Royal Society of London. Series A, Mathematical and Physical Sciences*, 211(1107):564–587, 1952.

[48] L. E. M. Lignarolo, D. Ragni, C. Krishnaswami, Q. Chen, C. J. Simão Ferreira, and G. J.W. van Bussel. Experimental analysis of the wake of a horizontal-axis wind-turbine model. *Renewable Energy*, 70:31–46, 2014. ISSN 09601481. doi: 10.1016/j.renene.2014.01.020. URL http://dx.doi.org/10.1016/j.renene.2014.01.020.

[49] L. E. M. Lignarolo, D. Ragni, C. Simao Ferreira, and G. J.W. van Bussel. Experimental quantification of the entrainment of kinetic energy and production of turbulence in the wake of a wind turbine with Particle Image Velocimetry. *32nd ASME Wind Energy Symposium*, (January):1–12, 2014. doi: 10.2514/6.2014-0706. URL http://arc.aiaa.org/doi/abs/10.2514/6.2014-0706{%}5Cnhttp://arc.aiaa.org/doi/10.2514/6.2014-0706.

[50] S. Luesutthiviboon. Design of an Optimized Acoustic Array for Aero-acoustic Research in an Open-jet Anechoic Wind Tunnel. Technical report, 2017.

[51] A. M. N. Malgoezar, M. Snellen, R. Merino-Martínez, D. G. Simons, and P. Sijtsma. On the use of global optimization methods for acoustic source mapping. *The Journal of the Acoustical Society of America*, 453, 2017.

[52] J. F. Manwell, J.G. Mcgowan, and A. L. Rogers. *Wind Energy Explained - Theory, Design and Application*. Second edition, 2009. ISBN 9780470015001.

[53] R. Merino-Martínez, A. Rubio Carpio, C. H. C. Vlemmix, F. Avallone, M. Kotsonis, D. Ragni, and M. Snellen. Aeroacoustic design and characterization of a vertical open-jet anechoic wind tunnel. *AIAA Journal*, (under review process), 2018.

[54] P. J. Moriarty and S. Oerlemans. Wind tunnel aeroacoustic tests of six airfoils for use on small wind turbines. In *42nd AIAA Aerospace Science Meeting and Exhibit*, 2004.

[55] T. J. Mueller and J. D. Delaurier. Aerodynamics of Small Vehicles. pages 89–111, 2003. doi: 10.1146/annurev.fluid.35.101101.161102.

[56] W. Musial and B. Ram. Large-Scale On-shore Wind Power in the United States: Assessment of Opportunities and Barriers. *NREL*, (September), 2010. doi: 10.2172/990101.

[57] E. C. Nash, M. V. Lowson, and A. McAlpine. Boundary layer instability noise on airfoils. *Journal of Fluid Mechanics*, 382(27), 1999.

[58] S. Oerlemans. Introduction to Aeroacoustics, 2016.

[59] S. Oerlemans and P. Sijtsma. Determination of Absolute Levels from Phased Array Measurements Using Spatial Source Coherence. *8th AIAA/CEAS Aeroacoustics Conference & Exhibit*, 2002. doi: 10.2514/6.2002-2464. URL http://arc.aiaa.org/doi/abs/10.2514/6.2002-2464.

[60] S. Oerlemans, P. Sijtsma, and B. Méndez López. Location and quantification of noise sources on a wind turbine. *Journal of Sound and Vibration*, 299(4-5):869–883, 2007. ISSN 10958568. doi: 10.1016/j.jsv.2006.07.032.

[61] R. W. Paterson, P. G. Vogt, M. R. Fink, and C. L. Munch. Vortex Noise of Isolated Airfoils. *Journal of Aircraft*, 10(5):296–302, 1973. doi: hhttps://doi.org//10.2514/3.60229.

[62] L.R. Rabiner and B. Juang. Fundamentals of signal processing. *VKI Laser Velocimetry*, pages 350–352, 1993. ISSN 00160032. doi: 10.1016/0016-0032(60)90684-0. URL http://adsabs.harvard.edu/abs/1991VKILV...1Q....P.

[63] RERL. Renewable Energy Research Lab, 2002. URL www.ecs.umass.edu/mie/labs/rerl/.

[64] P. Ricciardi. *Elementi di acustica e illuminotecnica*. Group Italia, Milan, 2009. ISBN 978-88-386-6010-8.

[65] A. L. Rogers, J. F. Manwell, and S. Wright. Wind turbine acoustic noise. *Renewable Energy Research Laboratory, Amherst: University of Massachusetts*, (January), 2006. ISSN 09574565. doi: 10.1260/0957456042872777.

[66] T. D. Rossing. *Handbook of Acoustics*, volume 77. 2009. ISBN 9780387304465. doi: 10.1119/1.3197171. URL http://aapt.scitation.org/doi/10.1119/1.3197171.

[67] A. Rubio Carpio, R. Merino-Martínez, F. Avallone, D. Ragni, M. Snellen, and S. van der Zwaag. Broadband trailing edge noise reduction using permeable metal foams. In *46th International Congress and Exposition of Noise Control Engineering, 27–30 August, 2017, Hong Kong*, pages 4373–4383, 2017.

[68] A. Rubio Carpio, F. Avallone, and D. Ragni. On the Role of the Flow Permeability of Metal Foams on Trailing Edge Noise Reduction. *AIAA Journal*, pages 2018–2964, 2018.

[69] G.J.J. Ruijgrok. *Elements of Aviation Acoustics*. 1993. ISBN 90-6275-899-1.

[70] M. Sagrillo. *Wind turbines and Noise*. 1997.

[71] R.D. Sandberg, L.E. Jones, N.D. Sandham, and P.F. Joseph. Direct numerical simulations of tonal noise generated by laminar flow past airfoils. *Journal of Sound and Vibration*, 320:838–858, 2009.

[72] E. Sarradj, C. Fritzsche, T. Geyer, and J. Giesler. Acoustic and aerodynamic design and characterization of a small-scale aeroacoustic wind tunnel. *Applied Acoustics*, 70:1073–1080, 2009.

[73] SET MSc course - Wind Energy. Turbine Topologies, 2006. URL http://mstudioblackboard.tudelft.nl/duwind/Windenergyonlinereader/Static{_}pages/upwind{_}downwind.htm.

[74] M. L. Shaltout, Z. Yan, D. Palejiya, and D. Chen. Tradeoff analysis of energy harvesting and noise emission for distributed wind turbines. *Sustainable Energy Technologies and Assessments*, 10:12–21, 2015. ISSN 22131388. doi: 10.1016/j.seta.2015.01.005. URL http://dx.doi.org/10.1016/j.seta.2015.01.005.

[75] P. Sijtsma. Experimental techniques for identification and characterisation of noise sources. *Advances in Aeroacoustics and Applications, VKI Lecture Series*, 5(April):15–19, 2004.

[76] P. Sijtsma. Using phased array beamforming to locate broadband noise sources inside a turbofan engine. Technical Report June, 2006.

[77] P. Sijtsma. Phased Array Beamforming Applied to Wind Tunnel And Fly-Over Tests. Technical report, 2010. URL http://papers.sae.org/2010-36-0514/.

[78] P. Sijtsma, S. Oerlemans, and H. Holthusen. Location of rotating sources by phased array measurements. *7th AIAA/CEAS Aeroacoustics Conference*, (March):1–13, 2001. doi: 10.2514/6.2001-2167.

[79] D.G. Simons. Aircraft Noise and Emissions - AE4431, 2017.

[80] M. Snellen, R. Merino-Martínez, and D. G. Simons. Assessment of Noise Variability of Landing Aircraft Using Phased Microphone Array. *Journal of Aircraft*, 54(6):1–11, 2017. ISSN 0021-8669. doi: 10.2514/1.C033950. URL `http://dx.doi.org/10.2514/1.C033950`.

[81] C. Tam. Discrete tones of isolated airfoils. *Journal Acoustic Society*, 55:1173–1177, 1974.

[82] B. Tóth and J. Vad. Fourier analysis of beamforming data at the tip of an axial fan rotor. *Periodica Polytechnica Mechanical Engineering*, 60(3):152–158, 2016. ISSN 1587379X. doi: 10.3311/PPme.8935.

[83] B. Toth, T. Kalmar-Nagy, and J. Vad. Rotating Beamforming with uneven microphone placements. 2018.

[84] Y. Tripanagnostopoulos, S. Tselepis, M. Souliotis, J. K. Tonui, and A. Christodoulou. Practical aspects for small wind turbine applications. *Proc. in Int. EWEC 2004 Conf., Track*, 7, 2004.

[85] TU Delft University. Vertical Low Turbulence Tunnel, . URL `https://www.tudelft.nl/en/ae/organisation/departments/aerodynamics-wind-energy-flight-performance-and-propulsion/facilities/vertical-low-turbulence-tunnel/`.

[86] TU Delft University. Open Jet Facility, . URL `https://www.tudelft.nl/en/ae/organisation/departments/aerodynamics-wind-energy-flight-performance-and-propulsion/facilities/open-jet-facility/`.

[87] J. R. Underbrink and R. P. Dougherty. Array design of non-intrusive measurement of noise sources. In *Noise-Con*, 1996.

[88] J.R. Underbrink. Aeroacoustic Phased Array Testing in Low Speed Wind Tunnels. In T. Mueller, editor, *Aeroacoustic Measurements*, pages 98–215. Berlin, springer edition, 2002.

[89] UNFCCC. Paris Agreement. *Conference of the Parties on its twenty-first session*, (December):32, 2015. ISSN 1098-6596. doi: FCCC/CP/2015/L.9/Rev.1. URL `http://unfccc.int/resource/docs/2015/cop21/eng/l09r01.pdf`.

[90] H. Van den Akker and R. F. Mudde. *Transport Phenomena - The Art of Balancing*. 2014. ISBN 978-90-6562-3584.

[91] I.L. Ver and L. L. Beranek. *Noise and Vibration Control Engineering - Principles and Applications (2nd Edition)*. John Wiley & Sons, 2006. ISBN 978-0-471-44942-3.

[92] A. Vilarasau Amorós. Turning noise-barriers into sustainable energy systems - A full approach from experimental data to energy and cost modeling with a focus on urban wind, 2018.

[93] S. Wagner, R. Bareiss, and G. Guidati. *Wind Turbine Noise*. Springer Verlag, 1996.

[94] M. Wang, J. B. Freund, and S. K. Lele. Computational Prediction of Flow-Generated Sound. *Annual Review of Fluid Mechanics*, 38(1):483–512, 2006. ISSN 0066-4189. doi: 10.1146/annurev.fluid.38.050304.092036. URL `http://www.annualreviews.org/doi/10.1146/annurev.fluid.38.050304.092036`.

[95] WindChallenge. Windleaf Specifications. URL `https://windchallenge.com/the-windleaf/{#}the-windleaf`.

[96] WindEurope. Wind energy in Europe: Scenarios for 2030. Technical report, 2017. URL `https://windeurope.org/wp-content/uploads/files/about-wind/reports/Wind-energy-in-Europe-Scenarios-for-2030.pdf{%}0Ahttp://www.ewea.org/fileadmin/files/library/publications/reports/EWEA-Wind-energy-scenarios-2030.pdf`.

[97] WindEurope. Wind in power 2017. Technical report, 2018. URL `https://windeurope.org/wp-content/uploads/files/about-wind/statistics/WindEurope-Annual-Statistics-2017.pdf`.

[98] WindEurope. Offshore Wind in Europe - key trends and statistics 2017. Technical report, 2018.

[99] J. Winkler, R. D. Sandberg, and S. Moreau. Direct Numerical Simulation of the Self-Noise Radiated by an Airfoil in a Narrow Stream. In *18th AIAA/CEAS Aeroacoustics Conference*, pages 1–15, 2012. ISBN 9781600869327. doi: 10.2514/6.2012-2059.

[100] R. G. Winter, A. M. Steinberg, and D. Attwood. Coherence, 2014.

[101] D. Wood. *Small Wind Turbines - Analysis, Design and Application*. Springer, 2011. ISBN 978-1-84996-174-5. doi: 10.1007/978-1-84996-175-2.

[102] D. Wood. Small Wind Turbines. In *Advances in Wind Energy Conversion Technology*, volume 3, pages 195–211. 2011. ISBN 9783642195358. doi: 10.1007/978-3-540-88258-9. URL http://books.google.com/books?hl=en{&}lr={&}id=LMjTXmTgXJoC{&}oi=fnd{&}pg=PR6{&}dq=Information+Technologies+in+Environmental+Engineering:+New+Trends+and+Challenges{&}ots={_}OFtnJFN1U{&}sig=WIAH21eAnJHempcNp5udXCVQePU.

[103] G. Zechel, A. Zeibig, and M. Beitelschmidt. Time-domain beamforming on moving objects with known trajectories. *3rd Berlin Beamforming Conference*, pages 1–8, 2010.